Thèse de doctorat de

L'UNIVERSITÉ DE BRETAGNE OCCIDENTALE

École Doctorale N° 598
Sciences de la Mer et du littoral
Spécialité : Océanographie Physique et Environnement

Par

Marine DE CARLO

Caractérisation du bruit ambiant atmosphérique d'origine océanique :

Modélisation des microbaroms à l'échelle globale et comparaison avec les observations infrasons du Système de Surveillance International

Thèse présentée et soutenue à Brest, le 15 décembre 2020
Unité de recherche : UMR 6523 Laboratoire d'Océanographie Physique et Spatiale et CEA

Rapporteurs avant soutenance :

Frédéric DIAS
Professeur, University College Dublin

Michel CAMPILLO
Professeur, Université Grenoble-Alpes

Composition du Jury :

Frédéric DIAS
Professeur, University College Dublin / *Rapporteur*

Michel CAMPILLO
Professeur, Université Grenoble-Alpes / *Rapporteur*

Guillaume ROULLET
Professeur, Université de Bretagne Occidentale / *Président du Jury*

France FLOC'H
Maître de Conférence, Institut Universitaire Européen de la Mer

Anne MANGENEY
Professeur, Institut de Physique du Globe de Paris

Lucia GUALTIERI
Assistant Professor, Stanford University

Fabrice ARDHUIN
Directeur de Recherche CNRS, LOPS / *Directeur de thèse*

Alexis LE PICHON
Directeur de Recherche CEA / *Co-directeur de thèse*

Invité :

Pierrick MIALLE Chargé de Recherche IDC, CTBTO

ACKNOWLEDGEMENTS 💬

feedbacks.

CONTENTS

LIST OF FIGURES

LIST OF TABLES

ACRONYMS

ACC Antarctic Circumpolar Current.

AH13 Ardhuin & Herbers (2013).

ARISE Atmospheric dynamics Research InfraStruture in Europe.

BK73 Brekhovskikh et al. (1973).

CPO Coefficient of Predicted Observations.

CTBT Comprehensive Nuclear-Test-Ban Treaty.

CTBTO Comprehensive Nuclear-Test-Ban Treaty Organization.

DC20 De Carlo et al. (2020).

ECMWF European Center for Medium-range Weather Forecast.

FPR False Positive Rate.

GJI Geophysical Journal International.

GRL Geophysical Research Letters.

HWM Horizontal Wind Model.

IDC International Data Center.

IFREMER Institut Français de Recherche pour l'Exploitation de la MER.

IFS Integrated Forecast System.

IMS International Monitoring System.

LH50 Longuet-Higgins (1950).

LHH Longuet-Higgins-Hasselmann.

MFON Model False, Observations Negative, also called true negative.

MFOP Model False, Observations Positive, also called false negative.

MSIS Mass, Spectrometer, Incoherent Scatter.

MTON Model True, Observations Negative, also called false positive.

MTOP Model True, Observations Positive, also called true positive.

NH Northern Hemisphere.

NWP Numerical Weather Prediction.

PE Parabolic Equations.

PMCC Progressive Multi-Channel Correlation.

SH Southern Hemisphere.

SSW Sudden Stratospheric Warming.

TPR True Positive Rate.

W07 Waxler et al. (2007).

WG06 Waxler & Gilbert (2006).

WW3 WAVEWATCH III®.

INTRODUCTION

Contents

1.1 Microbaroms and microseisms

All around the world, coherent acoustic signals originating from the ocean are continuously recorded at infrasound stations in the [0.1 - 0.6] Hz frequency band, with an energy peak around 0.2 Hz and a typical amplitude of few microbars. As these oceanic signals are ubiquitous and can hide signals of interest in the framework of the Comprehensive nuclear Test Ban Treaty, they are also known as ocean generated ambiant noise. This coherent noise was first observed in the early forties (Shuleykin, 1935; Benioff & Gutenberg, 1939; Baird & Banwell, 1940) and was named microbaroms by Benioff & Gutenberg (1939), due to the signals amplitude and by analogy with microseisms which are the corresponding noise in seismic signals (see Fig. 1.1).

Back in the beginning of the twentieth century, the seismic technology was far more mature than the infrasound one, thus, microseisms were observed and studied about 40 years prior to microbaroms. As a matter of fact, Benioff & Gutenberg (1939) performed one of the first observations of microbaroms while trying to determine microseisms generation phenomenon, and the generation theory was first solely developed for microseisms (Longuet-Higgins, 1950; K. Hasselmann, 1963).

Microbaroms and microseisms are signals with similar characteristics: amplitudes variations of few microbars and few micrometers respectively and frequencies around 0.2 Hz. Those similarities were investigated shortly after microbaroms first observations (Baird & Banwell, 1940; Gutenberg & Benioff, 1941), however, the definitive idea of a similar generation phenomenon came later and is generally associated with the works of Donn & Posmentier (1967) and Donn & Naini (1973). It is now known that the microbaroms and the most energetic microseisms are generated by non-linear second order interaction of nearly opposing waves.

A detailed knowledge of wave properties accurate to second order in the surface elevation slope is therefore needed in this work in order to study microbaroms and is developed in the following section 1.1.1.5. The second ordrer properties relevant for microseism and microbarom generation were first discovered by Miche (1944) who gave a full second order solution for monochromatic waves. Their generation to a spectrum of waves was given by K. Hasselmann (1962, 1963). A critical aspect is that the second order motion is dominated by acoustic-gravity modes over most of the ocean water column, so that the effect of water
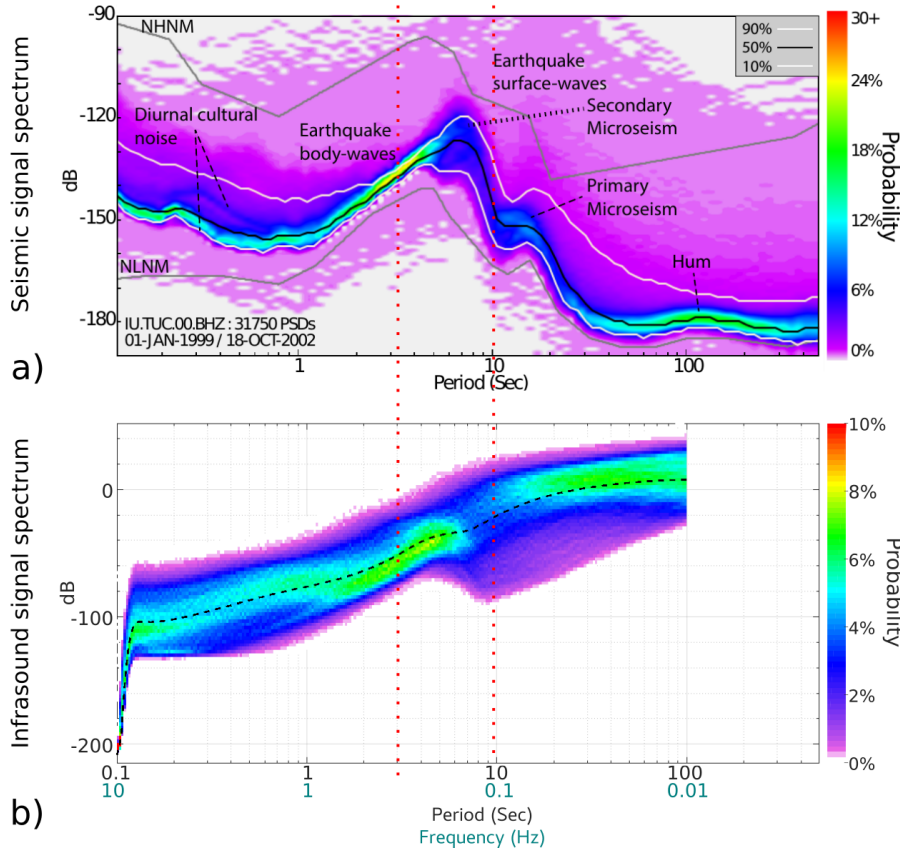
Figure 1.1 – Probability density function of power spectral density for a) seismic signal recorded at Tucson, Arizona from 01 Jan 1999 to 18 Oct 2002 (from McNamara & Boaz, 2019) and b) acoustic (infrasound) signal recorded at I33MG, Madagascar from 01 Jan 2018 to 31 Dec 2018 (courtesy of J. Vergoz). Red to green colours indicate the highest probability power levels at each period or frequency. Red dotted vertical lines highlight the microbaroms and microseisms range.

compressibility and seafloor deformations cannot be neglected. This was first realized by Longuet-Higgins (1950). The work of Brekhovskikh et al. (1973) on which most of the present thesis is based is a generalization of the Longuet-Higgins (1950) theory to an "active" air layer (i.e. with feedbacks on the ocean) over the ocean layer, and the use of a full spectral description of ocean waves following K. Hasselmann (1962, 1963, 1966).

1.1.1 Ocean waves interactions

The following section is based on the ocean waves textbook by Fabrice Ardhuin (Ardhuin, 2019, and references therein) and gives a short introduction on ocean waves, their representation and their modelling. This section's purpose is to allow the understanding of further developments.

The term 'waves' encompasses various types of ocean surface movements - from tides and tsunamis to small ripples in the surface - that can be represented as near-periodic variations of the sea surface elevation. All the aforementioned waves arise from different generation processes such as wind, Moon tidal effects or earthquakes yielding to different characteristic sizes and frequencies. Of interest for this study are the waves commonly known as ocean waves - as in the waves observed on the beach. These are ranging from few meters to few kilometres with periods of 1 to 30 s, and are generated by wind processes.

The common life cycle of waves consists of generation, propagation and dissipation. Generation and dissipation are complex phenomena (and still very active research fields) that are commonly parametrized in wave models. Such is the case of the wave action model WAVEWATCH III® used in this thesis (see Section 1.1.3.1). Therefore, discussions about

these phenomenon are out of the scope of this work. On the other hand, propagation is well known from earlier works (Munk & Traylor, 1947; Longuet-Higgins, 1957b; Munk et al., 1963; Mei, 1989) and the resulting equations describing the wave flow are needed for further developments of the interaction term between waves, thus propagation and these equations are described in this section.

The mechanics of the ocean wave motion are driven by an oscillating pressure gradient that is associated to the gravity combined with an oscillating sea level. These pressure gradients generate motions in the vertical plane that lead to a propagation of the surface elevation pattern. Due to properties of the fluid - incompressible and irrotational - horizontal displacements can not exist without vertical ones. Thus, without dissipation, the wave movement is self-sustained due to the gravity and ocean waves are 'surface gravity waves'. In the present work we consider only surface gravity waves with periods 2-20 s, which are predominantly generated by winds blowing over the ocean. For this reason, these waves are also often called 'wind waves'.

1.1.1.1   Notations

In cartesian coordinates $(x, y, z) = (\mathbf{x}, z)$, the bottom, ocean and atmosphere layers are mathematically defined by their vertical levels (z is oriented upward). The mean sea level is set at $z = 0$, and the free surface (interface between ocean and atmosphere) is defined by $z = \zeta(\mathbf{x}, t)$. The water level $h(\mathbf{x})$ is defined between the mean sea level and the bottom/ocean interface situated at $z = -h(\mathbf{x})$ (see Fig. 1.2).

The ocean is described by its pressure field p, its density ρ_{w} (where w stands for water) and its horizontal $\mathbf{u} = (u_x, u_y)$ and vertical w velocity fields.

Similarly, for the atmosphere the density ρ_a is considered; however, as $\rho_a \ll \rho_{\mathrm{w}}$, for the wave equations ρ_a is supposed to be a constant.
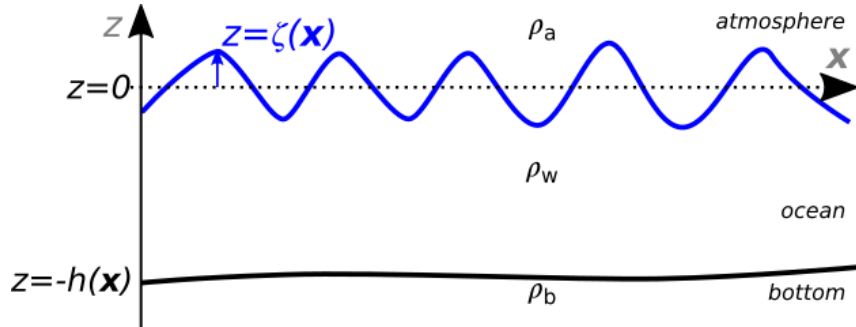
Figure 1.2 – Definition of vertical levels: $z = \zeta$ is the sea level, $z = -h$ is the bottom and the mean sea level is set to 0.

1.1.1.2   Ocean waves representations

In order to study these ocean gravity waves, and their local statistical properties - also called sea state - two representations coexist, the wave-by-wave analysis and the spectral analysis. These representations are shortly described here:

1. **The wave-by-wave analysis** is a way of describing the sea surface elevation with wave height statistics (see Fig. 1.3b and 1.3d). It comes from sea surface elevation time series. A wave is defined between two crossings of the mean-sea-level by the sea-surface going down ('down' instead of 'up' is a convention). For each wave, the period T is defined - as the time between the two crossings - and the wave height H is calculated from the sea surface elevation difference between the corresponding crest - maximum of elevation - and trough - minimum of elevation. Then the wave height distribution can be represented. The Rayleigh distribution is a good estimate of the height distribution for 98% (of the distribution). The main limitation of this distribution concerns extreme heights, thus the wave height distribution has been undergoing some refinements for these extreme waves and it is still an active research field.
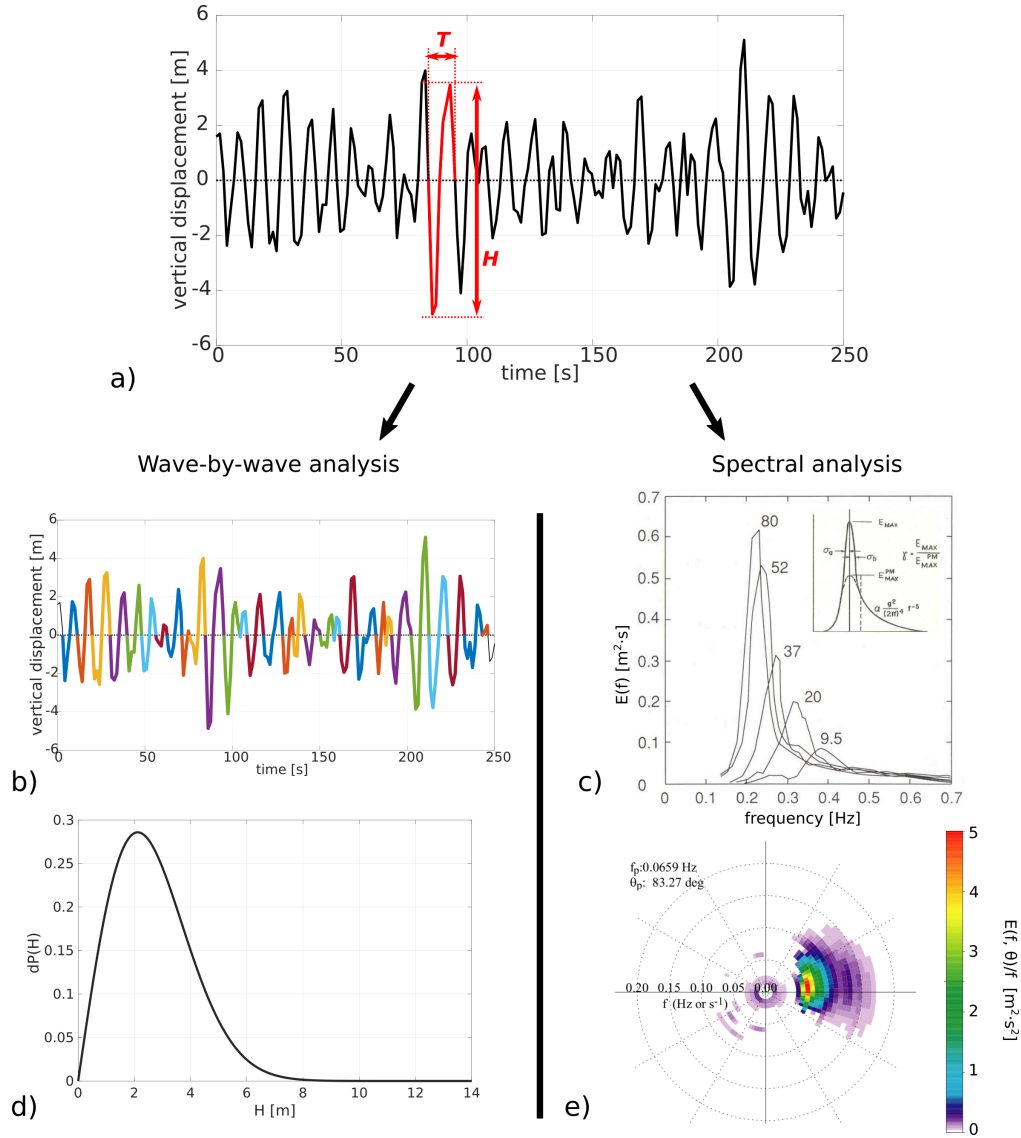
Figure 1.3 – From the time series of sea surface elevation (a) to the waves representations. In the wave-by-wave analysis, one considers the wave height (b) and work from the wave height probability density (d). In the spectral analysis, both non directional (c) and directional (e) spectra of the sea surface elevation are considered. c) Measured spectra on September 15, 1968 at 11h during JONSWAP experiment, with, inset, the proposed parameters for the JONSWAP spectrum. Numbers indicate the fetch in kilometers (K. Hasselmann et al., 1973). e) Example of frequency-direction wave spectra, divided by frequency, computed from 8 m depth pressure measurements in Duck, NC, October 19, 1994, 7:00 (EST) (Ardhuin, 2019).

2. **The spectral analysis** relies on the Fourier decomposition of the sea surface elevation record $\zeta(t)$ as a continuous sum of sine waves with different frequencies and random phases. When considering an elevation that varies spatially, the general form of the Fourier decomposition (over $N_1 \times N_2$ sine waves) writes as following:

$$\zeta(x, y, t) = \sum_{i=1}^{N_1} \sum_{j=1}^{N_2} a_{i,j} \sin(2\pi f_i t - k_i \cos(\theta_j)x - k_i \sin(\theta_j)y + \Theta_{0,i,j}) \qquad (1.1)$$

where the frequency f_i and the wavenumber k_i are related by the dispersion relation, θ_j is the direction of propagation and $\Theta_{0,i,j}$ is the random phase. This decomposition results in a continuous wave energy density spectrum $E(f, \theta)$ (an example is shown in Fig. 1.3e) describing the wave energy distribution as a function of frequency and

direction:

$$E(f, \theta) = \lim_{\Delta f \to 0} \lim_{\Delta \theta \to 0} \frac{1}{\Delta f \Delta \theta} \left\langle \frac{1}{2} \rho_{\mathrm{w}} g a_{i,j}^2 \right\rangle \tag{1.2}$$

where g is the gravitational acceleration, Δf is the frequency interval or spectral resolution and $\Delta \theta$ is the direction interval or azimuth resolution. $\langle \cdot \rangle$ represents the ensemble mean over various realisations of the process. As one can not observe various realisations of identical sea states in the ocean, the ergodicity theorem (the sea state is supposed to be stationary) is invoked, which allows to use a temporal mean instead of an ensemble mean.

As an example, the typical spectrum for the North Atlantic Ocean as been defined empirically by the JOint North Sea WAve Project (K. Hasselmann et al., 1973) as the JONSWAP spectrum (see Fig. 1.3c), this spectrum roughly peaks at 0.1 Hz. Most of the spectra defined empirically peak around 0.1 Hz, there main differences are for the higher frequencies (around 0.3 Hz).

These two descriptions can be complementary and have different domains of application. Indeed, on one hand the statistical analysis of wave height is particularly used for the design of coastal and oceanic structures. On the other hand, the interest of the spectral method lies on the slow variation - both spatially and temporally - of the spectral density, thus allowing numerical prediction of ocean wave spectra.

1.1.1.3 Eulerian equations

Airy's wave theory (Airy, 1841) is a linear theory for monochromatic waves over a flat bottom ($h(\mathbf{x}) = h$), that gives a good approximation of waves in an ocean more than 50 m deep. This theory is based on the Navier-Stokes equations considering an irrotational motion in an inviscid fluid and on a zero-divergence equation - conservation of mass - as the flow is considered incompressible. As the motion is irrotational the velocity field can write as the gradient of a potential ϕ. Then the horizontal velocity writes $\mathbf{u} = \nabla_{\mathbf{H}} \phi$ - where $\nabla_{\mathbf{H}} = (\partial \cdot / \partial x, \partial \cdot / \partial y)$ - and the vertical velocity writes $w = \partial \phi / \partial z$. Then the Navier-Stokes equations reduces to the Bernoulli equation and the wave equation system writes

$$\frac{\partial \phi}{\partial t} + \frac{1}{2} \left(|\nabla_{\mathbf{H}} \phi|^2 + \left(\frac{\partial \phi}{\partial z} \right)^2 \right) + \frac{p}{\rho_{\mathrm{w}}} + gz = C(t) \tag{1.3}$$

$$\frac{\partial^2 \phi}{\partial x^2} + \frac{\partial^2 \phi}{\partial y^2} + \frac{\partial^2 \phi}{\partial z^2} = 0 \tag{1.4}$$

For the model to be well constrained, boundary conditions are needed. The conditions considered are the continuity of the vertical velocity. At $z = -h$, as the bottom is considered fixed, the vertical velocity is zero. This assumption is typically relaxed when dealing with microseism generation, but the sea floor motion was usually neglected for microbaroms. At the free surface, the continuity of normal velocity gives:

$$w = \nabla \phi \cdot \nabla \zeta + \frac{\partial \zeta}{\partial t} \quad \text{at} \quad z = \zeta \tag{1.5}$$

1.1.1.4 Small perturbations theory - Airy's wave solutions

Classically, to obtain analytical or semi-analytical solutions, the small perturbation theory is applied: the fluid is considered initially at rest and undergoing small perturbations. In practice, this theory defines various scales: the scale where the fluid is at rest, then one with a small perturbing movement, then a smaller movement and so on. The variables can be separated onto different orders as following, where ε is a small parameter

$$\begin{cases} \zeta &= 0 + \varepsilon \zeta_1 + \varepsilon^2 \zeta_2 + \dots \\ \mathbf{u} &= 0 + \varepsilon \mathbf{u_1} + \varepsilon^2 \mathbf{u_2} + \dots \\ w &= 0 + \varepsilon w_1 + \varepsilon^2 w_2 + \dots \\ p &= p_0 + \varepsilon p_1 + \varepsilon^2 p_2 + \dots \end{cases} \tag{1.6}$$

The equations are solved for each order. The order 0 corresponds to the hydrostatic equilibrium where the fluid is at rest and the pressure increases with depth. Waves appear order 1 of the equations, and the first order solution is the approximation known as the Airy wave solution. As the considered wave is monochromatic and unidirectional, ζ_1 writes $a\cos(\mathbf{k} \cdot \mathbf{x} - \sigma t + \Theta_0)$, with a the amplitude, $\mathbf{k}$ the wave vector, and $\sigma = 2\pi f$ the radian frequency, where $k = |\mathbf{k}|$ and σ are related by the dispersion relation

$$\sigma^2 = gk\tanh(kh) \tag{1.7}$$

It comes that the field solutions of the system (1.3)-(1.5), for the waves are

$$\zeta_1(\mathbf{x}, t) = a\cos(\mathbf{k} \cdot \mathbf{x} - \sigma t + \Theta_0) \tag{1.8}$$

$$\mathbf{u}_1(\mathbf{x}, z, t) = a\frac{\mathbf{k}}{k}\sigma\frac{\cosh(kz + kh)}{\sinh(kh)}\cos(\mathbf{k} \cdot \mathbf{x} - \sigma t + \Theta_0) \tag{1.9}$$

$$w_1(\mathbf{x}, z, t) = a\sigma\frac{\sinh(kz + kh)}{\sinh(kh)}\sin(\mathbf{k} \cdot \mathbf{x} - \sigma t + \Theta_0) \tag{1.10}$$

$$p_1(\mathbf{x}, z, t) = \rho_\text{w}ga\frac{\cosh(kz + kh)}{\cosh(kh)}\cos(\mathbf{k} \cdot \mathbf{x} - \sigma t + \Theta_0) \tag{1.11}$$

Albeit the Airy theory is defined for monochromatic wave and is quite simple compared to refined theories - derived later, notably by Stokes, to account for wave asymetry and non linear effects -, it makes it easy to understand waves physics.

1.1.1.5 Small perturbations theory - Second order interactions

Although ocean waves (first order solutions of the small perturbation theory described in Section 1.1.1.4) decay exponentially with ocean depth, it was shown by Miche (1944) that standing waves can, at second order, generate pressure variations not attenuated with depth, that ultimately dominates the first order. On the basis of this work, Longuet-Higgins (1950) developed it further to explain microseisms and pressure variations of twice the frequency of ocean waves at the bottom, by deriving the second order solutions in the case of two opposing wave trains with the same frequency. The second order equations of the problem include more terms due to first order interactions, and the author very thoroughly considered them all until simplifications. Then, K. Hasselmann (1963) generalised this theory for random waves and for interactions between almost opposing waves of similar frequency. Thus, the interaction term was defined as an integral, known nowadays as the Hasselmann's integral

$$\mathcal{H}(f) = \int_{\theta=0}^{2\pi} E(f, \theta)E(f, \theta + \pi)d\theta \tag{1.12}$$

with f the ocean wave frequency (the microseisms and microbaroms frequency being $f_s = 2f$), θ the wave direction and $E(f, \theta)$ is the wave energy density spectrum defined in eq. (1.2).

The idea of this interaction is the following: when two waves trains interact two new wave trains are generated, one with a wave vector and a frequency corresponding to the sum of the wave vectors and to the sum of the frequencies, respectively, and the other corresponding to their difference. Ocean waves have quite large wavenumbers (around $4 \cdot 10^{-2}$ rad·m^{-1} for the 0.1 Hz peak, while for the same frequency the characteristic wavenumber of acoustical propagation is $1.8 \cdot 10^{-3}$ rad·m^{-1}), however interaction of two almost opposing ocean waves can generate waves with very small wavenumbers (if we consider the 'sum' part of the interaction). These waves could then excite the propagation media, such as the crust or the atmosphere, as their parameters allow to satisfy dispersion relation (which is not the case for the 'difference' part).

The presence, in the sea-state, of waves of similar frequencies in almost opposing directions can occur in three configurations (Ardhuin et al., 2011, 2012), also referred to as classes. The first configuration is when waves from two different storms coincide - usually, when a storm generates wind sea where a swell from a remote source already exists. This configuration can also occur in the case of a single big storm moving slowly with opposing

waves generated consecutively by the front and the rear of the storm, as their winds blow in opposite directions. The second configuration corresponds to interactions between waves and their reflection from the coast - or any reflecting ocean boundary. The last configuration corresponds to a single wind sea system with very broad directional distribution.

1.1.2 Microbaroms generation models: history and state-of-the-art

From the quasi-simultaneous and independent discovery of microbaroms by Shuleykin (1935), Benioff & Gutenberg (1939) and Baird & Banwell (1940), their generation phenomenon has been investigated and various theories have been developed. In particular, some early explanations were proposed by Daniels: first, he suggested that microbaroms were generated by the piston-like motion of transient group of standing waves (Daniels, 1952, 1953); in a later study, he suggested that microbaroms were generated by pressure fluctuations caused by an oscillatory wind drag (Daniels, 1962).

The work by Posmentier (1967)[1] is usually considered as the first theory derived about microbaroms, based on the results by Longuet-Higgins (1950). In this paper, the author calculated the pressure flow of the air above a standing wave, thus using the results of Longuet-Higgins (1950) for the standing wave. Later on, Arendt & Fritts (2000) extended this work, considering an acoustical propagation in the air generated by a general combination of ocean waves.

Unlike these two works that are from a purely atmospheric perspective, others have considered the coupling of the two layers {*ocean*, *atmosphere*} following the same derivation as Longuet-Higgins (1950) and K. Hasselmann (1963). Brekhovskikh et al. (1973) were the first in re-deriving the microseisms theory for microbaroms and, as they considered also interactions of almost-opposing waves, the amplitude of their acoustical pressure varies with the elevation angle. In 2006, Waxler & Gilbert (2006) revisited this theory and added propagation considerations, resulting in monopolar sources. This work was extended to a three layers coupling {*crust*, *ocean*, *atmosphere*} by Waxler et al. (2007), accounting for potential resonances due to the bathymetry. The sources with and without accounting for bathymetry present large differences as shown in Smets (2018). However, whether these differences are of interest for microbaroms' modelling has not been shown yet; unlike for microseisms, for which the bathymetry resonance is known to be an important factor.

As these models (Brekhovskikh et al., 1973; Waxler & Gilbert, 2006; Waxler et al., 2007) are based on the LHH[2]'s theory, their output is a source strength spectrum squared proportional to the Hasselmann's integral $\mathcal{H}(f)$ (see eq. 1.12). Comparison between these models are detailed in Chapter 3.

1.1.3 Sources of wave interactions

In this section we present shortly the modelling of the wave interaction term, and the dominant sources of microbaroms both modelled and observed.

1.1.3.1 Wave action modelling and interaction term

In absence of any oceanic current, the wave energy is a conservative quantity, thus the energy balance, in terms of wave energy spectrum, writes

$$\frac{dE}{dt} = \text{input} - \text{output} \tag{1.13}$$

where the *input* corresponds mainly to energy added to the system by wind that generates waves $S_{in}(f)$, and the *output* is the wave dissipation $S_{dis}(f)$ - notably by breaking. Another phenomenon that can correspond both to *input* and *output* is a non-linear evolution that comes from exchange of energy between different spectral components $S_{nl}(f)$.

However, for waves over currents, the energy E is not conserved anymore, because the conserved energy is that of the entire system { waves + current }. Then, it appears that

---

[1] The introduction of this paper presents a complete review on early (occidental) works on microbaroms, both observational and theoretical.

[2] LHH stands for Longuet-Higgins—Hasselmann

another quantity, known as the 'wave action' is conserved for waves over currents, and is defined as follow

$$A = \frac{E}{\sigma} \tag{1.14}$$

To study its evolution, the wave action can be decomposed into a five-dimensional spectrum $N(k, \theta, \phi, \lambda, t)$ where ϕ is the latitude and λ the longitude of the position, θ is the wave propagation azimuth and k is the wavenumber. Then, the spectral wave action equation is (Komen et al., 1994)

$$\frac{\partial}{\partial t}N + \frac{\partial}{\partial \phi}\left(\dot{\phi}N\right) + \frac{\partial}{\partial \lambda}\left(\dot{\lambda}N\right) + \frac{\partial}{\partial k}\left(\dot{k}N\right) + \frac{\partial}{\partial \theta}\left(\dot{\theta}N\right) = \frac{S}{\sigma} \tag{1.15}$$

With $S = S_{in} + S_{nl} + S_{dis}$ the sum of the inputs and outputs, and $\dot{\phi}$, $\dot{\lambda}$, $\dot{k}$ and $\dot{\theta}$ are the propagation speeds both in physical and spectral spaces (Tolman, 1990). Spectral phase-averaged models, such as WAVEWATCH III® (hereafter noted as WW3), are numerical models that solve this wave action equation with a discretization of the horizontal dimensions, of the spectral space using usually a fixed grid in frequency and direction, and marching forward in time.

The complex air-sea interaction processes that give S_{in} and S_{dis} are not known exactly, and have been parametrized and adjusted to reproduce a small set of observable parameters (e.g. Ardhuin et al., 2019), in particular the total energy of the sea state, which is proportional to the square of the wave height. The energy transfer in the spectrum S_{nl} is also parametrized in wave action models used for long simulations, usually following S. Hasselmann & Hasselmann (1985), because of the very high cost of computing the full interaction integral (e.g. Gagnaire-Renou et al., 2010). Besides the many different parametrisations used to represent the source/sink of energy, the WW3 framework offers the possibility to use adaptive time steps for source term integration (Tolman et al., 2014). Indeed, as the different propagation and input/output effects do not have the same characteristic time, in order to reduce the calculation cost, each of them is integrated within its characteristic time step.

The interest in the WW3 wave action model for this work lies on the fact that a particular choice of parametrizations has demonstrated good performances in simulating the variability of microseisms (Ardhuin et al., 2011). Also, the code directly computes the equivalent second-order surface pressure spectrum for very large wavelengths, so that it is not necessary to use full directional spectral output, reducing the size of the data by a factor that is the number of discrete directions in the model, typically 24 or more. In this thesis we use the WW3 outputs produced at LOPS, as described in Rascle & Ardhuin (2013). The WAVEWATCH III® model computes the evolution of wave spectra, however, due to their huge size, storing the entire wave spectra is not very practical. Thus, the computation of the Hasselmann's integral (see eq. 1.12) has been introduced in the version 3.14-Ifremer of the WAVEWATCH III® model and is now included in public releases. Global modelling results are available at Ifremer's ftp[3], where $\mathcal{H}(f)$ is stored as the second order equivalent surface pressure spectral density F_{p2} which writes

$$F_{p2}(\lambda, \varphi, f, K, t) = \log(\rho_{\mathrm{w}}^2 g^2 f_s \frac{1}{2}\mathcal{H}(f)) \tag{1.16}$$

In practice, the logarithm of this equivalent surface pressure spectrum - the 'p2l' variable - is stored (in '*.__p2l.nc' files) , in order to preserve the very large dynamic range of the values it takes. As described in Section 1.1.1.5, second-order wave interactions can be generated by coastal reflection of waves, therefore this effect has also been included in the wave model. Given uncertainties on the physical parameters that control this reflection, in particular the ocean topography slope near the shoreline (Ardhuin & Roland, 2012), we follow the simple approach used by Ardhuin et al. (2011). Namely, we compute the second-order interactions with two parametrisations: one without any coastal reflection - corresponding to the 'NOREF' files - and one with coastal reflection at its maximum capacity (with reflection coefficients of 10% for the continents, 20% for the islands, and 40% for icebergs) - corresponding to the 'REF102040' files. And then, for each seismic station,

---

[3]ftp://ftp.ifremer.fr/ifremer/ww3/HINDCAST/SISMO/

Ardhuin et al. (2011, see also ; Stutzmann et al., 2012) used a linear combination of the two model results that use these parametrisations.

It should be noted that the modelling of this second order pressure field is very sensitive to details of the directional wave spectrum (e.g. Peureux et al., 2018) and is very hard to validate directly. Only pressure measurements near the ocean surface are dominated by the local second order spectrum that can be related to the local first order spectrum (Cox & Jacobs, 1989; Ardhuin et al., 2014). There are, however, to our knowledge no co-located measurements of near surface pressure and detailed directional wave measurements (e.g. Leckler et al., 2015) that would allow a direct validation of the theory. Instead, pressure measurements have been compared to second order spectra estimated from modelled wave spectra by Ardhuin et al. (2014). More studies of that kind, in a wider range on sea states are needed to firmly establish the validity and define the limitations of the numerical modelling of microseism or microbarom sources.

1.1.3.2 Microbarom dominant sources

Fig. 1.4 shows some examples of typical spatial patterns of the second order equivalent surface pressure spectral density $F_{p2}(K)$ integrated over frequencies and months in the case of maximum reflection. The main sources are seasonally dependent, in correlation with the storm's seasonality, and dominate during local winter. In the Northern Hemisphere (NH), there are two clusters of sources, one in the North Pacific, the other in the North Atlantic. The North Atlantic source, located south the Greenland, near Iceland, is a relatively stable source of microbaroms and microseisms as it corresponds to a stable zone of storms. In the Southern Hemisphere, as there are less continents, large storms and corresponding swell systems can travel all along the Antarctic Circumpolar Current (ACC).
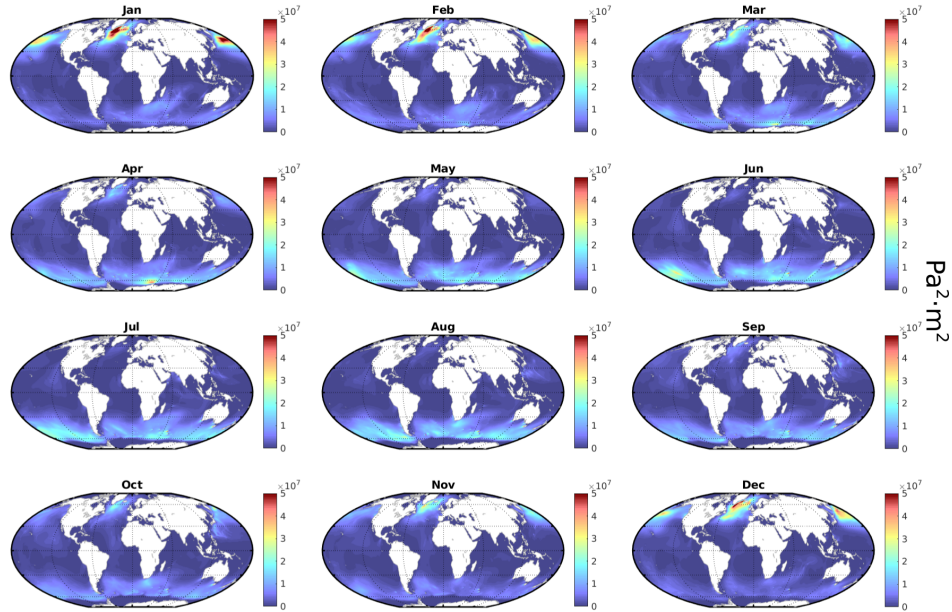
Figure 1.4 – Monthly average of equivalent second order surface pressure spectrum sources as given by eq. (1.16) and computed by WW3-Ifremer - in colour - integrated over frequencies between 2012 and 2018.

Landès et al. (2012) used infrasound observations performed between 2006 and 2010 on a global network (described in Section 1.3.1) to determine microbaroms dominant sources by using the measured arrival azimuth at different receiving arrays and assuming a single source contributed to the signal at neighbouring arrays. Their results are shown in Fig. 1.5. One should note the similarities and the differences with the sources modelled shown in Fig. 1.4. In January, there is one major source observed, which corresponds to the source in the North Atlantic; but, on the other hand, other modelled sources, such as the source in the North Pacific, do not appear in the observed map. In July, the dominant observed

sources are also located around the ACC, like the modelled sources; with a small observed source in the Eastern North Atlantic. These differences emphasise the effect of propagation on the received signals, which can enhance detection in some directions or others depending on the atmospheric characteristics.

This study shows that atmospheric effects play an important part in microbaroms detection at ground station as their propagation depends strongly on winds that are described in the following section.
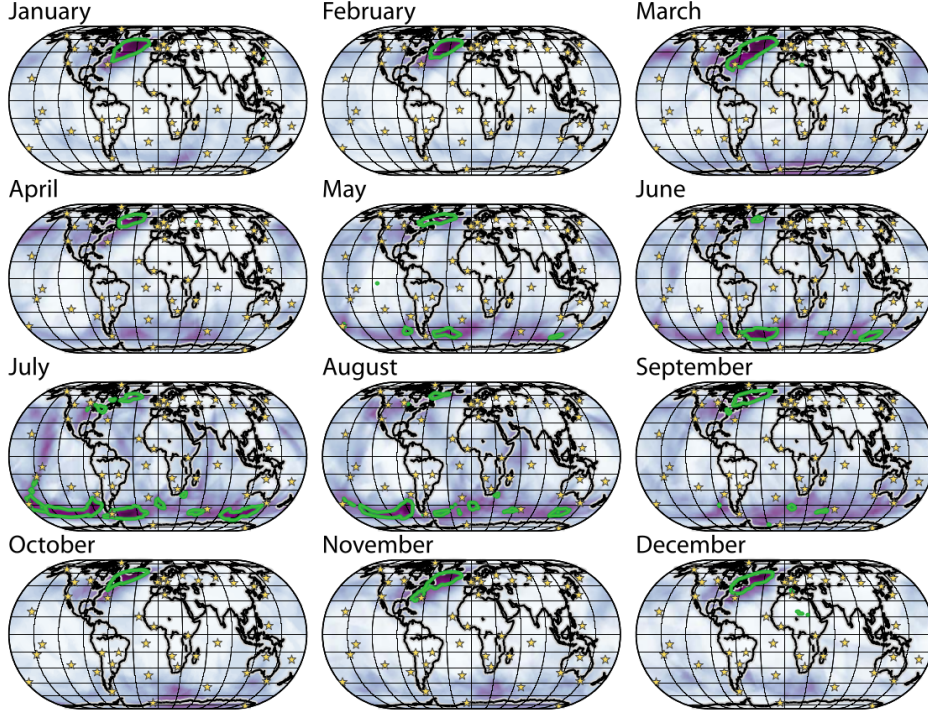
Figure 1.5 – Dominant source variations, as obtained from observations and cross-bearing. Dark purple colour corresponds to a high probability of source location while white is associated to null probability. Clusters with high probability are delimited by green contours (from Landès et al., 2012).

1.2 Infrasound propagation through the atmosphere

1.2.1 Infrasound

1.2.1.1 Generalities

Infrasound waves are acoustic waves with low frequency, ranging from 0.01 Hz to 20 Hz, corresponding to the lower threshold of human hearing (e.g. Evers & Haak, 2010). These waves can be generated by a wide range of phenomena, and are usually separated into two classes: infrasound of natural origin - such as earthquakes, microbaroms, auroras, volcanoes (e.g. Hedlin et al., 2012, and references therein) - and infrasound of anthropogenic origin - such as industrial activities, quarry blasts, accidental explosions, supersonic planes.

1.2.1.2 Propagation and Snell's law

Infrasound waves are present all over the atmosphere, and can propagate over long ranges. At first order infrasound propagation follows geometrical optics and can be computed using the ray tracing method, which combines Snell's refraction law and the effective speed of sound in the atmosphere $c_{\text{eff},a}$. The effective speed of sound is the speed that influences the infrasound propagation, namely the sum of the celerity of sound in the air c_a and the wind velocity in the direction of propagation.

The physics associated to the ray properties is that when the temperature decreases, so does the celerity and the acoustic wave is refracted towards the vertical. On the contrary, when the temperature and the celerity decrease, the acoustic waves is refracted towards the horizontal. When the celerity becomes higher than the horizontal celerity on the ground the infrasound wave is no longer refracted, but totally reflected and therefore directed downwards, thus allowing a return to the ground where the infrasound can be measured.

In first approximation, i.e. considering no dispersion and the air as a perfect gas, the celerity of sound in the air can be related to the air temperature T in Kelvin by

$$c_a = \sqrt{\frac{\gamma R T}{M}} \tag{1.17}$$

where R is the molar gas constant, M the molar mass of the air and γ the adiabatic index. Thus, the propagation of infrasound waves over long distances is dependent on atmospheric conditions, notably on the wind and temperature profiles in the atmosphere.

1.2.2 Atmospheric characteristics and impact on propagation

The atmosphere extends from the ground to some 500 km of altitude, and is often considered as a superposition of distinct layers. Different classifications exist, however, the more common for infrasound propagation studies is a layer separation based on the sign of temperature gradients.
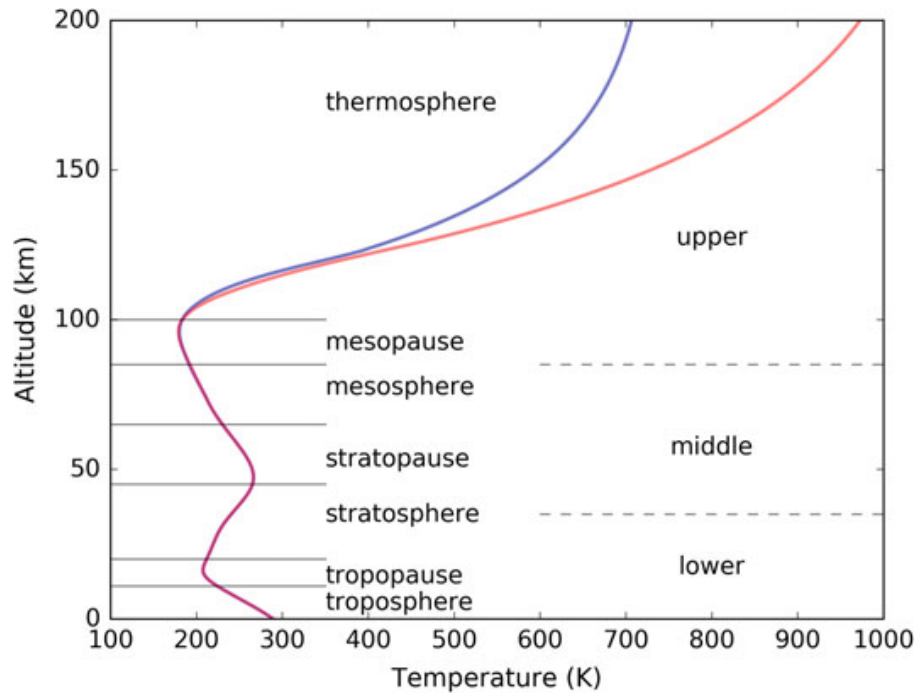
Figure 1.6 – Atmospheric temperature profiles, with representation of the layers. The blue curve corresponds to low Extreme Ultraviolet (EUV) solar flux conditions (low sunspot number) and the red curve to high EUV solar flux conditions (high sunspot number) (from D. Drob, 2019).

1.2.2.1 Temperature structure

This representation consists on four layers based on local average temperature profiles and altitudes shown in Fig. 1.6 (D. Drob, 2019). These layers are (from bottom to up):

- **(0 - 20 km)** the *troposphere* is the layer in contact with the ground, showing a strong temperature decrease with the altitude to reach a minimum around $-50°C$ at 10-20 km altitude. This minimum is known as the *tropopause*.

— **(20 - 50 km)** the *stratosphere* ranges from the upper limit of the troposphere - the tropopause - to an altitude of 50 km. In this layer, the ozone concentration is particularly important. Thus, due to its absorption of ultraviolet radiation emitted by the sun, the temperature gradient is positive in the stratosphere, the temperature increasing up to $0°C$. The *stratopause* is the small layer with constant temperature close to $0°C$ that separate the stratosphere and the mesosphere.

— **(50 - 80 km)** the *mesosphere* ranges from 50 to 80 km of altitude. The temperature decreases again until reaching a minimum at $-100°C$ which is known as the *mesopause* and is also, incidentally, the coldest region of the atmosphere. The stratosphere, stratopause, mesosphere and mesopause constitute what is known as the *middle atmosphere*.

— **(from 80 km)** the *thermosphere* lies above 80 km of altitude and is characterised by a strong positive temperature gradient due to solar heating. As an example, around 160 km, the temperature is close to $500°C$. Then, infrasound waves are usually either strongly absorbed or reflected in the lower thermosphere (corresponding to the first hundred kilometres of the thermosphere). Thus, there is a permanent acoustic waveguide between the ground and the lower thermosphere, known as the thermospheric waveguide.

1.2.2.2 Winds structure and seasonality

The atmosphere is known to be a dynamic media. Its movements, i.e. the winds, are controlled by the atmosphere temperature and the solar radiations, which are different depending on the latitude and on the season. Two main physical phenomena are responsible for the air masses movements: the horizontal pressure gradient variations, yielding masses from high pressure zones to go towards low pressure zones; and the Coriolis force, deflecting moving masses to the right in the Northern Hemisphere and to the left in the Southern Hemisphere due to the Earth rotation.

In order to account for these two phenomena, winds are usually decomposed into two components: one along a parallel, from West to East, i.e. positive towards the East, called the *zonal wind* and the second along a meridian, from South to North, i.e. positive towards the North, known as the *meridional wind*.

The wind profile in the atmosphere depends on the heat distribution over the latitude, which differs with the altitude:

In the troposphere: the heat mainly originates from below, driven by ocean atmospheric exchanges. Indeed, due to its high heat capacity, the ocean stores heat radiated from the sun, leading the equatorial region to present the maximum temperature in the troposphere. In other words, the equatorial region is a zone of high pressure and the poles are low pressure zones. Thus, in the stratosphere, meridional winds go from the equator towards the poles (they are positive in the Northern Hemisphere and negative in the Southern Hemisphere). It also comes, from the Coriolis force, that zonal winds are positive (towards the East) in both hemispheres.

In the middle atmosphere: the heat distribution is driven by ozone formation and infrared radiations, which are seasonally dependent, as they depend on the proximity with the sun. During the equinoxes, the heat distribution is similar to the one in the troposphere, whereas around the solstices the heat is maximum for the summer pole and decreases continuously to the opposite pole. For the solstices, meridional winds go from the summer pole to the winter pole. Then, due to the opposite direction of the Coriolis force in both hemisphere, it comes that zonal winds are positive (i.e. eastwards) in the winter hemisphere and negative (i.e. westwards) in the summer hemisphere.

In the thermosphere: wind structure is dominated by semi-diurnal effects due to solar tides and geomagnetic effects.
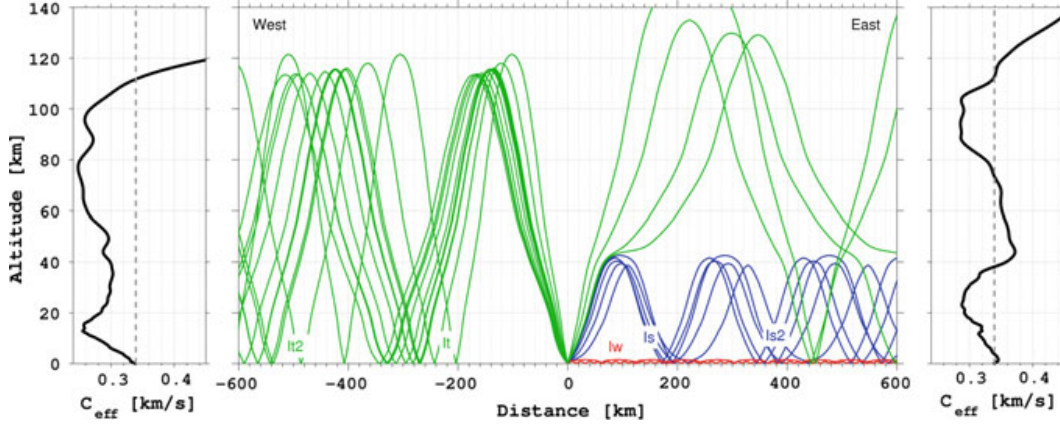
Figure 1.7 – Simulation of infrasonic wave propagation using 1-D ray-tracing. The red, blue, and green paths represent the tropospheric, stratospheric, and thermospheric paths respectively. The effective sound velocity models toward the West and the East are displayed in black on the left and right side of the figure, respectively, with the gray-dashed line representing the effective velocity at the ground. Exemple for the meteor explosion observed offshore Portugal (40.5N, 18.0W) on March 9, 2017 (CNEOS 2017) with the ECMWF weather model (from Marty, 2019).

Most microbaroms arrivals detected on the ground come from stratospheric return. Therefore, stratospheric zonal winds and their seasonality are of importance for the infrasound propagation, especially since meridional winds are weak in comparison with zonal winds in the lower and middle atmosphere. Indeed, as shown in Fig. 1.7, in the case of stratospheric winds in the propagation direction, the effective speed of sound can be higher than the ground one. Thus, a stratospheric duct can develop, implying a total reflection of the infrasound wave and the possibility of a ground return.

1.2.2.3 Atmospheric absorption

As mentioned previously, two main waveguides can exist in the atmosphere, the thermospheric waveguide that is always established due to the high temperatures above 100 km high, and the stratospheric waveguide whose existence is seasonally dependent. In order to understand the importance of the latter one, the attenuation in the atmosphere has to be taken into account. Indeed, the attenuation becomes higher with the altitude, therefore the thermospheric duct does not always allow an effective propagation.

In the atmosphere, sound attenuation during propagation $\alpha_{tot}(z)$ is due to different energy loss mechanisms (Sutherland & Bass, 2004):

- classical absorption $\alpha_{cl}(z)$ combines both viscosity losses and thermic conductivity effects;

- mass and thermal diffusion losses α_d;

- relaxation absorptions (both rotational α_r and vibrational α_{vibr}) are associated with redistribution of translational or internal energy of the molecules. As vibration frequencies depends on the molecules, α_{vibr} is calculated as the sum of the vibrational losses for the four primary gas components in air, O_2, N_2, CO_2 and O_3.

These different effects have been quantified by Sutherland & Bass (2004) (see Fig. 1.8a), and were found to depend on the frequency of the infrasound wave and on its altitude . Thus, the total attenuation coefficient also varies with the frequency and the altitude, as shown in Fig. 1.8b. One may note that for low frequencies - below 1 Hz - the attenuation is weak, however, for long range propagation the total attenuation can become important. One may also note that the attenuation in the thermosphere is higher than the one in the stratosphere by one to two orders of magnitude. Thus, infrasound waves propagating through the thermospheric duct both follow a longer path and are more attenuated than infrasound waves travelling through the stratospheric waveguide, therefore a signal is more likely to be received at the station if it propagates through the stratospheric waveguide.
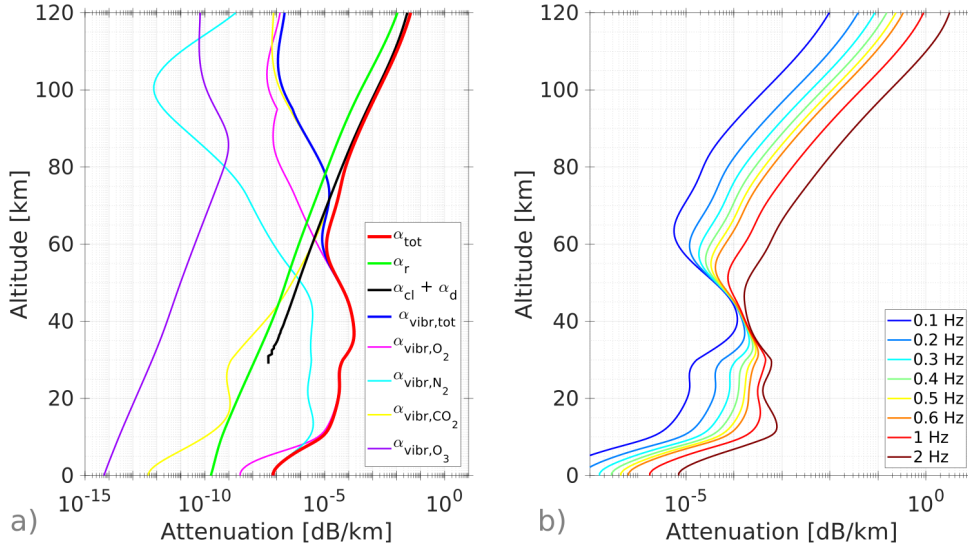
Figure 1.8 – Atmospheric attenuation profile $\alpha_{tot}(z)$ in dB/km. a) Vertical profiles of partial attenuation coefficients and of the total attenuation coefficient - in red - at 0.2 Hz. b) Vertical profiles of the total attenuation coefficient depending on frequency, with frequencies ranging from 0.1 Hz to 2 Hz.

1.2.2.4   Atmospheric impacts on microbaroms propagation

This paragraph presents a summary of the atmospheric impacts on microbaroms propagation that were evoked in the previous ones.

Microbaroms are infrasound waves that propagate through the atmosphere. The low frequency of microbaroms limits their attenuation with altitude and allows them to propagate either through the stratospheric duct or through the thermospheric one. In the case without a stratospheric waveguide, microbaroms travel through the thermospheric waveguide. However, due to a higher attenuation in altitude, waves propagating through the thermospheric duct have a limited propagation range. In the case of an established stratospheric waveguide, a wave propagates through one of the waveguides depending on the launching angle of the propagating wave. Again due to attenuation differences with altitude, the stratospheric duct is more efficient than the thermospheric one and allows microbaroms to propagate very far, up to thousands of kilometres. Therefore, most of the ground stations are likely to detect microbaroms arrivals when a stratospheric duct is established as the International Monitoring System (IMS, see Section 1.3.1) station I26DE (see Fig. 1.9). Some exceptions exist for stations that are quite close (less than around 1000 km, Garcés et al. (1998)) from microbaroms sources, such as stations close to the sea, and can therefore detect thermospheric arrivals of microbaroms (as the IMS station I37NO, see Fig. 1.9).

The establishment of the stratospheric waveguide depends on the seasonality of stratospheric winds, therefore ground stations show seasonality in microbaroms detection. Fig.1.9 shows the seasonal distribution of microbaroms detections by three stations - sub-figures b), e) and h) - along with the relation between those detections and the stratospheric wind - sub-figures c), f), i). The black dots in panels c), f) and i) are microbaroms detections at the station, represented against their detection time and their azimuth - the azimuth at which they arrived at the station. In colour, the ratio between stratospheric effective sound speed - sound speed + wind in the direction of interest - and sound speed at the ground is represented. This ratio is an indicative of the establishment of the stratospheric duct: when its higher than 1 (red in the figure), the stratospheric waveguide is likely to be established in this propagation direction, on the contrary when the ratio is lower than 1 the stratospheric duct does not exist. Three stations of the IMS (see Section 1.3.1) are presented in order to see different impacts:

- I26DE, in Germany, is a station far from any microbaroms source (see Fig.1.9d), thus depending strongly on stratospheric ducting. Fig.1.9e shows strong variations in the number of microbaroms detections. This is due to the fact that the main
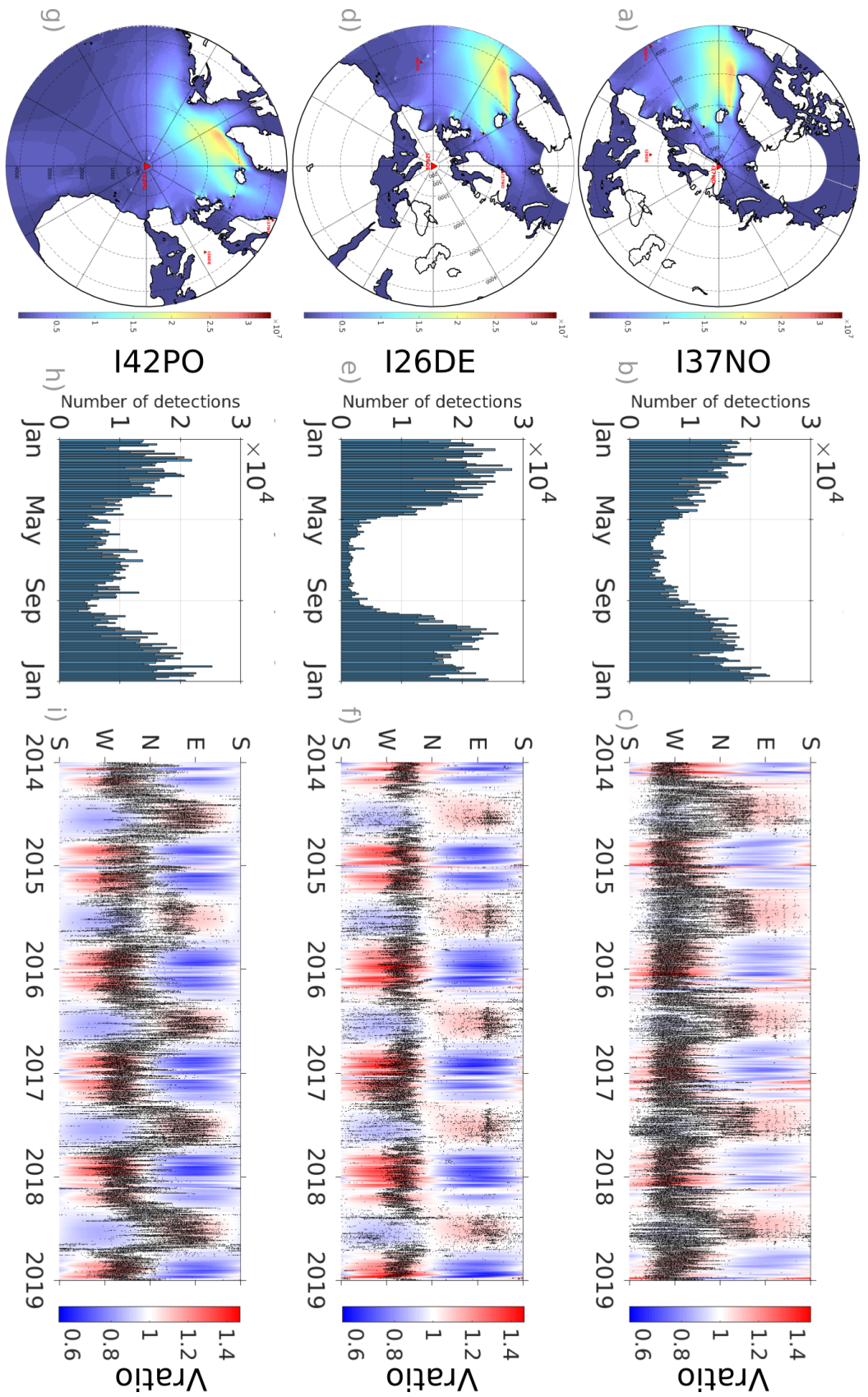
Figure 1.9 – Stratospheric winds effects on microbaroms detection for three different IMS infrasound stations (by latitude order): I37NO (*a*), *b*) and *c*)), I26DE (*d*, *e*), and *f*)) and I42PO (*g*), *h*) and *i*)). The left column (*a*), *d*) and *g*)) displays the locations of the station and the averaged microbaroms source (over the whole year), the dashed black circles represent distances in km from the stations (located at 200, 500, 1000, 2000, 3000 and 4000 km), whereas the dot black lines represent constant azimuth directions. The middle column (*b*), *e*) and *h*)) shows the seasonal distributions of detections between 0.1 and 0.6 Hz. The distribution has been computed accounting for the entire period of activity of the stations (from 2014 for I37NO, 2006 for I26DE and 2010 for I42PO). The column on the right (*c*), *f*) and *i*)) shows the time and azimuth of every detection in the [0.1 - 0.6] Hz frequency band - black dots - and relates them to the existence of a stratospheric duct in a given direction - represented by the Vratio parameter in colours. When the Vratio is greater than 1 (respectively lower than 1) - in red (resp. in blue) - the stratospheric duct is established (resp. not established)

31

microbaroms source detected by this station is located in the North Atlantic - in the North-West direction from the station -, therefore in winter, when the stratospheric duct is established from the source to the station - red in the figure -, there are lots of microbaroms detections. During local summer, winds blow in the opposite direction thus the possible sources detected are from the Eastern Mediterranean Sea. However, those sources are not as strong as in the North Atlantic and then generates less detections at the station (see Fig.1.9f)

- I37NO is a station located in northern Norway (see Fig.1.9a) which has the particularity to detect two main microbaroms sources in the North Atlantic and in the Barents Sea. The seasonal impact on the number of detections (see Fig.1.9b is less pronounced than for I26DE. Indeed, during summertime, the proximity of the North Atlantic source (around 1000 km) allows the station to receive thermospheric returns, this is shown in Fig.1.9c as there are returns with a stratospheric ratio lower than 1 - blue colour. At the same time, the station detects also signal from the Barents Sea. Two reasons make these detections possible. First, the simultaneous detections of North Atlantic and the Barents Sea is only possible because the sources radiate in different frequency bands (around 0.2 Hz for North Atlantic and 0.5-0.6 Hz for the Barents Sea). Second, the distance between the Barents Sea and the station is very small - around 200 to 300 km - , therefore allowing those higher frequencies (acoustic signals are more attenuated at 0.5-0.6 Hz than at 0.2 Hz, see Fig. 1.8) to propagate to the station when the stratospheric duct is established.

- I42PO is located in the Azores, and is therefore surrounded by the sea and potential microbaroms sources (see Fig.1.9g). The seasonal distribution of detections presented in Fig.1.9h shows an almost constant number of detections, with only a slight decrease around equinoxes. As a matter of fact, as there are sources in every direction around the station, the direction of the main arrival (the detected one) corresponds to the direction of the stratospheric waveguide as it is the direction containing more energetic signal (such as shown in Fig.1.9i). Yet, around equinoxes, stratospheric winds are gradually reversing loosing intensity, therefore the stratospheric duct is less well established at this period, resulting in fewer detections at the station.

These examples demonstrate the different impacts of the stratospheric winds in the microbaroms detections. One may note that in the Southern Hemisphere most stations show a wind impact similar to the wind impact in I42PO. Indeed there are proportionally more oceans in the Southern Hemisphere and sources are well distributed around the longitudes, therefore the direction of arrival is directly related to the direction of the stratospheric duct.

These important wind effects must be accounted for while modelling microbaroms, thus modelling the infrasound propagation through the atmosphere is necessary.

1.2.3 Infrasound propagation modelling

Propagation modelling is necessary to relate infrasound sources with observations. How infrasound propagation depends on atmospheric characteristics was explained - in a simplified way - in the previous section. This section gives an overview of existing propagating methods based on Waxler & Assink (2019) and references herein, which provides a thorough review on the subject with all mathematical derivations.

1.2.3.1 Overview of propagation methods

Let the considered atmosphere be stratified and defined by a mean density $\rho_{a,0}(z)$, a sound speed $c_a(z)$, and horizontal wind velocity $\mathbf{v}_{0,H}$. If the acoustic pressure is $p_{ac}(\mathbf{x}_H, z, t)$ and its Fourier components write $\hat{p}_{ac}(\mathbf{x}_H, z, \omega)$, the wave equation can be reduced to:

$$\left[\nabla_H^2 + \rho_{a,0}\frac{\partial}{\partial z}\left(\frac{1}{\rho_{a,0}}\frac{\partial}{\partial z}\right) + \frac{1}{c_a(z)^2}\left(\omega + i\mathbf{v}_{0,H}(z)\cdot\nabla_{\mathbf{H}}\right)^2\right]\hat{p}_{ac}(\mathbf{x}_H, z, \omega) = 0 \qquad (1.18)$$

This equation is the fundamental wave equation for the Fourier method. Various methods exists to solve this wave equation:

- The **ray tracing** is an asymptotic method based on the *geometric acoustic approximation* which is a high-frequency approximation, that considers both the wavelength and the period to be small compared to temporal and spatial characteristic scales of the propagation media. The ray-tracing method solves two coupled equations governing ray trajectories, and calculates the cinematic parameters of the acoustic wave (such as the propagation time or the azimuth deviation).
  Advantages: Representing the ray paths allows to visually understand the propagation, as presented in Fig. 1.7, where ray tracing is used to show the thermospheric and stratospheric ducts. This method is quit fast and allows to compute ray paths over the entire globe, accounting for a range dependent atmosphere, and 3D effects due to the Earth sphericity.
  Drawbacks: The high frequency approximation corresponds to omitting the diffraction in the propagation, however, for low frequencies (typically around 0.1 Hz), this effect is important. Therefore, for low frequencies (typically around 0.1 Hz), the high frequency approximation is not verified anymore, and ray-tracing is problematic around caustics and shadow zones.

- **Modal expansion** consists in considering the wave equation with the attenuation coefficient $\alpha(z)$, and then seeking a solution in the form of eigen function expansion, where each eigen function is called a mode.
  Advantages: For a given atmospheric state, the propagation is totally independent from the source. Therefore, determining the modes is only done once, and can be applied to different sources, thus it decreases computation efforts needed in case of various simulations with the same atmospheric state.
  Drawbacks: This method considers a range-independent atmosphere, thus not accounting for horizontal variations that could be important for long-range propagation. A way to overcome this issue would be to compute the modes at various points along the propagation, however, this would increase computational time.

- **Parabolic Equation (PE)** models approach the hyperbolic wave equation with parabolic equations that model the acoustic wave evolution in a given direction. The equation is factored into a forward propagating wave and a backward propagating one, of which only the forward propagating wave is studied. Thus, this method models the propagation into a vertical advancing plane.
  Advantages: This method allows the media to be range dependent and accounts for the majority of physical phenomenon affecting the propagation such as the diffraction or even the topography.
  Drawbacks: The validity of these equations are limited in azimuth, thus to overcome this issue and have a 3D representation the PE equations have to be solved over a range of azimuths. However, horizontal coupling is not accounted for by this so-called 'N-by-2D' technique. Added to that, computational time is quite important and 3D effects due to the Earth sphericity are not included, hence, this method won't be interesting for propagation over the globe.

- **Direct Resolution** discretizes the wave equation and solves it by finite-differences method for example, integrating a spatially and temporally variable atmosphere.
  Advantages: This method allows to consider all mechanisms affecting the wave propagation with a complete variable atmosphere, thus it is interesting in complex media, with complex geometry.
  Drawbacks: Computation time and numerical limitations prevent the use of this method for global simulations.

All these methods solve the wave equation and provide the resulting acoustical pressure in points of interest (such as a station). Another way to account for atmospheric propagation and to obtain an approximation of the acoustical pressure at a point of interest is to consider an attenuation law.

1.2.3.2 Semi-empirical attenuation law

The historical motivation for deriving an attenuation law was to relate the pressure observed at stations to the yield of an explosion in an operational way, in the framework of monitoring explosions and nuclear tests. Indeed, Whitaker et al. (2003) empirically developed the Los Alamos National Laboratory (LANL) relation by adding an attenuation term - depending on the mean stratospheric wind velocity over the propagation path - to the existing relation between local pressure and yield of the explosion (Whitaker, 1995). The limitations of this law, such as strong variability in the yield estimates, lead to a more comprehensive study of long-range propagation using atmospheric simulations (Le Pichon et al., 2012).

For their study, Le Pichon et al. (2012) performed PE simulations with various atmospheric profiles over different frequency bands. The atmospheric profiles were defined by considering a standard atmospheric profile and adding a Gaussian jet in its stratosphere in the direction of the propagation. Various simulations were performed varying the altitude of the jet and its intensity, which was characterised by the $V_{\text{eff}-\text{ratio}}$ dimensionless parameter defined as the ratio of the effective sound speed in the stratosphere to the sound speed at ground level. Horizontal velocity perturbations of winds were also included in the atmospheric profiles - into 40 different realisations - to account for natural fluctuations due to gravity waves. In total, 9120 PE simulations were performed and the following attenuation law, considering both stratospheric and thermospheric returns, was derived

$$Att(f, V_{\text{eff}-\text{ratio}}, R) = \frac{1}{R} 10^{\frac{\alpha(f)R}{20}} + \frac{R^{\beta(f, V_{\text{eff}-\text{ratio}})}}{1 + 10^{\frac{\delta - R}{\sigma(f)}}} \qquad (1.19)$$

where the attenuation coefficient *Att* is calculated at a reference distance of 1 km to the receiver, with f the frequency of the signal, R the distance in km between the source and the receiver and α, β, δ and σ the attenuation parameters obtained from the simulations. α is the parameter representing the dissipation of direct waves in the near-field. The other parameters control the far-field attenuation: β represents the geometrical spreading and dissipation of waves, δ (in km) is the width of the shadow zone - zone without any return - and σ (in km) controls the attenuation in the shadow zone. This attenuation coefficient includes both conservative propagation effects and dissipation effects.

The PE simulations have shown that the most important parameters for the propagation were the frequency and the $V_{\text{eff}-\text{ratio}}$. On the contrary, the jet altitude has presented weaker effects on the attenuation, thus, for the eq. 1.19, $V_{\text{eff}-\text{ratio}}$ is the ratio between the effective sound speed at 50 km of altitude and the sound speed at the ground. Parameters α, β and σ have been tabulated for frequencies between 0.1 and 3.2 Hz and for effective sound speed ratio $V_{\text{eff}-\text{ratio}}$ ranging from 0.85 - winds against the propagation - to 1.18 - winds enhancing the propagation.

The drawbacks of this method come from the PE method drawbacks, namely the horizontal coupling not accounting for and possible 3D missing effects. On the other hand, the advantage of using an attenuation law lies in its almost non existent computational time which makes it of great interest for operational or global propagation.

1.2.4 Representations of the atmosphere properties

Infrasound propagation modelling relies on atmospheric characteristics that are usually obtain through atmospheric modelling. There are two main types of atmospheric models: the climatology models and the Numerical Weather Prediction models. Climatology models, such as *HWM* (Horizontal Wind Model, Hedin et al., 1991, 1996) or *MSIS* (Mass, Spectrometer, Incoherent Scatter, Hedin, 1987, 1991), are empirical models that have been derived from observation datasets of the atmosphere (like satellite observations, radars or soundings) and give the seasonal evolution of the atmosphere. Indeed, in those models an atmospheric profile from 0 to 180 km is associated with each day of the year and location on the Earth. Those empirical models are also called statistical models as they represent statistically the seasonality of the atmosphere. However, they fail to represent specific cases of the atmospheric state. Therefore, more realistic atmospheric models have been developed: the so-called semi-empirical or Numerical Weather Prediction models.

In these models, the atmospheric dynamics equations are solved and coupled with data assimilation of observations. Among these models, the European Center for Medium-range Weather Forecast (ECMWF) has been developing the Integrated Forecast System (IFS), a global data assimilation and forecasting system. For each time step, IFS equations are solved giving a estimate of the atmosphere. During a given period - typically 3 to 6 hours - available data are collected and combined with the estimate of the atmosphere state to give an adjusted atmospheric state, known as the *analysis* which is the best possible estimate of the present state. From this estimate of the atmosphere, theoretical extrapolations forward in time gives the *forecast* which is the best possible estimate of the future state of the atmosphere (D. Drob, 2019).

For this work, the semi-empirical *ECMWF-HRES* (standing for High-RESolution Forecast) analysis product is used. The ECMWF-HRES is described over 137 vertical pressure levels, with an horizontal resolution of 9 km, and a temporal resolution of 6 hours, including additional Medium Range forecasts, for the analysis. This means that the model can be available with a smaller temporal resolution, however, the data assimilation is only done each 6 hours.

1.3   Stations and infrasound observations

1.3.1   The CTBT and IMS network

In order to limit the proliferation of nuclear weapons, the Comprehensive Nuclear-Test-Ban Treaty (CTBT) was opened to signature on 1996 (Tavernier, 1996). Scientific discussions followed in order to decide how to ensure compliance with the treaty. The International Monitoring System (IMS) emerged from these discussions, consisting in four networks used for enforcing the CTBT, each using a different technology to monitor nuclear tests: seismology, hydroacoustic, radionuclide and infrasound. The IMS was designed to have uniformly distributed sensors all over the world in order to detect and locate any nuclear explosion above 1 kT (of TNT equivalent) performed at any point of the globe. The construction of the IMS networks is almost completed with 300 facilities certified - running and following the requirement of the CTBT - over the 337 that will compose the IMS when complete. The IMS infrasound network, represented in Fig. 1.10 will consist of 60 stations, of which 52 are certified as of October 2020 (Marty, 2019).
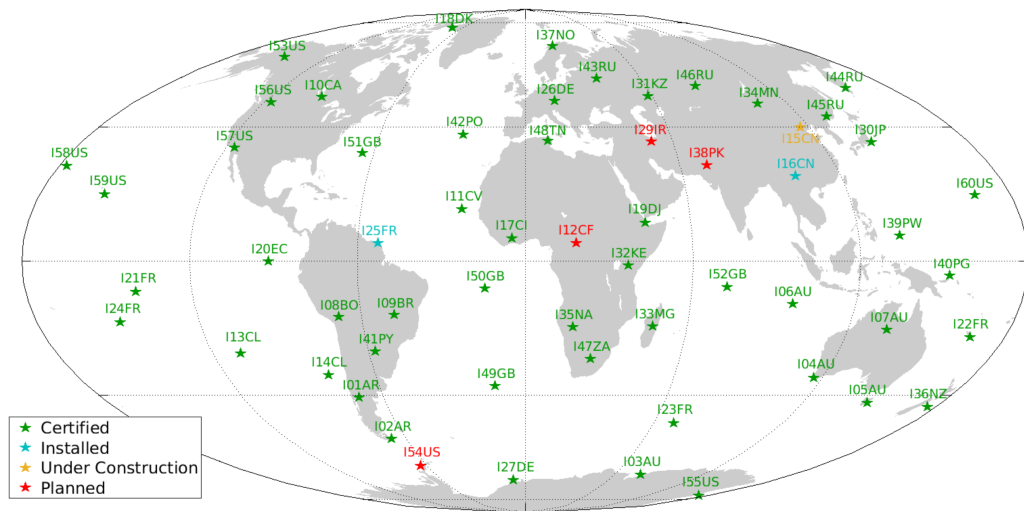
Figure 1.10 – Overview of the IMS infrasound network as of October 2020 with certified stations (green), installed stations (cyan), stations under construction (orange) and planned stations (red).

Infrasound stations are composed of microbarometers, which are instruments able to detect small variations in the atmospheric pressure (around 1 μbar). Albeit various types

of microbarometers are used for the purpose of the IMS, they all present a pass-band filter for the range [0.05 - 4] Hz.

Due to their high sensibility, needed to detect small pressure variations, microbarometers are quite sensitive to wind noise. Setting the sensor in a sheltered location (such as deep forest) can help reducing wind noise effects, however, this was not always feasible due to the diversity of locations in the IMS network (e.g. the station IS22 is situated in the Kerguelen Island, where there is no shelter from the winds). Therefore, noise-reducing systems were developed to overcome this issue, the most common noise-reducing system used in the IMS network consists of a system of pipes sampling the air all around the sensor and averaging it in order to reduce wind noise induced by local atmospheric turbulence, as reviewed by Raspet et al. (2019) and illustrated in Fig. 1.11.

For each sensor, the output consists of a pressure evolution time series. Albeit the amplitude variations of pressure can be used to detect a signal, information about the location of the source can not be extracted from one sensor time series. Therefore, each IMS station consists of one array[4] of microbarometers, composed of at least four elements, in order to obtain information about the origin of propagating waves: the azimuth and the apparent horizontal celerity vector, or 'slowness' as used in seismology.
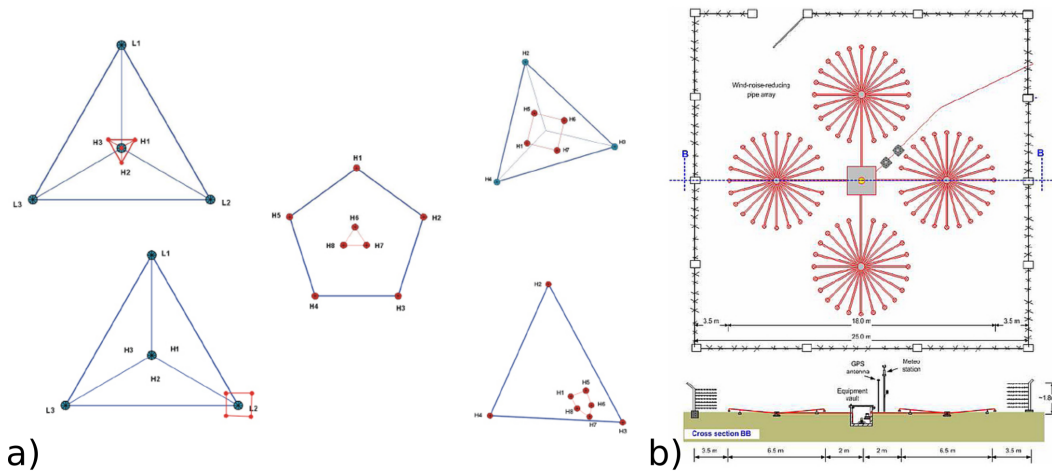
Figure 1.11 – a) Possible configurations of IMS infrasound stations: the red and blue dots are infrasound sensors, the red geometrical forms correspond to small arrays that are usually used at the beginning of the PMCC processing while the blue geometrical forms correspond to larger arrays that favor low frequencies detections b) zoom on a sensor - yellow central dot - and its noise-reducing pipe system - red lines (from `www.ctbto.org`).

In order to detect infrasound waves, the distances between sensors composing an array range from hundreds of meters to around three kilometres - corresponding to the wavelengths of the signal of interest. The geometry of the array is not standardised among IMS stations as it depends on the number of sensors in the array and on the local geography.

1.3.2   Standard processing

Time series for each sensor are sent in real-time to the International Data Center (IDC)in Vienna (for a review of IDC processing see Mialle et al., 2019). After quality control, these time series are processed station by station to extract and separate propagating wave fronts received at the station. Processing is performed by the Progressive Multi-Channel Correlation (PMCC)method developed by Cansi (1995). The main advantages of this processing method are its computational efficiency and its ability to extract coherent waves of small amplitude from background incoherent noise (Brachet et al., 2010).

Based on the planar wave representation (infrasound waves are locally represented by propagating planar waves), PMCC correlates the signals from a pair of sensors on a varying time-frequency windows - the signal is filtered around the frequency and a sliding window

---

[4]Note that the term station refers to an array, not to a single sensor that is referred to as 'an element'

is considered. The maximum of this correlation gives the wave propagation delay between the two considered sensors. When considering more than two sensors, various delays are available and they are used to determine wavefront parameters such as the azimuth. In an ideal case, the sum of the delays should be equal to zero, however, in real cases the sum is not equal to zero, but should be the smaller possible for the wavefront parameters obtained to be reliable. A consistency criteria is defined by comparing the sum of delays to a given threshold. When the sum of delays is below the threshold, the consistency criteria is met and a detection is constructed in a given time-frequency window (known as a *pixel*).

The progressive aspect of the PMCC method is an important one as it enhances detections by reducing aliasing. Indeed, in traditional processing, the array aperture needs to be a trade-off between resolution and aliasing. Whereas with PMCC, the correlation analysis is first performed on various small sub-arrays of 3 sensors, of which the one with the minimum sum of delays is considering as the starting point of the study. The first wave parameters estimate obtained from this small sub-array presents poor resolution and low aliasing. Then, the analysis is performed again from this first estimate while adding the other sensors one by one to the sub-array. Thus, the aperture increases (by adding sensors) and the wave parameter estimate resolution is enhanced, without increasing the aliasing along - as the first estimate guides the parameter search.

The pixels are then gathered into *families* according to their similarities both in wave parameters (speed, frequency, azimuth, amplitude) and time-frequency. Only families that contain more than a certain number of pixels (usually 40) are of interest for this study and they are indifferently referred to as observations or detections. A microbaroms detection is therefore characterised by several parameters including the incoming horizontal angle (back-azimuth, that is called azimuth from now on), the horizontal trace velocity (that allows to derive the elevation angle), the time, the frequency, and the amplitude of the signal.

One may note that PMCC processing does not give distribution of azimuths, similar to a directional spectrum used for ocean waves. Instead, PMCC processing only detects one signal per time-frequency windows. This signal is usually the dominant one as the maximum of correlation is considered, however, in the case of various sources with same frequency, the processing is not able to separate them.

1.4 Thesis' objectives and outline

Our interest of microbaroms is twofold: one is related to the Comprehensive Nuclear-Test-Ban Treaty and the second concerns atmospheric modelling and Numerical Weather Prediction (NWP).

In the framework of the CTBT, the IMS infrasound network was installed to detect any nuclear test explosion. However, infrasound detection of nuclear explosion strongly depends on both incoherent noise, such as local winds, and coherent noise, such as microbaroms. Therefore, a better knowledge of microbaroms shall help to separate them from signals of interest and to better understand the conditions of observability of those signals of interest.

Concerning atmospheric modelling and NWP studies, significant improvements have been made over the last decades, notably up to 30 km of altitude with the integration of various types of observations to constrain atmospheric models (Bauer et al., 2015). However, for altitudes higher than 30 km, the observations are scarce and poorly sampled resulting in a lack of data for assimilation and therefore the atmospheric models poorly resolve wind and temperature above 30 km (see for example Charlton-Perez et al., 2013; Le Pichon et al., 2015). Due to the long-range infrasound propagation strong dependence on the atmospheric characteristics, it has been shown that infrasound can be used to probe the atmosphere dynamics, and particularly the middle atmospheric dynamics (e.g. Donn & Rind, 1971, 1972; D. P. Drob et al., 2010; Assink et al., 2014; Smets & Evers, 2014; Amezcua et al., 2020; Vanderbecken et al., 2020). In this perspective, the European Project ARISE (Atmospheric dynamics Research InfraStruture in Europe) that aims at harvesting from synergies between ground-based infrasound observations, radar and lidar systems, as well as airglow and satellite observations to monitoring the middle atmosphere, promoted the use of infra-

sound measurements to help constrain middle atmospheric models (Blanc et al., 2018). Microbaroms are infrasound that present characteristics of particular interest for atmospheric modelling. Firstly, their very low frequency allows their propagation over thousands of kilometres and their detection worldwide. Secondly, microbaroms sources are spatially extended and almost continuous in time. Therefore probing the atmosphere from microbaroms should result in atmospheric observations almost continuous in time and well-sampled in space, thus useful to constrain middle atmospheric models.

On the other hand, the fact that microbaroms are spatially extended and almost continuous tends to complicate the inversion of the signal by increasing the number of variables and preventing to represent microbaroms waveforms. Therefore, an easier way to proceed towards the assimilation is to use a direct approach by modelling microbaroms arrivals at infrasound stations and compare them with observations. In the long run, it is expected that these simulations would be useful to develop new observational constraints for the modelling of middle atmospheric dynamics.

This thesis objective is to develop a methodology to model microbaroms arrivals at ground based stations and to compare them with observations on a global scale using the IMS database. Chapter 2 is dedicated to the set up and presentation of the global modelling methodology. Chapter 3 focuses on the development of a new source model that was published in De Carlo et al. (2020). The application of the modelling defined in Chapter 2 and including the new source model is presented in Chapter 4. This global modelling is performed for 7 years and for the whole newly reprocessed IMS database. Finally, the conclusions are drawn in Chapter 5 along with perspectives for further investigations.

PRELIMINARY CONSIDERATIONS

Contents

The main purpose of this chapter is to present a methodology to integrate the source model into a global model including propagation and source summation in order to model microbaroms arrivals at IMS stations and to compare them with observations.

As the objective is to apply the developed methodology to the IMS database in an operational way, this methodology needs to be universal - applicable everywhere, at every time - and not to require high computation time. To do so, simplifications and choices are needed. Therefore the second purpose of this chapter is to present those simplifications and to explain the choices made for the modelling.

2.1 Modelling microbaroms arrivals

Modelling microbaroms arrivals at a station (see Fig. 2.1) requires to follow various steps - described below with the result of the step in bold:

1. The sea state is modelled by a wave action model and gives a wave spectrum $N(f, \theta, t, \lambda_i, \phi_i)$ for each point along the sea surface, which is then transformed into the **second order equivalent surface pressure spectral density** $F_{p2}(\lambda_i, \varphi_i, f, K, t)$ (see eq. 1.16), based on the Hasselmann's integral $\mathcal{H}(f, t, \lambda_i, \phi_i)$ (see eq. (1.12)).

2. From wave spectrum, the **acoustic source spectrum** $P_{2,source,i}(f, t, \lambda_i, \phi_i)$ is obtained by applying the source model to $F_{p2}(\lambda_i, \varphi_i, f, K, t)$.

3. Considering the distance between the source and the station, as well as the atmospheric model, the **attenuation** of the source is computed: $Att(f, t, \lambda_i, \phi_i, \lambda_{sta}, \phi_{sta})$

4. The attenuation is applied to the acoustical spectrum of the corresponding source point, giving the **contribution of this source point** to the acoustic level **at the station**: $P_{2,sta,i}(f, t, \lambda_i, \phi_i)$

5. To compute the **acoustic directional spectrum at the station** $P_{2,sta}(f, t, \theta)$, all contributions - spectrum of the source as seen by the station - of sources within an azimuth band are summed.

$$P_{2,sta}(f, t, \theta) = \sum_{i \in \mathcal{A}_\theta} P_{2,sta,i}(f, t, \lambda_i, \phi_i) \tag{2.1}$$

with $\mathcal{A}_\theta$ the set of the model cells seen by the station with an azimuth θ.

These steps are developed with more details in the following subsections and Fig. 2.2 gives an illustrated example of these steps.
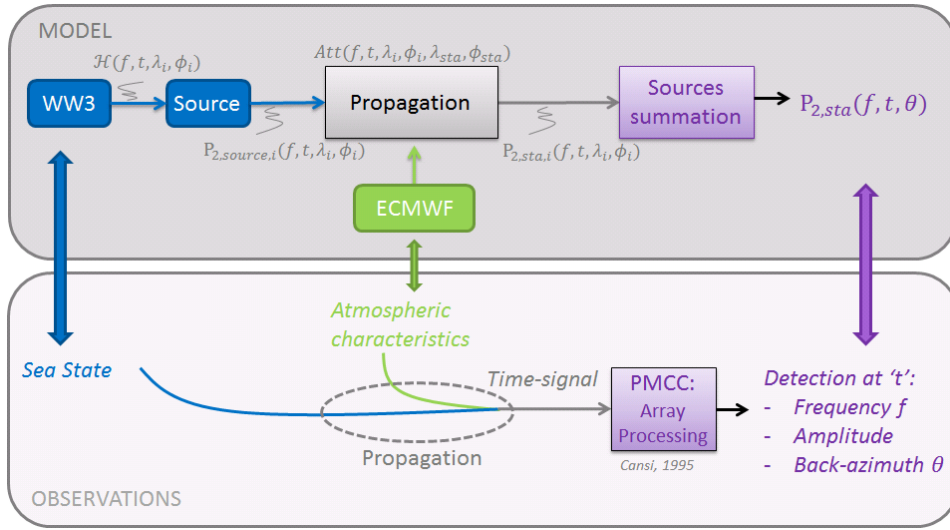
Figure 2.1 – Global modelling of microbaroms arrivals at station.

2.1.1 Step 1 - Ocean wave model

In order to model the sea state, the WW3 wave action model is used, including the computation of the Hasselmann's integral.

Coastal reflection parametrisations have been implemented in the WW3 code for microseisms studies (Ardhuin et al., 2011). In order to investigate the effect of coastal reflection on microbaroms arrivals modelling, the modelling is done (in Chapter 4) with two parametrisations (see Section 1.1.3): one without coastal reflection - NOREF - and the second accounting for the maximum reflection - REF102040.

This step is shown in Fig. 2.2a where $F_{p2}(\lambda, \varphi, f, K = 0)$ - representing the amount of wave interaction (see eq. (1.16)) - computed without reflection is represented.

2.1.2 Step 2 - Source model

Source models usually give a relation between the wave interaction term and the acoustic pressure in the air just above the ocean. An important part of the work that has been done for this thesis was to develop a source model unifying the theories of Brekhovskikh et al. (1973) and Waxler et al. (2007); these developments are presented in Chapter 3.

Fig. 2.2b represents the source model presented in Chapter 3 and integrated over elevation angles. Integrating over the complete integration interval [0 - 90]° requires to include an energy dampening parameter Q_R (see Section 3.2.3.1) for near-vertical angles in order not to overestimate the Rayleigh wave energy in the atmosphere. In practice, to avoid including this parameter, and as the integration over [20 - 90]° and the one over [0 - 90]° are of the same order of magnitude, the source model is integrated for angles between 20° and 90°.
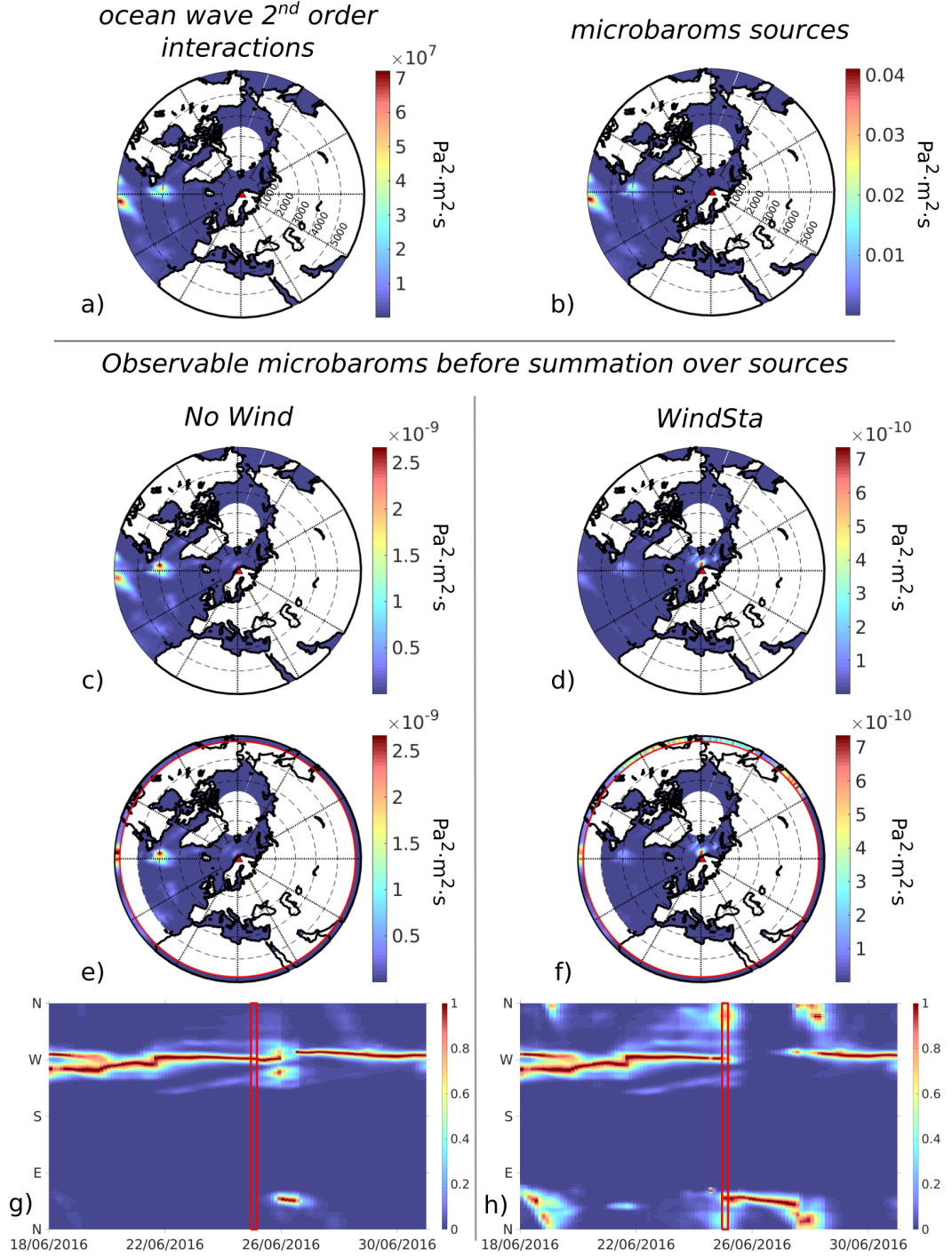
Figure 2.2 – Example of modelling steps for I37NO - red triangle -, on 25th June 2016 00:00:00, for a frequency $f_s = 0.23413$ Hz: a) $F_{p2}(\lambda, \varphi, f, K = 0)$ map (see eq. (1.16)) in the configuration NOREF, b) microbaroms sources after applying the source model (see Chapter 3), c) and d) attenuated sources map - i.e. contribution of each grid cell to the acoustic level at the station -, e) and f) representation of the contributions that are summed by azimuth: for distances further than 5000 km the sources are not considered, the external circle gives the sum by azimuth, g) and h) acoustical amplitude at the station against the time and the direction - normalised for each time step by the maximum of amplitude over the directions -, the red rectangle evidences the time step shown in a-f). The Model is applied both for the NoWind - c), e) and g) - and for the WindSta - d), f) and h) - configurations.

2.1.3 Step 3 - Atmospheric attenuation

Because every single location of the ocean has sources of microbaroms, any propagation modelling would be computationally too expensive to apply to the global database in an operational way. Thus, the attenuation law derived by Le Pichon et al. (2012) is used. As described in Section 1.2.3.2 this attenuation law depends on the acoustic frequency, the distance between the source and the receiver and the $V_{\text{eff}-\text{ratio}}$, the effective sound speed ratio between the stratosphere and the ground.

Various points need to be raised about this attenuation law:

— First, the Parabolic Equation simulations used to derive the attenuation equation were run for distances - between source and receiver - ranging from 1 to 3000 km. Thus for distances greater than 3000 km the attenuation equation is extrapolated and may be underestimated. However, microbaroms sources can be quite distant from the stations, thus looking beyond 3000 km might be needed. Therefore a study about the distance is needed in order to determine a good threshold to account for most sources without extrapolating too much.

— The effective sound speed ratio $V_{\text{eff}-\text{ratio}}$ is the parameter that represents the atmospheric state during the propagation. One may note that this parameter reduces the 4 dimensions of a dynamic atmosphere (three for the space, one for the time) into a constant over the propagation:

   ✓ The reduction over time dimension is quite reasonable for our purpose as the atmospheric model we consider is updated only each 6 hours, therefore, except for very long propagation, the change in atmospheric model would not impact the propagation - at 300 $m \cdot s^{-1}$, an acoustic wave travels around 6500 km in 6 hours.

   ✓ The reduction over the vertical dimension is physically similar to the Snell's approximation of a stratospheric return, as the parameter is a ratio of the effective sound speed in the stratosphere to the one at ground level. Therefore, as stratospheric returns favour long range propagation, the vertical reduction is representative of the physics involved in infrasound propagation.

   × On the contrary, the reduction over the horizontal dimension is quite problematic. This reduction arises from the fact that the simulations were made in a horizontally uniform atmosphere. Therefore the choice of how to reduce the dimension is important in order to consider a $V_{\text{eff}-\text{ratio}}$ representative of the whole propagation.

— There are different ways of defining $V_{\text{eff}-\text{ratio}}$ to reduce the horizontal dimension. One, as suggested by Le Pichon et al. (2012), averages both the stratospheric wind - taken at 50 km of altitude (to avoid further averages in altitude) - and the sound speed at ground level, along the great circle of the propagation. Another methods were proposed by de Groot-Hedlin & Hedlin (2014) and Tailpied (2016): instead of averaging the winds, attenuation coefficients are calculated all along the propagation path and then, combined into one single attenuation coefficient for the propagation (see Tailpied, 2016, eq. (17) and de Groot-Hedlin & Hedlin, 2014, eq. (2)).
These two methods aim at considering atmospheric variations along the propagation, however, they require to store one value of attenuation for each pair {source point, station}, which slows down the calculation. Thus, they are not used for the global study. A simpler definition of $V_{\text{eff}-\text{ratio}}$ consists of extracting the atmospheric profiles at one point that should be characteristic of the propagation.
Two points are quite characteristic of the propagation: the source, modelling the capacity of a microbaroms wave to enter a stratospheric or a thermospheric duct, and the station, representing the capacity of an infrasound wave present in the duct to be returned at the station. Extracting the atmospheric profiles at source points presents the same drawbacks as for the two methods previously explained. Therefore, for the global study, the atmosphere was considered to be horizontally uniform and described by the profile at the station.

In order to quantify the effect of attenuation generated by the winds, the modelling is done for two configurations in Chapter 4: one with the wind at the station, as described above - WindSta -, the other without wind - NoWind. The configuration without wind is not strictly without wind, in fact, this is a configuration without any directional effect of the wind, i.e. no direction is enhanced nor weakened by the wind as $V_{\text{eff}-\text{ratio}}$ is set constant and equal to 1.

For the WindSta configuration, atmospheric profiles were extracted from the ECMWF-HRES analysis (see Section 1.2.4).

2.1.4   Step 4 - Applying the attenuation

The acoustic source spectrum is equivalent to the pressure squared (see Chapter 3). Therefore, the acoustic source spectrum is multiplied by the squared attenuation Att^2, in order to obtain the acoustic contribution of the source point i at the station. Fig. 2.2c and Fig. 2.2d show the acoustic contribution of each source point at the Norwegian station I37NO, considering the attenuation computed with the two configurations NoWind (Fig. 2.2c) and WindSta (Fig. 2.2d). One may note the difference in the dominant sources between both configurations given that the stratospheric wind was likely blowing westwards.

2.1.5   Step 5 - Discretization and summation by azimuth

In order to study directional effects of the source, the wave model grid $(0.5° \times 0.5°)$ is discretized into azimuth bands of $1°$ width for each station. All sources are summed, after applying the attenuation, within these azimuth bands, thus giving the acoustic energy directional spectrum at the station. To reduce computation costs and to avoid remote sources that could be attenuated poorly (see Section 2.1.3), a distance limitation is set, beyond which the sources are not included in the total summation.

In Fig. 2.2e (NoWind configuration) and 2.2f (WindSta configuration), the sources shown are the ones considered for the summation; and the summation along the azimuth is represented in the outer circle (in order for the colour scale to show both the sources and the sum; this later was normalised in the representation). Directional distributions at a given frequency obtained from various time steps are represented in Fig. 2.2g (NoWind configuration) and 2.2h (WindSta configuration).

2.1.6   Modelling outputs and propagation time

Microbaroms arrivals modelling results depend both on the wave action model WW3 and on the atmospheric model ECMWF-HRES, which are updated respectively on a 3-hours time step and on a 6-hours time step. To simplify the problem, the values are considered constant over the time step and the microbaroms arrivals are modelled with a 3-hours time step.

Another approximation, motivated by a need for simplification, made was not to consider the propagation time of the acoustic wave. This approximation is particularly appropriate for sources closer than 3200 km (from the station) as they propagate to the station in less than 3 hours - if we consider an acoustic wave travelling at the speed of sound, taken as $300 \text{ m} \cdot \text{s}^{-1}$ for a stratospheric propagation. For longer ranges, the approximation is still interesting as remote sources are more attenuated and have therefore less impact on the total amplitude at the station.

2.2   Observations vs modelling

In order to determine the best modelling configuration, it is necessary to quantify the adequacy between modelling results and observations. The main issue to determine a metric lies in the difference of format between observations and modelling.

2.2.1   Types of data

2.2.1.1   Modelling results

As described previously, the characteristics for modelling microbaroms arrivals are the same as the ones of WW3: arrivals are modelled with a 3 hours time-step, for frequencies following a geometric expansion defined by $f_{i+1} = 1.1 f_i$, from $f_0 = 0.0821$ Hz to $f_N = 0.6073$ Hz. Therefore, for each time step and frequency, the model gives an amplitude (of pressure squared) depending on the azimuth. Fig. 2.2g (NoWind configuration) and 2.2h (WindSta configuration) give a representation of the directional distribution for $f_i = 0.234$ Hz, over two weeks. These distributions are normalised by time step in order to show the azimuths with higher acoustical energy.

2.2.1.2   Observations

Observations, on the other hand, are not regularly sampled as they depend on the detection of a coherent signal by the PMCC algorithm. The number of observations by 3-hours time step varies from 0 to 450 detections families in the frequency band $[0.1 - 0.6]$ Hz as shown in Fig. 2.3a.

By definition, a PMCC detection is a vector containing acoustic wave parameters, such as:

- t_{obs}: the detection time is obtained from two parameters t_{start} and t_{end}, respectively the time when the detection begun and ended.

- Az_{obs}: the back-azimuth of the signal - i.e. the angle (from North) at which the source is seen from the station.

- A_{obs}: the amplitude of the signal is the peak-to-peak amplitude of the signal.

- Tp_{obs}: the pseudo-period is the period estimated the peaks of the signal.

- f_{obs}: the acoustic frequency is obtained by taking the inverse of the pseudo-period.

- Sp_{obs}: the horizontal speed at which the acoustic wave passes through the array.
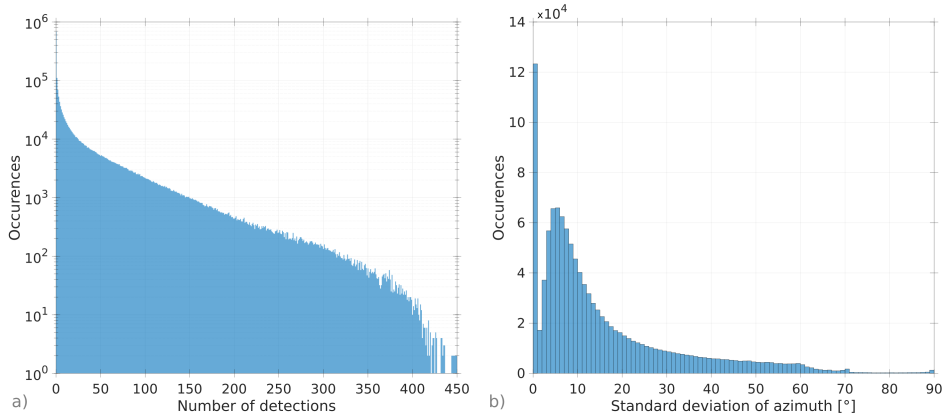
Figure 2.3 – Observation characteristics for the whole IMS database in the frequency band [0.1 - 0.6] Hz: a) number of observations per 3 hours time step and b) standard deviation of azimuths detected during a 3 hours time step.

2.2.2   Comparison of dominant parameters

As the PMCC processing considers the signal that gives the maximum of correlation, it is more likely to pick the dominant signal for each frequency. Therefore, it seems logical to apply a similar processing to the modelling results. As those are directional spectra, it is not possible to apply directly the PMCC processing on them. Thus, the idea is to extract the dominant signal from the modelled spectra and to define *pseudo-detections* for the model,

described by a time t_m - the time step of the model -, an amplitude A_m, a frequency f_m and an azimuth Az_m - where the m index stands for *model*. For each time step t_m, those parameters are defined by:

$$A_{\mathrm{mod}} = \max_{\substack{f \in [f_0, f_N] \\ \theta \in [0, 2\pi]}} \left(\sqrt{P_{2,sta}(f, t_{\mathrm{mod}}, \theta) \mathrm{d}f \mathrm{d}\theta} \right) \tag{2.2}$$

$$= \sqrt{P_{2,sta}(f_{\mathrm{mod}}, t_{\mathrm{mod}}, Az_{\mathrm{mod}}) \mathrm{d}f \mathrm{d}\theta} \tag{2.3}$$

At this point the observations and modelling data have a similar format with different temporal resolution. Of particular interest among the parameters are the azimuth and the normalised amplitude (normalised by the year average as there is still an offset between modelled and observed amplitude). Fig. 2.4 shows the comparison between the observations and the dominant modelled signal. To enhance the visibility, for each time step, only the detections with the greatest amplitude is kept.
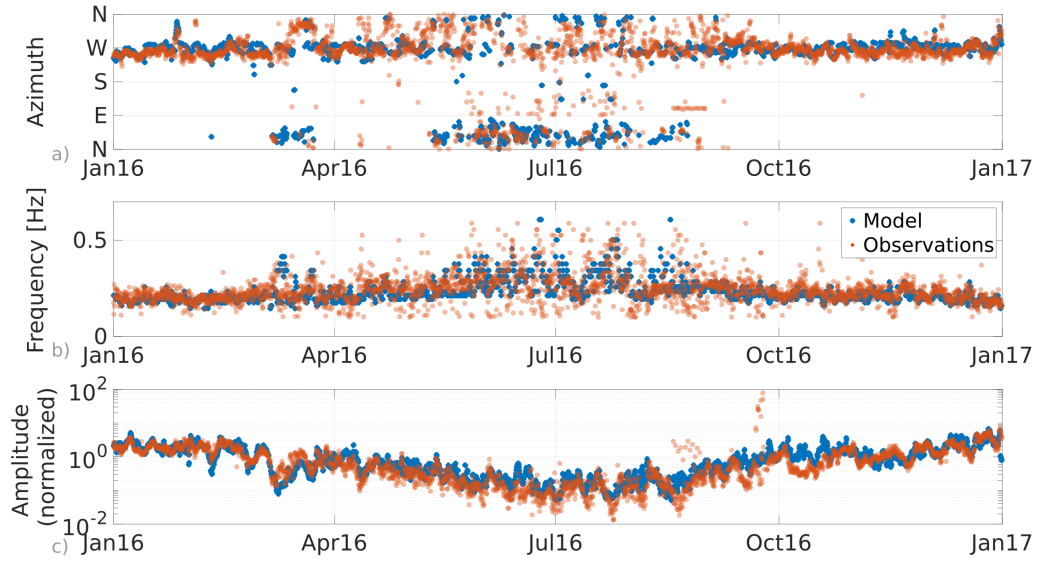
Figure 2.4 – Comparison between observed - orange dots - and modelled - blue dots - dominant signal parameters at I37NO: a) azimuth, b) frequency and c) the normalised amplitude.
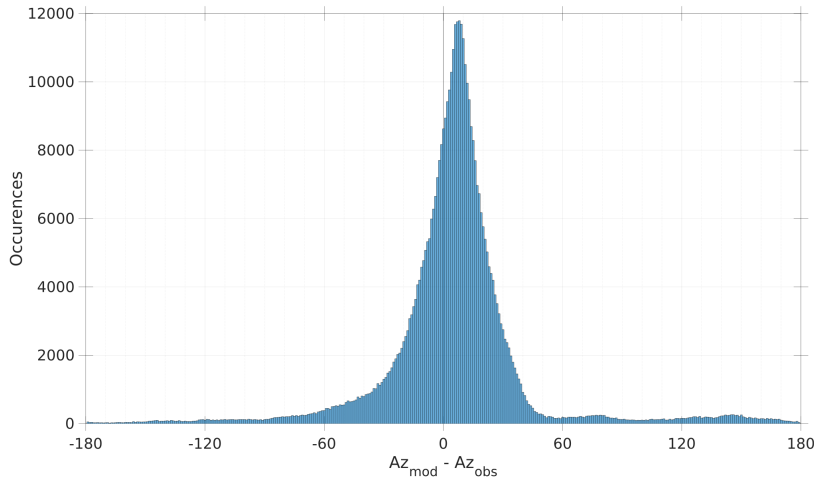
Figure 2.5 – Distribution of the azimuth difference between observation and model, for I37NO. The model is done with the REF102040 and WindSta configuration.

Visually the agreement is quite good between the model and the observations, however, when trying to quantitatively define the agreement one may note the important differences,

notably in the azimuth comparison as shown in Fig. 2.5. This figure represents the distribution of the difference $Az_{\text{mod}} - Az_{\text{obs}}$, accounting for all the detections with Az_{mod} constant over the 3 hours time step.

This variability is to be related with the azimuth spreading both in the model and in the observations (see Fig. 2.3b). This spreading originates both from the spatial extent of the sources and from detections capacity of the infrasound array.

In order to define a more robust metric, the spatial extent of the sources needs to be accounted for, and therefore, the azimuth width of the signal needs to be considered.

2.2.3 Binary classification test

2.2.3.1 Principle

The point is to consider that the directions with higher modelled energy are the ones with microbaroms arrivals predictions by the modelling. Therefore, a threshold is defined and for each time step, the directions whose amplitudes are higher than the threshold are considered to predict microbaroms arrivals ('Model = True'), whereas the other directions are considered to predict no arrival ('Model = False'). In order for the threshold to be constant for the whole time period, amplitudes are normalised - by the highest amplitude - for each time step, and then the threshold is defined between 0 and 1. The binarization process in shown in Fig. 2.6.

Observations can also be seen as a *True condition* where the condition is positive when there is at least one detection for a given time step and azimuth, and negative otherwise. Therefore, the time-direction pixels are classified into 4 categories corresponding to the confusion matrix of a binary classification test (see Fig. 2.6b):

- **MTOP** (Model = True, Observations = Positive), also called **True positive**: when the model predicts an arrival (amplitude greater than the threshold) and there is at least one detection.

- **MTON** (Model = True, Observations = Negative), also called **False positive**: when the model predicts an arrival (amplitude greater than the threshold) but there is no detection.

- **MFOP** (Model = False, Observations = Positive), also called **False negative**: when the model does not predict any arrival (amplitude lower than the threshold) but there is at least one detection.

- **MFON** (Model = False, Observations = Negative), also called **True negative**: when the model does not predict any arrival (amplitude lower than the threshold) and there is, indeed, no detection.

It follows that the two main interesting measures are: (i) the True Positive Rate (TPR) or sensitivity - which corresponds to the ratio of the number of true positive to all positive observations - and (ii) the False Positive Rate (FPR) - which corresponds to the ratio of the number of false positive to all negative observations. With the previous definitions those rates write:

$$TPR = \frac{MTOP}{MTOP + MFOP} \tag{2.4}$$

$$FPR = \frac{MTON}{MTON + MFON} \tag{2.5}$$

Those rates are based on a model perspective, accounting for the presence/absence of detections within a 3-hours$\times 1°$ cell without considering their quantities. To shift to an observations perspective (accounting for the number of detections), the **Coefficient of Predicted Observations (CPO)** is defined in eq. (2.6).

$$\text{CPO} = \frac{\text{card}(\{\text{Obs} \in O_{tot} \mid \theta_{\text{obs}} \in [\theta_m, \theta_m + \Delta\theta],\ t_{\text{obs}} \in [t_m, t_m + \Delta t], A_m(\theta_m, f, t_m) \geqslant thr\})}{\text{card}(O_{tot} = \{\text{Obs} \mid t_{\text{obs}} \in \text{month}, f_{\text{obs}} \in \cdot[f, f + 0.1]\})} \tag{2.6}$$
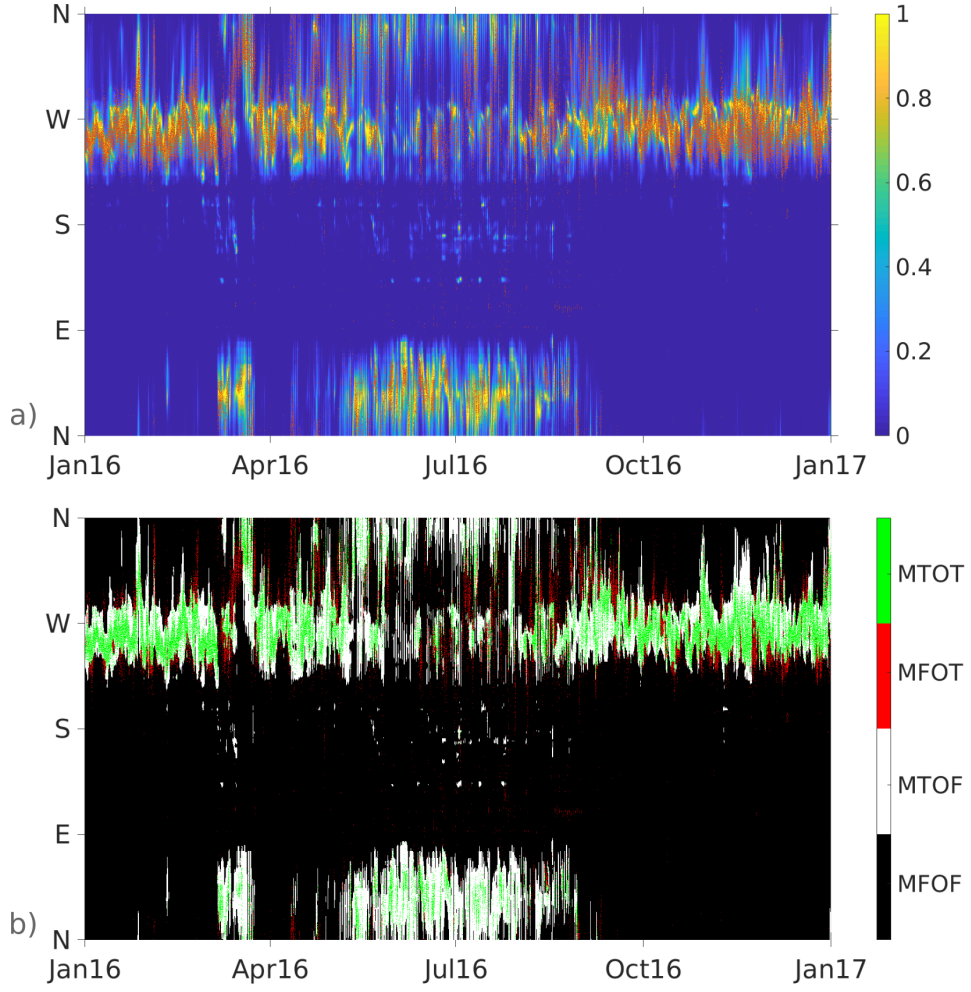
Figure 2.6 – Binarization of modelling results and comparison with detections. a) Azimuth distribution of normalised amplitude modelled - in colour - compared with the detections - orange dots. b) Result of the binarization: in white and green the model predicts arrivals whereas in black and red it does not; on the other hand, detections (i.e. 'observations = True') are coded in green and red. Therefore, black corresponds to MFOF, white to MTOF, green to MTOT and red to MFOT. The model was applied at I37NO between 0.1 and 0.6 Hz for the year 2016.

It corresponds to the ratio of predicted observations - those that fall into pixels where the model is true - to all observations. The CPO is similar to the TPR in its definition, however, it better reflects the capacity of the model to predict the observations. In order to smooth the variability of observations number by time step, the CPO is computed over a month.

Considering that this model purpose is to correctly predict as many observations as possible, the CPO is then chosen as the metric to quantify the match between the observations and the model.

2.2.3.2 Threshold definition

The chosen metric is highly impacted by the threshold used to binarize the model: the lower the threshold, the higher the CPO. This trend is quite logical as the lower the threshold the higher the part of the model that predicts arrivals. Yet, this variation is also associated with an increase of the False Positive Rate (see Fig. 2.7 with the increase of the white part - MTON - with the threshold).

The best threshold should then be a good trade-off between TPR and FPR. To do so, we defined a score that simply counts positively the True Positive and True Negative and

counts negatively the False Positive and Negative:

$$Score(i) = \widehat{MTOP}_i + \widehat{MFON}_i - \widehat{MTON}_i - \widehat{MFOP}_i \tag{2.7}$$

where i is the threshold and $\widetilde{M_\sqcup O_{\sqcup i}}$ is the number of $M_\sqcup O_\sqcup$ elements for the threshold i that has been modified to have a standardised distribution over the thresholds:

$$\widetilde{M_\sqcup O_{\sqcup i}} = \frac{M_\sqcup O_{\sqcup i} - \operatorname*{mean}_{j\in[0.1:0.9]} M_\sqcup O_{\sqcup j}}{\operatorname*{std}_{j\in[0.1:0.9]} M_\sqcup O_{\sqcup j}} \tag{2.8}$$

This modification is made in order for all the parameters to have a similar weight in the score function. This score function has been calculated for the whole IMS database from 2012 to 2018 with 8 different configurations. The results are shown in table 2.1. The threshold 0.4 is the one that maximises the score function, therefore this threshold is used in this study from now on. The False Positive issue is addressed by defining the threshold as the best trade-off between TPR and FPR, and therefore, the focus can be made only in the Coefficient of Predicted Observations.
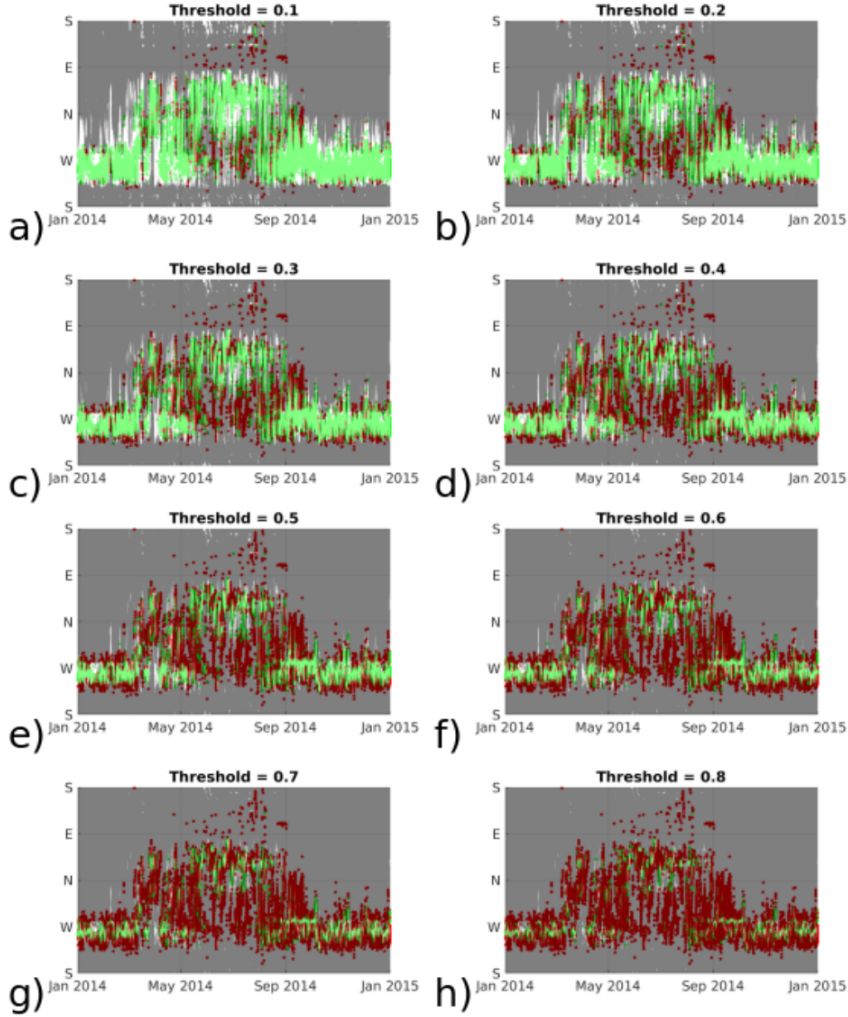
Figure 2.7 – Binarization of modelling results and comparison with detections - green dots are predicted observations and red dots are detections missed by the model - for 8 thresholds from 0.1 to 0.8 - a) to h) -. Model was applied at I37NO between 0.2 and 0.3 Hz for the year 2014.

Table 2.1 – Score function values for different thresholds, obtained from the whole database.

Threshold	Score
0.1	-0.5276
0.2	0.1537
0.3	0.3496
0.4	0.3538
0.5	0.2638
0.6	0.1247
0.7	-0.0457
0.8	-0.2345
0.9	-0.4378

2.2.4 Frequency bands

As previously stated in Section 2.2.1.1, modelling outputs are computed for 22 frequency bands following a geometric expansion, with frequency band width varying from 0.008 Hz to 0.055 Hz. On the other hand, for the observations, the filter frequency bands are much larger as they are logarithmically spaced and their widths vary from 0.02 Hz to 0.13 Hz in the interest range of [0.1-0.6] Hz. Moreover, as the order of the filter used is low (=2), the frequency bands of detections are even larger than the ones defining the filter. Therefore, using the frequency band refinement of the wave model is not necessary, and we degrade the frequency sampling by integrating over wave model frequencies. The new frequency bands are thus defined between 0.1 Hz and 0.6 Hz with a width of 0.1 Hz.

2.3 Distance limitation for source summation

2.3.1 Presentation of the study

In Section 2.1.3, the need for a limitation of the distance between modelled sources and ground observation station was demonstrated. This maximum distance needs to be a good trade-off between accounting for all the sources (this tends to increase the maximum distance) and not extrapolating too much the attenuation law (that was defined for 0-3000 km ranges, therefore, this tends to reduce the distance).

To define the maximum distance, the modelling has been performed for one year - 2018 - at all the IMS stations. Then the sources summation was realised as in eq. (2.1), with the set $\mathcal{A}_\theta(\mathrm{dist}_{max})$ depending on the maximum distance chosen:

$$\mathcal{A}_\theta(\mathrm{dist}_{max}) = \{i \mid \theta_i \in [\theta + \mathrm{d}\theta] \text{ and } \mathrm{dist}_i \leqslant \mathrm{dist}_{max}\} \tag{2.9}$$

where i is a WW3 model grid-cell, θ_i is the azimuth of the cell i seen from the station and dist_i is the distance between the cell i and the station.

A set of 8 dist_{max} was considered (in km): 2000, 3000, 4000, 5000, 6000, 7000, 8000, 10000.

2.3.2 Results

To determine the optimum distance, the CPO is calculated for each station and dist_{max}. As one of the objectives for this modelling is to apply it to all currently working stations and to also be applicable for new stations when they get working, the purpose is to consider only one dist_{max} for all stations with the best fit possible. Therefore, the average CPO is computed over all stations and is shown against the maximum distance in Fig. 2.8. The highest CPO average corresponds to a maximum distance dist_{max} of 5000 km. Thus, from now on, sources summation is performed using both eq. (2.1) and eq. (2.9), and dist_{max} is taken as 5000 km.
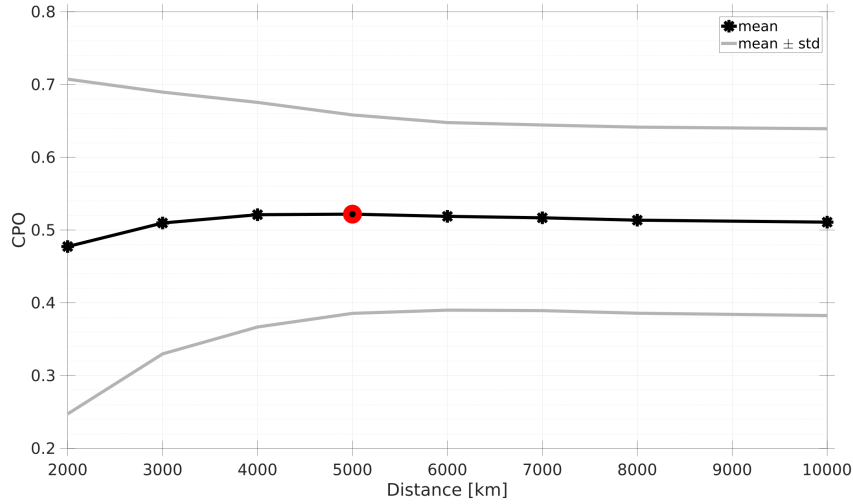
Figure 2.8 – Variations of the Coefficient of Predicted Observations (CPO) with the maximum distance considered. Mean - black line with circles - and standard deviation - grey lines - over the IMS stations. The red circle shows the highest mean CPO value.

2.4 Conclusions

In this chapter, we set up a global modelling to predict microbaroms arrivals at ground stations, along with a metric to quantify the fit between those predictions and the observations. The modelling methodology is shown in Fig. 2.9 and the main features are the following:

- 2 configurations are to be considered for wave modelling: one with coastal reflection - REF102040 - and the second without any coastal reflection - NOREF.

- 2 configurations are to be considered for attenuation law: one with constant stratospheric wind ratio equal to 1 that corresponds to conditions without wind impact - No Wind - and the second with atmospheric characteristics taken at the station each 6 hours - WindSta.

- All contributing sources are summed within a $1°$ interval and within a maximum distance from the station $\text{dist}_{\max} = 5{,}000$ km.

- Contributions are integrated into 5 frequency bands of 0.1 Hz width.

- The CPO - Coefficient of Predicted Observations, eq. (2.6) - is applied with a threshold of 0.4.
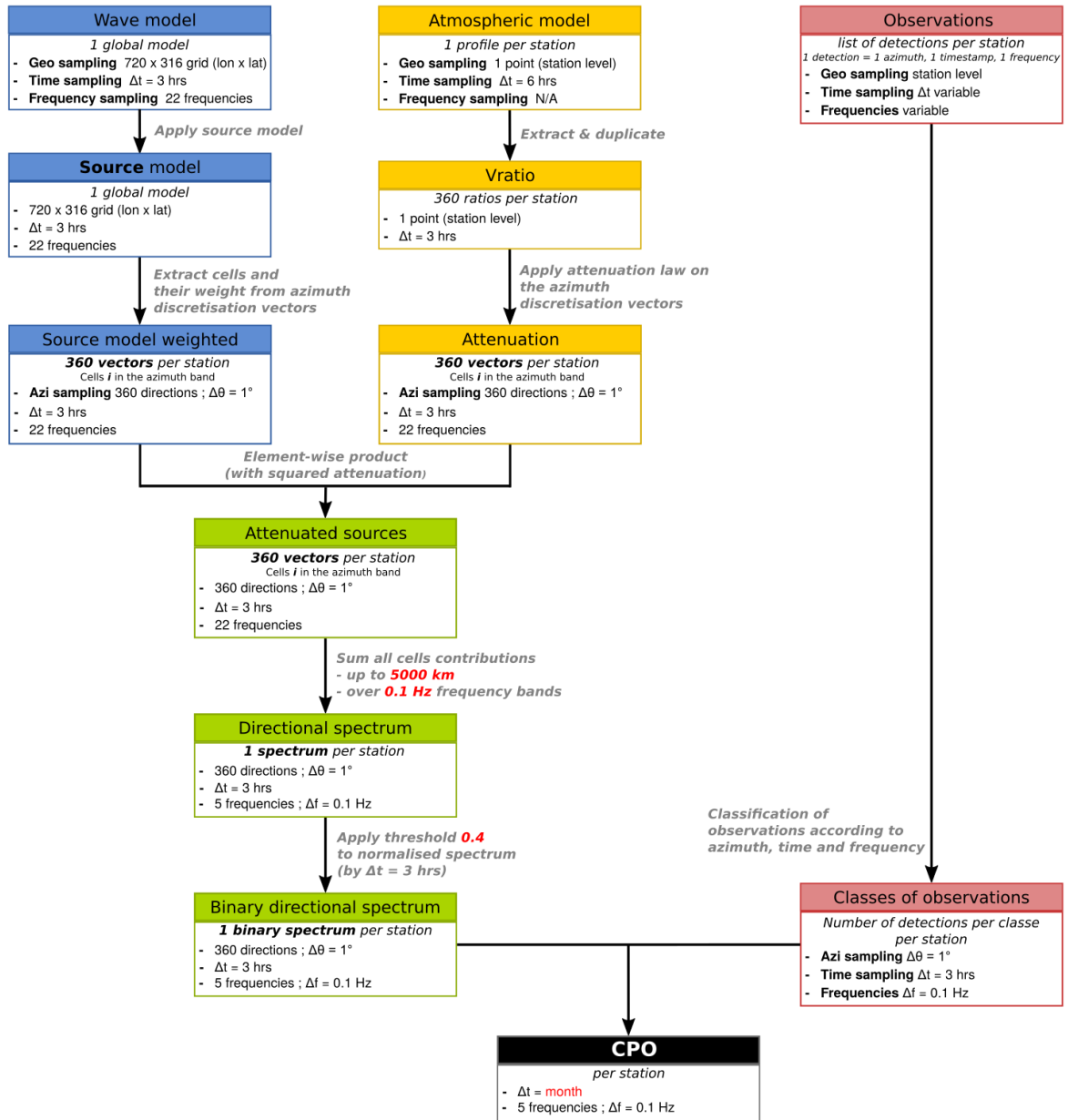
Figure 2.9 – Flowchart of the methodology described in this chapter.

MICROBAROMS SOURCE GENERATION: A UNIFYING APPROACH

Contents

3.1   Chapter preamble

As explained in Section 1.1, the fact that nearly-opposing wave interactions generate acoustic waves was already demonstrated by Longuet-Higgins (1950) and K. Hasselmann (1963). From these interactions, two main theories have been developed about the generation of microbaroms atmospheric infrasound. In an ocean with infinite depth, Brekhovskikh et al. (1973) (hereafter BK73) derived a source with a value depending on the elevation angle ; whereas - also in an ocean with infinite depth - the summation over the source area led Waxler & Gilbert (2006) to consider that the source radiates in a monopolar way. Following this development, Waxler et al. (2007) (hereafter W07) included the bottom in the theory to account for eventual resonances as the wavelength of these waves in the water is close to 7.5 km which corresponds to the order of magnitude of ocean depth (from 0 to 10 km). The impact of the bathymetry on the modelled microbaroms sources by W07 has been found important (Smets, 2018). As this important impact is a result of the monopolar radiation, the question of the bathymetry impact with a non monopolar radiation arises. Therefore, in the framework of this thesis, the source model equations have been derived again in order to extend the previous theories to the combined effects of both finite depth ocean and non monopolar radiation.

   This derivation is presented in this chapter which consists of a published paper by De Carlo et al. (2020)[1] (hereafter DC20) that discussed the inclusion of the bathymetry in the theory as well as a non-monopolar radiating source. The Supplementary Material of the paper presents all the theory derivations - almost line by line - in Appendix A, its main purpose was to facilitate reviewer's and future PhD students' work.

---

[1]De Carlo, M., Ardhuin, F., Le Pichon, A. (2020). Atmospheric infrasound generation by ocean waves in finite depth: unified theory and application to radiation patterns. *Geophysical Journal International, 221*(1), 569-585. doi: 10.1093/gji/ggaa015

3.1.1   Summary of De Carlo et al. 2020

In this paper, microbaroms radiated power P writes in a generic way:

$$P(f_s) = a\mathcal{H}(f)\int_0^{\frac{\pi}{2}}|R_a(\theta_a,h)|^2 d\theta_a$$

$$= a\int E(f,\theta)E(f,\theta+\pi)d\theta\int_0^{\frac{\pi}{2}}|\sin\theta_a\cos\theta_a R_a(\theta_a,h)|^2 d\theta_a \qquad (3.1)$$

where f_s is the microbaroms frequency, f the ocean wave frequency, θ the horizontal direction of ocean waves, a a multiplicative factor and R_a a function defined accordingly to the microbaroms model considered - see table 3.1 - that may depend on θ_a the launching elevation angle and h the water depth. $\mathcal{H}(f)$ is the Hasselmann's integral as defined in equation (1.12).

Fig. 3.1 shows the value of $R_a(\theta_a,h)$ for the three models: on the right R_a is represented against θ_a as derived by BK73 in an infinite depth ocean. At the bottom, W07's solution is represented as a function of depth and resonant depths can be clearly identified. On the top left, color levels represent R_a against both θ_a and h as derived in DC20. It can be noted that the new model is coherent with W07 - for $\theta_a = 0$ - and BK73 - for an infinite ocean depth - and unites them.

One may note that, following Snell's law at the ocean-atmosphere interface, all propagating waves in the ocean, where the sound speed is α_w around $1500\,\text{m}\cdot\text{s}^{-1}$, are radiated in the atmosphere, where the sound speed is α_a around $330\,\text{m}\cdot\text{s}^{-1}$, within $\arcsin(\alpha_a/\alpha_w)\sim 13°$ from the vertical. Thus, except in very shallow water, these atmospheric propagation angles are the only ones for which the bathymetry can have an influence. Indeed, as shown in Fig 3.1, for $\theta_a > 13°$, resonances are not observed anymore. The only remaining effect of the water depth is a small diminution of the coefficient for shallow water. However, on a global scale this effect is weak, as for the year 2018, the emitted microbaroms flux between 20 and 90° calculated without accounting for the depth is different from the one computed with the whole model by only 7%.

Added to that, elevation angles of received signals at ground stations are rather horizontal - from 0 to 40° from the horizontal, therefore the impact of the bathymetry in microbaroms signals strongly depends on the radiation pattern of the source.
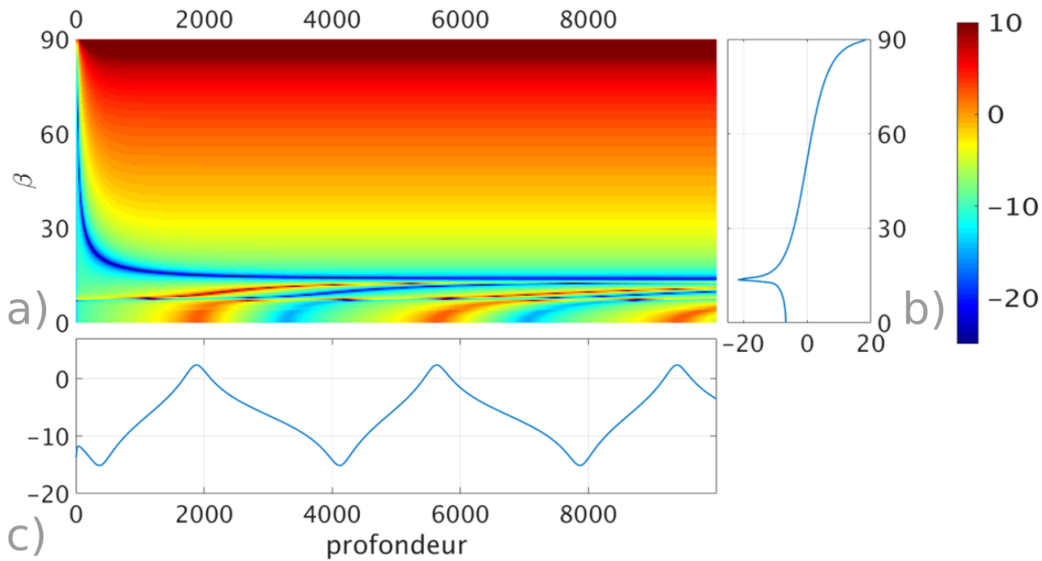
Figure 3.1 – R_a values $[log_{10}]$ for the three studied models: a) DC20 model with $R_a(\theta_a,h)$ depending on the depth and the elevation angle, b) BK73 model with $R_a(\theta_a)$ depending on the elevation angle in a infinite ocean depth and c) W07 model with $R_a(\theta_{a,0},h)$ depending on the water depth.

Table 3.1 – Summary of R_a forms depending on the models

Model	R_a	Depends on θ_a	Finite Depth	Equation in DC20
BK73	$\int_0^{\frac{\pi}{2}} \|R_a(\theta_a)\|^2 d\theta_a$	✓	✗	eq. (3.39)
W07	$\int_0^{\frac{\pi}{2}} \|R_a(\theta_{a,0}, h)\|^2 d\theta_a$ $= \frac{\pi}{2}\|R_a(\theta_{a,0}, h)\|^2$	=	✗	eq. (3.44)
DC20	$\int_0^{\frac{\pi}{2}} \|R_a(\theta_a, h)\|^2 d\theta_a$	✓	✓	eq. (3.50)

3.1.2 Physical interpretation of R_a terms and tribute to Brekhovskikh et al. (1973)

In order to present the physical meaning of the different terms gathered in R_a, we focus first on the value of R_a for an infinite ocean. We can write eq. (3.39) as follow:

$$
R_a(\theta_a) = \frac{\overbrace{l}^{1} - \overbrace{\delta_a}^{2} - \overbrace{\delta_a \left[1 - 2\sin^2\theta_a \left(1 - \frac{1}{2}\cos^2(\varphi_2 - \varphi) \right) \right]}^{3} - \overbrace{\delta_a n^2}^{4} - \overbrace{\frac{\delta_a}{4} n^2}^{5}}{\underbrace{\cos\theta_a}_{6} - \underbrace{\delta_a \cos\theta_a l/2}_{7} - \underbrace{\mathrm{i}\delta_a/4}_{8} - \underbrace{\mathrm{i}ml}_{9}}
$$

(3.2)

where l is the vertical wavenumber in the water without accounting for corrections due to the gravity, φ is the wave azimuth, and φ_2 is the resulting acousting wave horizontal azimuth. δ_a, n and m are small parameters corresponding respectively to the ratio between the acoustic wavenumber and the ocean wavenumber, the ratio of the sound speed in the air to the sound speed in the water and the ratio between the air and the water densities.

The different parts of equation (3.2) originate from:

① the velocity continuity at the interface, and the medium difference (different celerities) leading to the refraction of acoustic waves. This term corresponds to the vertical wavenumber in the ocean without gravity correction;

② the compressibility of the air - through the particular solution and the forcing term on the right hand side of the acoustic wave equation;

③ the advection of the free surface by ocean waves in the velocity continuity equation: because the sea surface is not flat, the wave motion is not a simple "piston" that communicates water velocity to the air and the velocity of one wave train advects the slope of a second wave train. This is the only term that, for almost opposing waves, varies with the azimuth of the acoustic wave relative to the ocean wave;

④ the compressibility of the water - through the particular solution and the forcing term of interaction in the acoustic wave equation;

⑤ the gravity effect in acoustic wave equation on the water side, leading to a corrective term on the vertical wavenumber in the water;

⑥ the velocity continuity at the interface, and the medium difference (different celerities) leading to the refraction of acoustic waves. This term corresponds to the vertical wavenumber in the air without gravity correction and is the dominant term except for very grazing angles;

⑦ the hydrostatic pressure and finite wave amplitude, coming from the Taylor expansion of the boundary condition around $z = 0$;

⑧ the gravity effect in the air in the wave equation leading to a corrective term on the vertical wavenumber in the air;

⑨ the feedback of the air-side pressure on the water-side pressure, which cannot be ignored for propagation angles close to the horizontal.

While ⑥ is the term that drives the general pattern with an increasing amplitude with θ_a; ⑧ and ⑨ allow the solution to be finite when $\theta_a \to 90°$. Except for the sign before ⑨, this is the same equation as the one derived by Brekhovskikh et al. (1973).

When accounting for water depth h and removing the small term in $\delta_a n^2$, we obtain (based on eq. (3.50))

$$R_a(\theta_a, h) = \frac{-①R - Q\left[② + ③\right]}{Q\left(⑥ - ⑧\right) + R\left(⑦ + ⑨\right)} \tag{3.3}$$

where $R = \sinh(\mu h) + r\cosh(\mu h)$ and $Q = \cosh(\mu h) + r\sinh(\mu h)$ are coefficients that appear due to boundary conditions between the ocean and the crust - continuity of velocity and a zero tangential stress -, with μ the complex vertical wave number in the ocean (μ corresponds to l with the corrective term from the gravity) and r the reflection coefficient at the bottom.

The difference between eq. (3.2) and eq. (3.3) only impacts near vertical angles $\theta_a < 13°$, and depths below 1000 m for higher vertical angles. Thus, the acoustic radiation of microbaroms found by Brekhovskikh et al. (1973) was a good approximation of the total acoustic radiation, even including bathymetry effects. Albeit their work was very thorough, it was quite difficult to read and understand (even if translated in English) as it rederived all the equations from Longuet-Higgins (1950) for the air, without giving as much details. Therefore, it was not very well understood and mainly left aside by the community.

3.1.3 Main difference with Waxler et al. (2007)

In Waxler & Gilbert (2006), there are some differences with eq. (3.2). Firstly, the authors did not account for gravity effects thus accounting only for half of ③. Secondly, θ_a was taken equal to zero, simplifying ③ to $\delta_a/2$, ⑥ to 1 and ⑦ to $\delta_a l/2$. As the leading order of the denominator ⑥ no longer tends to zero, the authors have troncated the smaller order terms thus removing ④,⑤,⑦,⑧ and ⑨.

Waxler et al. (2007) model was based on WG06 simplifications and it appears that the main disagreement between W07 (based on WG06; WG06-W07) and DC20 is the consideration of a monopolar source radiation by WG06-W07 $\theta_a = 0$. As a matter of fact, they did not state that the source is monopolar, it came from their derivation when simplifying the problem for long-range propagation. They took interest on the power P_r^2 received by a sensor at a position x. As the pressure $P_r(x)$ corresponds to the integral over the source surface of the source amplitude multiplied by the Green function - function representing the propagation - the power spectrum writes[2]:

$$P_r^2(x) = \iint_S \iint_S \left\langle G(x,y)G^*(x,y')\right\rangle |R_a(\theta_a, h)|^2 e^{i\theta_a(y-y')}\mathrm{d}y\mathrm{d}y' \tag{3.4}$$

Then, as the source is small compared to the distance to the sensor, they consider that the propagation is the same for all points and that the Green function does not vary inside the source. It comes that in the integral over y' leads to a Dirac function of θ_a - so the only remaining angle would be the vertical one:

$$P_r^2(x) = \iint_S \left\langle G(x,y)G^*(x,y')\right\rangle |R_a(\theta_a, h)|^2 \iint_S e^{i\theta_a(y-y')}\mathrm{d}y'\mathrm{d}y \tag{3.5}$$

$$P_r^2(x) = \iint_S \left\langle G(x,y)G^*(x,y')\right\rangle |R_a(\theta_a, h)|^2 \delta(\theta_a)\mathrm{d}y \tag{3.6}$$

---

[2]N.B: Notations have been simplified for the sake of comprehension.

To consider the Green function constant over the source seems coherent as the source is not big enough for variations to be important. However, by considering it constant, any possible phase shift between different source point is neglected. From a technical point of view, the Green function used latter in their article by Waxler and Gilbert contains a phase term that can be factorized to obtain:

$$G(x,y)G*(x,y') = \tilde{G}(x,y)\tilde{G}^*(x,y)e^{i\theta_a(y'-y)} \tag{3.7}$$

With $\tilde{G}$ the Green function without the exponential term. Then, using this formula in equation (3.4) leads to:

$$P_r^2(x) = \iint\limits_S \iint\limits_S \langle \tilde{G}(x,y)\tilde{G}^*(x,y) \rangle e^{i\theta_a(y'-y)} |R_a(\theta_a,h)|^2 e^{i\theta_a(y-y')} \mathrm{d}y\mathrm{d}y' \tag{3.8}$$

And

$$P_r^2(x) = \iint\limits_S \iint\limits_S \langle \tilde{G}(x,y)\tilde{G}^*(x,y) \rangle |R_a(\theta_a,h)|^2 \mathrm{d}y\mathrm{d}y' \tag{3.9}$$

And then, the hypothesis leading to $\theta_a = 0$ - and to a monopolar radiation - disappears.

3.2 Atmospheric infrasound generation by ocean waves in finite depth: unified theory and application to radiation patterns[3]

Abstract

Between 0.1 and 0.5 Hz, infrasound signals recorded in the atmosphere are dominated by ocean-generated noise called microbaroms. Microbaroms propagate through the atmosphere over thousands of kilometers due to low absorption and efficient ducting between the ground and the stratopause. Different theoretical models have been developed to characterize the source of microbaroms, all based on the second-order non-linear interaction of ocean waves. While early theories considered an infinite ocean depth and a source radiation depending on the acoustic wave elevation angle, other works have approximated the radiation pattern as a monopole, and found a considerable effect of the water depth. This paper reviews these models and extends the previous theories to the combined effects of both finite depth ocean and source directivity in both elevation and azimuth angles. It is found that the water depth has a negligible effect for the near-horizontally propagating acoustic waves that should dominate the measured microbarom records. Another important result is that the microbarom azimuthal variation can be highly directive locally, but it generally becomes isotropic when integrated over a realistic source region.

3.2.1 Introduction

Continuous oscillations of the ground displacement and atmospheric pressure, named respectively secondary microseisms and microbaroms, are measured worldwide by seismological and infrasound networks with a dominant frequency around 0.2 Hz (Benioff & Gutenberg, 1939). They are generated by second-order non linear interaction of ocean gravity waves of similar frequency propagating in almost opposite directions (Longuet-Higgins, 1950; K. Hasselmann, 1963).

Microbarom propagate through the atmosphere over large distances due to low absorption rates and efficient atmospheric ducting between the ground and the stratopause (D. Drob, 2019; Waxler & Assink, 2019). Studying microbaroms recorded for four years at Palisades, New York, (Donn & Rind, 1971) have revealed the importance of winds in the higher atmosphere for their propagation, pointing to the capability of ground-based measurements to probe the higher atmosphere, for which very few other observations are available.

Recent developments of infrasound networks at global and continental scales facilitate the analysis of acoustic waves for probing unresolved atmospheric structures in the middle atmosphere (Marty, 2019; Blanc et al., 2018). This has motivated mathematical developments of geophysical inverse problems using infrasound from well identified sources (D. P. Drob et al., 2010; Assink et al., 2014). Ducting of infrasound depends on the 3-D wind and temperature fields and is most efficient if the propagation direction coincides with the polar vortex at mid-latitude regions. In particular, the main characteristics of Sudden Stratospheric Warming events have been successfully derived from directional microbarom amplitude variations resulting from changes in stratospheric and thermospheric propagation conditions (e.g. Garcés et al., 2002; Landès et al., 2010; Smets & Evers, 2014). Such studies demonstrate the advantage of an infrastructure that integrates independent middle atmospheric measurement techniques currently not assimilated in numerical weather prediction models (NWP) and provides quantitative understanding of stratosphere-troposphere dynamical coupling useful for NWP applications (Le Pichon et al., 2015).

So far, microbarom studies have used qualitative comparisons between source models and received signals, with difficulties of interpretation associated with uncertainties in the measurements and in the propagation. Thanks to novel measurements from a stratospheric balloon fitted with microbarometers, (Bowman & Lees, 2018) were able to verify quantitatively the predictions based on numerical ocean wave models and the microbarom source theory of Waxler et al. (2007) using measured sound spectra over the Southern Ocean. Their

---

[3]N.B.: Apart from the layout, this version presents some differences with the published article, as minor errors were found after publication in eq. (3.50) and Figure 3.5.
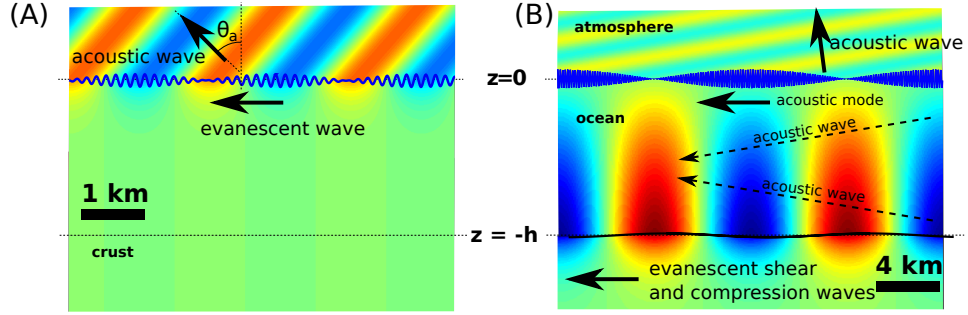
Figure 3.2 – Example of vertical cross-section of the pressure pattern, in colors, radiated by a pair of interacting ocean wave trains of period around 10 s. The sea surface elevation, plotted as a blue line around $z = 0$ is the sum of the elevations of the two wave trains and has a wave group structure. (A) The periods of the two wave trains are 10 s and 9.66 s (B) 10 s and 9.94 s. Note that the vertical displacement of the sea surface is strongly exaggerated in order to make waves visible. A realistic ocean wave field includes many wave trains and thus all possible pairs of interactions radiating acoustic waves in all directions θ_a. As the two periods of the wave train get closer, from (A) to (B), the lengths of the groups get larger and the angle θ_a becomes smaller. This paper focuses on the radiated power as a function of θ_a.

further interpretation of microbaroms as a major heat source for the thermosphere, well
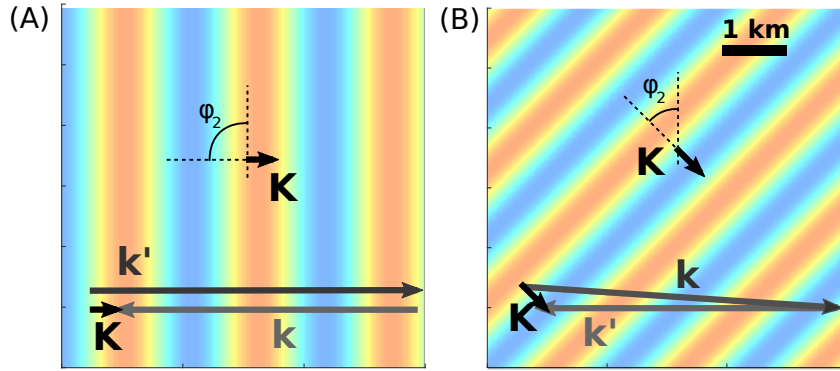
Figure 3.3 – Example of horizontal pressure patterns, in colors, radiated by a pair of interacting ocean wave trains of periods 10 s and 9.66 s with (A) opposing directions (B) not exactly opposing directions. For acoustic waves, the maximum magnitude K of the wavenumber vector **K** corresponds to horizontal propagation with $K = \Omega/\alpha_a$ and can be in any azimuth φ_2 depending on the exact ocean wave wavenumbers **k** and **k'**. Modes with larger values of K decay exponentially over the vertical and are not relevant for microbaroms measured on land.

above their measurement altitude, relies on the monopolar radiation pattern predicted by Waxler & Gilbert (2006).

Following the work of Longuet-Higgins (1950) on microseisms, a first theory of microbarom generation was proposed by Posmentier (1967), with the atmospheric motion coming from the continuity of the velocity field at the air-sea interface, and no feedback of the atmosphere on the pressure field in the ocean. A more complete theory for random waves, consistent with the microseism generation theory of K. Hasselmann (1963) and an accurate treatment of the air-sea boundary condition is given by Brekhovskikh et al. (1973), leading to significant differences for near-horizontal propagation. However, that work only considered an ocean of infinite depth. The effect of the ocean depth, with the amplification of particular frequencies corresponding to an 'organ pipe resonance' of the water column, was later considered by Waxler et al. (2007), extending the work done by Waxler & Gilbert (2006).The major difference between that work and the earlier analysis of Brekhovskikh et al. (1973) is the monopole radiation pattern that, as we show here, comes from an assumption on the coherence of the source over only very short scales whereas Brekhovskikh et al. (1973) did not introduce this assumption. A unified theory is thus necessary for further quantitative analysis of microbarom records and the analysis of their impact in regions where

no measurement is available, such as the thermosphere.

Given that microbaroms and microseisms are related (Donn & Naini, 1973) it is interesting to discuss microseisms for which more quantitative analyses are available. Microseisms have their most energetic sources associated to severe ocean storms but not necessarily co-located with the storm due to the propagation of ocean waves as swells (Obrebski et al., 2012). In particular, measurements at seismic stations near coasts can be dominated by the interaction of storm waves with their reflection from the coast (Bromirski et al., 1999; Ardhuin et al., 2011). In general, the sources at a frequency f_s correspond to the interaction of waves with similar frequencies $f = f_s/2$ and nearly opposite directions, as illustrated in Fig. 3.2.

The generation of acoustic and seismic modes in the ocean and solid Earth with horizontal propagation speeds that exceed 1500 m/s, much more than the typical ocean waves phase speeds around 15 m/s, was explained quantitatively by K. Hasselmann (1963) as the result of an interference of pairs of ocean wave trains of wavenumbers $\mathbf{k}$ and $\mathbf{k}'$, giving seismic or acoustic waves at the wavenumber $\mathbf{K} = \mathbf{k} + \mathbf{k}'$. The microseism generation theory is one particular example of the general theory of wave-wave interactions developed by K. Hasselmann (1966). The horizontal radiation pattern of a single pair of ocean waves gives a single sinusoidal pressure field propagating in the direction φ_2 of the wavenumber vector $\mathbf{K}$. For microseisms $K = |\mathbf{K}|$ is generally much smaller than the width of the ocean wave spectrum, so that the combination of all pairs of ocean waves gives an isotropic source.

In the case of microbaroms of frequency 0.2 Hz, the sound speed in the air is only 20 times the phase speed of the ocean waves, so that K is comparable to the ocean wave spectrum width, and there may be a preferential radiation in some directions φ_2. Applications and further analysis of microbaroms require a knowledge of the source magnitude and variability. In recent work, Waxler et al. (2007) investigated the influence of the water depth on the source magnitude, similar to what is found for microseisms. The conclusion of the present paper is that the effect of water depth depends on the angle θ_a of the sound propagation relative to the vertical direction, and that the pressure field of microbaroms over the ocean generally contains a wide range of angles. Indeed, the coupling of the ocean and atmosphere strongly depends on θ_a, as demonstrated by Brekhovskikh et al. (1973), but neglected by Waxler & Gilbert (2006).

This importance of θ_a is now well known for microseisms and is easy to understand in relation to the physical properties of the solid Earth, ocean, and atmosphere. A usual approximation of the propagating medium is a stack of uniform horizontal layers l characterized by different velocities of propagation α_l and β_l for compression and shear waves. Close to the source, microseisms are dominated by Rayleigh waves that correspond to relatively slow components, with horizontal propagation speeds between the sound speed in water α_w, and the shear wave speed in the crust β_c. These Rayleigh modes combine motions that decay exponentially with depth in the solid Earth, with propagating acoustic waves in the ocean, and their acoustic propagation angles in the water θ_w are larger than $\arcsin(\alpha_w/\beta_c) \simeq 30°$ (Ardhuin et al., 2019). For very large distances, seismic body waves may dominate the signal because of their weaker attenuation with distance, and these are due to the ocean acoustic noise that is more nearly vertical, allowing propagation in the crust, with $\theta_w < \arcsin(\alpha_w/\alpha_c) \simeq 16°$. The water depth effect is clearly different for Rayleigh and body waves, as predicted by Ardhuin & Herbers (2013) and Gualtieri et al. (2014), and demonstrated by (Obrebski et al., 2013) and Meschede et al. (2017).

Now looking at microbaroms, we expect similar dependencies on θ_a because different components of the ocean wave forcing field, with wavenumbers $\mathbf{K} = \mathbf{k} + \mathbf{k}'$ give acoustic modes that have different apparent horizontal speeds $C = 2\pi f_s/|\mathbf{K}|$. Speed faster than the compression speed in the crust $C > \alpha_c$ leads to the generation of compression P-waves in the solid Earth, corresponding to nearly vertical propagation in the ocean layer and even more vertical propagation in the atmosphere, given by Snell's law. The limit $C \to \infty$ corresponding to vertical propagation and $|\mathbf{K}| = \mathbf{0}$, which are the exactly standing waves of Longuet-Higgins. At the other extreme, $C < \alpha_w$ gives evanescent waves in the water layer that correspond to acoustic-gravity (AG) modes that dominate the pressure field measured in the top 300 m of the ocean, as observed by Cox & Jacobs (1989) and Ardhuin et al. (2013). For these AG modes, we expect no influence of water depths larger than 300 m on the pressure at the ocean surface. These AG waves are coupled to atmospheric acoustic

Table 3.2 – Notations used in different papers: LH50 stands for Longuet-Higgins (1950), BGKN73 stands for Brekhovskikh et al. (1973), WG06 stands for Waxler & Gilbert (2006) and AH13 stands for Ardhuin & Herbers (2013).

quantity	this paper	LH50	BGKN73	WG06	AH13
vertical coordinate	z	$-z$	z	z	z
angle relative to vertical	θ_a or θ_w	–	θ_1 or θ_2	–	–
surface elevation	ζ	ζ	ζ	ξ	ζ
azimuth of spectrum	φ	θ	φ	θ	θ
azimuth of acoustic signal	φ_2	–	φ_a	–	–
velocity potential	ϕ	$-\phi$	$-\varphi$	ϕ	ϕ
layer index	l	–	j	σ	–
sound speed	α_l	c	c_j	c_σ	α
density ratio	m	–	m	–	–
horizontal wavenumber	$\mathbf{K}$	–	$\mathbf{q}$	–	$\mathbf{K}$
radian frequency	Ω	–	Ω	–	$2\pi f_s$
horizontal wavenumbers	$\mathbf{k}, \mathbf{k}'$	$(-uk, -vk)$	$\varkappa, \varkappa_1$	$\mathbf{k}, \mathbf{q}$	$\mathbf{k}, \mathbf{k}'$
radian frequencies	σ, σ'	σ	$\omega(\varkappa), \omega(\varkappa_1)$	$\omega(\mathbf{k}), \omega(\mathbf{q})$	σ, σ'
pressure	p	p	$\rho\mathcal{P}$	p	p
vertical wavenumbers	ν, μ	$-, \alpha$	λ_1, λ_2	–	l_a, l
upward amplification	$g/2\alpha_l$	γ	–	–	–

waves that have propagation angles larger than $\theta_{a0} = \arcsin \alpha_a/\alpha_w \simeq 12°$.

The difference in water depth effects between body waves, Rayleigh waves and AG modes should influence the amplitude of acoustic waves radiated in the atmosphere, and the amplitude of microbaroms should strongly depend on the direction of propagation θ_a relative to the vertical. The decomposition of the ocean wave forcing in different horizontal wavenumbers $\mathbf{K} = K (\cos\varphi_2, \sin\varphi_2)$ allows to consider separately the different acoustic wave components and how they may contribute to different acoustic modes. Each K corresponds to a propagation angle such that $\sin\theta_l = K \alpha_l/(2\pi f_s)$ where α_l is the sound speed in the layer l, which is related to Snell's law.

Because the ocean wave spectra are relatively broad, they contain a wide range of pairs $\mathbf{k}$ and $\mathbf{k}'$ so that all possible $\mathbf{K}$ are excited simultaneously. For microseisms, this produces a spectrum of the excitation that is white in wavenumber, and thus equivalent to a point force. In the case of microbaroms, the conversion from wave motion to acoustic pressure is a function of the wavenumber K, first given by Brekhovskikh et al. (1973), which determines the radiation pattern in the atmosphere.

Hence the previous works either lack the possible important effect of finite depth in the ocean, or important aspects of the radiation pattern in the atmosphere. In order to progress towards a quantitative understanding of microbarom signals it is thus necessary to have both effects in the same theory, and this is the objective of the present paper. For the sake of simplicity, we only consider the case of a homogeneous atmosphere, and extend the theory of Brekhovskikh et al. (1973) to take into account a finite water depth. The theoretical formulation and the main results are given in section 2, with details of the derivation in the Supporting Information presented in Appendix A. These results are interpreted in section 3 and conclusions follow in section 4.

3.2.2 A general theory of microbarom sources

In order to facilitate the translation between the different papers we have listed in table 3.2 the correspondence of the main symbols used. We have also included Longuet-Higgins (1950) because it treats almost the same physical problem, with a focus on the water layer, and the same decomposition in particular and homogeneous solutions of the forced wave equation.

As detailed in the Supporting information (Annex A), which follows the method of Brekhovskikh et al. (1973), the basis of microseism and microbaroms generation theory is the coupling of motions in different layers, with a forcing coming from nonlinear ocean wave effects, in which the nonlinearity is necessary to allow the generation of waves with long wavelenghts $2\pi/|\mathbf{k}+\mathbf{k}'|$ from the interference of shorter ocean waves with wavelengths $2\pi/|\mathbf{k}|$

and $2\pi/|\mathbf{k}|'$. The velocity potential ϕ in layer l is solution of a wave equation (Brekhovskikh et al., 1973),

$$\frac{\partial^2 \phi}{\partial t^2} - \alpha_l^2 \nabla^2 \phi = -\frac{\partial}{\partial t}(\nabla \phi)^2 - g\frac{\partial \phi}{\partial z}, \tag{3.10}$$

where ∇^2 is the 3-dimensional Laplace operator. The two terms on the right hand side can be neglected in the water layer (Longuet-Higgins, 1950), but are generally significant in the air. The first term corresponds to the effect of compressibility. It adds one particular solution ϕ_p that is zero away from the boundary but modifies the homogeneous solution via the boundary condition at the air-sea interface. The second term is the effect of gravity, which gives a weak additional $\exp(gz/2\alpha_l^2)$ vertical decay, with a half-decay distance of 15 km in the atmosphere and 300 km in the ocean. That second effect was considered by Brekhovskikh et al. (1973) but neglected in Waxler & Gilbert (2006).

Neglecting these two terms for the water layer, solutions that are periodic in time and space take the following homogeneous form, with $\Omega = 2\pi f_s$ the radian frequency and $\kappa_a = \nu_+$ and $\kappa_w = \mu_-$ the vertical wave-numbers (going upwards in the air and downwards in the water)

$$\begin{aligned} \phi &= \sum_{\mathbf{k}} \Phi_l \exp\left[i\left(\mathbf{K} \cdot \mathbf{x} + \kappa_l z - \Omega t\right)\right] + \text{c.c.} \\ &= \sum_{\mathbf{k},s} \Phi_l \exp\left[i\left(\mathbf{K} \cdot \mathbf{x} + \kappa_l z - s\Omega t\right)\right], \end{aligned} \tag{3.11}$$

where c.c. stands for the complex conjugate and $s = 1$ or $s = -1$ is a sign index. Neglecting the right hand side of (3.10), one gets

$$\kappa_l^2 + K^2 = \Omega^2/\alpha_l^2. \tag{3.12}$$

With N the number of unknown potential amplitudes $(\Phi_i)_{1 \leqslant i \leqslant N}$, there are N continuity conditions for stresses and displacements at the layer interfaces, linking the N amplitudes of velocity potentials.

All the variables, the pressure p, the density ρ, the velocity potential ϕ and the sea surface elevation ζ are expanded in powers of $\varepsilon = ak$ that is the product of a typical ocean wave wavenumber k and surface elevation amplitude a,

$$p = p_0 + p_1 + p_2 + ... \tag{3.13}$$

$$\rho = \rho_0 + \rho_1 + \rho_2 + ... \tag{3.14}$$

$$\phi = \phi_0 + \phi_1 + \phi_2 + ... \tag{3.15}$$

$$\zeta = \zeta_0 + \zeta_1 + \zeta_2 + ... \tag{3.16}$$

In addition to the wave slope ε, two other small parameters are defined, the ratio between the air and water densities $m = \rho_a/\rho_w$ and $\delta_l = \sigma/k\alpha_l$ the ratio between the speed of surface waves and the speed of sound in the air or water.

Collecting the terms of same order, we obtain at each order a system of N equations for N unknowns with a detailed derivation in Supporting Information. At order ε^0, the solution is the hydrostatic equilibrium of pressure and gravity. The first order solution corresponds to Airy waves, which are linear gravity waves, with negligible $O(\delta_w^2)$ and $O(m)$ corrections due to the presence of air and the compressibility of air and water, as given by Brekhovskikh et al. (1973, eqs. 11 and 12. See also Supporting information). Namely the surface elevation is given by K. Hasselmann (1962),

$$\zeta_1(\mathbf{x}, t) = \sum_{\mathbf{k},s} Z_{1,\mathbf{k}}^s \exp\left[i\left(\mathbf{k} \cdot \mathbf{x} - s\sigma t\right)\right], \tag{3.17}$$

where $Z_{1,\mathbf{k}}^s$ is the amplitude of the first order sea surface elevation for wavenumber $\mathbf{k}$ and propagation direction s and $s = \pm 1$ is a sign index that gives the direction of propagation

relative the direction of the wave vector $\mathbf{k}$. The velocity potential in the water is given by,

$$\phi_w(\mathbf{x}, z, t) = \sum_{\mathbf{k},s} \Phi_{1,\mathbf{k}}^s \frac{\cosh(kz + kh)}{\cosh(kh)} \exp\left[\mathrm{i}\left(\mathbf{k} \cdot \mathbf{x} - s\sigma t\right)\right] \tag{3.18}$$

with

$$\Phi_{1,\mathbf{k}}^s = \frac{g}{\mathrm{i}\sigma} Z_{1,\mathbf{k}}^s. \tag{3.19}$$

In the air, the effects of gravity and compressibility (i.e. the right hand side terms in eq. 1), are less negligible, and we have,

$$\phi_a(\mathbf{x}, z, t) = \sum_{\mathbf{k},s} \frac{k}{k_a} \Phi_{1,\mathbf{k}}^s \exp\left[-k_a z + \mathrm{i}\left(\mathbf{k} \cdot \mathbf{x} - s\sigma t\right)\right] \tag{3.20}$$

with eq. 12 in Brekhovskikh et al. (1973),

$$k_a = k\left(\sqrt{1 - \delta_a^2 + \delta_a^4/2} - \delta_a^2/2\right) \simeq k\left(1 - \delta_a^2\right) \tag{3.21}$$

where $\delta_a = \sqrt{g/k}/\alpha_a$. We note that half of this correction to k_a comes from the $\delta_a^2/2$ that is due to gravity, and the other half comes from the air compressibility.

Finally, in the ε^2 system, the wave spectrum acts as a forcing, coming through either the particular solutions that satisfy the wave equation with the right hand side, or from the boundary conditions between the different layers. In other words the wave forcing $\boldsymbol{\Lambda} = (\Lambda_i)_{1 \leqslant i \leqslant N}$ is a vector on the right hand side of a matrix equation

$$\mathbf{M}\boldsymbol{\Phi} = \boldsymbol{\Lambda}. \tag{3.22}$$

The only differences between all the theories discussed here are in the approximations of the boundary conditions between ocean and atmosphere and ocean and solid Earth. Mathematically, different terms are neglected in the coefficients of the matrix $\mathbf{M}$ or in the forcing vector $\boldsymbol{\Lambda}$, as detailed below.

Further extensions to multiple layers in the atmosphere and solid Earth give rise to different horizontally propagating modes, which correspond to zeros of the determinant of $\mathbf{M}$, for which a growth rate of the energy can be computed as done for seismic Rayleigh waves by K. Hasselmann (1963). The size of the matrix $\mathbf{M}$ grows by two lines and columns for each extra fluid layer, for which the two unknowns are one upward and one downward propagating potential amplitudes. For a solid layer there are four unknowns due to the presence of both compression and shear motions (see K. Hasselmann, 1963, eq. 1.4). The important difference with K. Hasselmann (1963) is that Λ_i was non-zero only for the sea surface pressure continuity equation in Hasselmann's case, whereas in our case we consider forcing in both the pressure and velocity equations. We also note that for finite water depth there is also a forcing term in the boundary condition for the ocean bottom pressure coming into Λ_3 (Ardhuin & Herbers, 2013).

3.2.2.1 Existing solutions

3.2.2.1.1 Case of infinite water depth - Brekhovskikh et al. (1973) Brekhovskikh et al. (1973) considered only two layers, air and water, that are half spaces. As a result, for each frequency Ω and wavenumber vector $\mathbf{K}$, there are only two unknowns, one amplitude A for the velocity potential of upgoing acoustic waves in the atmosphere, and one amplitude W for downgoing acoustic waves or evanescent modes in the ocean. The approximation $m = \rho_a/\rho_w \ll 1$ removes the feedback of the atmospheric pressure on the air pressure, so that the atmosphere is only driven by the continuity of vertical velocities at the interface.

The coupling of air and water layers at $z = 0$ by the continuity of pressure and velocity gives a 2 by 2 matrix $\mathbf{M}$, with one line for the continuity of vertical velocity $w = \partial\phi/\partial z$ and the other for the continuity of pressure p ,

$$M_{1,1}A + M_{1,2}W = \Lambda_1 \tag{3.23}$$

$$M_{2,1}A + M_{2,2}W = \Lambda_2 \tag{3.24}$$

Following Brekhovskikh et al. (1973), we introduce the small parameters

$$\delta_a^2 \;=\; g/(k\alpha_a^2) \tag{3.25}$$

$$m \;=\; \rho_a/\rho_w \tag{3.26}$$

$$n \;=\; \alpha_a/\alpha_w \tag{3.27}$$

and we note that $|K/k| < 2\delta_a$. We now keep only the lowest order terms in δ_a and m, giving the following matrix coefficients and right hand side (see Supporting information for details),

$$M_{1,1} \;=\; \nu_+ \;=\; \mathrm{i}\frac{\Omega}{\alpha_a}\cos\theta_a + \frac{k}{2}\delta_a^2 \tag{3.28}$$

$$M_{1,2} \;=\; -\mu_- \;=\; 2k\delta_a l - \frac{\delta_a^2}{2}kn^2 \tag{3.29}$$

$$M_{2,1} \;=\; -m\Omega^2 - g\mathrm{i}\frac{\Omega}{\alpha_a}\cos\theta_a \tag{3.30}$$

$$M_{2,2} \;=\; \Omega^2 \tag{3.31}$$

$$\Lambda_1 \;=\; \mathrm{i}s\Omega k\delta_a^2\left(2 - 2\sin^2\theta_a(1 - \tfrac{1}{2}\cos^2(\varphi_2 - \varphi)) + n^2\right) \tag{3.32}$$

$$\Lambda_2 \;=\; \frac{\mathrm{i}s\Omega}{\rho_w}p_{\mathrm{surf}}^s(\mathbf{K},\Omega) + o(\delta_a^2) \tag{3.33}$$

where we have defined

$$l = (\sin^2\theta_a - n^2)^{1/2} = n\cos\theta_w \quad \text{if} \quad \theta_a < \theta_{a0}. \tag{3.34}$$

Following K. Hasselmann (1963), we define the amplitude of the equivalent surface pressure induced at second order by the wave motion. Assuming that $kh \gg 1$ we take the following definition,

$$p_{\mathrm{surf}}^s(\mathbf{K},\Omega) = -2\rho_w \sum_{\mathbf{k}+\mathbf{k}'=\mathbf{K},\sigma+\sigma'=\Omega} \sigma\sigma' Z_{1,\mathbf{k}}^s Z_{1,\mathbf{k}'}^s. \tag{3.35}$$

In the following we write p_{surf}^s instead of $p_{\mathrm{surf}}^s(\mathbf{K},\Omega)$.

The solution of the matrix equations eq. (3.23)–(3.24) is given by Cramer's rule,

$$A = \frac{\Lambda_1 M_{2,2} - \Lambda_2 M_{1,2}}{\det(\mathbf{M})}, \qquad \text{and} \qquad W = \frac{\Lambda_2 M_{1,1} - \Lambda_1 M_{2,1}}{\det(\mathbf{M})}. \tag{3.36}$$

Following details in Supporting material section S4.1, We find the amplitudes of the velocity potentials at the air-sea interface to be, for the water and air respectively,

$$W \;\simeq\; \frac{\mathrm{i}}{\rho_w}\frac{1}{2\sigma'}p_{\mathrm{surf}}^s \tag{3.37}$$

$$A \;\simeq\; \frac{R_a}{\rho_w}\frac{1}{2\sigma'}p_{\mathrm{surf}}^s \tag{3.38}$$

with

$$R_a = \frac{l - 2\delta_a\left[1 - \sin^2\theta_a\left(1 - \tfrac{1}{2}\cos^2(\varphi_2 - \varphi)\right) + \tfrac{5}{8}n^2\right]}{\cos\theta_a\left(1 - \delta_a l/2\right) - \mathrm{i}\left(\delta_a/4 + ml\right)}. \tag{3.39}$$

This form of R_a is identical to Brekhovskikh et al. (1973, eq. 22), except for the addition of one extra term $\cos\theta_a l\delta_a/2$ in the denominator, and a change in the sign of the denominator term ml. As shown in Fig. 3.4, these two terms have a negligible impact on the solution, except for $\theta_a > 89.5°$, with less than 1% change in the total radiated acoustic power.
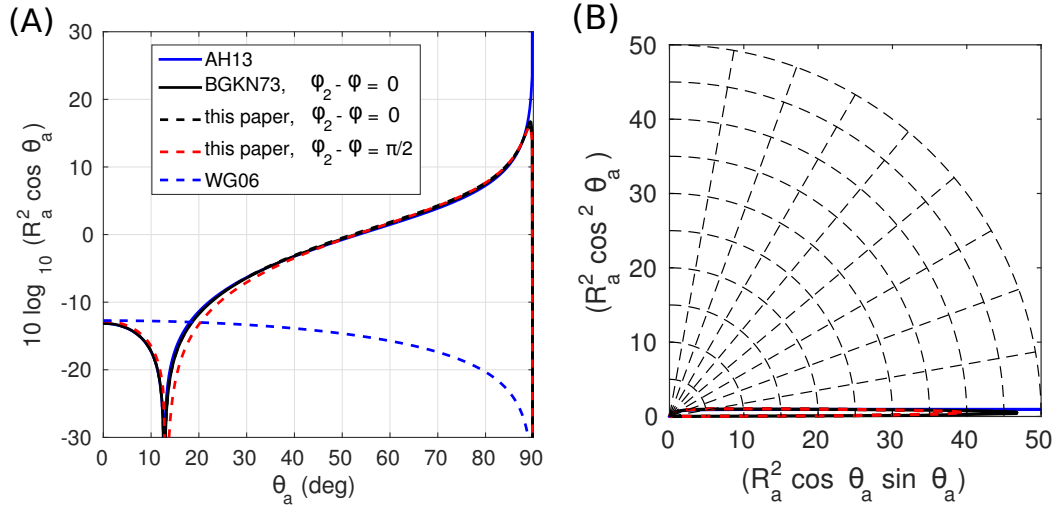
Figure 3.4 – Patterns of acoustic pressure variance as a function of the elevation angle θ_a for an ocean wave period of 10 s, given by the different theories without ocean bottom, in cartesian (A), and polar (B) representation. Note that when the radiated power is considered, these patterns must be multiplied by $\sin \theta_a$ before integration over θ_a, as given by eq. (3.61). In general, as given by eq. (30) the radiated power is also a function of the relative azimuth of the first ocean wave train φ and the azimuth of the radiated acoustic power φ_2.

3.2.2.1.2 A simplified case - Ardhuin & Herbers (2013)

The solution given by Ardhuin et al. (2013) corresponds to the simplified solution given by eq. (21) in Brekhovskikh et al. (1973), with m and δ_a terms neglected, corresponding to an absence of feedback from the atmospheric pressure on the oceanic pressure, i.e. $M_{1,1} = 0$, and neglecting the right hand side of the acoustic wave equation in the air, i.e. $\Lambda_1 = 0$, giving

$$R_a = \frac{l}{\cos \theta_a} = \frac{\mathrm{i}(n^2 - \sin^2 \theta_a)^{1/2}}{\cos \theta_a} \tag{3.40}$$

where we recall that l is imaginary for $\theta_a < \theta_{a0}$.

This simplified solution corresponds to infinite water depth. It presents a singularity for horizontal acoustic propagation as $\cos \theta_a$ goes to zero. That singularity is removed when the feedback of the air on the water motion is taken into account.

3.2.2.1.3 Theory by Waxler and Gilbert (2006)

Following Brekhovskikh et al. (1973), Waxler & Gilbert (2006) showed that microbarom signals are due both to ocean radiation and to compression of the air by the surface motion, but Waxler & Gilbert (2006) neglected the effect of gravity in the air. As detailed in the Supporting information, accounting for gravity in the air changes their term $3\delta_a^2/2$ in their eq. (57) to $2\delta_a$ in eq. (3.41). we also note a change of sign from -2 to 1.5,

$$R_a^{\mathrm{WG06}} = \mathrm{i}n + 1.5\delta_a. \tag{3.41}$$

The particularity of the derivation by Waxler & Gilbert (2006) is the fact that they neglect the phase shift in the Green's function within the source region. They justified that approximation by assuming that the coherence length scale in the acoustic source is small compared to the acoustic wavelength. Here we do not use such an approximation, as detailed in the Appendix A, as the correlation function of the source is given by the pressure spectrum $p_{\mathrm{surf}}^s(\mathbf{K}, \Omega)$ (our eq. 3.35) that overlaps with the acoustic wavelengths. The assumption in (Waxler & Gilbert, 2006) comes between their equations (50) and (51) and simplifies the expression of the radiation pattern in the atmosphere to a monopolar radiation pattern. It also reduces all expressions to their values for $\mathbf{K} = 0$, corresponding to strictly opposing wave trains, so that the evanescent ocean motions that correspond to $\theta_a > \theta_{a0}$ are not properly represented. Without this assumption, (Brekhovskikh et al., 1973) found that the radiation pattern is very different from a monopole, with an overwhelming radiation at very grazing angles, as illustrated in Fig. 3.2.A.

3.2.2.2   Generalization of Brekhovskikh et al. (1973) to a finite ocean depth

The first discussion of water depth effects on microbarom sources is due to Waxler et al. (2007). That work extended the analysis by Waxler & Gilbert (2006), limiting the water depth to h and including an interface with a solid half space below. The velocity potential in the water is now

$$\phi_{w,2} = \sum \left(W_+ \mathrm{e}^{\mu_+ z} + W_- \mathrm{e}^{\mu_- z} \right) \mathrm{e}^{\mathrm{i}\Theta}. \tag{3.42}$$

with the complex wavenumber $\mu_\pm = g/(2\alpha_w) \pm \sqrt{K^2 - \Omega^2/\alpha_w^2} \simeq \pm\mu = \pm\sqrt{K^2 - \Omega^2/\alpha_w^2}$.

Taking an acoustic reflection coefficient $r = \rho_w \alpha_w/(\rho_s \alpha_s)$, Waxler et al. (2007) found the reflection condition for the down-going acoustic waves, with potential ϕ_w^- at the ocean bottom

$$W^+ = \frac{1+r}{1-r} \mathrm{e}^{2\mu h} W^-. \tag{3.43}$$

This gives,

$$R_a^{\mathrm{W07}} \simeq \mathrm{i}n \frac{r\cos(\Omega h/\alpha_w) + \mathrm{i}\sin(\Omega h/\alpha_w)}{\cos(\Omega h/\alpha_w) + \mathrm{i}r\sin(\Omega h/\alpha_w)} + 1.5\delta_a. \tag{3.44}$$

In order to properly consider the effect of the propagation angles, we can go back to the derivation of Brekhovskikh et al. (1973), now including an upgoing acoustic wave in the water layer. For oblique incidence we have to consider the contribution of compression waves and shear waves in the crust with velocities α_s and β. Defining the vertical wavenumbers in the the crust

$$\chi_p = \sqrt{K^2 - \frac{\Omega^2}{\alpha_s^2}}, \quad \text{and} \quad \chi_s = \sqrt{K^2 - \frac{\Omega^2}{\beta^2}}. \tag{3.45}$$

The reflection at the bottom generalizes to

$$r \simeq \frac{\Omega^4 \rho_w \chi_p}{\rho_s \mu \left[(\Omega^2 - 2K^2\beta^2)^2 - 4\beta^4 K^2 \chi_p \chi_s \right]}. \tag{3.46}$$

This is obtained by eliminating the potentials of the compression and shear motions in the crust, using the continuity of velocity and a zero tangential stress (see also Ardhuin & Herbers, 2013; Gualtieri et al., 2014).

When only the dominant terms are kept we find,

$$R_a = \frac{l}{\cos\theta_a} \frac{R}{Q} \tag{3.47}$$

with

$$R = \sinh(\mu h) + r\cosh(\mu h), \tag{3.48}$$
$$Q = \cosh(\mu h) + r\sinh(\mu h). \tag{3.49}$$

In the case $\theta_a = 0$, eq. (3.47) corresponds to the first term of eq. (3.44).

When going to first order in δ_a and m, the problem can be simplified by neglecting the effect of gravity in the water layer, which contributed to the n^2 term in the numerator of eq. (3.39). This gives $-\mu_- = \mu_+ = \mu$. It is then more simple to eliminate the amplitude W^- by using the bottom boundary condition on the vertical velocity. This amounts to replacing $-\mu_-$ by $-2\mu R \mathrm{e}^{-\mu h}/(1+r)$ in $M_{1,2}$ and Ω^2 by $2Q\Omega^2 \mathrm{e}^{-\mu h}/(1+r)$ in $M_{2,2}$, giving,

$$R_a = \frac{-lR - 2\delta_a Q \left[1 - \sin^2\theta_a \left(1 - \frac{1}{2}\cos^2(\varphi_2 - \varphi) \right) \right]}{\cos\theta_a \left(Q + R\delta_a l/2 \right) - \mathrm{i}\left(Q\delta_a/4 - Rml \right)} \tag{3.50}$$

3.2.2.3   Radiated acoustic power as a function of elevation and azimuth

We introduce the spectral density of the homogeneous (propagating) pressure field at $z = 0$, in the three spectral dimensions (K_x, K_y, f_s) using the Fourier amplitude of $p_{a,2}$ at $z = 0$,
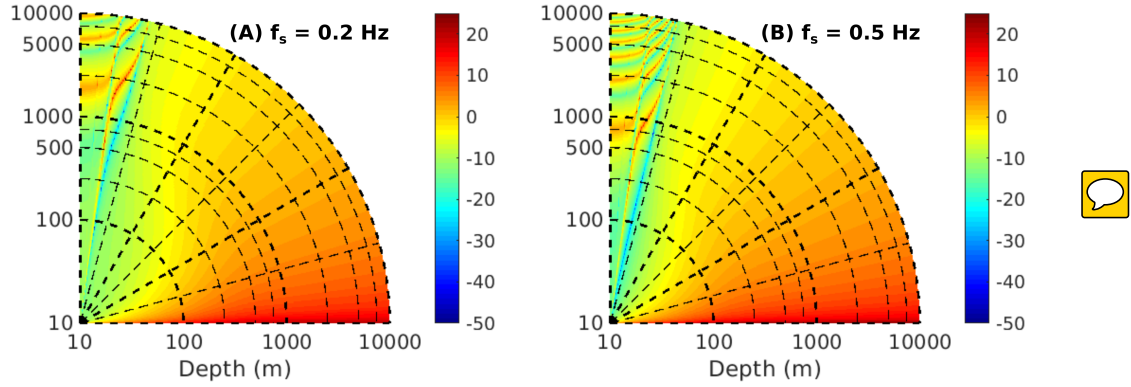
Figure 3.5 – Radiation patterns of $10\log_{10}|R_a|$ according to eq. (3.50) for (A) $f_s = 0.2$ Hz , (B) $f_s = 0.5$ Hz with $f_s = \Omega/2\pi$ - polar representation against the angle θ_a and the depth h.

Table 3.3 – Summary of differences between models, with R_a defined on eq. (3.38)

Model	depends on θ_a	depth	compressible	gravity	R_a
BGKN73	✓	∞	✓	✓	eq. (3.39)
AH13	✓	∞	✗	✗	eq. (3.40)
WG06	✗	∞	✓	✗	eq. (3.41)
W07	✗	any	✓	✗	eq. (3.44)
this paper	✓	any	✓	✓	eq. (3.50)
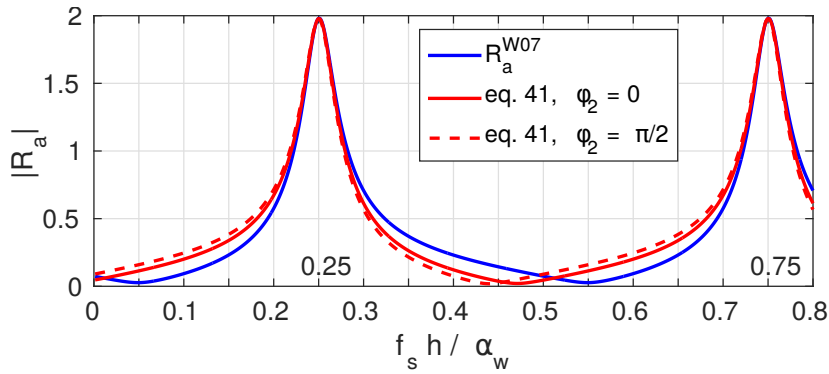
Figure 3.6 – Magnitude of the velocity potential amplification from the water to the air, R_a, as a function of the ratio of the water depth and acoustic wavelength, in the case of vertical propagation, i. e. $\theta_a = 0$. For $f_s = 0.2$ Hz, the two peaks corresponds to depths of 1900 and 5600 m. Here we have used $\alpha_s = 5540$ m/s, $\beta = \alpha_s/\sqrt{3}$, $\rho_s = 2500$km/m^3.

obtained from the average over realizations of the sea state, represented by angular brackets, of the pressure amplitude squared,

$$F_{p,2h}(\mathbf{K}, f_s) = 2 \lim_{\Delta K_x \to 0, \Delta K_y \to 0, df_s \to 0} \frac{\left\langle \left| P_{2,h}^+ \right|^2 (\mathbf{K}, f_s) \right\rangle}{\Delta K_x \Delta K_x \Delta f_s} \tag{3.51}$$

Given the dispersion relation of ocean surface gravity waves in deep water, the Jacobian of the transformation from (k_x, k_y) to (f, φ) is $2\pi k/(\partial \sigma/\partial k) = 4\pi\sigma^3/g^2$.

We now define the ocean wave spectrum as

$$
\begin{aligned}
E(f, \varphi) &= \frac{4\pi\sigma^3}{g^2} E(k_x, k_y) = 2 \lim_{\Delta k_x \to 0, \Delta k_y \to 0} \frac{|Z_{\mathbf{k}}^+|^2}{\Delta K_x \Delta K_y} \frac{4\pi\sigma^3}{g^2} \\
&= 2 \lim_{\Delta f \to 0, \Delta\varphi \to 0} \frac{|Z_{\mathbf{k}}^+|^2}{\Delta f \Delta\varphi}.
\end{aligned}
\tag{3.52}
$$

We use eq. (3.35) and replace the amplitude $P_{2,h}^+$ by $i(\sigma + \sigma')\rho_a A$, namely,

$$P_{2,h}^+ = \frac{i\rho_a(\sigma + \sigma')}{\rho_w 2\sigma'} R_a p_{\text{surf}}^+. \tag{3.53}$$

This gives,

$$
\begin{aligned}
2\left| P_{2,h}^+ \right|^2 &= 2\rho_a^2 |R_a|^2 \sigma^2(\sigma + \sigma')^2 \left| \sum_{\mathbf{k}+\mathbf{k}'=\mathbf{K}, \sigma+\sigma'=\Omega} Z_{1,\mathbf{k}} Z_{1,\mathbf{k}'} \right|^2 \tag{3.54} \\
&= \sigma^2(\sigma + \sigma')^2 \rho_a^2 |R_a|^2 \sum_{\mathbf{k}+\mathbf{k}'=\mathbf{K}, \sigma+\sigma'=\Omega} 2\left| Z_{1,\mathbf{k}}^+ \right|^2 2\left| Z_{1,\mathbf{k}'}^+ \right|^2, \tag{3.55}
\end{aligned}
$$

where the last equality is obtained by considering that each pair of wavenumbers $(\mathbf{k}_1, \mathbf{k}_2)$ is counted twice, a first time when $\mathbf{k} = \mathbf{k}_1$ and $\mathbf{k}' = \mathbf{k}_2$ and a second time when $\mathbf{k} = \mathbf{k}_2$ and $\mathbf{k}' = \mathbf{k}_1$. This is well understood when considering the simplest form with the ocean wave field consisting of only two cosine waves (See Supporting information, eqs. S124–S128).

Taking the limit to continuous sums and using a change of variable from (k_x, k_y, k_x', k_y') to (f_s, φ, K_x, K_y), with $K_x = k_x + k_x'$, $K_y = k_y + k_y'$ and $f_s = (\sqrt{gk} + \sqrt{gk'})/(2\pi)$ the Jacobian of the coordinate transform is

$$
\begin{aligned}
\det\left(\frac{\partial f_s \partial\varphi \partial K_x \partial K_y}{\partial k_x \partial k_y \partial k_x' \partial k_y'} \right) &=
\begin{vmatrix}
g\cos\varphi/(4\pi\sigma) & -\sin\varphi/k & 1 & 0 \\
g\sin\varphi/(4\pi\sigma) & \cos\varphi/k & 0 & 1 \\
g\cos\varphi'/(4\pi\sigma') & 0 & 1 & 0 \\
g\sin\varphi'/(4\pi\sigma') & 0 & 0 & 1
\end{vmatrix} \\
&= \frac{g^2}{4\pi\sigma^3\sigma'} \left[\sigma' - \sigma\cos(\varphi - \varphi') \right], \tag{3.56}
\end{aligned}
$$

and gives

$$
\begin{aligned}
\int F_{p,2h}(\mathbf{K}, f_s) dK_x dK_y df_s &= \rho_a^2 \int \sigma^2(\sigma+\sigma')^2 |R_a|^2 E(k_x, k_y) E(k_x, k_y) dk_x dk_y dk_x' dk_y' \\
&= \rho_a^2 \int \sigma^2(\sigma+\sigma')^2 |R_a|^2 \frac{E(k_x, k_y)E(k_x', k_y')4\pi\sigma^3\sigma'}{g^2 \left[\sigma' - \sigma\cos(\varphi - \varphi')\right]} df_s d\varphi dK_x dK_y.
\end{aligned}
$$

Now we use the unicity of the Fourier transform to identify the spectral density in the left and right hand sides, and using eq. (3.52) gives

$$F_{p,2h}(\mathbf{K}, f_s) = \frac{1}{2}\rho_a^2 g^2 f_s \int_0^{2\pi} \frac{\sigma^2(\sigma+\sigma')}{\sigma'^2} |R_a|^2 \frac{E(f, \varphi)E(f', \varphi')}{\sigma' - \sigma\cos(\varphi - \varphi')} d\varphi. \tag{3.57}$$

We note that the form of the acoustic power given by eq. (3.57) is generally a function of the direction φ_2 of the horizontal wave vector $\mathbf{K}$ of the acoustic waves.

In the limit $\delta_a \ll 1$, this simplifies to a horizontally isotropic form

$$F_{p,2h}(\mathbf{K}, f_s) \quad \simeq \quad \frac{1}{2}\rho_a^2 g^2 f_s \left|R_a\right|^2 \int_0^{2\pi} E(f,\varphi)E(f,\varphi+\pi)\mathrm{d}\varphi. \tag{3.58}$$

This last expression, with $\left|R_a\right|^2 \simeq \left|(\sin^2\theta_a - n^2)\right|/\cos^2\theta_a$, is the one used by Ardhuin & Herbers (2013).

The pressure spectrum can be re-written as a directional spectrum, with the proper change of coordinate this gives,

$$F_{p,2h}(\theta_a, \varphi_2, f_s) \quad = \quad \frac{4\pi^2 f_s^2 \cos\theta_a \sin\theta_a}{\alpha_a^2} F_{p,2h}(\mathbf{K}, f_s). \tag{3.59}$$

When δ_a terms are kept with eq. (3.57), the acoustic power radiated by the ocean surface in direction φ_2 can be integrated in any range of incidence angles $\theta_{a,1}$ to $\theta_{a,2}$,

$$\begin{aligned} P(\theta_{a,1}, \theta_{a,2}, f_s, \varphi_2) \quad &= \quad \frac{2\pi^2 \rho_a g^2}{\alpha_a^3} f_s^3 \int_{\theta_{a,1}}^{\theta_{a,2}} \sin\theta_a \cos\theta_a \\ &\times \quad \int_0^{2\pi} \frac{\sigma^2(\sigma+\sigma')\left|R_a\right|^2 E(f,\varphi)E(f,\varphi')}{\sigma'^2\left[\sigma' - \sigma\cos(\varphi-\varphi')\right]}\mathrm{d}\varphi\mathrm{d}\theta_a, \end{aligned} \tag{3.60}$$

Taking the isotropic form (3.58) the radiated acoustic power becomes isotropic and the sum over all directions is 2π times eq. (3.60), giving

$$2\pi P(\theta_{a,1}, \theta_{a,2}, f_s, \varphi_2) = \frac{4\pi^3 \rho_a g^2}{\alpha_a^3} f_s^3 H(f_s/2) \int_{\theta_{a,1}}^{\theta_{a,2}} \sin\theta_a \cos\theta_a \left|R_a\right|^2 \mathrm{d}\theta_a, \tag{3.61}$$

with units of W/m^2/Hz, where the so-called 'Hasselmann integral' can be defined from the 'overlap integral' (Farrell & Munk, 2008) and the wave spectrum in frequency,

$$H(f) = \left[E(f)\right]^2 I(f) = \int_0^{2\pi} E(f,\varphi)E(f,\varphi+\pi)\mathrm{d}\varphi. \tag{3.62}$$

The total integrated radiated power, with units of W/m^2, is obtained by integrating eq. (3.61) across acoustic frequencies f_s. In Fig. 3.7, the mean acoustic intensity over the year 2018 is represented for six ranges of vertical incidence angles. The distribution pattern of sources for the vertical angles $[0°, 5°]$ shows the effect of bathymetry, unlike the near-horizontal angles with similar patterns depending almost solely on the Hasselman integral. For near-vertical angles - $[5°, 10°]$ and $[10°, 15°]$ - the distribution pattern is not continuous, there are resonant points all over the globe. The acoustic intensity is higher for near-horizontal angles, as predicted in Fig. 3.5.

3.2.3 Practical implications and discussion

3.2.3.1 Near-vertical propagation and Rayleigh wave overestimation

We note that for vertical propagation ($\theta_a = 0$) the effect of the finite depth changes the amplitude by a factor that ranges from 0.125 to 8.5 with sharp maxima corresponding to the organ pipe resonance at $h = (0.25 + n/2)\alpha_w/f_s$, as illustrated in Fig. 3.6, which is similar to fig. 11 in Ardhuin & Herbers (2013).

The behaviour at other angles is very interesting as θ_a goes through the different regimes of associated seismic waves, from P-waves for $\sin\theta_a < \alpha_a/\alpha_s$ – i.e. $\theta_a < 3.41°$ for our choice of parameters – to Rayleigh waves, which usually contain most of the microseism signal, with $\arcsin\alpha_a/\beta < \theta_a < \arcsin\alpha_a/\alpha_w$ corresponding to a range of 5.9 to 12.7° which is shaded in Fig. 3.8.

The two maxima that appear in the Rayleigh domain in Fig. 3.8.A are the two modes that can exist at 5000 m depth, whereas only one mode can exist at 1900 m depth. As discussed by Ardhuin & Herbers (2013) the depth and frequency at which the amplification is maximum is shifted compared to Fig. 3.6. This is because the acoustic water component
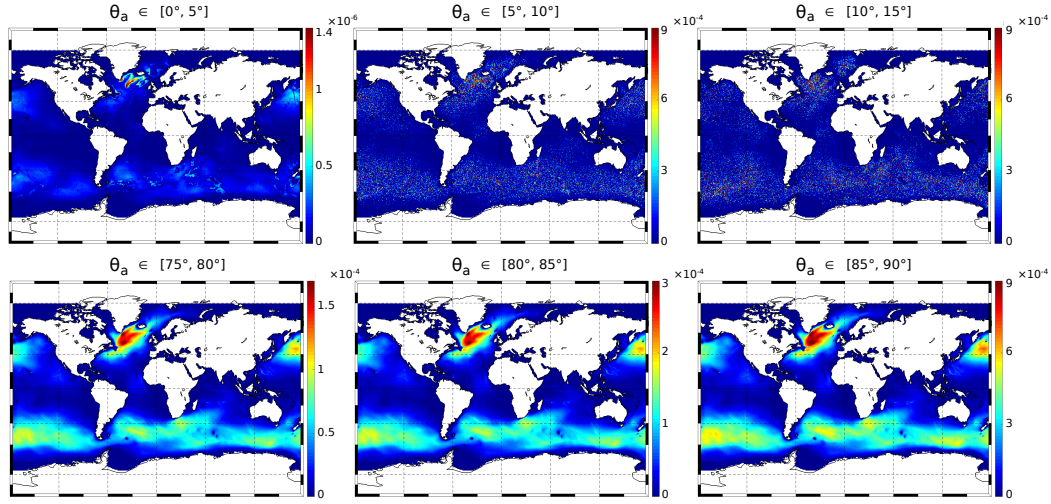
Figure 3.7 – Acoustic intensity in W/m^2 - computed by integrating eq. 3.61 over f_s - for 6 ranges of incidence angles: A) $[\theta_{a,1}, \theta_{a,2}] = [0°, 5°]$, B) $[\theta_{a,1}, \theta_{a,2}] = [5°, 10°]$, C) $[\theta_{a,1}, \theta_{a,2}] = [10°, 15°]$, D) $[\theta_{a,1}, \theta_{a,2}] = [75°, 80°]$, E) $[\theta_{a,1}, \theta_{a,2}] = [80°, 85°]$, F) $[\theta_{a,1}, \theta_{a,2}] = [85°, 90°]$. Mean of a 3-hourly model over 2018. These were computed from numerical ocean wave model output already described by Rascle & Ardhuin (2013) and available at (ftp://ftp.ifremer.fr/ifremer/ww3/), using the WAVEWATCH III® code (The WAVE-WATCH III® Development Group, 2016)

.
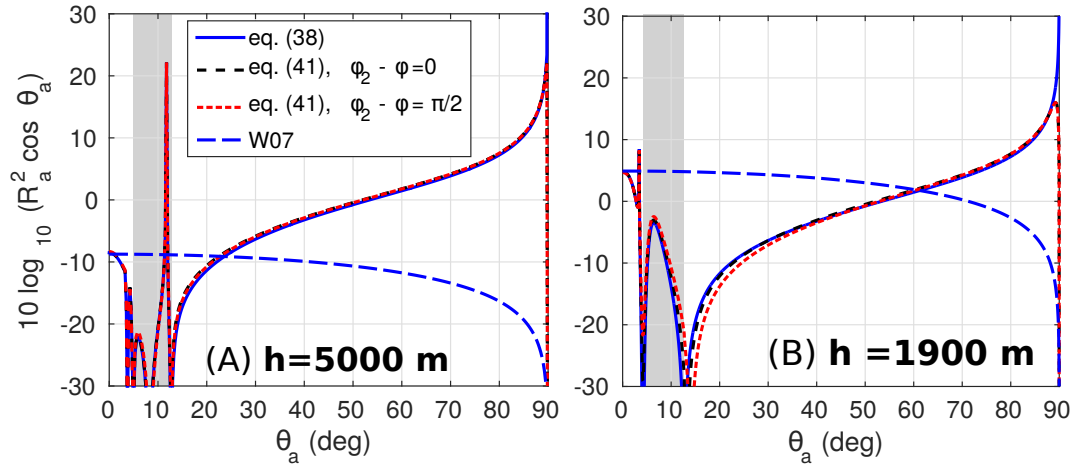
Figure 3.8 – Radiation patterns for an ocean wave period of 10 s, given by the different theories with an ocean bottom at (A) $h = 5000$ m, (B) $h = 1900$ m. Note that when the radiated power is considered, these patterns must be multiplied by $\sin \theta_a$ before integration over θ_a, as given by eq. 3.61. The shaded region corresponds to the domain of seismic Rayleigh waves with $\arcsin(\alpha_a/\beta) < \theta_a < \arcsin(\alpha_a/\alpha_w)$.

of these Rayleigh modes do not propagate vertically but obliquely at an angle θ_w, as shown in Fig. 3.2.B, giving a resonance at $h = (0.25 + n/2)\alpha_w/(f_s \cos\theta_w)$.

Our model certainly overestimates the amplitude of these Rayleigh waves and associated microbaroms because we looked for solutions that are homogeneous in space and time. In the solution given above, the leak of energy to the atmosphere is the only loss of energy of the Rayleigh waves and it compensates the source of energy from the local waves. In reality, two important effects limit the microbarom amplitude to a much lower level. First, the ocean storm area of microbarom generation may not be large enough to reach the stationary solution, and second there is a much larger (6 to 1000 times or more) sink of seismic energy, due to the presence of fluid in the crust, varying with the age of the crust (Stutzmann et al., 2012). The dissipation rate of the energy E is generally parameterized as proportional to $dE/dt = -\Omega E/Q_R$ where Q_R is of the order of 200 to 1000. Including this effect in the present paper amounts to replacing Ω by $\Omega(1 - \mathrm{i}/(2Q_R))$ which is done in Fig. 3.9. In other words, the Rayleigh wave energy is overestimated when dissipation in the crust is neglected because in that case, the leakage of Rayleigh wave energy to the atmosphere is the loss of seismic energy. Hence, our calculation has a seismic attenuation with a very large quality factor $Q_{\max} = \Omega E/S$, where S is the source of seismic energy that equals the radiated power given by eq. (3.61): $P(\arcsin(\alpha_a/\beta), \arcsin(\alpha_a/\alpha_w), f_s)$. Taking twice the kinetic energy in the water column as a lower bound for the total energy we find that, for $h = 5000$ m and $f_s = 0.2$ Hz, $Q_{\max} > 10^6$ (Supporting information, section S6.3), meaning that the present solution overestimates the real microbarom amplitude by a factor that exceeds $Q_{\max}/Q_R > 1000$.
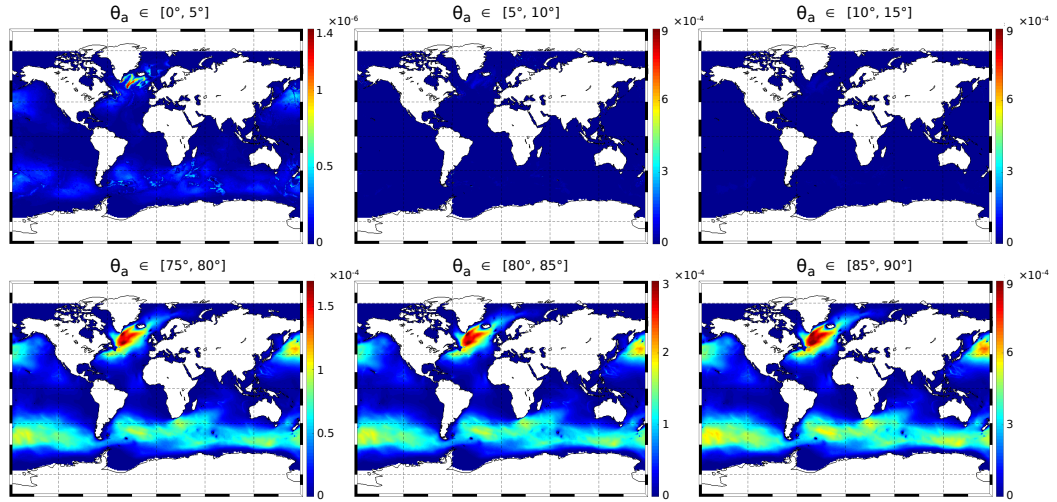
Figure 3.9 – Same as Fig. 3.7 replacing Ω by $\Omega(1 - \mathrm{i}/(2Q_R))$ with $Q_R = 201$ in order not to overestimate Rayleigh wave energy.

Alternatively, instead of looking for the homogeneous solution to the atmosphere-ocean-crust problem, we can use solutions for the ocean-crust problem with an energy that grows over the source region (K. Hasselmann, 1963; Ardhuin & Herbers, 2013), and compute the microbaroms radiated by microseisms (free Rayleigh waves). These microbaroms are radiated both in the source region of microseism but also all along the propagation path of the Rayleigh waves, even on land. For example, a huge microseism with amplitude $a = 10$ micrometers vertical displacement of the sea or land surface corresponds to an energy flux $\rho_a\alpha_a\Omega^2a^2/2$ of only 3×10^{-8} W/m^2 for $f_s = 0.2$ Hz. This is 2000 times smaller than the peak power measured by Bowman & Lees (2018). It is thus unlikely that these measurements are dominated by near-vertical propagating sound waves. Indeed, the near-horizontal energy level is usually much stronger.

3.2.3.2 Radiation patterns as a function of azimuth

The variation of the radiated acoustic power with azimuth φ_2 has not been described before as most studies focused on near-vertical radiation ($K = 0$). In eq. (3.60) there are two
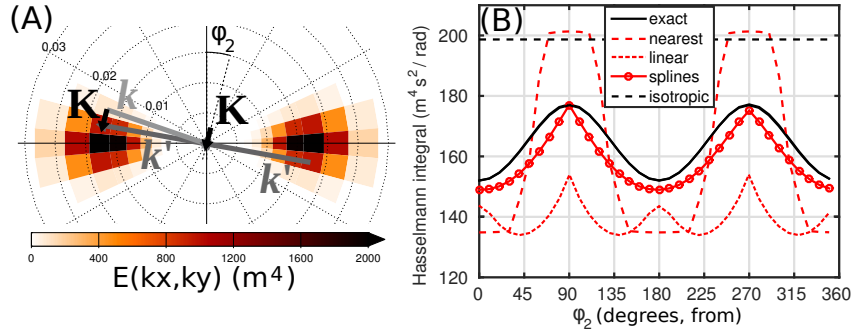
Figure 3.10 – (A) Example spectrum discretized with 36 directions and frequency exponentially spaced with an 1.1 increment from one frequency to the next, typically used in numerical wave models. The spectral density of the ocean waves is shown in colors, in directions from where the waves come. (B) Resulting integrals for the acoustic frequency $f_s = 0.13$ Hz, and horizontal propagation ($\theta_a = 90°$, $K = 0.0025$ rad/m). Three methods were used to compute the integral: the analytic spectral expression or interpolation of the discrete spectrum using nearest neighbor or linear interpolation.

reasons why the radiated power varies with φ_2 .

As expressed by the general form given in eq. (3.60), the radiated power varies with azimuth $\varphi2$ due to the general form of R_a, as shown in Fig. 3.4 and 3.6 but that variation is limited to a few percent. More important is the fact that the Hasselmann integral $H(f)$ is modified by the interaction of $E(f, \varphi)$ with $E(f', \varphi')$ instead of $E(f, \varphi + \pi)$, and should be replaced by,

$$H(f, \varphi_2) = \int_0^{2\pi} \frac{\sigma^2(\sigma + \sigma')E(f, \varphi)E(f, \varphi')}{\sigma'^2 \left[\sigma' - \sigma \cos(\varphi - \varphi')\right]} d\varphi. \tag{3.63}$$

.

Following the classification in (Ardhuin et al., 2011), the oceanic conditions in which the Hasselmann integral takes the largest values correspond to 'class III' events, with two narrow swells propagating in opposite directions. These are also conditions in which $E(f', \varphi')$ may be most different from $E(f, \varphi + \pi)$.

3.2.3.2.1 Case of analytical ocean wave spectra
To illustrate this effect, we take an example of a family of wave spectra adapted from the case discussed in (Obrebski et al., 2012). This family of spectra is defined by the analytic expression,

$$E(f, \varphi) = E_0 \left[e^{-\frac{(f-f_1)^2}{2f_2^2} - \frac{(\varphi - \varphi_1)^2}{2\varphi_3^2}} + e^{-\frac{(f-f_3)^2}{2f_4^2} - \frac{(\varphi - \varphi_4)^2}{2\varphi_5^2}} \right], \tag{3.64}$$

where the f_1, f_2, f_3, f_4 parameters define the peak frequency and width for the two swell trains, and φ_1, φ_3, φ_4, φ_5 define the mean direction and width. The present theory is not restricted to this family of spectra and generally applies to any wave spectrum. Such an analytical form is particularly useful for testing the influence of the discretization when the spectrum is given by a numerical model.

Fig. 3.10.A shows this spectrum transformed to wavenumber space $E(k_x, k_y) = g^2 E(f, \varphi)/4\pi\sigma^3$, with the mean frequency and direction set to $f_1 = 0.066$ Hz, $f_3 = 0.066$ Hz, $\varphi_1 = 90°$, $\varphi_3 = 270°$, the widths $f_2 = 0.007$ Hz, $f_4 = 0.007$ Hz, $\varphi_4 = 8°$, $\varphi_5 = 8°$, and the normalization factor $E_0 = 20$m^2/Hz, giving a significant wave height of 2 m.

The azimuthal variation of the generalized Hasselmann integral, as given by eq. (3.63) is illustrated in Fig. 3.10.B.

The exact calculation uses the analytic expression of the spectrum, and exhibits variations of 7% of the radiated acoustic power as a function of φ_2, with a maximum in the direction of the waves because the spectrum, in k-space is more narrow in the k_y than in the k_x direction and when K is aligned with the y-axis, as shown, the wavenumber vector $\mathbf{k}'$ falls away from the peak faster than when K is aligned with the x-axis. For the present
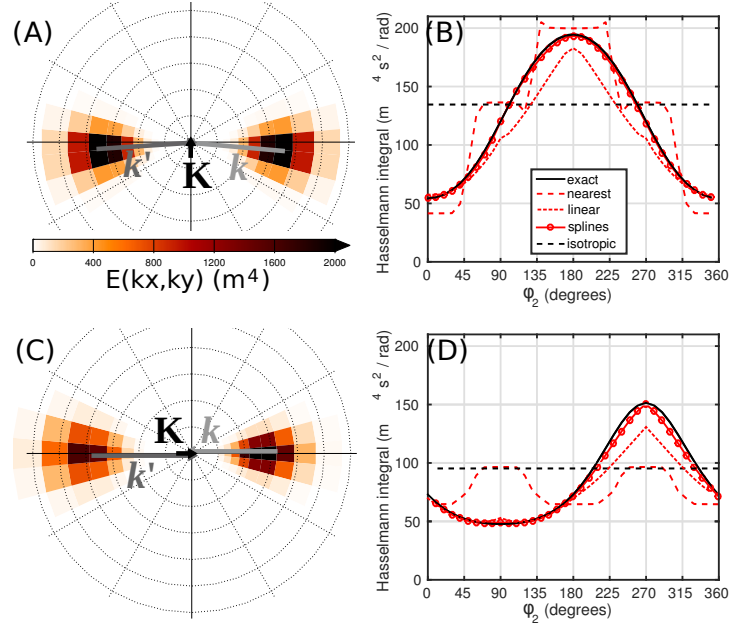
Figure 3.11 – Same as Fig. 3.10 with different ocean wave spectra (A) that have mean directions shifted by 5 degrees to $\varphi_1 = 95°$ and $\varphi_3 = 265°$ producing the Hasselmann integral in (B). The wave spectrum in produces the Hasselmann integral in (D), with a peak frequencies shifted by 0.006 Hz to $f_1 = 0.072$ Hz and $f_2 = 0.060$ Hz. For both cases, the configuration of $\mathbf{k}$ and $\mathbf{k}'$ that gives the largest contribution to the Hasselman integral in indicated in (A) and (C) with arrows.

example the azimuthal variation goes away when the directional spread is increased from 8 to 12° and it has a maximum at 0 and 180° for wider directional spectra.

The practical estimation of the integral is very sensitive to the discretization used, which is not an issue when K is much smaller than the discretization of the spectrum and the isotropic form can be used. Numerical wave models that typically use 10% increments from one frequency to the next and 24 or 36 directions do not resolve very well the narrow swell peaks such as those in Fig. 3.10.A. As a result, a linear interpolation underestimates the integral because the peak appears narrower. On average this is corrected by using the nearest point, but that approach can exaggerate the anisotropy of the acoustic source.

Besides causing anisotropic sources when two swell peaks are exactly opposed, the generalized integral may broaden the region where sources are significant, as shown in Fig. 3.11, because it allows a wider range of directions and frequencies to interact compared to $\mathbf{k} = \mathbf{k}'$ in the simplified form.

3.2.3.2.2 General case using numerical wave model output

In order to test this idea, we have computed the Hasselmann integral from wave-model output which are 'real' spectrum (non idealised spectrum) with the usual form and its generalization in the case of the event discussed by Bowman & Lees (2018). Fig. 3.12 shows modeled maps of wave source magnitude, in color, using the isotropic or azimuth-dependent form of the Hasselmann integral over a 10 degree by 10 degree region located to the south-east of New Zealand, valid for May 2016, at 06:00 UTC. The wave model used here is very similar to the one used in Ardhuin et al. (2015), with a number of discrete directions increased from 24 to 36. This strong microbarom source is associated to a strong local wind, up to 18 m/s, blowing against swell coming from a remote storm, typical of a class-III event described by Ardhuin et al. (2011).

The first striking result is that the colors are very similar, with a correlation of 0.9998, meaning that the simplified isotropic form is a good approximation of the total radiated power, at least for this example. We also note that the highest sources are most isotropic, such as at location D in Fig. 3.12.B. Where sources are more strongly radiated in one direction, such as at locations C and E, this is due to a gradual shift in the direction of both
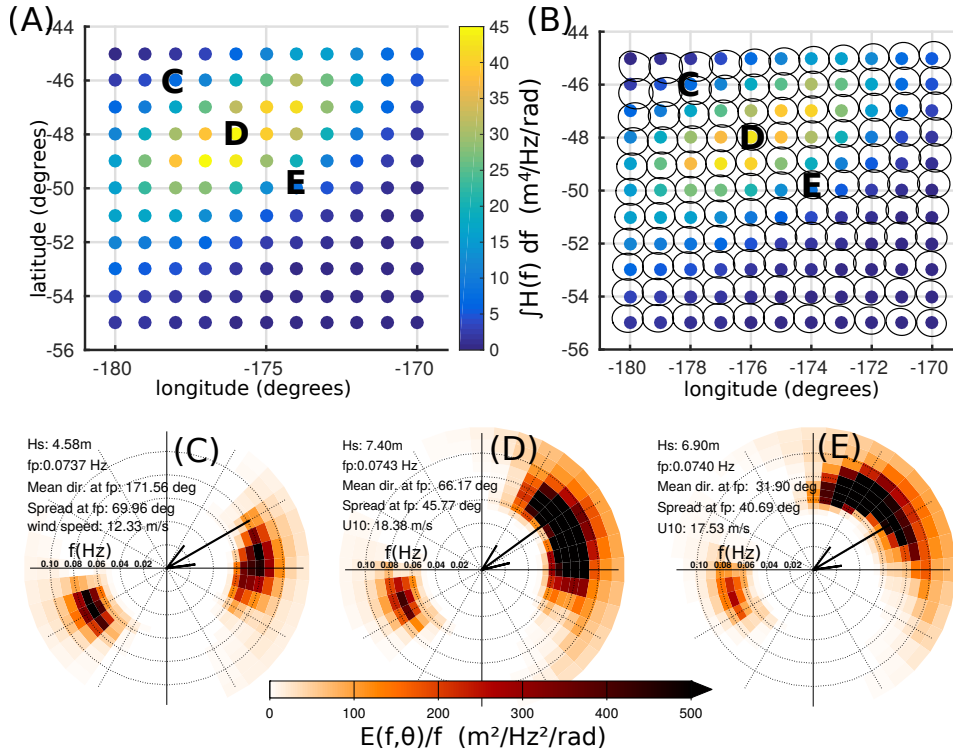
Figure 3.12 – Maps of the Hasselmann Integral for (A) the isotropic and (B) non-isotropic expressions. In (B) the black curve around each location represents the Hasselmann integral estimated as a function of the acoustic propagation azimuth, and plotted in direction from where the acoustic waves are coming and normalized so that the average radius is half the distance between neighboring locations. (C), (D) and (E) are showing modeled directional spectra at the C , D, and E locations mentioned in (A) and (B). The large arrows indicate the wind direction, from the north-east, associated to a broad windsea spectrum which opposes a more narrow swell spectrum from the south-west.

interacting wave trains, the swell from the south-west has a local direction that is close to $240°$ at C, and $255°$ at E, and the time evolution of the local wind means that the wind sea is rather from the East at C and the North-East at E. In this particular example this gives a dominant radiation from the south-east at C and the north at E.

When averaged over the entire area, the difference between the radiated power in any given direction and the isotropic solution is less than 15%, suggesting that the isotropic approximation may be accurate enough for most applications.

3.2.4   Conclusions

In this paper we have reviewed and unified the microbarom source theories developed by Brekhovskikh et al. (1973) and Waxler et al. (2007). A prominent feature of Brekhovskikh et al. (1973), that was not taken into account by Waxler et al. (2007), is the radiation pattern as a function of the elevation angle θ_a. In Waxler et al. (2007), the radiation pattern is monopolar due to an assumed lack of coherence of the sources at scales comparable to the acoustic wavelength. In Brekhovskikh et al. (1973) the acoustic power at near-horizontal incidence that up to 1000 times larger because the main coupling of water and air via the vertical velocity of the air-sea interface gives a much stronger amplification for grazing angles. Including finite depth ocean effects in Brekhovskikh et al. (1973) model is only relevant for near-vertical propagation, and has almost no effect on the predicted dominant near-horizontal propagation of infrasound. For shallow propagation angles that generally correspond to ground-based measurements (i.e. $\theta_a > 40°$, relative to vertical) Brekhovskikh et al. (1973)'s formulation is compared to the more complete depth-dependent model presented here. We find that in regions of water depths under 1000 m, which cover 10% of the total ocean surface, - Brekhovskikh et al. (1973)'s formulation overestimates the source

amplitude and underestimates it for deeper waters. On average there is a 7% understimation and Brekhovskikh et al. (1973) gives overall acceptable results, with a negligible effect of the water depth for near-horizontal propagation angles.

For near-vertical propagation, the generation of microbaroms involve both a source mechanism similar to the one of microseism dominated by the non-linear interaction of near-opposing waves, and Rayleigh waves propagating away from microseism sources. However, the associated acoustic power is at least 2 orders of magnitude lower than the near-horizontal radiated power. These vertical angles can be of interest for altitude measurements such as balloon measurements (Bowman & Lees, 2018); in such situation, the bathymetry can still impact the received signal. The horizontal anisotropy of the source has also been investigated, leading to the conclusion that, for computational applications, the isotropic approximation may be accurate enough and could then be used. Hence, the discretization of the wave spectrum might not be an issue.

Beyond theoretical issues, efforts should be pursued to validate the proposed model by considering available observations of infrasound ambient noise as recorded by the global infrasound network of the International Monitoring System (IMS) (Ceranna et al., 2019). For practical applications, further developments of a numerical model are needed to propagate microbarom signals over large distances through a realistic atmosphere. The implementation of this source model, based on a state-of-the-art numerical wave model (Ardhuin, 2019) should help building a global and time-dependent reference database. Exploiting this database of oceanic noise sources will be useful for developing middle-atmospheric remote sensing methods. The evaluation of infrasound ambient noise model is essential in the context of the future verification of the Comprehensive nuclear Test Ban Treaty (CTBT), as accurate atmospheric models are basic prerequisite to assess the IMS network performance in higher resolution, reduce source location errors, and improve source characterization methods.

Acknowledgments

3.2.A   Green function phase, spatial correlations and treatment by Waxler and Gilbert, 2006

In order to clarify the difference between our derivation and the derivation by (Waxler & Gilbert, 2006), we go back to their expression of the atmospheric pressure spectrum as recorded at the horizontal position $\mathbf{x}_H$ and vertical altitude z, from a collection of sources over positions y and y' in domain S. The variance of pressure is given by their eq. (49) with $\mathbf{x}'_H = \mathbf{x}_H$, $z' = z$ and $\tau = 0$

$$\left\langle P^2 \right\rangle = \rho^2 \int_{-\infty}^{\infty} \int_{-\infty}^{\infty} \int_S \int_S \left\langle G(x,y,-\tau_1)G^*(x,y',\tau-\tau_2) \right\rangle \left\langle \frac{\partial v(y,\tau_1)}{\partial \tau_1} \frac{\partial v(y',\tau_2)}{\partial \tau_2} \right\rangle_S d^2y \, d^2y' \, d\tau_1 d\tau_2 \tag{3.2.A.1}$$

Following their derivation, we use the Fourier in time $\widehat{G}$ of the Green's function, representing the propagation of acoustic waves in a layered medium as a sum of discrete modes. As given by Waxler & Gilbert (2006, eq. 65) the Fourier transform of the Green function for mode j and frequency ν is given by,

$$\widehat{G}(\mathbf{x}_H, z, \mathbf{y}_H, \nu) = f(r,z) \sum_j \frac{e^{ik_j|\mathbf{x}_H - \mathbf{y}_H|}}{\sqrt{k_j}} \psi_j(z)\psi_j(z'), \tag{3.2.A.2}$$

where $r = |\mathbf{x}_H - \mathbf{y}_H|$ is the horizontal distance, the k_j are the horizontal wavenumbers pointing in the direction of $\widehat{\mathbf{k}} = (\mathbf{x}_H - \mathbf{y}_H)/r$, and ψ_j are normal modes satisfying the bi-orthogonality condition and their phases are assumed to be uniformly distributed and statistically independent.

Considering that for each y in the source $|\mathbf{y}'_H - \mathbf{y}_0|/|\mathbf{x}_H - \mathbf{y}_0| << 1$ with y_0 the center of the source (i.e. the receptor is far from the source), and defining the vector $\mathbf{k}_j = k_j \widehat{\mathbf{k}}$, the product of the Green's function for $\mathbf{y}_H$ and its complex conjugate for $\mathbf{y}'_H$ writes

$$\widehat{G}(\mathbf{x}_H, z, \mathbf{y}_H, \nu)\widehat{G}(\mathbf{x}_H, z, \mathbf{y}'_H, \nu)^\star = |f(r_0, z)|^2 \sum_j e^{i\mathbf{k}_j \cdot (\mathbf{y}' - \mathbf{y})} \frac{|\psi_j(z)|^2 |\psi_j(z')|^2}{k_j} \qquad (3.2.A.3)$$

The phase of this product then contains the phase shift of the propagation from $\mathbf{y}$ to $\mathbf{y}'$ with a wavenumber k_j. When correlated with the source structure, that contains a phase $\exp[i(\mathbf{k} + \mathbf{q}) \cdot (\mathbf{y}' - \mathbf{y})]$ it gives,

$$
\begin{aligned}
\langle P^2 \rangle &= \rho^2 \int_S \int_S \left(|f(r_0, z)|^2 \sum_j \frac{e^{i\mathbf{k}_j(\mathbf{y}'-\mathbf{y})}}{|k_j|} |\psi_j(z)|^2 |\psi_j(z')|^2 \right) \\
&\quad \times \left(2 \int \int \nu^2 F(\mathbf{k})F(\mathbf{q})|C^+|^2 |\Omega|^2 e^{i(\mathbf{k}+\mathbf{q})(y-y')} d^2\mathbf{k}d^2\mathbf{q} \right) d^2yd^2y' \\
&= \rho^2 \int_S \int_S |f(r_0, z)|^2 \sum_j \int \int \left[\frac{|\psi_j(z)|^2 |\psi_j(z')|^2}{|k_j|} e^{i(\mathbf{k}_j - (\mathbf{k}+\mathbf{q}))(\mathbf{y}'-\mathbf{y})} \right. \\
&\quad \left. \times 2\nu^2 F(\mathbf{k})F(\mathbf{q})|C^+|^2 |\Omega|^2 \right] d^2\mathbf{k}d^2\mathbf{q}d^2yd^2y' \qquad (3.2.A.4)
\end{aligned}
$$

This can be simplified as the integral over $\mathbf{y}'$ in the the source area S gives a term proportional to

$$\int_S \int_S e^{i\left[(\mathbf{k}_j - (\mathbf{k}+\mathbf{q}))\cdot(\mathbf{y}_H - \mathbf{y}'_H)\right]} d^2yd^2y' = (2\pi)^2 \delta(\mathbf{k}_j - (\mathbf{k}+\mathbf{q}))S \qquad (3.2.A.5)$$

instead of the $(2\pi)^2 \delta(\mathbf{k} + \mathbf{q})$ term found by (Waxler & Gilbert, 2006).

The pressure variance becomes

$$\langle P^2 \rangle = \rho^2 (2\pi)^2 \, S |f(r_0, z)|^2 \sum_j \int_{\mathbf{k}+\mathbf{q}=\mathbf{k}_j} \frac{|\psi_j(z)|^2 |\psi_j(z')|^2}{|k_j|} 2 \, \nu^2 F(\mathbf{k})F(\mathbf{q})|C^+|^2 |\Omega|^2 d^2\mathbf{k}d^2\mathbf{q}.$$
$$(3.2.A.6)$$

This is the same as eq. (51) in (Waxler & Gilbert, 2006), except for the fact that we did not replace $\mathbf{q}$ with $-\mathbf{k}$, we thus need to compute the the air pressure over the source for all $\mathbf{K} = \mathbf{k}_j$. Although $|\mathbf{K}| \ll |\mathbf{k}|$, the approximation $|\mathbf{K}| = \mathbf{0}$, which is only strictly valid for an azimuth angle $\theta_a = 0$, leads to very large differences in the source amplitude, up to 30 dB as shown in Fig. 3.4.

3.3   Conclusions of the chapter

The main conclusions of this chapter are the following:

- A new source model has been developed including all physical effects (bathymetry, gravity, non-monopolar radiation). This model is coherent with the existing ones within their working range (infinite depth for BK73, and monopolar radiation for W07).

- The bathymetry has been shown to be of importance only for acoustic waves propagating with near-vertical angles, whereas ground stations mainly receive infrasound within 40° from the horizontal.

- For ground stations measurements, due to the non-monopolar radiation of microbaroms, accounting for bathymetry only changes the total emitted microbaroms flux by 7%, therefore the DC20 source model is practically the same as the source model of Brekhovskikh et al. (1973).

GLOBAL MODELLING RESULTS AND SOURCE MODEL VALIDATION

Contents

4.1 Introduction and scope of the study

This chapter presents an application of the global modelling of microbaroms arrivals presented in Chapter 2, with the source model developed in Chapter 3 (DC20). The main objective is to validate the source model through systematic comparisons between the modelled microbaroms and observations using the Coefficient of Predicted Observations (CPO) defined in Chapter 2, eq. (2.6).

The observation database for this global study consists of the reprocessed IMS database (Ceranna et al., 2019) for detections in the frequency band [0.1-0.6] Hz and in the 2012-2018 period. While 51 stations were certified at the end of 2018, only 45 were certified in 2012. For the global results presented in the next Section, the stations considered are the 45 stations that have been certified for the time period of the study[1].

Global modelling and comparison with observations are also run with the widely used source model developed by Waxler et al. (2007) (W07). The performance of both configurations to fit observations are then compared in order to determine the relevance of the new source model.

As explained in Chapter 2, the impact of the wind and the impact of including coastal reflection in wave modelling are also investigated. Therefore the global modelling is run for 8 ($= 2^3$) configurations defined by 3 parameters and their possible values:

- Coastal reflection parameter i_1:

    - **NOREF:** wave modelling does not account for any coastal reflection;

---

[1]The modelling, however, was also run for the other stations, which are included in the more detailed results presented in Section 4.3.

> – **REF102040:** wave modelling accounts for complete reflection.

- Wind parameter i_2:

  > – **NoWind:** $V_{\text{eff-ratio}} = 1$, therefore no propagation direction is favoured;
  > – **WindSta:** $V_{\text{eff-ratio}}$ is considered at the station.

- Source model i_3:

  > – **DC20:** source model developed by De Carlo et al. (2020) (see Chapter 3);
  > – **W07:** source model developed by Waxler et al. (2007).

For each configuration, the modelling is run for 45 stations over 7 years from 2012 to 2018 included (and for 6 stations over smaller time periods).

Applying the CPO calculation allows to quantify the capability of the model (with a given configuration) to predict the observations. As the CPO is calculated over one month, $\text{CPO}(i_1, i_2, i_3, i_4, i_5, i_6, i_7)$, values depend on seven parameters i_1 to i_7, of which three - i_1, i_2 and i_3 - are the modelling parameters corresponding to the eight configurations. The other parameters i_4, i_5, i_6 and i_7 represent respectively the frequency band, the month, the year and the IMS stations at which the CPO is calculated. Accounting for all those parameters, there are 151,200 CPO values in total. Other characteristic numbers of this global study are summarised in Table 4.1.

To quantify the impact of each modelling parameter (e.g. coastal reflection parameter i_1), the normalised element-wise difference of CPO values is realised between the 4 configurations with one value of the parameter (e.g. $i_1 = 1$, NOREF) and the 4 other configurations (e.g. $i_1 = 2$, REF102040):

$$\Delta\text{CPO}_{k_1}(k_2, k_3, i_4, i_5, i_6, i_7) = \tag{4.1.1}$$
$$\frac{\text{CPO}(k_1 = 2, k_2, k_3, i_4, i_5, i_6, i_7) - \text{CPO}(k_1 = 1, k_2, k_3, i_4, i_5, i_6, i_7)}{\max(\text{CPO}(k_1 = 1, k_2, k_3, i_4, i_5, i_6, i_7), \text{CPO}(k_1 = 2, k_2, k_3, i_4, i_5, i_6, i_7))}$$

where (k_1, k_2, k_3) is a permutation of $\{i_1, i_2, i_3\}$, and ΔCPO_{k_1} depends on $(k_2, k_3, i_4, i_5, i_6, i_7) \in \{1, 2\}^2 \times [\![1; 5]\!] \times [\![1; 12]\!] \times [\![1; 7]\!] \times [\![1; 45]\!]$. The distribution of ΔCPO_{k_1} over $(k_2, k_3, i_4, i_5, i_6, i_7)$ allows to determine which value of the modelling parameter provides the best fit with the observations.

The following section 4.2 consists of a paper submitted to *Geophysical Research Letters* (GRL) that presents the overall results of this study. Complementary results are presented in Section 4.3.

Table 4.1 – Characteristics of the global modelling.

Study's features	Values
Model configurations	8
Stations	45 (for the whole duration; 51 in total)
Number of years	7
Total time steps	20,456
Frequency bands for model runs	22 (for the run, before summation)
Frequency bands for the results	5 (width 0.1 Hz)
Directions	360 (width 1°)
Runs per configuration	20,251,440 ($45 \times 20,456 \times 22$)
Modelling outputs per configuration	1,656,936,000 ($45 \times 20,456 \times 5 \times 360$)
Observations	25,264,100 (median per station: 411,880)
CPO values per configuration	18,900 ($45 \times 7 \times 12 \times 5$)
CPO values in total	151,200 ($8 \times 18,900$)
CPO differences for one parameter	75,600 ($4 \times 18,900$)

4.2 Global Microbarom Patterns: a First Confirmation of the Theory for Source and Propagation[2]

Abstract

Microbarom signals are generated by wind-waves at the ocean surface and propagate all around the globe through the stratosphere and ionosphere. Microbaroms dominate the coherent infrasound ambient noise measured worldwide, with a peak around 0.2 Hz. This ubiquitous signal can be used to monitor its sources or its propagation medium, allowing to probe the properties of the upper atmosphere. Here we show the first quantitative validation of a new global model of microbaroms based on ocean wave models, a new source models and atmospheric attenuation effects. The modelling results are compared to a reference database of microbaroms detected by the global infrasound International Monitoring System over seven years to evaluate the influence of ocean waves, source and propagation parameters. This study demonstrates that new source model performs better than previous models, and is best when combined with a wind-dependent attenuation, and when the ocean wave model includes coastal reflection.

Plain Language Summary

Microbaroms are atmospheric ambient noise below the human hearing threshold. They are generated by ocean waves and can be detected by infrasound sensors worldwide. A better understanding is important because microbaroms could hide signals of interest in the context of the Comprehensive Nuclear-Test-Ban Treaty, established to unveil clandestine nuclear explosions worldwide. Furthermore, as microbaroms propagate over long-ranges through the middle atmosphere, a better knowledge of the received signals provides new insights of middle atmosphere dynamics features that are unresolved in global circulation models. In this study, we use a historical database of microbarom detections to evaluate state-of-the-art models and propose a methodology to simulate microbaroms worldwide.

4.2.1 Introduction

Infrasound can propagate over large distances due to low absorption rates and efficient ducting in the stratospheric waveguide. In the 0.05 to 4 Hz band, infrasound signals are routinely recorded by the infrasound International Monitoring System (IMS) being deployed to verify compliance with the Comprehensive Nuclear-Test-Ban Treaty (CTBT) (Marty, 2019). As of July 2020, 52 certified stations already provide global coverage of explosive events of both geophysical and anthropogenic origin (Fig. 4.1a). These include, for instance, refinery incidents (e.g. Ceranna et al., 2009), natural hazards such as volcanic eruptions (e.g. R. Matoza et al., 2019) or atmospheric entries of large meteoroids (e.g. Pilger et al., 2019).

Microbarom signals, with frequencies ranging from 0.1 to 0.6 Hz, are dominating the infrasound ambient noise. Originating from ocean surface wave interactions, microbaroms are near-continuously detected worldwide. The detection capability of microbaroms exhibits significant spatiotemporal variation, which is partly controlled by dynamical features of the atmospheric circulation (Landès et al., 2014; Ceranna et al., 2019). Variations in coherent ambient noise result from changes in both the source distribution and the propagation conditions and can be characterised statistically (e.g. Assink et al., 2014). As microbaroms propagate into the middle-atmosphere (from around 12 to 90 km), significant features of the vertical structure of the temperature and wind are reflected in the detected signal on the ground. The lack of variability found in both temperature and wind models (e.g. Charlton-Perez et al., 2013; Lee et al., 2019) has motivated the development of atmospheric remote sensing methods for evaluating numerical weather prediction (NWP) model output (e.g. Le Pichon et al., 2005; Vanderbecken et al., 2020; Amezcua et al., 2020). With the increasing number of IMS stations complemented by dense regional networks, systematic studies using historical infrasound datasets and state-of-the- art reanalysis systems provide useful

---

[2]As per the sharing policy of the editor, this section presents the first submitted version of an article - De Carlo et al. (2021) -, which was accepted after modifications on December 17th 2020.
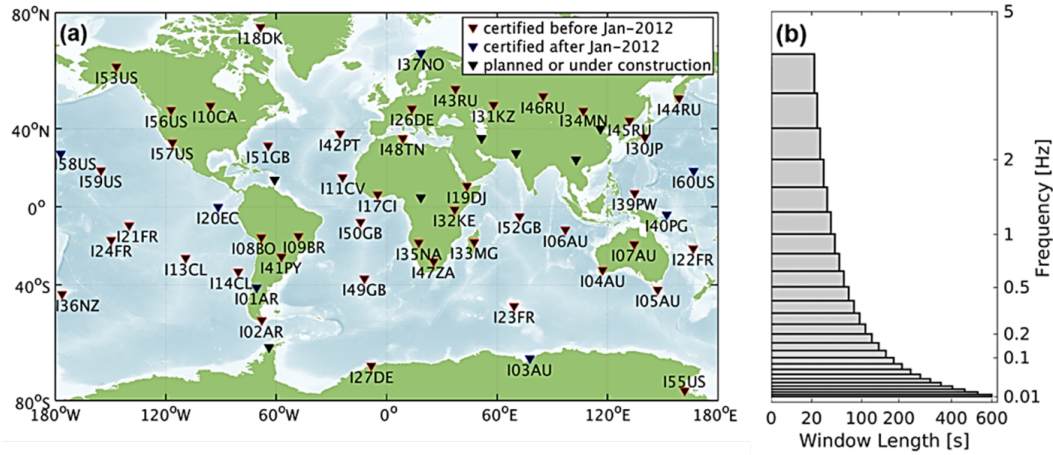
Figure 4.1 – a) Map of the IMS infrasound network showing the certified and planned stations as of July 2020. Seven of the currently operating stations were not certified before 2012 and are therefore not considered in this study. b) Third-octave frequency band configuration of the PMCC processing. Microbarom detections coincide with log-scaled bands between 0.1 and 0.6 Hz. The time step of the processing is 10% of the window lengths (Ceranna et al., 2019).

integrated information on middle atmosphere variability and biases where data coverage is sparse (Blanc et al., 2019). Beyond the atmospheric community, the evaluation of NWP models is essential for the verification of the CTBT as accurate models are needed to assess the IMS network performance in higher resolution and reduce source location errors. Improving the source knowledge of microbaroms is critical for operational infrasound monitoring as coherent noise may interfere with the detection and identification of transient signals being emitted by events of interest. Various microbaroms energy spectrum models have been developed in earlier works. Brekhovskikh et al. (1973) and Ardhuin & Herbers (2013) considered an infinite depth ocean with the radiating pressure depending on the wave elevation angle. Waxler & Gilbert (2006) and Waxler et al. (2007) investigated infrasound radiated by ocean waves in finite depth ocean from monopolar sources. More recently, De Carlo et al. (2020) developed a source model accounting for both directivity and water depth effects allowing to better characterise the source of microbaroms. In this study, a multi-year and global reference database of microbaroms recorded by the IMS network is constructed using logarithmically-scaled frequency bands between 0.01 and 4 Hz. Systematic comparisons between the modelled and observed directional amplitudes of microbaroms provide new insights on coupling mechanisms at the ocean-atmosphere interface and long-range propagation effects. Data and methods are presented in Section 4.2.2. The main results are given in Section 4.2.3. Discussion and conclusions follow in Sections 4.2.4 and 4.2.5.

4.2.2 Data and methods

4.2.2.1 IMS observations

The CTBT Organisation Preparatory Commission certified 45 of the IMS infrasound stations before 2012 (Fig. 4.1a); hence covering the whole studied period (from 2012 to 2018). IMS infrasound array data are routinely processed at the International Data Center (IDC) (Mialle et al., 2019) using the Progressive Multi-Channel Correlation (PMCC) method (Cansi, 1995). The PMCC algorithm automatically processes continuous waveforms in successive, overlapping time windows and adjacent frequency bands to detect coherent plane waves within the background noise. Each detected arrival is characterised by wavefront parameters – e.g., back- azimuth, frequency and root-mean-square amplitude – derived from the time delays between pairs of sensor triplets. Distant sensors within an array are progressively added during the processing to enhance the quality of the detected parameters (Cansi & Le Pichon, 2008). Adjacent detections in individual time-frequency cells exhibiting similar wavefront parameters are clustered into a family. A practical benefit was gained

by implementing PMCC with a variable window length and log-spaced frequency bands, allowing the efficient process of the full frequency range in a single computational run (e.g. Brachet et al., 2010). With this implementation, a first global and multiyear systematic broadband (0.01-5 Hz) analysis of historical IMS records was performed by R. S. Matoza et al. (2013). The PMCC configuration has been refined for reprocessing the IMS infrasound dataset; it relies on 27 third-octave frequency bands between 0.01 Hz and 4 Hz, with window lengths varying from 600 s down to 30 s, respectively (Fig. 4.1b). This configuration allows computationally efficient broadband processing and accurate estimates of frequency-dependent wave parameters useful for source separation (Ceranna et al., 2019). A detection is considered as a microbarom signal if its centre frequency covers the 0.1-0.6 Hz interval and if, for reasons of significance, the family size is larger than 40.

4.2.2.2 Source and propagation modelling

Ocean waves are generally well represented by a sum of many sine waves with random phases. Their local statistical properties are given by the power spectral density of the surface elevation $E(f, \theta)$ which gives the distribution of the surface elevation variance as a function of wave frequency f and azimuth of ocean wave propagation θ. Ocean wave models such as WAVEWATCHIII® (WW3DG, 2016) provide an estimate of $E(f, \theta)$, which is called the "wave spectrum", and its evolution in space and time, based on the surface wind fields. Such models account for wave generation by the wind, propagation (including slow non-linear evolution) and dissipation dominated by wave breaking. For the application to microseisms and microbaroms, the magnitude of wave energy in opposite directions is particularly important, because microbaroms are generated by second order non-linear interactions of almost opposing ocean waves. The source at the acoustic frequency f_s is proportional to $\mathcal{H}(f_s)$, the Hasselmann integral (K. Hasselmann, 1966),

$$\mathcal{H}(f_s) = \int_0^{2\pi} E(f, \theta) \cdot E(f, \theta + \pi)d\theta \qquad (4.2.2)$$

The Hasselmann integral is obtained from the p2l output of the numerical wave model (WW3DG, 2016) at a 3-hour temporal and a $0.5° \times 0.5°$ spatial resolution:

$$p2l(\frac{f_s}{2}) = \frac{1}{2}\rho_w^2 g^2 \mathcal{H}(f_s) \qquad (4.2.3)$$

where ρ_w is the density of water and g is the gravity coefficient. Following the developments of Waxler et al. (2007) and De Carlo et al. (2020), cell sources i radiating in azimuth φ_i can be expressed in terms of pressure spectrum $P_{2,source,i}$, and correspond to a sum over all elevation angles θ_a

$$P_{2,source,i}(\varphi_i, f_s) = \frac{2\rho_a^2 g^2 \phi^2 f_s^3}{\alpha_a^2}\mathcal{H}(f_s) \int_{\theta_a=0}^{\frac{\pi}{2}} |R_a|^2 \cos\theta_a \sin\theta_a a\mathrm{d}\theta_a \qquad (4.2.4)$$

where ρ_a and α_a are the air density and the speed of sound in the air, respectively. R_a is a coefficient accounting for finite depth ocean depending on the source model chosen (De Carlo et al., 2020). In this study, two models are confronted: (i) a monopolar source – i.e., no dependency on the elevation angle for R_a and thus a high bathymetry impact – as proposed by Waxler et al. (2007), hereinafter referred to as W07, and (ii) a non-monopolar source with R_a depending on the elevation angle (De Carlo et al., 2020, hereinafter DC20). A major source of model uncertainty is the reflection of ocean waves off the coast (Ardhuin et al., 2013). For this reason, two parametrisations of coastal reflection are used: (i) one without reflection ("NO REF"), (ii) the other one with reflection coefficients of 10% on the continents, 20% on the islands and 40% on the ice ("REF102040"). As the main objective of this study is to run massive simulations (45 stations over 7 years) using different models and to compare these outputs with PMCC processing results, propagation simulation with low calculation effort is needed. A good trade-off between low calculation effort and propagation accuracy is the attenuation law derived from Parabolic Equation simulations by Le Pichon et al. (2012). This relation provides the pressure attenuation $Att(f_s)$, which accounts for the propagation range, the source frequency f_s, and the stratospheric effective sound speed

ratio $V_{\text{eff-ratio}}(\varphi)$ (ratio between the effective sound speed at 50 km altitude and the sound speed at the ground level in the direction of propagation φ). For the sake of simplicity, the atmosphere is considered horizontally uniform. Two situations are considered: (i) an idealised windless atmosphere with $V_{\text{eff-ratio}}$ constant and equal to one, and (ii) $V_{\text{eff-ratio}}$ taken at the station, introducing directivity in the propagation depending on the vertical structure of the wind field. For situation (ii), $V_{\text{eff-ratio}}(\varphi)$ is derived from operational high-resolution analysis produced by the Integrated Forecast System of the European Centre for Medium-Range Weather Forecasts (ECMWF, HRES IFS cycle 38r2, http://www.ecmwf.int). The attenuation relative to the considered station is computed for each cell of the source model. Then, the source pressure spectrum $P_{2,source,i}(\varphi, f_s)$ is multiplied by the square of the attenuation *Att* and by the cell area $\mathrm{d}S_i$. To compute the directional spectrum $P_{2,sta}(\varphi, f_s)$ at the station, cells i intersecting azimuth bands of $1°$ resolution are summed:

$$P_{2,sta}(\varphi, f_s) = \sum_{\substack{i|\varphi_i = \varphi \\ i|r_i \leqslant 5000\ km}} P_{2,source,i}(\varphi_i, f_s) \cdot Att_i(f_s)^2 \cdot \mathrm{d}S_i \qquad (4.2.5)$$

As the attenuation law is not valid for long propagation ranges, cells further than $5,000$ km from the stations are not considered.

4.2.2.3 Observations and model comparisons

The direction of arrival of the incoming wavefront is calculated at IMS stations within an uncertainty of few degrees (Szuberla & Olson, 2004). As the detections are unevenly distributed in time, azimuths are averaged within consecutive 3 hours windows. Furthermore, considering that PMCC detects the dominant signal whereas the model output is a directional spectrum, the modelled dominant azimuth is taken at the direction maximising the pressure spectrum. The corresponding amplitude variations of the dominant signals, both observed and modelled, are compared after normalisation.

A quantitative comparison between observations and model is needed to evaluate and compare the models. However, calculating the difference between observations and modelling results leads to high deviation values and does not allow discriminating between models. Therefore, all sources and their spatial dimension are accounted for. For each time step and frequency band, the directional distribution of the modelled signals is normalised by the maximum amplitude over all azimuths. Then, a threshold is applied, below which the predicted signals are discarded. The detections are classified into predicted and non-predicted observations, according to their arrival time, azimuth ($1°$ resolution) and frequency. This allows the definition of a proxy to evaluate the models: the coefficient of predicted observations (CPO) is the ratio of predicted observations to all observations. Setting the threshold to 0.4 is an optimal trade-off between the CPO and the false-positive rate (see Section 2.2.3.2 and Fig. 4.12). The modelled pressure spectrum relies on three parameters: (i) coastal reflection effects in wave modelling – "No REF" or "REF102040", (ii) stratospheric wind effects – $V_{\text{eff-ratio}}(\varphi)$ equal to 1 or taken at the station, and (iii) the source model – W07 or DC20. Consequently, 8 parametrisations are run, and for each of them, the CPO is computed for each station, frequency band and month over the 7 years.

4.2.3 Results

4.2.3.1 Global comparison of azimuth and amplitude

Fig. 4.2 summarises the microbaroms detections (a, c) at 45 IMS stations from 2012 to 2018, compared with the modelling results representing the dominant sources (b, d). These simulations incorporate the ocean wave model with coastal reflections, the DC20 microbaroms model, and stratospheric winds at the stations. In the Northern Hemisphere (NH), the majority of the signals originate from north Pacific, Atlantic, and Indian Oceans. In the Southern Hemisphere (SH), signals essentially originate from large swell systems circulating along the Antarctic Circumpolar Current (ACC). The seasonal oscillation of the dominant azimuths correlates with the seasonal reversal of the stratospheric wind (e.g. Landès et al., 2014). This trend is well explained by the modelling, controlling where infrasound detections are predicted. However, short-time fluctuations in the dominant detection parameters are
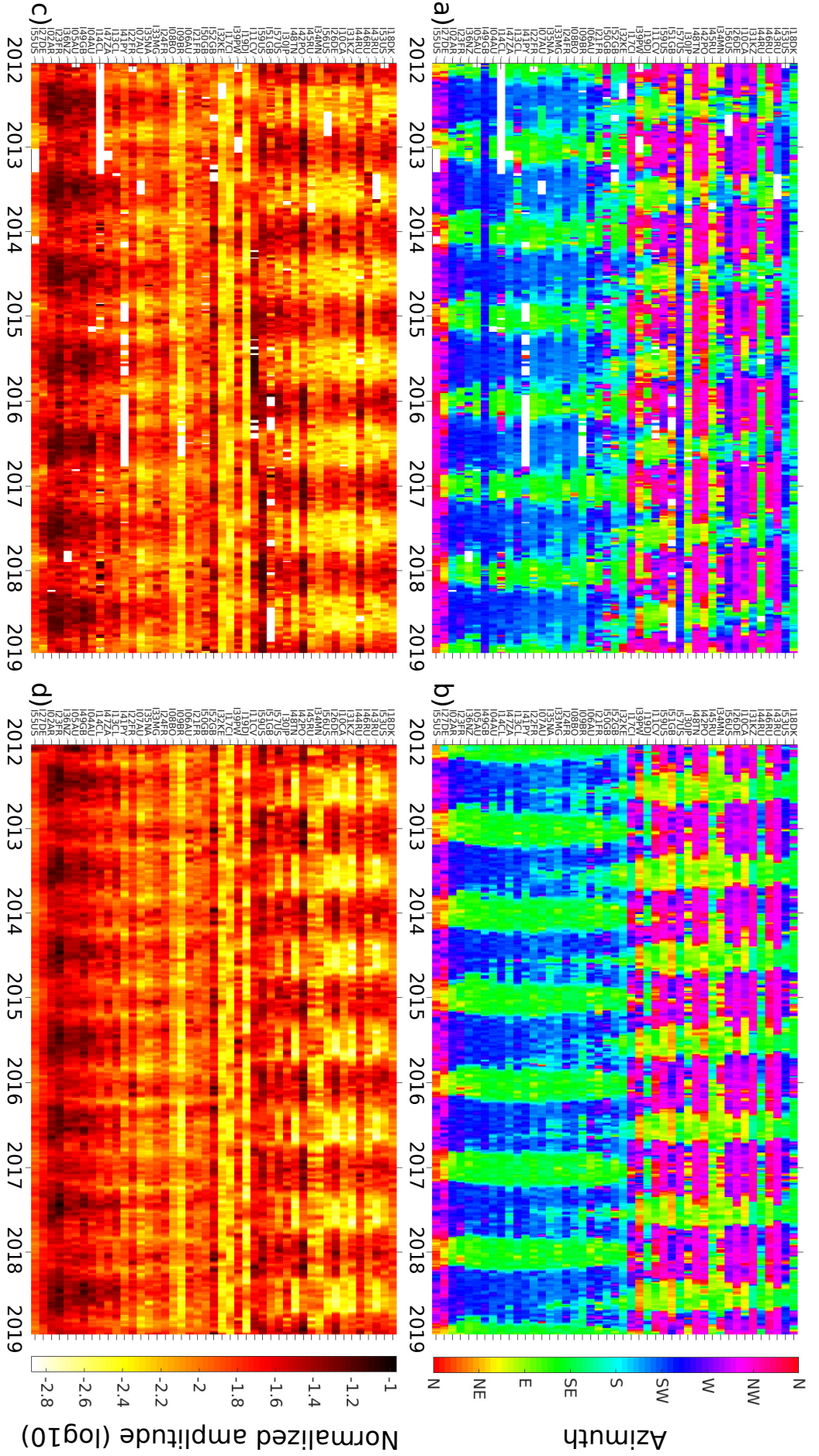
Figure 4.2 – The dataset of microbarom detections (left column) is compared with the output of the model incorporating stratospheric wind at the station and coastal reflections (right column). Each coloured line depicts the back-azimuth (top row) of the observed or modelled detection with the maximum RMS amplitude (bottom row, normalised logarithmic scale) within [T − 7 days, T + 7 days]. The time step is 4 days. White lines depict nil detections or missing infrasound station data within the respective time window

noted (Fig. 4.2), most frequently in the northern summer. These fluctuations, not represented by the model, have been related to dynamical features, such as unresolved gravity wave perturbations of temperature and wind in ECMWF models, when the effective sound speed ratio is close to one (Hupe et al., 2018).

Both detected and modelled normalised root-mean-square (RMS) amplitudes vary along with the dominant wind direction. The largest amplitudes are noted during the winter seasons when the polar vortices are established. Strong stratospheric winds cause high effective sound speed ratios resulting in low attenuation, while the microbaroms sources are intensified by storm systems. The combination of these effects is most evident in the SH at mid-latitudes where the ACC dominates the detections. In the NH, fewer tropical stations and stations close to the Pacific and Atlantic Oceans exhibit relatively high RMS amplitudes.

Striking outliers are I34MN, for which the model predicts an opposed seasonal variation in amplitude, and I49GB with hardly varying back-azimuths because of its location at the western bottom of the steep flank of the volcano island.

4.2.3.2 Comparison of models' performances

Fig. 4.3 represents monthly variations of the normalised distributions of CPO differences, for each of the three parameters (in column) and for both the NH (a-c) and SH (d-f). To calculate the CPO difference, the computed CPO using the parametrisation indicated on the left of the ordinate is subtracted from its counterpart indicated on the right. The dominant term normalises the CPO difference. Hence, the higher the occurrence and extremer the relative difference, the better is the agreement between the observations and the modelling compared to the counterpart parametrisation. The distribution represent-
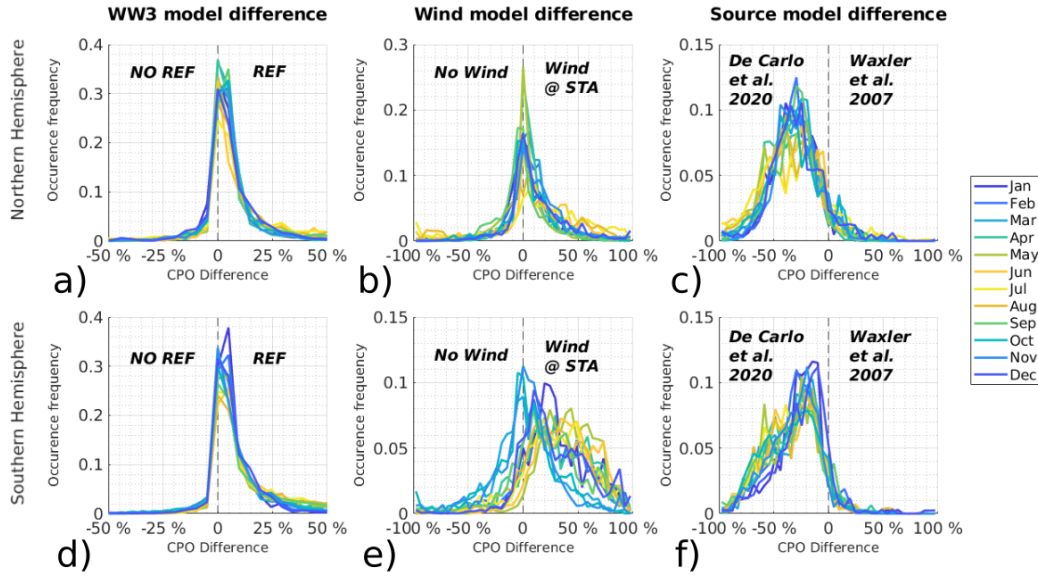
Figure 4.3 – Monthly distribution of the CPO difference for all three parameters, normalised by the number of detections – the 1st (*a), d)*), 2nd (*b), e)*) and 3rd (*c), f)*) columns correspond to the WW3 coastal reflection, stratospheric wind and the source model parameters, respectively. The coloured curves represent the monthly distributions for both the northern hemisphere (top row: *a), b), c)*) and southern hemisphere (bottom row: *d), e), f)*). For each panel, the x-axis denotes the CPO difference between the right-hand (minuend) and the left-hand parameter run (subtrahend), relative to the maximum CPO of the two parameter runs.

ing the coastal reflection (Fig. 4.3a, 4.3d) is peaking around zero. This implies that both parametrisations with and without coastal reflection provide similar results in the majority of events, regardless of the degree of agreement between predictions and detections. However, the asymmetry of the curves shows that incorporating coastal reflection in the wave model leads to slightly improved microbarom predictions. Indeed, "REF102040" shows a higher CPO than "NOREF" for around 60% of the cases. Similarly, in the NH, the wind

parameter distributions (Fig. 4.3d) peak around zero. Apart from the peak, the asymmetry indicates a higher CPO (difference up to +70%) when incorporating realistic wind conditions at the station, especially in the summer. In the SH (Fig. 4.3e), the monthly distributions peak at differences of +25% in the austral summer and +50% in the winter, whereas the parametrisations do hardly impact the monthly modelling performance around the equinoxes. During these months, the stratospheric circulation gradually reverses, with resulting unstable stratospheric zonal winds. In principle, setting $V_{\text{eff-ratio}}(\varphi)$ to 1 reflects this situation. Thus, a more realistic wind parametrisation leads to better predictions. This effect of including winds is maximised in the SH (Fig. 4.3e) during the solstices. Compared with the other parameters, the source model confrontation is most clearly favouring the one with a low bathymetry impact (Fig. 4.3c, 4.3f). Indeed, using the DC20 model results in a better agreement between predictions and observations in more than 90% of all cases. Furthermore, the distributions are centred at relative CPO differences of -10% to -30% (SH) and -25% to -45% (NH). An enhanced agreement between modelling and observations using DC20 is noted for SH stations in the austral winter with local peaks at CPO differences of -50% to -60%. Fig. 4.4 shows CPO absolute values for the eight simulations and each IMS
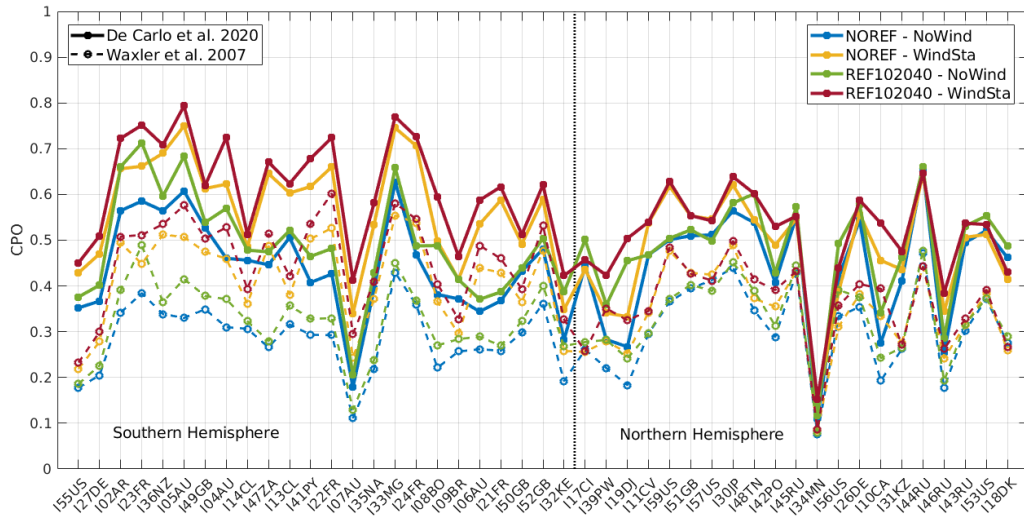
Figure 4.4 – Variation of the CPO along the IMS stations ordered by latitude - for the 8 parametrisations.

infrasound station. Except for seven stations, the configuration combining DC20, coastal reflection and wind at the station provides the best CPO values. Its overall CPO varies between 0.15 at I34MN and 0.8 at I05AU. For 34 of 45 stations, more than half of the observations are predicted using this configuration (CPO $\geqslant$ 0.5), and for 8 of these stations, the CPO exceeds 0.7. In contrast, the lowest CPO, generally obtained with W07, isotropic propagation conditions and no coastal reflection, ranges from 0.07 at I34MN to 0.47 at I44RU. Overall, this station-specific visualisation combines the effects of the individual parameters.

4.2.4 Discussion

The DC20 source model by De Carlo et al. (2020) improves the predictions such that the CPO is around 0.7 compared to about 0.5 when using the W07 source model by Waxler et al. (2007). Moreover, in those 10% of the cases of which the CPO is higher for W07 compared to DC20, no clear pattern arises with respect to stations (Fig. 4.4) nor frequency nor month (see complementary results in Section 4.3). For each parametrisation with DC20, CPO values mostly exceed those of any parametrisation with W07. Exceptions apply to the W07-wind parametrisation which often tops DC20-no-wind simulations (e.g., IS22), underlining the general importance of taking into account the wind. The stratospheric wind's impact on the CPO varies with the stations and the season. The differences between the two hemispheres are explained by the station locations relative to the source regions, or vice

versa. In the NH, the dominant sources and the wind direction have similar patterns. Major sources occur in winter and are mostly located upwind, west of the stations, which coincides with the prevailing wind direction. In the SH, fewer landmasses allow microbarom sources to exist throughout the whole ACC. Therefore, the stratospheric wind parametrisation is the key to predicting the actual sources of detected microbaroms as it controls the propagation direction. The shift of the seasonal peak is explained by stronger winds and source amplitudes during winter months highlighting the importance of a realistic wind parametrisation. Unlike for microseisms simulations where the coastal reflection is of great importance, the impact of coastal reflection for microbaroms is almost negligible as the distributions peak at zero with a small width and weak asymmetry. This is likely explained by a higher sensibility to propagation effects on microbaroms, thus limiting the impact of the wave model's coastal parametrisations. The ability to predict detections at outlier stations, such as I34MN (CPO<0.2), is significantly limited for all parametrisations. This station in Mongolia is far from any major sources, especially the Northern Atlantic hotspot, which coincides with the preferred arrival direction in the NH (Fig. 4.14 in the section 4.3.5 about complementary results). For this station, the parametrized propagation, constrained to $5,000$ km, excludes sources which would contribute the most to the detections. Furthermore, during summertime, the station does not receive any signal competing with the major sources from the SH, therefore the assumption of uniform atmosphere along the propagation is no longer valid here. These constraints are also applicable to I46RU (CPO between 0.18 and 0.39) and I31KZ to a lesser extent (CPO between 0.26 and 0.48). The metric was chosen to favour a model with more predicted observations. However, the false-positive rate – false positive corresponds to predicted arrivals without any observation – can also be of importance. Of specific interest is the increase of the false-positive rate in windless propagation (21% vs. 11% in a windy atmosphere), strengthening the importance of accounting for realistic wind in the propagation. Overall, in order to limit the false-positive impact, the threshold for the model binarization was set to 0.4. A smaller threshold would have increased CPO values along with the false-positive rate – e.g., for a threshold of 0.1 (respectively 0.4), the mean CPO value is 0.77 (0.43) and the mean false-positive rate is 38% (14%). Another limitation of this study lies in the known drawbacks of the conventional detection algorithm to characterise the interfering microbarom wavefields originating from different sources. The use of high-resolution detection processing techniques capable of extracting multidirectional coherent energy impinging simultaneously the station would contribute to a better assessment of the model prediction capability (e.g. den Ouden et al., 2020).

4.2.5 Conclusions

This study, supported by the reprocessed archive of continuous IMS waveform data, shows that modelling microbaroms worldwide in a straightforward way is feasible and yields overall good results. Introducing the CPO as a metric for objectivity leads to the conclusion that the best parametrisation for microbarom predictions worldwide is the recently developed DC20 source model using WAVEWATCHIII® with coastal reflection enabled (REF102040), and propagation accounting for the stratospheric wind at the station. Further studies should consider propagation over very large distances – more than $5,000$ km – and atmospheric variations along the propagation paths to enhance the simulation for outlier stations. Also, additional studies are required to explore time- and range-dependent full-wave propagation techniques (e.g. Waxler & Assink, 2019), while still maintaining computational efficiency. Applying such approaches would allow accounting for globally distributed microbarom sources. The differences between the observed and modelled azimuths are often larger than $5°$ and can partly be explained by cross-wind effects. Three-dimensional ray tracing simulations could correct these azimuth deviations, which potentially introduce errors in a range of $10°$ (e.g. Le Pichon et al., 2005).

Acknowledgments, Samples and Data

- The infrasound data have been processed using the PMCC software v5.7.4, developed at CEA (Département Analyse, Surveillance, Environnement). Access to the IMS network's data including differential pressure recordings of the infrasound stations is available to National Data Centers of the CTBTO and can be made available to others upon request through the virtual Data Exploitation Center (vDEC) at `https://www.ctbto.org/specials/vdec` (last accessed on 21 July 2020).

- The operational high-resolution atmospheric model analysis, produced by the Integrated Forecast System of the ECMWF, is accessible via `https://www.ecmwf.int/en/forecasts/datasets` (last accessed on 21 July 2020).

- The modelled second order equivalent surface pressure due to ocean wave interaction is available at `ftp://ftp.ifremer.fr/ifremer/ww3/HINDCAST/SISMO` (last accessed on 21 July 2020).

4.3 Complementary results and discussions

As the previous section 4.2 consists of a submitted article to *Geophysical Research Letters*, whose format is short and requires synthesis, only the main results of this study were presented. In this section, the main results are further detailed and complementary results are presented about the effects of the parameters i_1 to i_7 on the fit between model and observations.

4.3.1 Dominant signal comparison

The comparison of the dominant signal results, which is explained in Section 2.2.2, had been partially shown in the article where the observed dominant azimuth and amplitude are compared to the modelled ones for the REF102040, WindSta and DC20 configuration. Figure 4.5 shows similar results but also includes the results for the REF102040, NoWind and DC20 configuration. Changing REF102040 to NOREF or DC20 to W07 shows similar results, therefore, results with NOREF and W07 are not shown here. The observed dominant sources alternate seasonally between South West and South East in the Southern Hemisphere and vary seasonally from North West to East South East in the Northern Hemisphere (see Fig. 4.5a). The dominant arrivals modelled without wind - NoWind - represented in Fig. 4.5b, albeit showing roughly the global dominant direction for each hemisphere, i.e. south in the SH and North-North-West in the NH, fail to represent the seasonal variations. The dominant direction and its seasonality are therefore represented much better in a configuration including wind at the station - WindSta. One may note the effect of the wind on the dominant direction in the SH in Fig. 4.5c in comparison with in Fig. 4.5b where there is almost no seasonal variation of the dominant direction without wind in the SH. In the NH, one may notice a seasonality on dominant direction for the modelisation without wind (Fig. 4.5b), that may come from the source seasonality. However, the seasonality resulting of a modelisation with WindSta (Fig. 4.5c) fits better with the observations (Fig. 4.5a), as it accounts for both the source and the wind seasonality.

Fig. 4.5d represents the amplitude of the dominant signal observed which varies also seasonally showing a maximum of observed amplitude during local winter. The modelled amplitude presents an offset with regards to the observed amplitude, which is likely due to propagation uncertainties. Thus, to allow comparison between observed and modelled amplitude the average offset - over the time period - is removed for each station. Therefore, the modelled amplitude shown in Fig. 4.5e and Fig. 4.5f have been normalised, and in the configuration without wind (see Fig. 4.5e), the modelled amplitude fails to represent the entire extent of the amplitude seasonality, although a small amplitude seasonality may be observed in the NH, similarly to the dominant azimuth, and an seasonality with even smaller amplitude can be noticed in the SH. Adding the wind to the model amplifies the amplitude seasonal variations yielding to a better fit with the observations. Figure 4.6 further illustrates this comparisons by showing the distribution of the differences between observed and modelled dominant parameters, for all eight configurations. As explained above, the amplitude difference is computed with a normalised amplitude in order to allow comparison. The amplitude difference distributions for the configurations with WindSta, represented in yellow and red, are slightly narrower around 0 than for configurations with NoWind, represented in blue and green. Therefore, for the amplitude of the dominant signal configurations are slightly better when accounting for wind. The distributions of the azimuth differences all peak around 5°, however, for WindSta configurations the peak is twice as high and narrow as for configurations with NoWind. Furthermore, azimuth difference is lower than 16° for half of the distribution for configurations with WindSta, whereas for NoWind configurations the best half of the distribution presents azimuth differences up to 36°.

Comparison of the dominant parameters shows the importance of accounting for the wind in modelling microbaroms arrivals, as configurations with WindSta yield more accurate results than those with NoWind. One may note that there is almost no variation in the distributions of amplitude and azimuth difference between the four configurations with WindSta neither between the four configurations with NoWind. Thus, no conclusion can be drawn concerning the coastal reflection parameter nor the source model parameter.
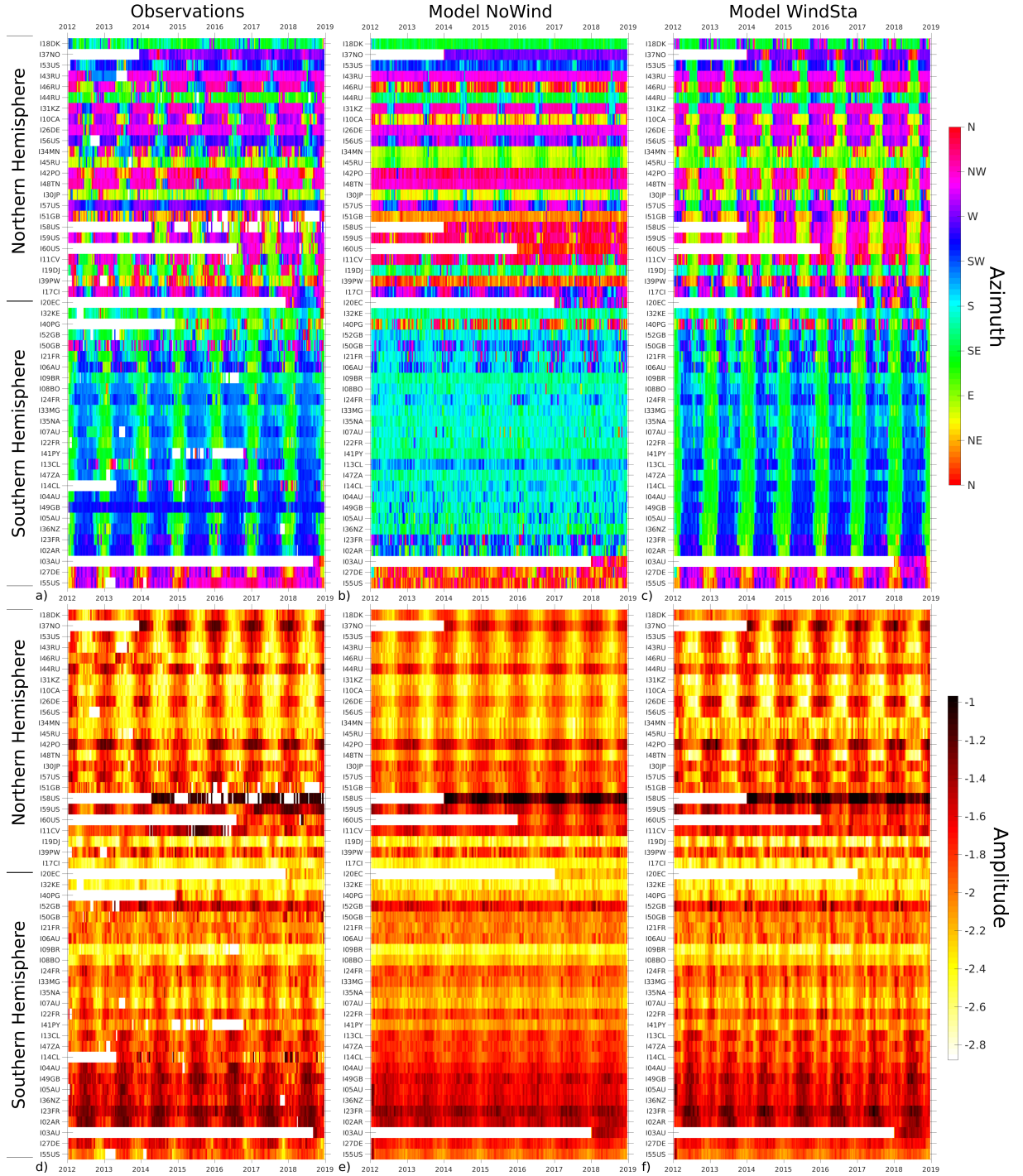
Figure 4.5 – The dataset of microbarom detections (left column) is compared with the outputs of a model that does not consider atmospheric characteristics - NoWind - (middle column) and of a model that incorporates stratospheric wind at the station - WindSta - (right column). Both models account for coastal reflections - REF102040 - and the DC20 source model. For the top row - *a), b), c)* - each coloured line depicts the back-azimuth of the observed or modelled detection with the maximum RMS amplitude within [T - 7 days, T + 7 days]. For the bottom row - *a), b), c)* - each coloured line depicts this maximum RMS amplitude within [T - 7 days, T + 7 days]. The time step is 4 days. White lines depict nil detections or missing infrasound station data within the respective time window. The 6 stations that were not yet certified in 2012 are also included in this figure.
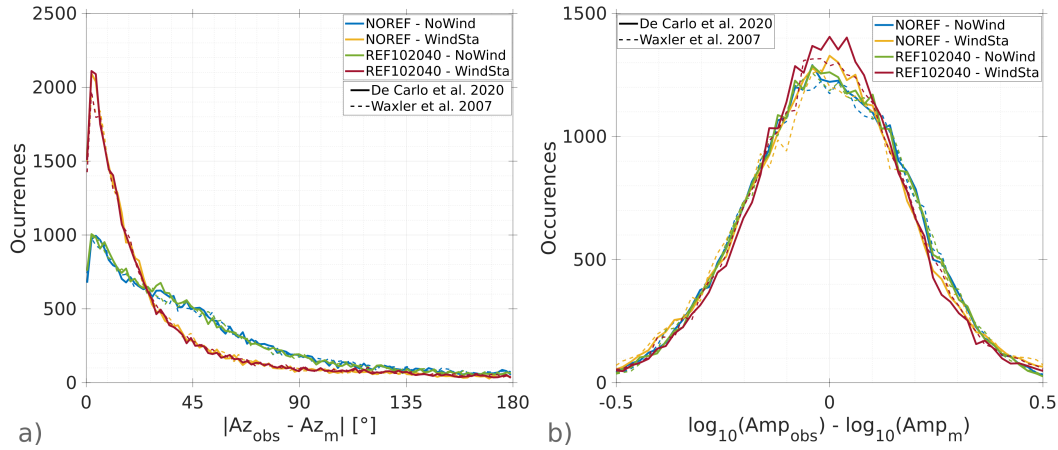
Figure 4.6 – Comparison of the a) azimuth and b) amplitude parameters of the dominant signal between observations and modelling results for the eigth modelling configurations. The lines represent the distributions, over the stations and the time steps, of those differences. Solid lines represent configurations with the DC20 source model while dash lines correspond to configurations with the W07 source model. Configurations with parameters NOREF-NoWind, NOREF-WindSta, REF102040-NoWind and REF102040-WindSta are respectively coloured in blue, yellow, green and red.

4.3.2 Variations of CPO with all parameters

As explained in Section 4.1, CPO values depend on seven parameters among which three are modelling parameters that define the eight configurations. The four remaining parameters are output parameters representing the modelling variability, namely the frequency band, the month, the year and the station. The CPO variations over these parameters are presented in Fig. 4.7 for the eight modelling configurations.

Figure 4.7a represents the CPO variations along the different IMS stations ordered by latitude, as in Fig. 4.4. Figure 4.7b and Figure 4.7d show the monthly variation of CPO for the NH and SH respectively. Figure 4.7c represents the CPO variation with the frequency while Figure 4.7e displays the yearly variation of CPO. Two striking observations can be made. Firstly, for all those parameters the configuration with REF102040, WindSta and DC20 has clearly the highest CPO value in almost all cases - exceptions can only be seen for one month and 3 stations - with the second best configuration being mostly the one with NOREF, WindSta and DC20. Secondly, in almost all cases, there is a CPO difference of roughly 0.15 between configurations with DC20 source model represented by plain lines and configurations with the W07 source model represented by dash lines.

Unlike Fig. 4.4, Figure 4.7a includes all the stations that were certified by the end of 2018, thus I03AU, I14CL, I20EC, I37NO, I40PG, I58US and I60US are added to the database. The extreme values of the CPO for the configuration REF102040-WindSta-DC20 are still 0.15 at I34MN and 0.8 at I05AU. For 5 of the added 7 stations, more than half of the observations are predicted using this configuration, and among those 5 stations, 2 present a CPO exceeding 0.7. This gives a total of 39 of 52 stations with a CPO$\geqslant$ 0.5 and 10 stations with a CPO $\geqslant$ 0.7.

The monthly variation of CPO differs with the hemisphere: in the NH, as shown in Fig. 4.7b, the pattern is quite similar for the 8 configurations whereas in the SH, as shown in Fig. 4.7d, the pattern mainly depends on whether the wind is accounting for or not. In the NH, for each configuration, the CPO decreases by less than 0.1 during the summer months and is mostly stable during other months. This decrease could be related to sources that are more scattered in NH in summer, as opposed to the well established winter sources (see Section 1.1). One may note that configurations with WindSta are better than their counterparts with NoWind by around 0.25-0.5, except in April, May and September, when both
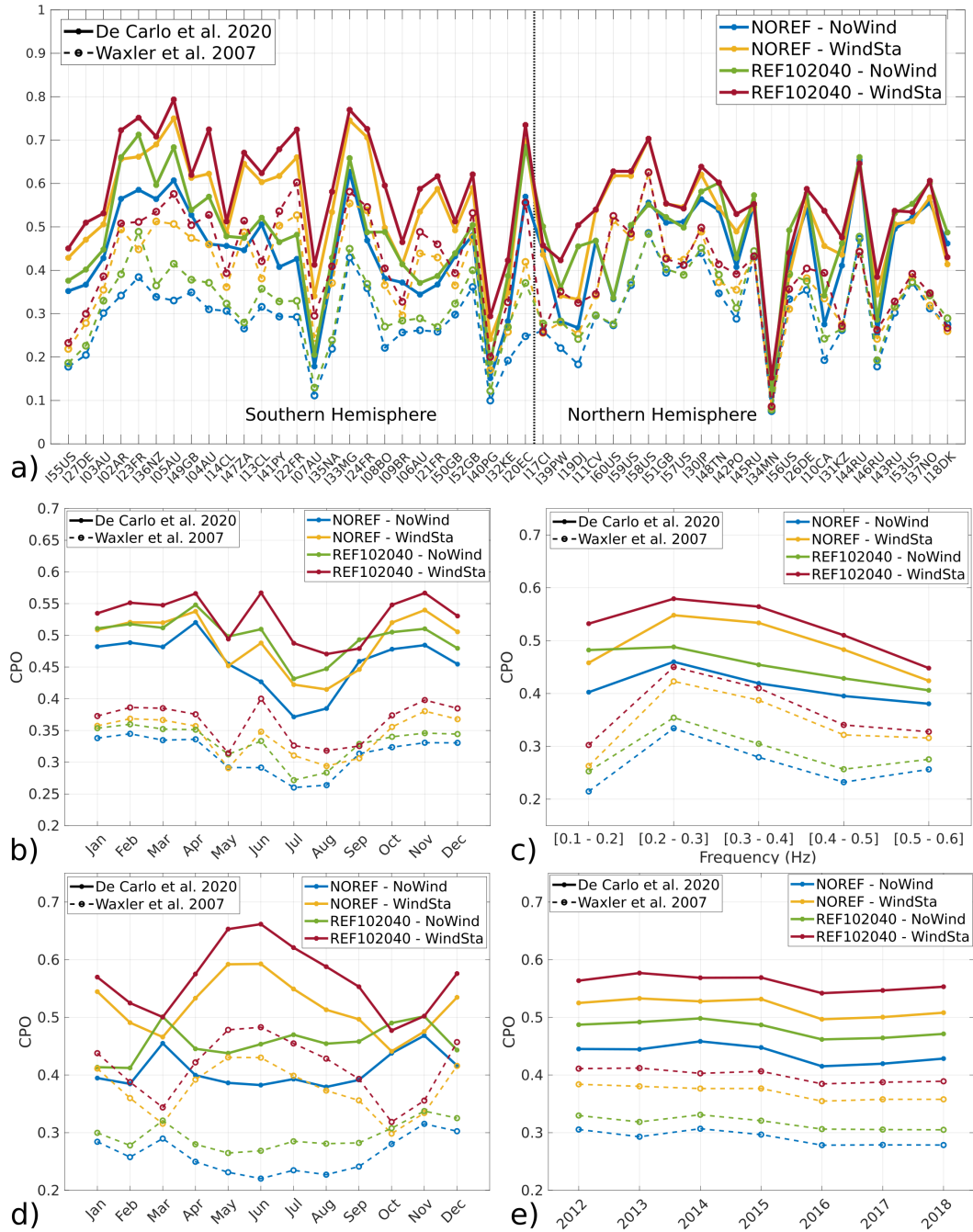
Figure 4.7 – CPO variations against output parameters - stations, months, years and frequency - for the eight modelling configurations. Solid lines represent configurations with the DC20 source model while dash lines correspond to configurations with the W07 source model. Configurations with parameters NOREF-NoWind, NOREF-WindSta, REF102040-NoWind and REF102040-WindSta are respectively coloured in blue, yellow, green and red. a) Variations over the 52 IMS stations certified in 2018. b) Monthly variations for stations in the Northern Hemisphere. c) Variations over the frequency bands. d) Monthy variations for stations in the Southern Hemisphere. e) Variations over the seven years of the study.

configurations have quite similar CPO values. These months correspond to a wind impact of lesser importance likely related to poor atmospheric modelling during stratospheric wind reversal periods in the NH.

In the SH, configurations with NoWind are almost constant over the months presenting only a slight increase in March, October and November. On the contrary, WindSta con-

figurations show seasonal amplitude variations of CPO of around 0.1 CPO point, with a maximum during local winter in June, a secondary maximum during local summer in December and minimums in March and October. These variations are likely related to the presence of strong sources the whole year in the SH, with the detection and modelling depending strongly on the propagation that is highly sensitive to wind variations when the waveguide is unstable during equinoxes.

Fig. 4.7c, representing the CPO variations with the frequency, shows higher CPO values for the frequency bands [0.2 - 0.3] Hz and [0.3 - 0.4] Hz. For the configurations with the source model W07, represented by dash lines, the worst CPO values are obtained for the lowest frequency band [0.1 - 0.2] Hz whereas for configurations with DC20, the highest frequency band [0.5 - 0.6] Hz shows the worst CPO values. Configurations with WindSta, represented in red and yellow, have higher CPO values than their counterparts with NoWind, with a CPO difference varying from 0.025 to 0.1 CPO point, with the higher differences for the mid frequencies [0.2 - 0.5] Hz. One may note that for [0.1 - 0.2] Hz, with the DC20 source model, coastal reflection shows some impact as both configurations with REF102040, represented in red and green, have higher CPO values than both configurations with NOREF.

Fig. 4.7e shows almost constant CPO values along the years for each configurations, and there is likely no yearly variation.

4.3.3 Distributions of ΔCPO and different configurations
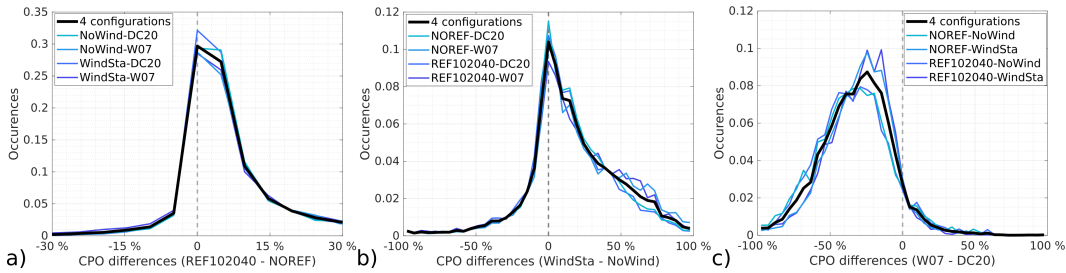
Figure 4.8 – Distribution of ΔCPO for each parameter - a) for the coastal reflection parameter, b) for the wind parameter and c) for the source model parameter. Each line coloured in a shade of blue represents one of the 4 configurations defined by the setting of the two other parameters. The black line represents the normalized distribution accounting all four configurations.

As presented in eq. (4.1.1), for each of the 3 modelling parameters i_1, i_2, i_3, we define a $\Delta\mathrm{CPO}_{k_1}$ that depends on the two other modelling parameters k_2 and k_3 (with (k_1, k_2, k_3) a permutation of $\{i_1, i_2, i_3\}$) and on the 4 other parameters i_4, i_5, i_6 and i_7. Each $\Delta\mathrm{CPO}_{k_1}$ depends then on 4 modelling configurations and while Fig. 4.3, in the previous section, represented the distribution including these 4 configurations, Fig. 4.8 shows the four distributions (for the four configurations) in shades of blue along with the distribution accounting for all configurations in bold black. All the distributions are normalised by their total size to allow comparison. For each modelling parameter $k_1 \in \{i_1, i_2, i_3\}$ the distributions of $\Delta\mathrm{CPO}_{k_1}$ for the 4 configurations (with k_2 and k_3 fixed) are very similar to the distribution including the 4 configurations. Therefore, for each modelling parameter, the determination of the best value (either NOREF or REF102040 for i_1, NoWind or WindSta for i_2, and DC20 or W07 for i_3) is almost not impacted by the selection of the other two modelling parameters, and the modelling parameters can be seen as independent.

Figures 4.9, 4.10 and 4.11 represent how the $\Delta\mathrm{CPO}_{k_1}$ is distributed over the frequency bands (i_4), the time (i_5 and i_6) and the stations (i_7). As the 4 configurations defined by k_2 and k_3 have a similar distribution (see Fig. 4.8), the configurations kept here are those with the best values: REF102040 for i_1, WindSta for i_2 and DC20 for i_3. There are five subfigures representing the five frequency bands. For each subfigure, the $\Delta\mathrm{CPO}_{k_1}$ is represented in
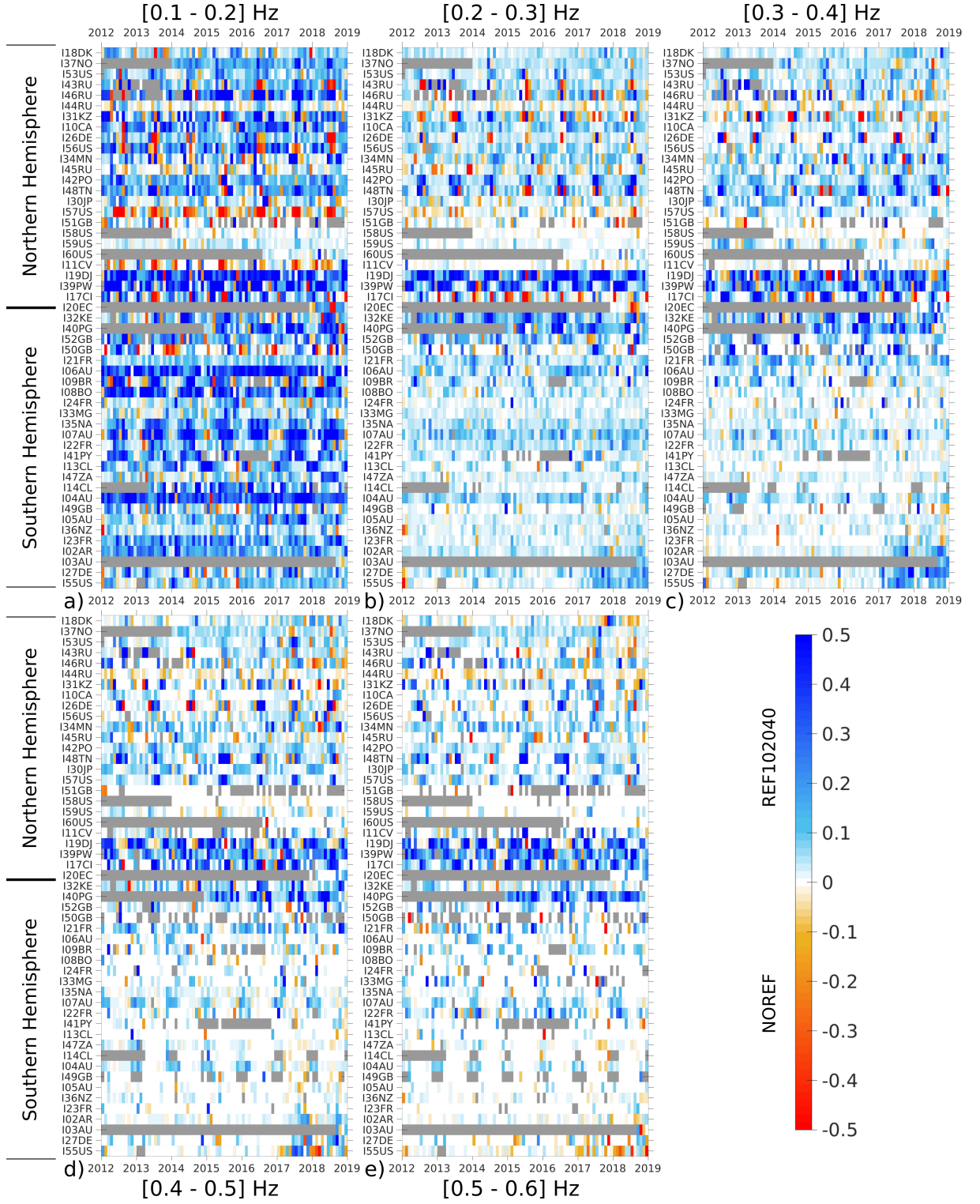
Figure 4.9 – CPO differences between parameterizations with REF102040 and with NOREF for *a)-e)* all frequency bands , all months and all IMS stations - ordered by latitude. In blue (respectively in red), the best parameterization is with REF102040 (respectively with NOREF). The wind parameter is set to WindSta and the source model parameter is set to DC20.
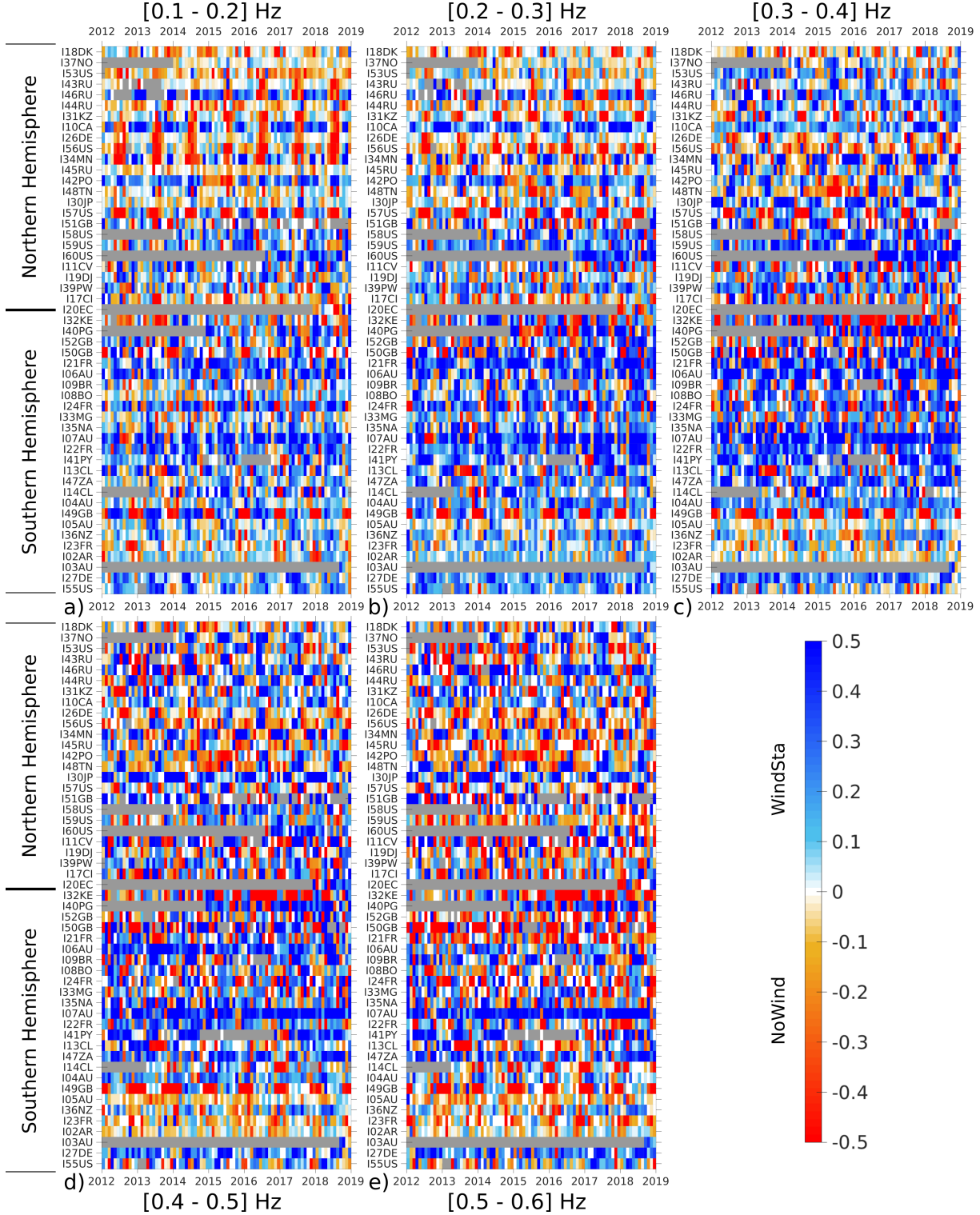
Figure 4.10 – CPO differences between parameterizations with WindSta and with NoWind for *a)-e)* all frequency bands , all months and all IMS stations - ordered by latitude. In blue (respectively in red), the best parameterization is with WindSta (respectively with NoWind). The coastal reflection parameter is set to REF102040 and the source model parameter is set to DC20.
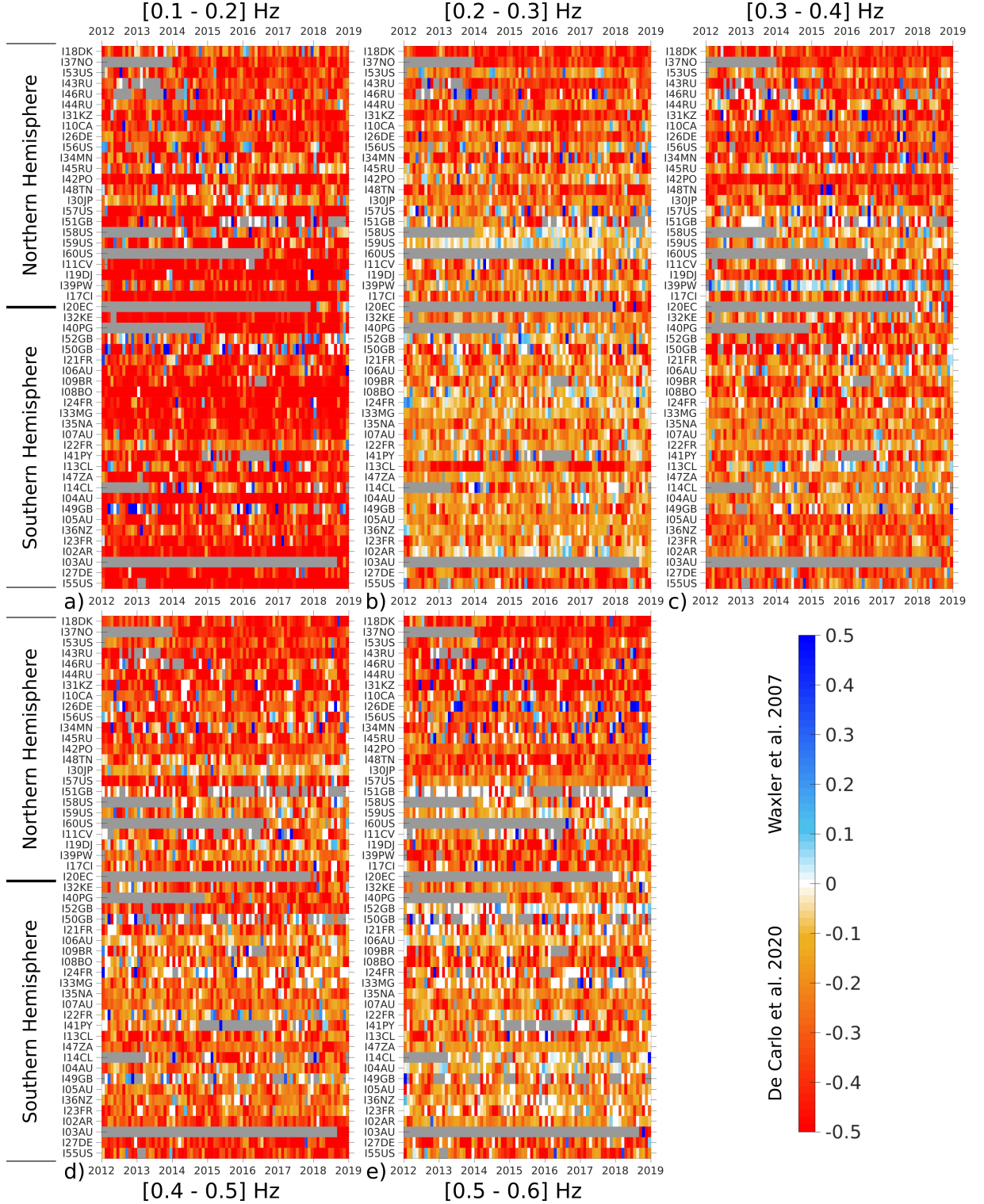
Figure 4.11 – CPO differences between parameterizations with W07 and with DC20 for *a)-e)* all frequency bands , all months and all IMS stations - ordered by latitude. In blue (respectively in red), the best parameterization is with W07 (respectively with DC20). The coastal reflection parameter is set to REF102040 and the wind parameter is set to WindSta.

colour with each column and each line corresponding respectively to a month and a station. For a clearer display, stations are ordered by latitude so that the northernmost stations are on the top of the subfigure and southernmost are at the bottom. Grey coloured pixels correspond to months when there is no observations for the given station and white coloured pixels correspond to months with a similar CPO for the 2 parameters.

For the coastal reflection parameter i_1, Fig. 4.9 shows a number of white pixels that increases with the frequency, except for stations I19DJ, I39PW, I17CI, I32KE and I40PG. Meaning that the difference between a configuration with coastal reflection and without reflection tends to disappear for most of the stations. For the frequency band [0.1 - 0.2] Hz the REF102040 configuration is better than the NOREF configuration in most cases, a striking exception is the station I57US for which each summer the NOREF configuration provides much better results with a ΔCPO_{i_1} around -0.5 and -0.4.

Fig. 4.10 shows that the ΔCPO_{i_2} distribution for wind parameter i_2 depends on the season for frequencies between 0.1 and 0.4 Hz. For higher frequencies the seasonality is less visible except for extreme latitudes, i.e. for stations located North of I46RU and stations located South to I49BG with the exception of I27DE and I55US. The number of red pixel seems to increase with the frequency, particularly for the [0.4 - 0.5] Hz and [0.5 - 0.6] Hz frequency bands, therefore for those frequencies the wind effect on propagation reduces.

Fig. 4.11 shows that the DC20 source modelling presents a higher CPO than the W07 source modelling in most cases, as already shown by Fig. 4.3 and Fig. 4.8. The interest of this figure lies in checking whether there is any pattern, either along frequencies, seasons or stations, in the 10% of cases where the modelling is better with W07. Fig. 4.11 suggests that there is no evident pattern within those cases.

4.3.4 ΔCPO and varying thresholds

Fig. 4.12 shows that the threshold does not impact our conclusions about the best configuration, and therefore, points out that the choice of a threshold 0.4, as presented in Section 2.2.3.2, was not motivated by the resulting conclusions.
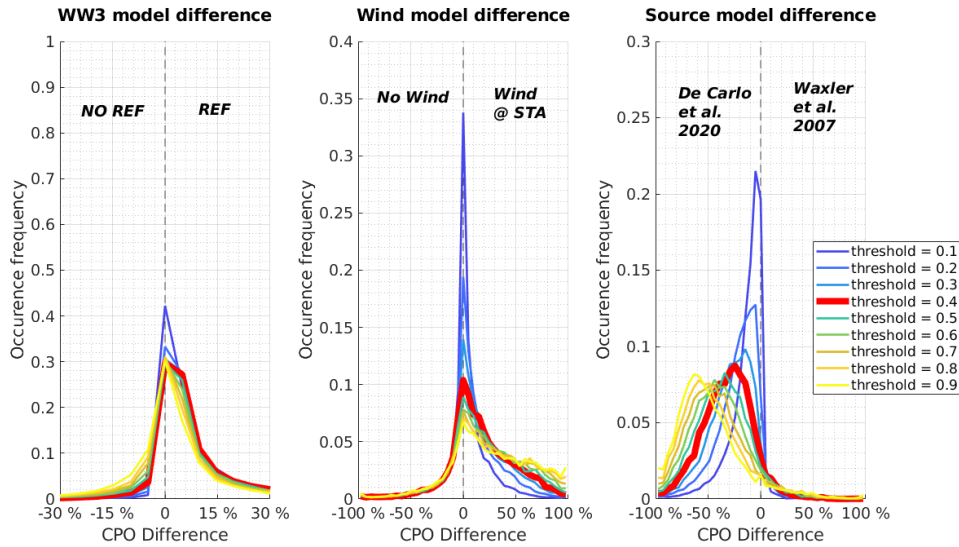
Figure 4.12 – Distributions of ΔCPO for each parameter - a) for the coastal reflection parameter, b) for the wind parameter and c) for the source model parameter - and for different thresholds - blue to yellow lines. The red line represents the distributions of ΔCPO for the selected threshold 0.4.

4.3.5 Discussion of particular stations

Although the CPO allows quantifying the fit between the observations and modelling results, it is quite abstract. In this subsection, we come back to the physical meaning of the CPO

and present both the binarised observations and modelling results in a time-azimuth grid, for I05AU (in Australia) and I34MN (in Mongolia).
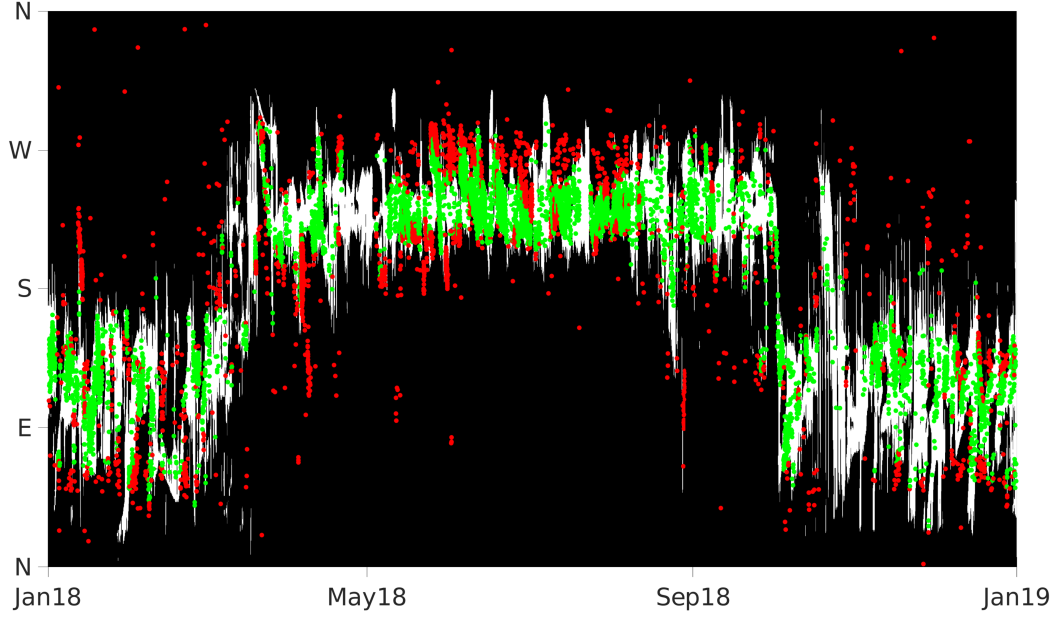
Figure 4.13 – Binarized modelling results and observations at I05AU : in white and green the model predicts arrivals at I05AU for a given direction and time step, in black and red it does not. Observations are represented by the dots: green when the model predicts the detection, red when it fails to predict the detection. The results are represented for 2018 on the $[0.2 - 0.3]$ Hz frequency band.
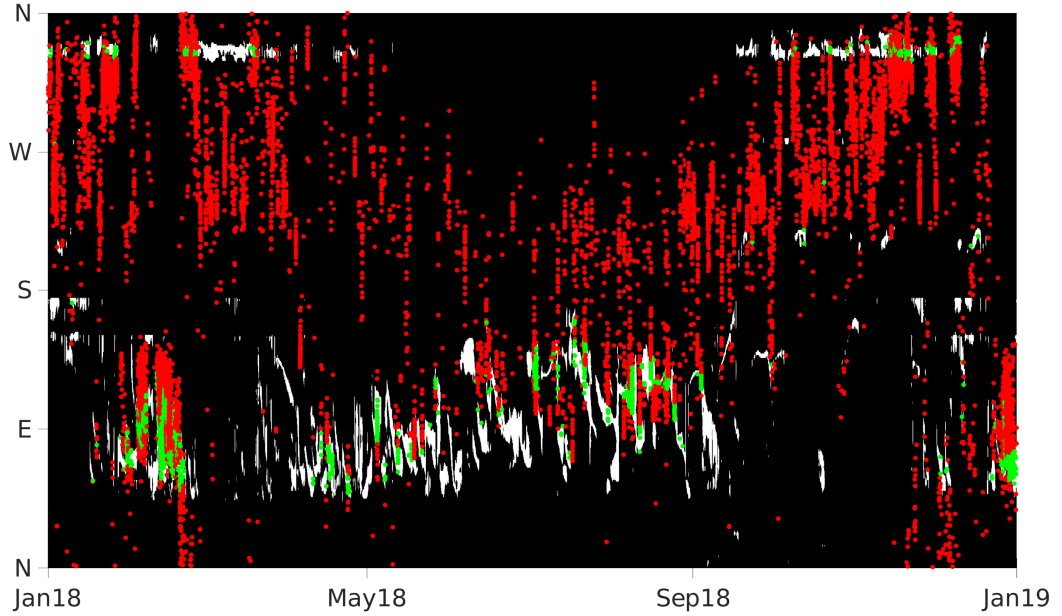
Figure 4.14 – Same as Fig. 4.13 for I34MN. The results are also represented for 2018 on the $[0.2 - 0.3]$ Hz frequency band.

Fig. 4.13 and Fig. 4.14 show the binary observations and modelling results for the station with the highest CPO - I05AU - and the station with the lowest CPO - I34MN -, respectively. These figures are quite similar to Fig. 2.6b: the green and red dots represent respectively the predicted and not predicted observations while the model is represented in black and white for azimuth respectively without and with predicted arrivals. Fig. 4.13 shows a good agreement between the observations and the model results, as suggested by the high CPO for this station. One may note that the red dots are close to the green ones, suggesting that the observations originate from an azimuth band wider than the modelled one. On the other hand, Fig. 4.14 explains the low CPO value at I34MN: in winter (from October to April), the observed azimuths range from around 200° (between South and West) to around 350° (almost North) while the model predicts detections in a narrow band around 330°. In summer, the arrivals are predicted between 50 and 150° whereas the observations are mostly detected from 130° to 250°.

At I34MN, the main issue in the modelling is related to the distance of this station from the microbarom sources. Fig. 4.15 represents the microbaroms sources, averaged for January 2018, multiplied by the attenuation with WindSta, and the distances from the stations. The outer circle corresponds to a distance of 10,000 km from the station whereas the inner circle corresponds to a distance of 5,000 km from the station. Therefore, all the sources summed during the modelling process are represented by the disk with bright colours. One can see
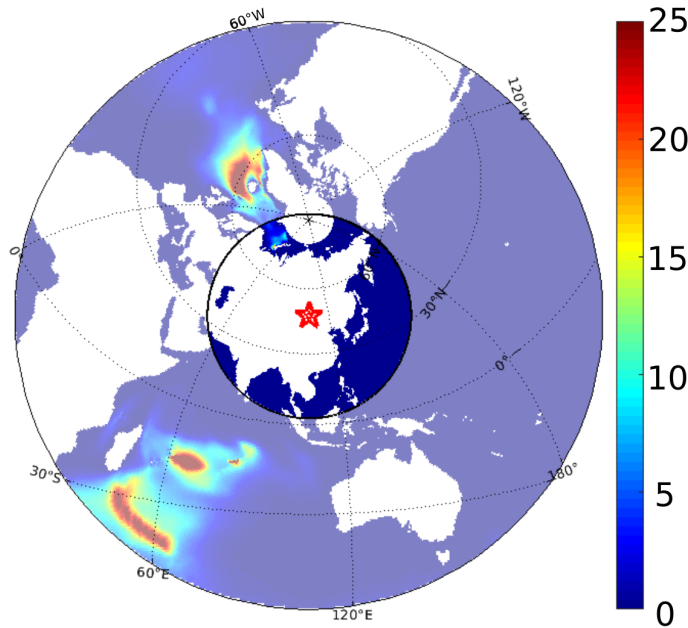
Figure 4.15 – Microbarom sources as visible by I34MN - multiplied by the attenuation with WindSta. Average for January 2018. The inner circle represents the 5,000 km limitation distance from the station - red star - while the outer circle corresponds to the 10,000 km distance from the station. Dominant sources are located between 5,000 and 10,000 km from I34MN.

that even with attenuation, that includes both the distance effect and the wind effect, the dominant sources are further away from the station than $dist_{max}$, set to $5,000$ km. Thus,the modelling is enhanced by summing sources over larger distances up to $10,000$ km. However, even with a $dist_{max}$ set to $10,000$ km, the fit does not improve significally (Fig. 4.16a is very similar to Fig. 4.14). Increasing $dist_{max}$ from $5,000$ km to $10,000$ km only increases the CPO by 0.02 CPO point, from 0.17 to 0.19, as shown in Fig. 4.16b representing the CPO values at I34MN depending on $dist_{max}$. Therefore, accounting for remote sources is not enough to enhance the modelling at I34MN.

To explain this misfit, future studies should explore the long-range propagation, above $5,000$ km, with the inclusion of atmospheric characteristics that vary along the propagation path.
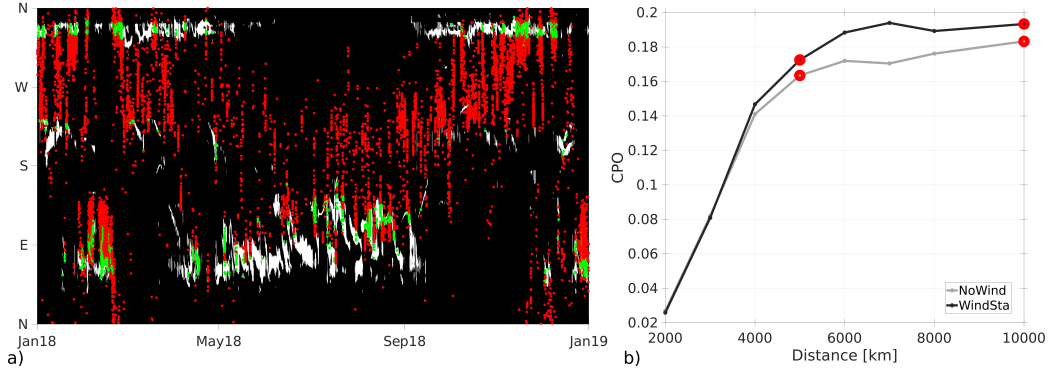
Figure 4.16 – a) Same as Fig. 4.14 for a model accounting to sources up to $10,000$ km ($dist_{max} = 10,000$ km). b) CPO variation with $dist_{max}$, the maximum distance of sources accounted for. The grey line shows the evolution for a configuration with DC20, REF102040 and NoWind while the black line represents the configuration with WindSta. CPO values at $5,000$ km and $10,000$ km are evidenced in red.

4.4   Conclusions of chapter

The global modelling presented in Chapter 2 has been run for 8 ($=2^3$) configurations in total, over 7 years from 2012 to 2018. The comparisons between the modelling results and the observations detected at the IMS stations through the CPO have led to draw the following conclusions:

- The best modelling configuration is the one with REF102040, WindSta and DC20.

- The source model developed in Chapter 3 is then validated and presents consequent enhancement compared to the existing source model by W07 when accounting for the global azimuth distribution of acoustic intensity.

- The impact of wind parametrisation is better evidenced when considering the dominant signal only, where the WindSta configuration clearly prevails.

- The impact of wave model parametrisation mainly impacts the low frequency bands where the configuration with coastal reflection - REF102040 - is better.

- The modelling capacity to predict microbaroms is impacted by the season, mainly when wind effects are accounted for.

- The CPO is highly variable along the stations, therefore the modelling capability to predict observed microbaroms is likely to be related with the geographical situation of each station.

CONCLUSIONS AND PERSPECTIVES

Contents

This Chapter presents the global conclusions of this thesis along with their limitations and suggests perspective studies to address these limitations.

5.1 Conclusions

5.1.1 Building a global catalog of microbarom model

In this thesis, a method to predict microbarom arrivals at global scales has been set up, along with a metric to quantify the fit between those predictions and the observations. This quantification has been applied to a 7 years database of observations detected at the International Monitoring System stations with 8 modelling configurations, allowing the assessment of this global modelling and determine the best modelling configuration.

The global modelling integrates a wave model, a source model transforming the ocean waves into pressure waves emitted in the atmosphere and a propagation model. Each of those component models has been subject to particular analysis in order to determine the best modelling configuration.

Concerning the wave model, in order to evaluate the importance of including the coastal reflection in wave action model to predict microbaroms, the global modelling was also run with two configurations for the wave action model WAVEWATCH III: one without any coastal reflection (NOREF) and one with maximum coastal reflection (REF102040).

The development of a new source model was a major development of this thesis and was carried out in Chapter 3 unifying the existing theories by accounting for both the bathymetry and a non monopolar radiation in the atmosphere (De Carlo et al., 2020, hereafter DC20). In that work and in the present thesis, we particularly revived the earlier theory by Brekhovskikh et al. (1973) which had not been well understood by the scientific community, probably because of a lack of details in its derivation, few illustrations and, so far, no validation. In all the applications of the following chapters, the DC20 source model is practically the same as the source model of Brekhovskikh et al. (1973), and their work should be fully acknowledged. The impact of the bathymetry on microbarom radiation is limited to vertical angles where the impact is strong, with barely no impact for angles larger than $13°$ from the vertical. On the other hand, the theory by Waxler et al. (2007, hereafter W07), widely used by the community, considers microbarom radiating in a monopolar way and therefore the strong impact of the bathymetry is present for all angles. As ground stations mainly receive signal between $40°$ and $90°$ from the vertical, the difference of bathymetry impact between the two models DC20 and W07 is strong. Therefore, in order to assess the validity of a non monopolar radiation, the new source model's capacity to predict observations has been tested and compared to the widely used model's, by running the global modelling with both DC20 and W07 source models.

To account for the infrasound propagation, an attenuation law derived in a horizontally uniform atmosphere, was used. The horizontally uniform atmosphere is represented by the stratospheric effective sound speed ratio to the sound speed at the ground. To emphasize the effect of stratospheric winds on the global microbaroms arrivals modelling, the model was run with two configuration settings for the propagation: in one case, the $V_{\text{eff}-\text{ratio}}$ is set constant (equal to 1) so that no direction is favoured by the wind (NoWind), whereas in the second case, $V_{\text{eff}-\text{ratio}}$ is computed by taking the atmospheric characteristics at the station (WindSta), accounting for the capacity of the station to receive acoustic signal by favouring the directions of upcoming stratospheric winds.

Other quantities have been set for the global microbaroms modelling and its predictability quantification:

- The sources have only been considered within a distance $\text{dist}_{\max}$ from the station, with $\text{dist}_{\max}$ set to 5000 km to account for most contributing sources without extrapolating the attenuation law too much, as it was defined up to 3000 km (Le Pichon et al., 2012).

- Both modelling and observations have been gathered into 0.1 Hz-width frequency bands, in order to allow comparison while reducing the number of outputs - as this allow the 22 frequency bands to be turned into 5, therefore enabling to get a reasonable computational time.

- The CPO metric (Coefficient of Predicted Observations), that has been used to compare observations and modelling and that ranges from 0 to 1, considers a binarised model that either predicts an arrival in a direction for a given time and frequency or not. From this binarised model the observations are classified into predicted observations and not predicted observations, and the ratio of predicted observations over all observations is studied as the ratio of interest. The threshold used for the binarization is set to 0.4, in order to have a good trade-off between predicted observations and false positive.

- The CPO metric is calculated over a month time step in order both to smooth the results and reduce the number of outputs, while conserving the seasonality.

5.1.2 Results from the global modelling

The modelling has been run for 8 ($=2^3$) configurations in total, over 7 years from 2012 to 2018 and for the 52 stations certified in 2018. The comparisons with the observations detected at the IMS stations have led to draw the following conclusions:

- **The best modelling parametrisation is the one with REF102040, WindSta and DC20**. The CPO value is indeed greater for configurations with coastal reflection (REF102040) rather than with no reflection (NOREF) in 62% of the cases. Configurations considering the wind at the station (WindSta) show a higher CPO value than configurations without wind (NoWind) in 68% of the cases. And configurations accounting for DC20 source model are better than those accounting for W07 source model in 94% of the cases.

- **The source model parameter shows the highest impact on the CPO.** The second highest impact is due to the wind parameter and is seasonally dependent. The coastal reflection parameter shows only small impact on the CPO; its main impact being for small frequencies [0.1-0.2] Hz.

- **The wind parametrisation has a high impact on dominant signal comparisons.** Indeed, when comparing modelled and observed dominant signals only, the main difference between configurations is due to the wind parametrisation, as WindSta allows to represent the seasonal variations of the dominant azimuth. The definition of the NoWind configuration, allowing equal propagation of all direction, combined with the application of the threshold - for the CPO definition - leads the configurations with NoWind to predict more microbaroms arrivals than the configurations with WindSta.

Therefore, NoWind configurations presents more false positive than WindSta configurations. Thus, it explains why the CPO difference does not show much differences between NoWind and WindSta, while the importance of accounting for the wind at the station is established only by looking at the dominant signal.

- **The season impacts the modelling capacity (variations of 0.1 to 0.15 CPO point), but no significant variation is observed over the years.** The seasonal evolution of the CPO - characterised by amplitude variation of 0.1 to 0.15 CPO point - is both a source effect, as the CPO is higher when the sources are stronger, resulting in more detections in a given direction, and a wind effect as, mainly in the Southern Hemisphere, the CPO is higher when the zonal winds are well established.

- **The modelling capacity shows variations of about 0.1 CPO point with the frequency.** The frequency bands with highest CPO values are [0.2 - 0.3] Hz and [0.3 - 0.4] Hz. The frequency dependence could be related equally to poor wave modelling with high frequencies and to observations limitations at low frequency.

- **The CPO exhibits large variations, around 0.6 CPO point, along the different stations, with overall good results as 39 stations over 51 present a CPO ⩾ 0.5.** CPO values range from 0.18 at I34MN to 0.79 at I05AU for the best modelling parametrisation, with values greater than 0.5 for 39 stations, i.e. more than half the observations are predicted by the model for these stations, among which 10 stations shows a CPO exceeding 0.7. This variation of the modelling capability to predict observed microbaroms over the stations is likely to be related to the geographical situation of each station and to its detection capacity and uncertainties. For the stations very distant from the dominant sources such as I34MN or I46RU (with propagation ranges larger than $4,000$ to $5,000$ km), the poor fit between observations and model is likely due to the setting of a restrictive $dist_{max}$ and to long-propagation issues and to the fact that the used attenuation law might not be enough to characterise the propagation - as it was established using range-independent atmospheric specifications and limited to a propagation distance of $3,000$ km.

5.2 Perspectives

The better characterization of microbarom sources and the model validation against observation data presented in this thesis offer new perspectives for further investigations about wave and atmospheric models.

By using a similar method as developed in Stutzmann et al. (2012) for microseisms, comparing microbaroms observations and modelling should help further refining coastal reflection effect on wave action models. In order to do so, long term averaging and coupling with microseisms results are expected to separate coastal reflection effects from propagation and wind effects. Moreover, accounting for the directional acoustical spectrum might allow to go further than defining only one linear combination per station by defining one linear combination per direction. In return, it is expected that enhancement in wave models, in particular in the directional distribution of energy, would produce more reliable microbaroms and microseisms sources, therefore enabling the use of tomography to probe the solid Earth and the middle atmosphere. Indeed, the wave action model WW3 is relatively accurate for wind seas ('young' waves generated by the local wind) provided that wind models at sea level are not underestimated (Pineau-Guillou et al., 2018). However, wave models are generally less accurate for swell heights, because a small variation in the center of a storm can produce large deviations when the waves have dispersed across an ocean basin. This misrepresentation is related to the initial conditions of the swell in the generating storm, therefore, it is expected that assimilating swell observations in the wave model in particular from satellite data, including Sentinel 1 wave mode and the SWIM instrument on CFOSAT, should adress this issue.

On the other hand, recent advances in measurements and processing methods performed during the european ARISE project had shown the interest of infrasound signal to passively

sound the middle atmosphere dynamics (e.g. Le Pichon et al., 2005; Vanderbecken et al., 2020; Amezcua et al., 2020). Retreiving significant features of the temperature and wind vertical structures had been performed from well identified and repetitive sources such as volcanoes. While these sources are well adapted to such atmospheric monitoring, they are ponctually localized. As microbaroms are ubiquitous, it is expected that using them to realize similar inversions will allow the generation of global diagnostics for atmospheric models, with respect to middle atmosphere representation.

Enhancing the representation of the middle atmospheric dynamics would enhance the source characterization for events of interest in the framework of the CTBT by allowing better propagation modelling of infrasound signals. Beyond these considerations, a better representation of the middle atmosphere dynamics is expected to improve meteorological predictions due to interactions between the different layers in the atmosphere. Sudden Stratospheric Warming (SSW) events are the largest dynamical events occuring in the middle atmosphere and they illustrate this point (Charlton-Perez et al., 2007). Indeed, SSW are warmings that produce an increase of the polar stratospheric temperature leading to the breaking of the polar vortex in mid-winter. While these events are misrepresented by modelling with a temperature underestimated by up to 40 K as measured during ARISE campaigns (Blanc et al., 2019), the strong dynamic perturbations they induce can propagate downward and dramatically affect the surface temperature and pressure fields. Therefore, SSW events are of particular interest. A global SSW event signature was obtained from the ambient noise generated by ocean (Smets & Evers, 2014) as a first confirmation of the use of microbaroms for representing the middle atmosphere dynamics. Following this example, using the global database of microbaroms detections by the IMS may enable the generation of a global catalog of sources to be assimilated in NWP models (Blanc et al., 2018).

In a more foreseeable future, three main perspectives are identified to further investigate on microbaroms and prepare for long term goals:

- **Study microbaroms closer to the source with balloon measurements** in order to assess the vertical radiation of the sources and the wave modelling impact;

- **Enhancing the long-range propagation** in order to improve the fit between observations and modelling results for the stations with poor CPO values;

- **Improving the comparison process** by accounting for observations uncertainties or variability or considering other processings (both for the model and the observations).

5.2.1 Study microbarom measurements by stratospheric balloons

Ground based stations are located several hundreds to thousands kilometers from microbarom sources, therefore, the received signal strongly depends on its propagation and differences in wave modelling are barely not visible at the station (see Conclusions of Chapter 4). On the contrary, stratospheric balloons evolving above the ocean are able to detect microbarom signals with lesser impact of the propagation. Thus, it is expected that studying microbaroms received by stratospheric balloons will emphasise the influence of wave modelling on the microbaroms modelling.

Another interest in the stratospheric balloons lies in the fact that they can also receive signals emitted with near-vertical angles which are not received at ground based stations as they mainly receive horizontal signals (from $0°$ and $90°$ from the vertical). As shown in Section 3.2, the radiation pattern of microbaroms depends on the elevation angle θ_a, with a bathymetry impact strongly localised around the vertical angles. Therefore, it was expected that studying infrasound data recorded during a stratospheric fligth above the ocean would allow to better characterise the near-vertical angles and to validate the vertical radiation pattern. However, a study by Le Pichon et al. (2020)[1], based on the infrasound recorded by the Ultra Long Duration Balloon (ULDB) which has been deployed around the Antarctic by the NASA in May-June 2016 (Bowman & Lees, 2018), has shown that the vertical radiation pattern have no significant impact on the modelled amplitude at the balloon, the only exception being when the source is located strictly under the balloon. This

---

[1]The study was realized together with Romain Fatout, in the framework of his Master project.

study also stresses the importance of the wave model considered as the time varying energy flux modelled with the WW3 model by Le Pichon et al. (2020) differs from the one modelled with the ECMWF wave model by Bowman & Lees (2018).

In order to validate the vertical radiation pattern, a suggestion was made to launch balloons with several sensors positionned along a wire forming a vertical array to detect infrasound.

5.2.2 Enhancing the long-range propagation

In this study, the maximum distance $\text{dist}_{\max}$ was set to 5000 km. For several stations, the fit between observations and predictions is improved when increasing $\text{dist}_{\max}$ and accounting for more sources. However, among these stations, the relative increase of CPO between 5000 km and 10000 km is weak, and 12 of the 14 stations with CPO values lower than 0.5 for $\text{dist}_{\max} = 5000$ km still have a CPO lower than 0.5 for $\text{dist}_{\max} = 10000$ km. Therefore, for those stations it is necessary to consider a propagation adapted for the very long distances in order to properly account for sources further away than 5000 km.

Dealing with very long-range propagation raises three issues. The first is that the atmosphere characteristics are likely to vary along the propagation path - even more when the propagation path crosses the equator, as zonal stratospheric winds reverse while changing hemisphere and the two others are related to the curvature of the Earth. On one hand, the shortest distance between two points on a sphere being a great circle, the local propagation angle varies along the path, and on the other hand, propagation is different in spherical coordinates (from cartesian coordinates) as horizontal distances increase with the altitude. The attenuation law (Le Pichon et al., 2012) used for this study neither accounts for the varying atmosphere along the path nor for the spherical effects of the Earth.

To account for variations along the path, Tailpied (2016) proposed a refined attenuation law by combining the local attenuations along the path (as mentioned in Section 2.1.3). The trajectory between a source and a receiver is divided into N segments of $1°$. For a point k, located at a distance d_k from the source with atmospheric conditions $V_{\text{eff}-\text{ratio},k}$, the attenuation $Att(d_k, f, V_{\text{eff}-\text{ratio},k})$ is defined by the attenuation law of Le Pichon et al. (2012). To obtain the attenuation in a segment $[k; k+1]$, the source attenuation at the point $k+1$ is divided by the source attenuation at the point k with the same $V_{\text{eff}-\text{ratio}}$. Therefore the total attenuation $Att_T(d, f)$ of a source located at a distance d from the receiver is:

$$Att_T(d, f) = \prod_{k=1}^{N-1} \frac{Att(d_{k+1}, f, V_{\text{eff}-\text{ratio},k+1})}{Att(d_k, f, V_{\text{eff}-\text{ratio},k+1})} \tag{5.2.1}$$

This formula accounts for the evolution of the $V_{\text{eff}-\text{ratio}}$ along the path, therefore it allows considering both the variations of the atmosphere characteristics and the variations of local angles due to the Earth sphericity. However, as equation (5.2.1) is based on the attenuation law by Le Pichon et al. (2012), it does not account for the long-range effects of the Earth sphericity such as increased distances in the thermosphere. Therefore the valid range of this attenuation is still limited around 5000 km.

To extend the range of the attenuation law and to account for spherical effect, we suggest to compare both the extrapolated attenuation law and the amplitude results of a 3D spherical ray-tracing (Dessa et al., 2005; Blom, 2019), for ranges from 5000 km to 20000 km and for all $V_{\text{eff}-\text{ratio}}$ values. In the case of significant differences, the attenuation law shall be modified to fit the amplitude evolution at long ranges.

5.2.3 Improving the model-data comparison method

Including uncertainties considerations in the CPO

The CPO metric defined in Section 2.2.3 does not account for observations uncertainties nor other observations characteristics such as the signal amplitude. This metric only accounts for the presence or absence of detections in an azimuth-time pixel. The binary aspect of this metric does not allow to discriminate between large or small azimuth differences between

the model and the observations, when they do not fit.

A practical solution to account for azimuth observation uncertainty is to consider an azimuth band $\pm\Delta\theta$ around each observed azimuth. If this observed azimuth band intersects any zone where the model is true, the observation is considered as predicted.

Changing metric by changing modelling output

A more complex solution would be to modify the comparison metric by changing either the model or the observations format, as the current formats are very different (see Section 2.2.1).

A first approach to have similar format for the model output would be to apply the same processing, namely the PMCC array processing, on the model. That would require to construct synthetic signals from the modelling in order to apply PMCC processing on these synthetic signals. However, a direct comparison between synthetic and observed detections will present similar drawbacks to the comparison of the dominant signal presented in Section 2.2.2 as it would still be highly impacted by the observations variability. Furthermore, the phasis of the modelled synthetic signals should be randomly distributed, and that would generate variability in the modelling detections also.

Based on this random phase, a lead for further investigations is to consider each detected azimuth in a given time step θ_k as a realization of the random variable θ with probability distribution $P(\theta)$. From the modelled directional spectrum we can define a modelled probability distribution of azimuth that would be detected at the station $P_{\mathrm{mod}}(\theta)$, that is a model estimate of the probability distribution P. A likehood metric L can then be defined:

$$L(t) = \prod_{k\,|\,t_k\in[t,t+\Delta t]} P_{\mathrm{mod}}(\theta_k) \tag{5.2.2}$$

The likehood metric accounts for the entire azimuth distribution and array response and limitations should be included in the $P_{\mathrm{mod}}(\theta)$. The main issue here is to define the distribution of modelled detections $P_{\mathrm{mod}}(\theta)$. A theoretical definition of $P_{\mathrm{mod}}(\theta)$ would be quite general as it would include both the acoustic directional spectrum and the array response. On the other hand, defining $P_{\mathrm{mod}}(\theta)$ numerically is simpler, albeit longer as it requires a random study for each directional spectrum and station.

Changing metric by changing array processing for observations

Another perspective is to use another signal processing in order to modify the observations format and to compare observations with modelling for all backazimuth directions. Recently, den Ouden et al. (2020) showed that an iterative decomposition of the array spatial covariance matrix using the CLEAN algorithm (Högbom, 1974) can be exploited to resolve the backazimuth and trace velocity of the most coherent wavefront arrivals, therefore allowing the microbarom soundscape at the station to account for the wide spatial distribution of microbarom sources.

In a similar ambition to account for all backazimuth directions, a collaborative paper, presented in Appendix B is currently in preparation about investigations on the use of a vespagram-based approach as a tool for multi-direction comparison between simulated microbaroms soundscapes and infrasound data recorded at I37NO in Norway. In array signal processing, velocity spectral (vespagram) analysis is an approach which analyzes recorded signals in terms of signal power as a function of time. The power is evaluated either at a fixed slowness, i.e. a constant apparent velocity with varying backazimuth — corresponding to a circle in the slowness space — or at a fixed backazimuth with varying apparent velocity — corresponding to a line in slowness space (Davies et al., 1971). For this study, we considered vespagrams for a fixed apparent velocity of 350 $m \cdot s^{-1}$ that corresponds to stratospheric arrivals. In order to compare observations and model while accounting for array response and observation resolution, a smoothing kernel - defined by the array response function main lobe - is applied to the microbarom model at the station, for each frequency band. As both the vespagram and the microbarom model output provide power estimates as function of time and backazimuth which can be displayed as an image, an image comparison approach based

on mean-square difference is proposed for benchmarking. The study considers 6 consecutive years of infrasound observations between 2014 and 2019 at a ground-based infrasound array located at Bardufoss, Norway (69.07 N, 18.61 E), denoted IS37 or I37NO (Fyen et al., 2014). This study shows that Vespagrams are particularly adapted to compare observations with modelling while capturing seasonal and sub-seasonal variations of microbaroms.

Synthèse de la thèse en français

Contents

6.1 Introduction

À l'échelle globale, les signaux infrasons sont dominés par du bruit ambiant cohérent d'origine océanique dans la gamme de fréquence [0.1 - 0.5] Hz avec un pic d'énergie autour de 0.2 Hz. Les premières observations de ces signaux acoustiques d'amplitude de l'ordre de quelques microbars ont été réalisées à la fin des années 30 (Shuleykin, 1935 ; Benioff & Gutenberg, 1939 ; Baird & Banwell, 1940) et Benioff & Gutenberg (1939) ont baptisé ces signaux "microbaroms" d'une part à cause de leur amplitude et d'autre part par analogie avec les microséismes - qui sont le pendant sismique des microbaroms. Ces signaux proviennent tous deux de l'océan et présentent des fréquences similaires correspondant au double de la fréquence des vagues. Il a été montré que ces similitudes sont dues à un seul et même phénomène de génération (par ex. Donn & Posmentier, 1967 ; Donn & Naini, 1973), et plus précisément qu'il s'agit des interactions d'ordre deux de vagues se propageant en sens opposés que l'on peut notamment trouver au sein de larges systèmes dépressifs (voir Miche, 1944 ; Longuet-Higgins, 1950 ; K. Hasselmann, 1963, pour les études théoriques pionières).

L'intérêt pour les microbaroms est double : le premier intérêt est lié au Traité d'Interdiction Complète des Essais nucléaires et le second concerne la modélisation atmosphérique et les modèles de prédictions météorologiques (NWP - Numerical Weather Prediction).

Dans le cadre du Traité d'Interdiction Complète des Essais nucléaires (TICE), un réseau international multitechnologies - le Système de Surveillance International (SSI) - a été installé pour détecter tout essai nucléaire. Les infrasons constituent l'une des quatre technologies du SSI avec la sismologie, l'hydroacoustique et les radionucléides. Cependant, la détection infrasonore des explosions nucléaires dépend fortement du bruit à la fois incohérent, comme les vents locaux, et cohérent, comme les microbaroms. Ainsi, une meilleure

connaissance des microbaroms permettrait de les séparer des signaux d'intérêts.

Les modèles d'atmosphère ont été significativement améliorés ces dernières décennies, notamment jusqu'à 30 km d'altitude grâce à l'intégration d'observations pour contraindre les modèles. Cependant, pour des altitudes supérieures à 30 km, les observations sont rares et faiblement échantillonnées ce qui implique que les modèles d'atmosphère restent mal résolus en vent et température (par ex. Le Pichon et al., 2015). Le projet européen ARISE (Atmospheric dynamic Research Infra Structure in Europe, Blanc et al., 2018) a encouragé l'utilisation des mesures infrasons pour aider à contraindre les modèles dynamiques de la moyenne atmosphère (30 à 60 km). En effet, la propagation des infrasons sur de longues distances dépend fortement des conditions atmosphériques étant donné que les infrasons se propagent à travers des guides d'ondes - zones de l'atmosphère dans lesquelles les ondes sont confinées par réflexion totale sur les parois et qui les font se propager horizontallement. Dans les conditions standards d'atmosphère, sans vent, un guide d'onde existe entre le sol et environ 100 km d'altitude - le guide d'onde thermosphérique -, cependant les signaux acoustiques sont très fortement atténués à de telles altitudes, même dans le cas de signaux de très basse fréquence comme les microbaroms. Avec du vent entre 30 et 60 km d'altitude, un guide d'onde stratosphérique peut être établi dans la direction de propagation du vent, permettant une propagation efficace des infrasons sur plusieurs centaines voire milliers de kilomètres. Il a ainsi été mis en évidence que les infrasons peuvent être utilisés pour sonder la variabilité atmosphérique, particulièrement la variabilité de la moyenne atmosphère. (par ex. Donn & Rind, 1971, 1972 ; D. P. Drob et al., 2010 ; Assink et al., 2014 ; Smets & Evers, 2014 ; Amezcua et al., 2020 ; Vanderbecken et al., 2020, ...).
Parmi toutes les sources d'infrasons (telles que les volcans, les météorites, les explosions industrielles ...), les microbaroms présentent des caractéristiques particulièrement intéressantes pour l'étude de la variabilité atmosphérique. Premièrement, la très basse fréquence des microbaroms (pour comparaison la gamme de fréquences des infrasons s'étend de 0.05 Hz à 20 Hz contre 0.1-0.5 Hz pour les microbaroms) leur permet de se propager sur plusieurs milliers de kilomètres et d'être détectés à l'échelle mondiale. Deuxièmement, les sources de microbaroms sont étendues spatialement et quasiment continues en temps. Ainsi, utiliser les microbaroms pour sonder la moyenne atmosphère permettrait d'avoir un échantillonage exploitable afin de contraindre les modèles dynamiques de la moyenne atmosphère.

D'un autre côté, inverser le signal infrason pour contraindre les modèles d'atmosphère tend à se compliquer par l'augmentation du nombre de variables due au fait que les microbaroms sont étendus spatialement et qu'il ne s'agisse pas de signaux impulsionnels. Par conséquent, une façon plus simple de procéder consiste à utiliser une approche directe en modélisant les arrivées de microbaroms aux stations infrasons et en les comparant aux observations. Sur le long terme, ces simulations devraient permettre à développer des nouvelles contraintes observationnelles pour la modélisation de la dynamique de la moyenne atmosphère.

L'objectif de cette thèse est de développer une méthodologie pour modéliser les arrivées de microbaroms aux stations et pour les comparer aux observations à l'échelle globale en utilisant la base de données du SSI. La section 6.2 (Chapitre 2 de la thèse) est dédiée à la présentation et la mise en place de la méthodologie de modélisation globale. La section 6.3 (Chapitre 3 de la thèse) reprend les principaux points du nouveau modèle de source développé par De Carlo et al. (2020). L'application du modèle global défini au chapitre 2 et incluant le nouveau modèle de source est présentée en section 6.4 (Chapitre 4 de la thèse). Cette modélisation globale est réalisée sur sept ans, à partir du récent traitement de la base de données du SSI. Finalement, les conclusions présentées au chapitre 5 sont reprises dans la section 6.5.

6.2 Chapitre 2 - Considérations préliminaires

L'objectif principal de cette section (et du Chapitre 2) est de présenter une méthodologie qui intègre un modèle de source de microbaroms dans un modèle plus global incluant la propagation et la prise en compte de l'ensemble des sources afin de modéliser les arrivées de microbaroms aux stations SSI et de comparer ces arrivées avec les observations.

 Étant donné que l'objectif est d'appliquer cette méhodologie à la base de données du réseau SSI de façon opérationnelle, cette méthodologie doit être universelle - applicable en toute station, pour tout temps - tout en nécessitant un temps de calcul raisonnable. Pour ce faire, des simplifications sont nécessaires : le deuxième but de cette section est de présenter les choix faits pour simplifier la modélisation globale.

6.2.1 Modélisation des arrivées de microbaroms
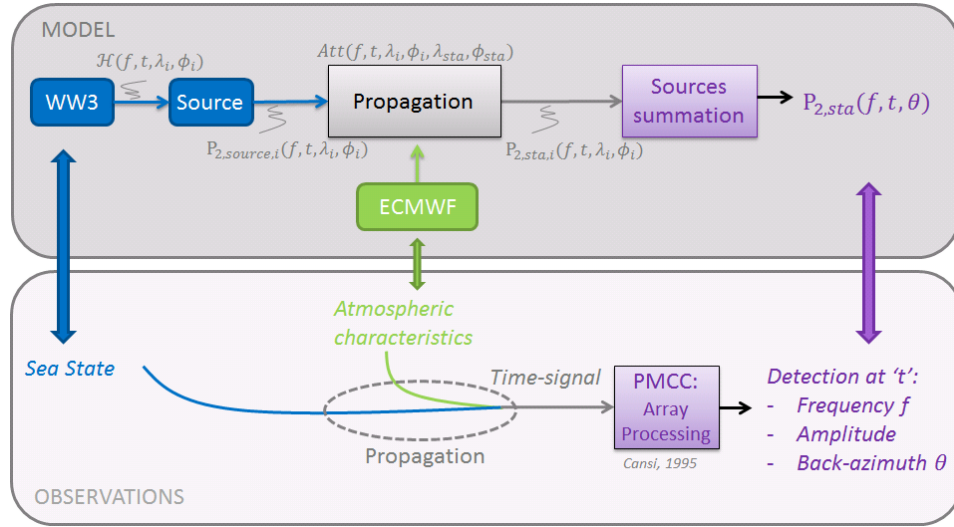
Figure 6.1 – Modélisation globale des arrivées de microbaroms aux stations.

Modéliser les arrivées de microbaroms aux stations nécessite de suivre plusieurs étapes (voir aussi Fig. 6.1) :

1. L'état de mer est modélisé par un modèle d'action de vagues qui donne un spectre de vagues $N(f, \theta, t, \lambda_i, \phi_i)$ pour chaque point de la surface libre. Ce spectre de vagues est ensuite transformé en une **densité spectrale de pression de surface équivalente d'ordre deux** $F_{p2}(\lambda_i, \varphi_i, f, K, t)$ (cf éq. 1.16) à travers l'intégrale d'Hasselmann $\mathcal{H}(f, t, \lambda_i, \phi_i)$ (cf. éq. (1.12))

2. À partir de la densité spectrale de pression de surface équivalente, le **spectre acoustique de la source** $P_{2,source,i}(f, t, \lambda_i, \phi_i)$ est obtenu en applicant un modèle de source à $F_{p2}(\lambda_i, \varphi_i, f, K, t)$

3. En prenant en compte la distance entre la source et la station de réception ainsi que le modèle atmosphérique, l'**atténuation** liée à la source est calculée : $Att(f, t, \lambda_i, \phi_i, \lambda_{sta}, \phi_{sta})$

4. Cette atténuation est appliquée au spectre acoustique du point source correspondant, afin d'obtenir la **contribution de ce point source** à la puissance acoustique **à la station** : $P_{2,sta,i}(f, t, \lambda_i, \phi_i)$

5. Pour calculer le **spectre directionnel acoustique à la station** $P_{2,sta}(f, t, \theta)$, toutes les contributions - spectres des points source tels que vus par la station - de sources comprises dans une bande d'azimut sont sommées :

$$P_{2,sta}(f, t, \theta) = \sum_{i \in \mathcal{A}_\theta} P_{2,sta,i}(f, t, \lambda_i, \phi_i) \tag{6.2.1}$$

avec $\mathcal{A}_\theta$ l'ensemble des cellules du modèle vues par la station dans un azimut θ

Ces étapes sont développées avec plus de détails dans le Chapitre 2.

Étape 1 - Modèle de vagues

Le modèle d'action de vagues utilisé est le modèle WAVEWATCH III® (abrégé en WW3) qui inclut le calcul de l'intégrale d'Hasselmann.

Des paramétrisations de la réflexion côtière ont été introduite dans le code WW3 pour les études des microséismes (Ardhuin et al., 2011). Afin d'étudier les effets de la réflexion côtière sur la modélisation des arrivées de microbaroms en station, deux configurations seront calculées pour le modèle de vagues : une sans réflexion côtière (NOREF) et l'autre prenant en compte une réflexion côtière maximale (REF102040) avec un coefficient de réflexion de 10% (respectivement 20% et 40%) pour les continents (respectivement les îles et la glace de mer).

Étape 2 - Modèle de source

Les modèles de source fournissent généralement une relation entre le terme d'interaction de vagues (l'intégrale d'Hasselmann) et la pression acoustique dans l'air à l'interface océan-atmosphère. Une contribution majeure de cette thèse a été de redévelopper un modèle de source unifiant les théories de Brekhovskikh et al. (1973) et Waxler et al. (2007) ; ces développements sont présentés en Section 6.3 ainsi qu'au Chapitre 3.

Étape 3 - Atténuation atmosphérique

Étant donné que l'ensemble de l'océan peut être source de microbaroms, le temps de calcul nécessaire pour appliquer n'importe quel modèle de propagation à ces sources serait exorbitant. En conséquence, on a choisi de ne pas utiliser un modèle de propagation mais une loi d'atténuation (Le Pichon et al., 2012) pour représenter la propagation. Cette loi d'atténuation dépend de la fréquence acoustique, de la distance entre la source et le récepteur et de $V_{\text{eff}-\text{ratio}}$, le rapport de célérité effective entre la stratosphère et le sol.

Afin de quantifier l'effet de l'atténuation générée par les vents, la modélisation est réalisée pour deux configurations : l'une prenant en compte le vent à la station (WindSta), représentatif de la capacité de la station à recevoir un signal se propageant dans le guide d'onde stratosphérique, et l'autre sans vent (NoWind). Cette seconde configuration n'est pas "sans vent" à strictement parler : il s'agit en réalité d'une configuration sans effets directionnels liés au vent, c'est-à-dire qu'aucune direction n'est favorisée par le vent étant donné que $V_{\text{eff}-\text{ratio}}$ est fixé constant égal à 1.

Pour la configuration WindSta, les profiles atmosphériques sont extrait des analyses ECMWF-HRES.

Étape 4 - Application de l'atténuation

Le spectre de source acoustique est équivalent à une pression au carré, par conséquent, le spectre acoustique de la source est multiplié par le carré de l'atténuation Att^2, afin d'obtenir la contribution acoustique du point source i.

Étape 5 - Discrétisation et sommation par directions

Afin d'étudier les effets directionnels, la grille du modèle de vagues $(0.5° \times 0.5°)$ est discrétisée en bandes d'azimut de $1°$ pour chaque station. Après application de l'atténuation, toutes les sources sont sommées dans ces bandes d'azimut, fournissant ainsi un spectre directionnel d'énergie acoustique à la station. Pour réduire les temps de calcul et éviter de prendre en compte des sources lointaines qui pourraient être mal atténuées (la loi d'atténuation n'a pas été définie au delà de 3000 km), on fixe une limite de distance à partir de laquelle les sources ne sont plus incluses dans la somme.

6.2.2 Définition d'une métrique pour comparer modèle et observations

La sortie de la modélisation globale consiste en un spectre directionnel acoustique de résolution 1° en direction et 0.1 Hz en fréquence. Chaque pas de temps du modèle est de trois heures. D'un autre côté, les observations de la base de données sont constituées de détections réparties irrégulièrement dans le temps, allant d'une absence de détections à plusieurs centaines pour des pas de temps de trois heures. Pour chaque détection les paramètres du front d'onde sont estimés. La direction d'origine du front d'onde varie fortement pendant un pas de temps de trois heures, avec une déviation standard moyenne de 15°. Ainsi une comparaison quantitative entre les observations et le modèle se doit de considérer toutes les sources et leur étalement directionnel (le fait qu'elles soient visibles dans un large pinceau d'angles depuis la station).

Pour chaque pas de temps et chaque bande de fréquence, la répartition directionnelle du signal modélisé est normalisée par son maximum sur les directions (cf. Fig 6.2a), afin de surmonter les problèmes d'incertitudes liés à la loi d'atténuation considérée. Ensuite, on applique un seuil à cette répartition normalisée en dessous duquel les signaux sont rejetés. On a donc un modèle binaire qui prédit (ou non) des arrivées de microbaroms dans une certaine direction. Toutes les détections sont ensuite classifiées en deux catégories : les observations prédites et les observations non prédites (cf. Fig. 6.2b) en fonction de leur temps d'arrivée, direction et fréquence. Cette classification permet la mise en place d'une métrique pour évaluer les résultats de la modélisation : le Coefficient d'Observations Prédites (CPO) qui est le rapport entre le nombre d'observations prédites et le nombre d'observations totales. Pour avoir un compromis optimal entre le CPO et le taux de faux positifs, le seuil pour la binarisation du modèle est fixé à 0.4 .
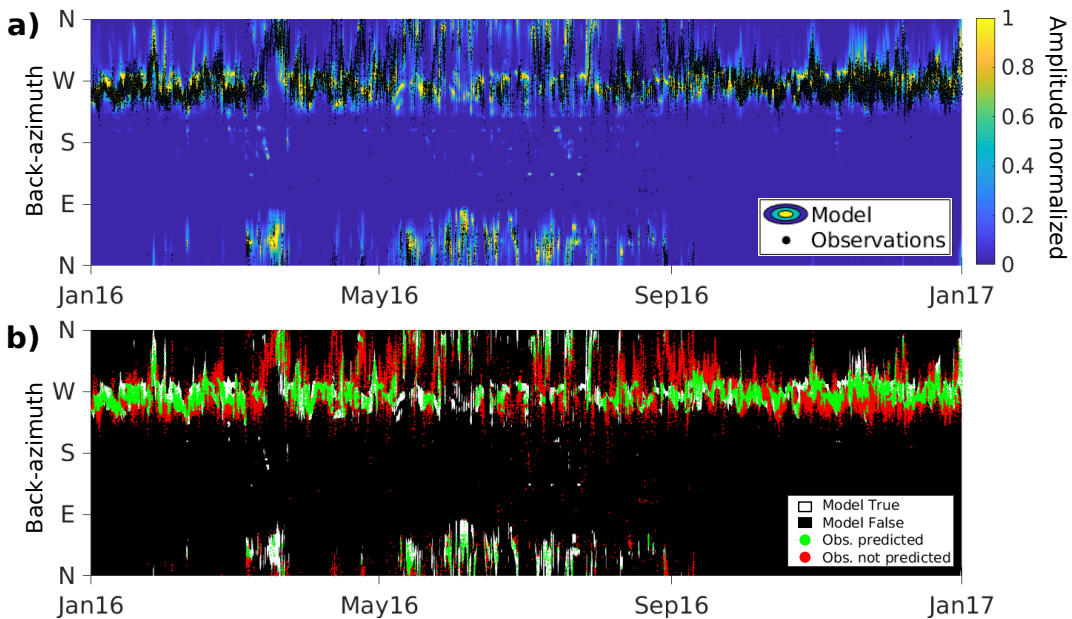
Figure 6.2 – Méthodologie de la comparaison entre le modèle - ici avec la configuration DC20, WindSta, REF102040 – et les détections, pour I37NO, Norvège dans la bande de fréquence [0.2-0.3] Hz. a) Répartition directionnelle de l'amplitude modélisée à la station (normalisée par pas de temps). Toutes les détections sont représentées par des points noirs. b) Après l'application du seuil - ici 0.4 - les détections sont classifiées en détections prédites (points verts) et non prédites (points rouges). Les directions pour lesquelles le modèle prédit des arrivées sont représentées en blanc, tandis que le noir représente les directions non favorables à la détection selon le modèle.

6.3 Chapitre 3 - Une approche unifiée de la génération des microbaroms

Le fait que les interactions de vagues de même fréquence et quasiment opposées génèrent des ondes acoustiques a été démontré pour les microséismes dans un premier temps, par Longuet-Higgins (1950) et K. Hasselmann (1963). À partir de ces interactions, deux théories principales ont été développées à propos de la génération de ces ondes acoustiques dans l'atmosphère, les microbaroms. Se plaçant dans un océan de profondeur infinie, Brekhovskikh et al. (1973) (abrégé BK73 dans la suite) ont calculé une source de microbaroms dont la valeur dépend de l'angle d'élévation. D'un autre côté, se plaçant aussi dans un océan de profondeur infinie, la sommation sur l'aire de la source a amené Waxler & Gilbert (2006) à considérer une source rayonnant de façon monopolaire. À la suite de cette étude, Waxler et al. (2007) (abrégé en W07 par la suite) ont inclus une profondeur finie à leur théorie afin de prendre en compte d'éventuelles résonances étant donné que la longueur d'onde de ces ondes acoustiques dans l'eau est proche de 7.5 km, correspondant à l'ordre de grandeur de la profondeur océanique (entre 0 et 10 km). Il a été montré, par (Smets, 2018) notamment, un impact important de la bathymétrie sur les sources de microbaroms modélisées par W07. Cet effet important de la bathymétrie résultant du rayonnement monopolaire de la source, la question de l'impact de la bathymétrie dans le cas d'un rayonnement non monopolaire se pose alors. Par conséquent, dans le cadre de cette thèse, les équations du modèle de source sont de nouveau développées afin d'étendre les théories précédentes à un effet combiné d'un océan de profondeur finie et un rayonnement non monopolaire.

Les développements présentés dans le Chapitre 3 ont fait l'objet d'une publication (De Carlo et al., 2020, abrégé par la suite en DC20)[1] qui discute l'inclusion de la bathymétrie dans la théorie ainsi qu'une source à rayonnement non monopolaire.

6.3.1 Résumé de De Carlo et al. 2020

Dans ce papier, la puissance des microbaroms émise s'écrit de façon générique :

$$P(f_s) = a\mathcal{H}(f) \int_0^{\frac{\pi}{2}} |R_a(\theta_a, h)|^2 d\theta_a$$

$$= a \int E(f, \theta) E(f, \theta + \pi) d\theta \int_0^{\frac{\pi}{2}} |\sin\theta_a \cos\theta_a R_a(\theta_a, h)|^2 d\theta_a \quad (6.3.2)$$

où f_s est la fréquence acoustique, f fréquence des vagues, θ la direction horizontale des vagues océaniques, a un facteur multiplicatif et R_a une fonction définie en fonction du modèle de source considéré - voir Tableau 6.1 - qui est susceptible de dépendre de θ_a l'angle d'élévation verticale et de h la profondeur d'eau. $\mathcal{H}(f)$ est l'équation d'Hasselmann définie à l'équation (1.12) et qui représente les interactions d'ordre 2 entre vagues presque opposées.

La Fig. 6.3 présente les valeurs de $R_a(\theta_a, h)$ pour les trois modèles : BK73, W07 et DC20. Sur la droite R_a est représenté en fonction de θ_a tel que formulé par BK73 dans un océan de profondeur infinie. En bas, la solution de W07 est représentée en fonction de la profondeur et des profondeurs de résonance sont clairement identifiables. En haut à gauche, les niveaux de couleur représentent R_a tel qu'obtenu par DC20 en fonction à la fois de θ_a et de h. On peut noter que le nouveau modèle est cohérent avec W07 - pour $\theta_a = 0$ - et BK73 - pour une profondeur infinie - et qu'il les réunifie.

Il peut être remarqué que, suivant la loi de Snell à l'interface océan-atmosphère, toutes les ondes acoustiques se propageant dans l'océan - où la vitesse du son α_w vaut environ 1500 m·s⁻¹ - sont émises dans l'atmosphère - où la vitesse du son α_a vaut autour de 330 m·s⁻¹ - dans un cône de $\arcsin(\alpha_a/\alpha_w) \sim 13°$ autour de la verticale. Ainsi, à l'exception des très faibles profondeurs, les angles de propagation atmosphériques proches de la verticale sont les seuls pour lesquels la bathymétrie peut avoir un effet. En effet, la Fig 6.3 montre que pour $\theta_a > 13°$ les résonances ne sont plus observées. Le seul effet résiduel de la profondeur d'eau est une faible diminution du coefficient pour les faibles profondeurs. Cependant, à l'échelle

---

[1]De Carlo, M., Ardhuin, F., Le Pichon, A. (2020). Atmospheric infrasound generation by ocean waves in finite depth : unified theory and application to radiation patterns. *Geophysical Journal International, 221*(1), 569-585. doi : 10.1093/gji/ggaa015

globale cet effet est minime étant donné que pour l'année 2018, le flux de microbaroms émis entre 20 et 90° (de la verticale) calculé sans prise en compte de la profondeur diffère de seulement 7 % de celui calculé avec le modèle complet.

De plus, les angles d'élévation des signaux reçus aux stations au sol sont globalement horizontaux - entre 0 et 40° de l'horizontale -, par conséquent, l'impact de la bathymétrie sur les signaux de microbaroms dépend fortement du type de rayonnement de la source.
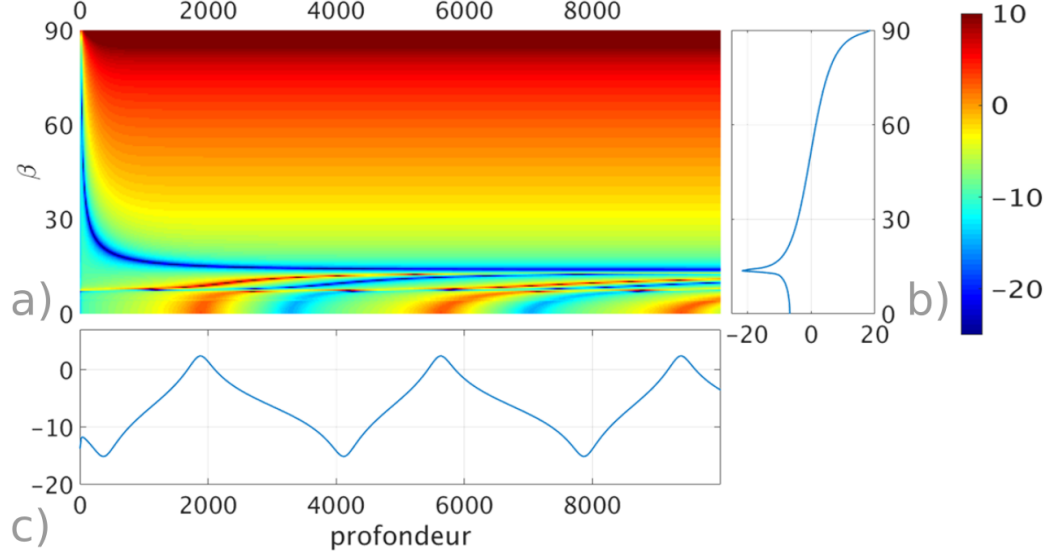
Figure 6.3 – Valeurs de R_a [log_{10}] pour les trois modèles étudiés : a) pour le modèle de DC20 avec un coefficient $R_a(\theta_a, h)$ dépendant de la profondeur et de l'angle d'élévation, b) pour le modèle développé par BK73 dans un océan de profondeur infinie avec un coefficient R_a dépendant de l'angle d'élévation et c) pour le modèle de W07 avec un coefficient $R_a(\theta_{a,0}, h)$ dépendant de la profondeur d'eau uniquement.

Table 6.1 – Résumé des formes de R_a en fonction des modèles de source.

Modèle	R_a	Dépend de θ_a	Profondeur finie	Equation dans DC20
BK73	$\int_0^{\frac{\pi}{2}} |R_a(\theta_a)|^2 d\theta_a$	✓	✗	eq. (3.39)
W07	$\int_0^{\frac{\pi}{2}} |R_a(\theta_{a,0}, h)|^2 d\theta_a = \frac{\pi}{2}|R_a(\theta_{a,0}, h)|^2$	✗	✓	eq. (3.44)
DC20	$\int_0^{\frac{\pi}{2}} |R_a(\theta_a, h)|^2 d\theta_a$	✓	✓	eq. (3.50)

6.3.2 Interprétation physique des termes de R_a et hommage à Brekhovskikh et al. (1973)

Afin de présenter le sens physique des différents termes réunis dans le terme R_a, nous nous intéressons à la valeur de R_a pour un océan de profondeur infinie. L'équation (3.39) s'écrit comme suit :

$$R_a(\theta_a) = \frac{\overbrace{l}^{①} - \overbrace{\delta_a}^{②} - \overbrace{\delta_a \left[1 - 2\sin^2\theta_a \left(1 - \frac{1}{2}\cos^2(\varphi_2 - \varphi)\right)\right]}^{③} + \overbrace{\delta_a n^2}^{④} - \overbrace{\frac{\delta_a}{4}n^2}^{⑤}}{\underbrace{\cos\theta_a}_{⑥} - \underbrace{\delta_a \cos\theta_a l/2}_{⑦} - \underbrace{\mathrm{i}\delta_a/4}_{⑧} - \underbrace{\mathrm{i}ml}_{⑨}}$$

$$(6.3.3)$$

117

où l est le nombre d'onde vertical dans l'eau sans prise en compte des corrections dues à la gravité, φ est l'azimut des vagues, et φ_2 est l'azimut horizontal de l'onde acoustique résultante. δ_a, n et m sont des petits nombres correspondant respectivement au rapport entre le nombre d'onde acoustique (dans l'air) et le nombre d'onde des vagues, au rapport entre les vitesses du son dans l'air et dans l'eau, et au rapport entre les masses volumiques de l'air et de l'eau.

Les différentes parties de l'équation (6.3.3) proviennent de :

① la continuité des vitesses à l'interface, et la différence de milieu (différence de vitesses du son) induisant la réfraction des ondes acoustiques. Ce terme correspond au nombre d'onde vertical acoustique dans l'océan sans correction due à la gravité ;

② la compressibilité de l'air - à travers la solution particulière et le terme de forçage au membre de droite de l'équation d'onde acoustique ;

③ l'advection de la surface libre par les vagues océaniques dans l'équation de continuité des vitesses : étant donné que la surface de l'eau n'est pas plate, le mouvement de l'onde n'est pas un simple "piston" qui transfère la vitesse de l'eau dans l'eau, et la vitesse d'un train de vagues advecte la pente d'un second train de vagues. Il s'agit de l'unique terme qui, pour des vagues presque opposées, dépend de l'azimut de l'onde acoustique résultante ;

④ la compressibilité de l'eau - à travers la solution particulière et le terme de forçage au membre de droite de l'équation d'onde acoustique ;

⑤ l'effet de la gravité sur l'équation d'onde acoustique dans l'eau, ajoutant un terme correctif au nombre d'onde vertical dans l'eau ;

⑥ la continuité des vitesses à l'interface, et la différence de milieu (différence de vitesses du son) induisant la réfraction des ondes acoustiques. Ce terme correspond au nombre d'onde vertical acoustique dans l'air sans correction due à la gravité. Il s'agit du terme dominant à l'exception des angles de propagation très rasants $\theta_a \to 90°$;

⑦ la pression hydrostatique et l'amplitude finie, provenant du développement de Taylor autour de $z = 0$ des conditions aux limites ;

⑧ l'effet de la gravité sur l'équation d'onde acoustique dans l'air, ajoutant un terme correctif au nombre d'onde vertical dans l'air ;

⑨ la rétroaction de la pression de l'air sur la pression de l'eau, qui ne peut pas être négligée pour des angles de propagation proches de l'horizontale.

Alors que ⑥ est le terme qui régit le profil général du rayonnement avec l'amplitude augmentant avec θ_a ; ⑧ et ⑨ permettent d'obtenir une solution finie quand $\theta_a \to 90°$. À l'exception du signe devant ⑨, cette équation est la même que celle obtenue par Brekhovskikh et al. (1973).

En considérant une profondeur d'océan h et en supprimant les termes négligeables en $\delta_a n^2$, on obtient (basé sur l'équation (3.50))

$$R_a(\theta_a, h) = \frac{-①R - Q\left[② + ③\right]}{Q\left(⑥ - ⑧\right) + R\left(⑦ + ⑨\right)} \tag{6.3.4}$$

où $R = \sinh(\mu h) + r\cosh(\mu h)$ et $Q = \cosh(\mu h) + r\sinh(\mu h)$ sont les coefficients qui apparaissent en raison des conditions aux limites à l'interface entre l'océan et la croûte terrestre - continuité des vitesses et contraintes tangentielles nulles -, avec μ le nombre d'onde vertical complexe dans l'océan (μ correspond à l avec le terme correctif de gravité) et r le coefficient de réflexion au fond de l'océan.

Les différences entre les équations (6.3.3) et (6.3.4) impactent uniquement les angles quasiment verticaux $\theta_a < 13°$, et les profondeurs en dessous de 1000 m pour des angles supérieurs à 13°. Ainsi, le rayonnement acoustique des microbaroms obtenu par Brekhovskikh et al. (1973) était une bonne approximation du rayonnement acoustique total (même en incluant les effets de la bathymétrie). Bien que très approfondi, le travail de ces auteurs est relativement difficile à lire et à comprendre étant donné qu'ils y redéveloppaient toutes les équations de Longuet-Higgins (1950) pour l'air, tout en donnant beaucoup moins de détails. Par conséquent, ce travail fondamental n'a jamais été suffisament compris et a été majoritairement laissé de côté par la communauté.

6.3.3 Principale différence avec Waxler et al. (2007)

Le résultat de Waxler & Gilbert (2006) présente quelques différences avec l'équation (6.3.3). Premièrement, les auteurs n'ont pas pris en compte les effets de la gravité, ainsi seule la moitié de ③ est considérée. Deuxièmement, θ_a a été pris égal à zéro, ce qui simplifie ③ en $\delta_a/2$, ⑥ en 1 et ⑦ en $\delta_a l/2$. Comme l'ordre dominant du dénominateur ⑥ ne tend plus vers zéro, les auteurs ont tronqués les termes de plus petits ordre de grandeur, supprimant ainsi ④, ⑤, ⑦, ⑧ et ⑨.

Le modèle de Waxler et al. (2007) est basé sur les simplifications de WG06 et il apparaît que le principal désaccord entre W07 (basé sur WG06) et DC20 repose sur la considération d'un rayonnement de source monopolaire par W07-WG06 tel que $\theta_a = 0$. En réalité, WG06 n'ont pas déclaré gratuitement que leur source était monopolaire, il s'agit d'un résultat qui apparaît lors de la simplification du problème pour les propagations longue distance. Ils se sont intéressés à la puissance P_r^2 reçue par un capteur positionné en x. Étant donné que la pression $P_r(x)$ correspond à l'intégrale surfacique de l'amplitude de la source multipliée par la fonction de Green - fonction représentant la propagation -, le spectre de puissance s'écrit[2] :

$$P_r^2(x) = \iint_S \iint_S \langle G(x,y)G^*(x,y') \rangle |R_a(\theta_a,h)|^2 e^{i\theta_a(y-y')} \mathrm{d}y \mathrm{d}y' \tag{6.3.5}$$

Puis, étant donné que la source est petite par rapport à la distance entre la source et le récepteur, ils ont considéré que la propagation était la même pour tous les points et que la fonction de Green ne variait pas à l'intérieur de la source. Il en résulte que l'intégrale sur y' génère une fonction de Dirac de θ_a - ainsi le seul angle restant serait l'angle vertical :

$$P_r^2(x) = \iint_S \langle G(x,y)G^*(x,y') \rangle |R_a(\theta_a,h)|^2 \iint_S e^{i\theta_a(y-y')} \mathrm{d}y' \mathrm{d}y \tag{6.3.6}$$

$$P_r^2(x) = \iint_S \langle G(x,y)G^*(x,y') \rangle |R_a(\theta_a,h)|^2 \delta(\theta_a) \mathrm{d}y \tag{6.3.7}$$

Le fait de considérer la fonction de Green comme constante sur la source semble être cohérent avec le fait que la source soit suffisament petite pour que les variations ne soient pas importantes. Cependant, en considérant la fonction de Green constante, n'importe quel déphasage entre les différents points sources est négligé. D'un point de vue technique, la fonction de Green qu'ils utilisent plus loin dans leur article contient un terme de phase qui peut être factorisé de façon à obtenir :

$$G(x,y)G*(x,y') = \tilde{G}(x,y)\tilde{G}^*(x,y)e^{i\theta_a(y'-y)} \tag{6.3.8}$$

Avec $\tilde{G}$ la fonction de Green sans le terme d'exponentielle. Puis, en utilisant l'équation (6.3.5), il vient :

$$P_r^2(x) = \iint_S \iint_S \langle \tilde{G}(x,y)\tilde{G}^*(x,y) \rangle e^{i\theta_a(y'-y)} |R_a(\theta_a,h)|^2 e^{i\theta_a(y-y')} \mathrm{d}y \mathrm{d}y' \tag{6.3.9}$$

Et

$$P_r^2(x) = \iint_S \iint_S \langle \tilde{G}(x,y)\tilde{G}^*(x,y) \rangle |R_a(\theta_a,h)|^2 \mathrm{d}y \mathrm{d}y' \tag{6.3.10}$$

---

[2]N.B : Les notations ont été simplifiées dans un souci de compréhension.

Et donc, l'hypothèse amenant $\theta_a = 0$ - et un rayonnement monopolaire - disparaît.

6.4 Chapitre 4 - Résultats de la modélisation globale et validation du modèle de sources

6.4.1 Introduction et cadre de l'étude

Le chapitre 4 présente une application du modèle global d'arrivées de microbaroms présenté au Chapitre 2, avec le modèle de source développé au Chapitre 3 (noté DC20). L'objectif principal de ce chapitre est de valider le nouveau modèle de source à travers des comparaisons systématiques entre les microbaroms modélisés et les observations grâce au Coefficient des Observations Prédites (CPO) défini au Chapitre 2, eq. (2.6).

La base de données d'observations pour cette étude globale est constituée des détections de la base de données SSI retraitée (Ceranna et al., 2019) réalisées dans la bande de fréquence [0.1 - 0.6] Hz entre 2012 et 2018. Tandis que fin 2018 le réseau infrason du SSI comportait 51 stations certifiées, seules 45 l'étaient déjà en 2012. Les résultats généraux sont présentés pour les 45 stations ayant fourni des observations sur l'ensemble de la période considérée.

La modélisation globale et la comparaison avec les observations sont aussi calculées avec le modèle de source développé par Waxler et al. (2007) (W07) et largement utilisé dans la communauté. Les capacités des deux configurations à représenter les observations sont ensuite comparées (via le CPO) afin de déterminer la pertinence et l'intérêt du nouveau modèle de source.

Comme évoqué dans le Chapitre 2, l'impact de la prise en compte du vent et celui de l'intégration de la réflexion côtière dans le modèle de vagues sont aussi étudiés. Par conséquent, la modélisation globale est calculée pour huit ($= 2^3$) configurations définies par 3 paramètres et leurs valeurs possibles :

- Paramètre de réflexion côtière i_1 :

    - **NOREF :** le modèle de vagues n'inclut aucune réflexion côtière ;

    - **REF102040 :** le modèle de vagues considère une réflexion côtière maximale.

- Paramètre de vent i_2 :

    - **NoWind :** $V_{\text{eff-ratio}} = 1$, ainsi aucune direction de propagation n'est favorisée ;

    - **WindSta :** $V_{\text{eff-ratio}}$ est considéré à la station.

- Modèle de source i_3 :

    - **DC20 :** modèle de source développé par De Carlo et al. (2020) (voir section 6.3) ;

    - **W07 :** modèle de source développé par Waxler et al. (2007).

Pour chaque configuration, la modélisation est calculée pour 45 stations, pendant sept ans (de 2012 à 2018).
Le calcul du CPO permet de quantifier la capacité de la modélisation (pour une configuration donnée) à prédire les observations. Comme le CPO est calculé sur un mois, sa valeur $\text{CPO}(i_1, i_2, i_3, i_4, i_5, i_6, i_7)$ dépend de sept paramètres i_1 à i_7, parmi lesquels trois - i_1, i_2 et i_3 - sont les paramètres de modélisation correspondant aux huit configurations. Les paramètres restants i_4, i_5, i_6 et i_7 représentent respectivement la bande de fréquence, le mois, l'année et la station SSI pour lesquels le CPO est calculé. En considérant tous ces paramètres, on obtient en tout 151 200 valeurs de CPO.

6.4.2 Principaux résultats

Les variations du CPO en fonctions des paramètres de sortie i_4, i_5, i_6 et i_7 sont présentées en Fig. 6.4 pour les huit configurations.
La Fig. 6.4a représente les variations de CPO en fonction des différentes stations du SSI, ordonnées par latitudes. Les Fig. 6.4b et Fig. 6.4d montrent les variations mensuelles du CPO pour l'Hémisphère Nord (abrégé HN dans la suite) et l'Hémisphère Sud (abrégé HS dans la suite) respectivement. La Fig. 6.4c représente les variation du CPO avec la fréquence tandis que la Fig. 6.4e montre la variation annuelle du CPO. Deux principales observations peuvent
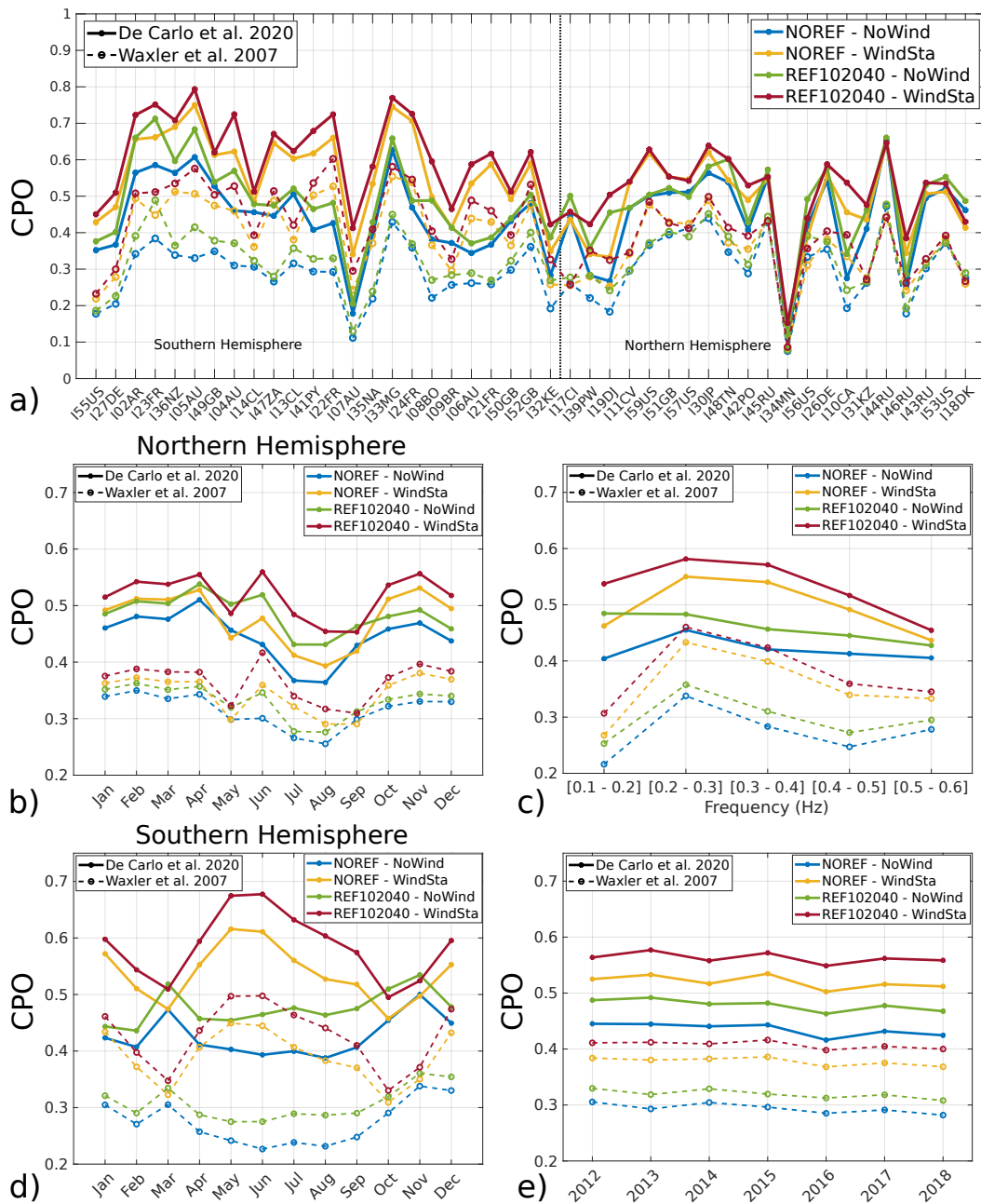
Figure 6.4 – Variations du CPO en fonction des paramètres de sortie - stations, mois, années et fréquences - pour les huit configurations. Les traits pleins représentent les configurations avec le modèle de source DC20 tandis que les lignes pointillées correspondent aux configurations avec le modèle de source W07. Les configurations avec les valeurs NOREF-NoWind, NOREF-WindSta, REF102040-NoWind et REF102040-WindSta sont respectivement représentées en bleu, jaune, vert et rouge. a) Variations en fonction des 45 stations du SSI certifiées en 2012. b) Variations mensuelles pour les stations de l'Hémisphère Nord. c) Variations en fonction de la fréquence. d) Variations mensuelles pour les stations de l'Hémisphère Sud. e) Variations en fonction de l'année.

être réalisées. Premièrement, pour tous ces paramètres, la configuration avec REF102040, WindSta et DC20 est celle qui donne la plus grande valeur de CPO dans la plus grande majorité des cas - exception faite pour un mois et 6 stations - et la deuxième meilleure configuration est généralement celle avec NOREF, WindSta et DC20. Deuxièmement, dans la majorité des cas, il y a une différence de CPO d'environ 0.15 point entre les configurations

avec le modèle de source DC20 (représentées en traits pleins) et celles avec le modèle de source W07 (représentées en pointillés).

Pour la configuration REF102040 - WindSta - DC20 le CPO varie en fonction des stations entre 0.15 (à I34MN, Mongolie) et 0.8 (à I05AU, Australie). Pour 34 des 45 stations, plus de la moitié des observations sont prédites en utilisant cette configuration (CPO $\geqslant$ 0.5), et pour huit de ces stations le CPO dépasse 0.7. Par comparaison, le plus faible CPO est généralement obtenu avec la configuration NOREF-NoWind-W07 avec un CPO variant de 0.07 (à I34MN) à 0.47 (à I44RU, Russie).

Les variations mensuelles du CPO varient selon l'hémisphère : dans l'HN, tel que montré en Fig. 6.4b, les variations sont similaires pour les huit configurations tandis que dans l'HS, tel que présenté en Fig. 6.4d, le motif de variation dépend principalement de la prise en compte du vent ou non. Dans l'HN, pour chaque configuration, le CPO décroît de moins de 0.1 point de CPO durant l'été et est globalement stable le reste du temps. Cette décroissance serait liée au fait que les sources sont plus dispersées spatialement en été dans l'HN, par opposition aux sources hivernales bien établies (notament au sud-est de l'Islande). On peut aussi noter que les configurations prenant en considération le vent à la station sont meilleures que leurs équivalents sans vent d'environ 0.025-0.05 point, à l'exception des mois d'avril, mai et septembre, où les deux configurations ont des valeurs de CPO similaires. Ces mois correspondent à un impact du vent moins important probablement lié à une mauvaise modélisation atmosphérique durant le renversement des vents stratosphériques saisonniers dans l'HN.
Dans l'HS, les configurations avec NoWind ont un CPO presque constant le long des mois, avec une très légere amélioration en mars, octobre et novembre. Au contraire, les configurations avec WindSta présentent des variations saisonnières de CPO d'environ 0.1 point, avec un maximum principal pendant l'hiver local en juin, où les configurations WindSta sont meilleures que les configurations NoWind d'environ 0.2 point. Ces variations présentent aussi un maximum secondaire pendant l'été local en décembre, avec des configurations WindSta meilleures que celles avec NoWind d'environ 0.1-0.15 point, et des minimums en mars et octobre, où, au contraire, les configurations NoWind sont très légèrement meilleures que les configurations WindSta. Ces variations sont vraisemblablement liées à la présence, dans l'HS, de sources relativement importantes toute l'année et dans toutes les directions. Leur détection et leur modélisation dépendent fortement de la propagation, qui s'avère être très sensible aux variations de vents quand le guide d'onde est instable pendant les équinoxes.

La Fig. 6.4c, représentant les variations de CPO en fonction de la fréquence, montre des valeurs de CPO plus importantes pour les bandes de fréquence [0.2 - 0.3] Hz et [0.3 - 0.4] Hz. Pour les configurations avec le modèle de source W07 - représentées en pointillés - les moins bonnes valeurs de CPO sont obtenues pour les plus basses fréquences [0.1 - 0.2] Hz tandis que pour les configurations avec DC20, les moins bonnes valeurs de CPO sont obtenues pour les plus hautes fréquences [0.5 - 0.6] Hz. Les configurations avec WindSta - représentées en rouge et jaune - présentent des valeurs de CPO plus élevées que leurs équivalents avec NoWind - en bleu et vert - avec une différence de CPO variant entre 0.025 et 0.1 point, avec des différences plus importantes pour les fréquences médianes [0.2 - 0.5] Hz. On peut aussi remarquer que pour la bande de fréquence [0.1 - 0.2] Hz, avec le modèle de source DC20, la réflexion côtière montre un léger impact étant donné que les deux configurations avec REF102040 - en rouge et vert - ont des valeurs de CPO plus élevées que les deux configurations avec NOREF.

La Fig. 6.4e montre que les valeurs du CPO sont quasiment constantes en fonction des années et ce pour chaque configuration, il n'y a donc a priori aucune variation annuelle.

6.4.3   Conclusions du chapitre

La modélisation globale présentée dans le Chapitre 2 a été appliquée pour huit ($=2^3$) configurations, sur sept années de 2012 à 2018. À travers le CPO, les comparaisons entre les résultats de la modélisation et les observations détectées aux stations du réseau SSI ont permis de tirer les conclusions suivantes :

- La meilleure configuration (parmi celles testées) est celle avec REF102040, WindSta et DC20.

- Le modèle de source développé au Chapitre 3 est ainsi validé et présente une amélioration certaine comparé au modèle de source existant (W07) lorsque la distribution directionnelle de l'énergie acoustique est considérée.

- L'impact de la paramétrisation du vent est plus facilement mis en évidence lorsqu'on compare uniquement le signal dominant, où la configuration avec WindSta prévaut. (cf. Chapitre 4)

- L'impact du paramètre de réflexion côtière est principalement restreint aux basses fréquences, où la configuration avec REF102040 est clairement meilleure.

- La capacité de prédire les arrivées de microbaroms est influencée par la saison, principalement lorsque les vents sont considérés.

- Le CPO est très variable entre les stations, par conséquent, la capacité de modélisation des microbaroms est vraisemblablement liée à la situation géographique propre à chaque station.

6.5 Conclusions

6.5.1 Un catalogue global de modèle de microbaroms

Dans cette thèse, on a élaboré une méthode pour prédire les arrivées de microbaroms à l'échelle globale ainsi qu'une métrique pour quantifier l'accord entre ces prédictions et les observations. Cette quantification a été ensuite appliquée pour comparer une base de données d'observations détectées par le SSI durant sept ans avec les résultats de la modélisation globale pour huit configurations. Ce qui a ainsi permis d'évaluer cette modélisation globale et de déterminer la meilleure des huit configurations.

La modélisation globale inclut un modèle de vagues, un modèle de source - transformant les vagues en ondes acoustiques émises dans l'atmosphère - et un modèle de propagation. Chacun de ces composant a fait l'objet d'une analyse particulière afin de déterminer la meilleure configuration pour la modélisation.

Pour le modèle de vagues, afin d'évaluer l'intérêt, pour les microbaroms, d'inclure la réflexion côtière dans le modèle d'action de vagues, la modélisation globale est calculée avec deux configurations pour le modèle d'action de vagues WW3 : une sans aucune réflexion à la côte (NOREF) et l'autre avec une réflexion à la côte maximale (REF102040).

Le développement d'un nouveau modèle de source est une des contributions majeures de cette thèse et a été présenté au Chapitre 3 de façon à unifier les théories existantes en prenant en compte à la fois la bathymétrie et un rayonnement non monopolaire dans l'atmosphère (De Carlo et al., 2020, abrégé en DC20). Dans cet article et dans cette thèse, on a tout particulièrement exploré et explicité la théorie de Brekhovskikh et al. (1973) qui n'avait pas été appréciée à sa juste valeur par la communauté scientifique, probablement à cause d'une dérivation trop peu détaillée, d'un manque d'illustrations et, jusqu'à présent, d'aucune validation. Dans toutes les applications des chapitres suivants, le modèle de source DC20 est pratiquement le même que celui de Brekhovskikh et al. (1973), et leurs travaux méritent d'être pleinement reconnus. L'impact de la bathymétrie sur les microbaroms émis est limité à des angles très proches de la verticale - où l'impact est fort - avec un impact quasiment nul pour des angles supérieurs à 13° (par rapport à la verticale). D'un autre côté, la théorie développée par Waxler et al. (2007, abrégé W07), largement utilisée par la communauté, considère des microbaroms qui rayonnent de façon monopolaire et pour qui, par conséquent, le fort impact de la bathymétrie est présent pour tous les angles. Étant donné que les stations au sol reçoivent principalement du signal compris entre 40° et 90° par rapport à la verticale, la différence d'impact de la bathymétrie entre les modèles DC20 et W07 est importante. Ainsi, afin de tester la validité d'un rayonnement non monopolaire, les capacités du nouveau modèle de source à prédire les observations ont été testées et comparées au modèle actuellement largement utilisé, en modélisant les arrivées avec les deux modèles de source.

Pour prendre en compte la propagation infrason, une loi d'atténuation obtenue dans une atmosphère horizontalement uniforme est considérée. L'atmosphère horizontalement uniforme est représentée par $V_{\text{eff}-\text{ratio}}$, le rapport de la célérité stratosphérique (à 50 km) effective sur la célérité au sol. Pour mettre en évidence l'effet des vents stratosphériques sur les arrivées de microbaroms prédites, la modélisation a été calculée pour deux configurations pour la propagation : dans un cas, $V_{\text{eff}-\text{ratio}}$ est une constante égale à 1 afin qu'aucune direction ne soit favoriser par le vent (NoWind), tandis que dans l'autre cas, $V_{\text{eff}-\text{ratio}}$ est calculé en prenant les caractéristiques de l'atmosphère à la stations (WindSta), afin de prendre en compte la capacité de la station à recevoir un signal acoustique via le guide stratosphérique.

D'autres quantités ont été fixées par hypothèse pour la modélisation globale des microbaroms et la quantification de l'accord entre les observations et le modèle :

— Les sources ont été considérées jusqu'à une certaine distance dist_{max} de la station, avec dist_{max} choisi égal à 5000 km afin the prendre en compte les sources contribuant le plus, tout en évitant de trop extrapoler la loi d'atténuation - qui n'avait été définie que jusqu'à 3000 km (Le Pichon et al., 2012).

— Les résultats du modèles tout comme les observations ont été réunis dans des bandes de fréquence de largeur 0.1 Hz, afin de permettre une bonne comparaison tout en

réduisant la taille des fichiers de sortie. Cela permet en effet de restreindre le nombre de bandes de fréquence de 22 à 5, diminuant considérablement le temps de calcul.

— La métrique du CPO (Coefficient des Observations Prédites), qui a été utilisée pour comparer les résultats de la modélisation et les observations et qui prend ses valeurs entre 0 et 1, considère un modèle binaire qui prédit (ou non) une arrivée de microbarom dans une direction pour un certain temps et une certaine fréquence. À partir de ce modèle binaire, les observations sont classifiées en deux catégories : les observations prédites et les observations non prédites, et le rapport des observations prédites sur l'ensemble des observations est le rapport CPO d'intérêt. Le seuil utilisé pour la binarisation du modèle de source est fixé à 0.4, afin d'avoir un bon compromis entre les observations prédites et les faux positifs.

— La métrique du CPO est calculée sur une période d'un mois.

6.5.2 Résultats de la modélisation globale

La modélisation a été calculée pour huit ($=2^3$) configurations, sur sept années de 2012 à 2018 et pour les 51 stations certifiées en 2018[3]. Les comparaisons avec les observations détectées par les stations du SSI permettent de tirer les conclusions suivantes :

- **La meilleure des huit configurations est celle avec REF102040, WindSta et DC20**. La valeur du CPO est en effet plus grande pour les configurations avec réflexion à la côte (REF102040) que pour celles sans réflexion à la côte (NOREF) dans 62% des cas. Les configurations considérant le vent à la station (WindSta) présentent une valeur de CPO plus grande que les configurations sans vent dans 68% des cas. Et les configurations avec le modèle de source de DC20 sont meilleures que celles avec le modèle de source W07 dans 94% des cas.

- **Le paramètre de modèle de source est celui qui présente le plus fort impact sur le CPO.** Le paramètre avec le deuxième plus fort impact est celui du vent, et son impact dépend de la saison. Le paramètre de réflexion côtière n'a qu'un faible impact sur le CPO, et uniquement sur les basses fréquences.

- **Le paramètre de vent a un fort impact sur les comparaisons du signal dominant.** En effet, lorsqu'on compare seulement les directions des signaux dominants modélisés et observés, la principale différence entre les configurations est liée au paramètre de vent, étant donné que la prise en compte du vent à la station (WindSta) permet de représenter les variations saisonnières de l'azimut dominant. La définition de la configuration NoWind, permettant une propagation égale pour toutes les directions, combinée à l'application du seuil - pour la mise en place du CPO - conduit les configurations NoWind à prédire plus d'arrivées de microbaroms que les configurations WindSta. Par conséquent, les configurations NoWind génèrent plus de faux positifs que les configurations WindSta. Ceci explique pourquoi les différences de CPO ne sont pas plus prononcées entre NoWind et WindSta, alors que l'importance de prendre en compte le vent est connue et établie ne serait-ce qu'en considérant le signal dominant.

- **Les capacités de modélisation sont impactées par la saison (variations de 0.1 à 0.15 point de CPO), mais aucune variation notable n'est observée au cours des années.** L'évolution saisonnière du CPO - caractérisée par une variation d'amplitude 0.1 à 0.15 point de CPO - est à la fois un effet de source, le CPO est plus élevé quand les sources sont plus fortes car celles-ci génèrent plus de détections dans la même direction, et un effet du vent puisque le CPO est plus grand quand les vents zonaux sont bien établis, principalement dans l'HS.

- **Les capacités de modélisation présentent des variations d'environ 0.1 point de CPO avec la fréquence.** Les bandes de fréquences avec le CPO le plus élevé sont [0.2 - 0.3] Hz et [0.3 - 0.4] Hz. La dépendance fréquentielle pourrait être reliée de façon égale à une mauvaise résolution directionnelle du modèle d'action de vagues en haute fréquences, et à des limitations d'observations en basse fréquence.

---

[3]N.B : dans la section précédente, par simplicité, on a présenté uniquement les résultats pour les 45 stations qui étaient certifiées en 2012 mais la modélisation a été réalisé pour les 51 stations.

- **Le CPO présente de fortes variations, autour de 0.6 point de CPO, en fonction des différentes stations, avec de bons résultats : 39 des 51 stations présentent un CPO $\geqslant$ 0.5.** Les valeurs du CPO vont de 0.18 à I34MN, à 0.79 à I05AU, pour la meilleure configuration, avec des valeurs supérieures à 0.5 pour 39 stations, soit plus de la moitié des observations sont prédites par le modèle pour ces stations. Parmi ces 39 stations, 10 ont même un CPO supérieur à 0.7. Cette variation en fonction des stations des capacités des modélisation à prédire les microbaroms observés est liée à la situation géographique de chaque station, ses capacités de détection et incertitudes. Pour les stations très éloignées des sources dominantes telles que I34MN et I44RU, avec des gammes de propagation supérieures à 4 000 km voire 5 000 km, le mauvais accord entre observations et modèle est principalement dû à la fixation d'un $\text{dist}_{\max}$ restrictif et à des incertitudes dans la loi d'atténuation, d'autant plus que l'hypothèse d'atmophère horizontallement uniforme peut être invalidée au delà d'une certaine distance.

REFERENCES

Airy, G. B. (1841). Tides and waves. In H. J. R. et al. (Ed.), *Encyclopedia metropolitana (1817–1845)*. London.

Amezcua, J., Näsholm, S. P., Blixt, E. M., & Charlton-Perez, A. J. (2020). Assimilation of atmospheric infrasound data to constrain tropospheric and stratospheric winds. *Quarterly Journal of the Royal Meteorological Society*.

Ardhuin, F. (2019). *Ocean waves in geosciences.* doi: 10.13140/RG.2.2.16019.78888/5

Ardhuin, F., Balanche, A., Stutzmann, E., & Obrebski, M. (2012). From seismic noise to ocean wave parameters: General methods and validation. *Journal of Geophysical Research: Oceans*, *117*(C5). Retrieved from https://agupubs.onlinelibrary.wiley.com/doi/abs/10.1029/2011JC007449 doi: 10.1029/2011JC007449

Ardhuin, F., Gualtieri, L., & Stutzmann, E. (2015). How ocean waves rock the earth: two mechanisms explain seismic noise with periods 3 to 300 s. *Geophys. Res. Lett.*, *42*, 765–772. doi: 10.1002/2014GL062782

Ardhuin, F., Gualtieri, L., & Stutzmann, E. (2019). Physics of ambient noise generation by ocean waves. In N. Nakata, L. Gualtieri, & A. Fichtner (Eds.), *Surface waves and fluxes.* Cambridge University Press.

Ardhuin, F., & Herbers, T. H. C. (2013). Noise generation in the solid earth, oceans and atmosphere, from nonlinear interacting surface gravity waves in finite depth. *J. Fluid Mech.*, *716*, 316–348. doi: 10.1017/jfm.2012.548

Ardhuin, F., Lavanant, T., Obrebski, M., Marié, L., Royer, J.-Y., d'Eu, J.-F., ... Aucan, J. (2013). A numerical model for ocean ultra low frequency noise: wave-generated acoustic-gravity and Rayleigh modes. *J. Acoust. Soc. Amer.*, *134*(4), 3242–3259.

Ardhuin, F., Rawat, A., & Aucan, J. (2014). A numerical model for free infragravity waves: Definition and validation at regional and global scales. *Ocean Modelling*, *77*, 20–32. doi: 10.1016/j.ocemod.2014.02.006

Ardhuin, F., & Roland, A. (2012). Coastal wave reflection, directional spreading, and seismo-acoustic noise sources. *J. Geophys. Res.*, *117*, C00J20. doi: 10.1029/2011JC007832

Ardhuin, F., Stutzmann, E., Schimmel, M., & Mangeney, A. (2011). Ocean wave sources of seismic noise. *Journal of Geophysical Research: Oceans*, *116*(C9). Retrieved from https://agupubs.onlinelibrary.wiley.com/doi/abs/10.1029/2011JC006952 doi: 10.1029/2011JC006952

Arendt, S., & Fritts, D. C. (2000). Acoustic radiation by ocean surface waves. *J. Fluid Mech.*, *415*, 1–21.

Assink, J., Le Pichon, A., Blanc, E., Kallel, M., & Khemiri, L. (2014). Evaluation of wind and temperature profiles from ecmwf analysis on two hemispheres using volcanic infrasound. *Journal of Geophysical Research: Atmospheres*, *119*(14), 8659–8683.

Baird, H., & Banwell, C. (1940). Recording of air-pressure oscillations associated with microseisms at christchurch. *NZJ Sci. Technol., Sect. B*, *21*, 314–329.

Bauer, P., Thorpe, A., & Brunet, G. (2015). The quiet revolution of numerical weather prediction. *Nature*, *525*(7567), 47–55. doi: https://doi.org/10.1038/nature14956

Benioff, H., & Gutenberg, B. (1939). Waves anc currents recorded by electromagnetic barographs. *Bull. Seismol. Soc. Am.*, *20*(10), 421–426. doi: 10.1175/1520-0477-20.10.421

Blanc, E., Ceranna, L., Hauchecorne, A., Charlton-Perez, A., Marchetti, E., Evers, L. G., ... others (2018). Toward an improved representation of middle atmospheric dynamics thanks to the arise project. *Surveys in geophysics*, *39*(2), 171–225.

Blanc, E., Pol, K., Le Pichon, A., Hauchecorne, A., Keckhut, P., Baumgarten, G., ... Smets, P. (2019). Middle atmosphere variability and model uncertainties as investigated in the framework of the arise project. In A. Le Pichon, E. Blanc, & A. Hauchecorne (Eds.), *Infrasound monitoring for atmospheric studies: Challenges in middle atmosphere dynamics and societal benefits* (pp. 845–887). Cham: Springer International Publishing. Retrieved from https://doi.org/10.1007/978-3-319-75140-5_28 doi: 10.1007/978-3-319-75140-5_28

Blom, P. (2019). Modeling infrasonic propagation through a spherical atmospheric layer—analysis of the stratospheric pair. *The Journal of the Acoustical Society of America*, *145*(4), 2198-2208. doi: 10.1121/1.5096855

Bowman, D. C., & Lees, J. M. (2018). Upper atmosphere heating from ocean-generated acoustic wave energy. *Geophys. Res. Lett.*, *45*, 5144–5150. doi: 10.1029/2018GL077737

Brachet, N., Brown, D., Le Bras, R., Cansi, Y., Mialle, P., & Coyne, J. (2010). Monitoring the earth's atmosphere with the global ims infrasound network. In A. Le Pichon, E. Blanc, & A. Hauchecorne (Eds.), *Infrasound monitoring for atmospheric studies* (pp. 77–118). Dordrecht: Springer Netherlands. Retrieved from https://doi.org/10.1007/978-1-4020-9508-5_3 doi: 10.1007/978-1-4020-9508-5_3

Brekhovskikh, L. M., Goncharov, V. V., Kurtepov, V. M., & Naugolnykh, K. A. (1973). The radiation of infrasound into the atmosphere by surface waves in the ocean. *Izv. Atmos. Ocean. Phys.*, *9*, 899–907 (In the English translation, 511-515.).

Bromirski, P. D., Flick, R. E., & Graham, N. (1999). Ocean wave height determined from inland seismometer data: implications for investigating wave climate changes in the NE Pacific. *J. Geophys. Res.*, *104*(C9), 20753–20766.

Cansi, Y. (1995). An automatic seismic event processing for detection and location: The p.m.c.c. method. *Geophysical Research Letters*, *22*(9), 1021-1024. Retrieved from https://agupubs.onlinelibrary.wiley.com/doi/abs/10.1029/95GL00468 doi: 10.1029/95GL00468

Cansi, Y., & Le Pichon, A. (2008). Infrasound event detection using the progressive multi-channel correlation algorithm. In D. Havelock, S. Kuwano, & M. Vorländer (Eds.), *Handbook of signal processing in acoustics* (pp. 1425–1435). New York, NY: Springer New York. Retrieved from https://doi.org/10.1007/978-0-387-30441-0_77 doi: 10.1007/978-0-387-30441-0_77

Ceranna, L., Le Pichon, A., Green, D. N., & Mialle, P. (2009, 05). The Buncefield explosion: A benchmark for infrasound analysis across Central Europe. *Geophysical Journal International*, *177*(2), 491-508. Retrieved from https://doi.org/10.1111/j.1365-246X.2008.03998.x doi: 10.1111/j.1365-246X.2008.03998.x

Ceranna, L., Matoza, R., Hupe, P., Le Pichon, A., & Landès, M. (2019). Systematic array processing of a decade of global ims infrasound data. In *Infrasound monitoring for atmospheric studies* (pp. 471–482). Springer.

Charlton-Perez, A. J., Baldwin, M. P., Birner, T., Black, R. X., Butler, A. H., Calvo, N., . . . Watanabe, S. (2013). On the lack of stratospheric dynamical variability in low-top versions of the cmip5 models. *Journal of Geophysical Research: Atmospheres*, *118*(6), 2494-2505. Retrieved from https://agupubs.onlinelibrary.wiley.com/doi/abs/10.1002/jgrd.50125 doi: 10.1002/jgrd.50125

Charlton-Perez, A. J., Polvani, L. M., Perlwitz, J., Sassi, F., Manzini, E., Shibata, K., . . . Rind, D. (2007, 02). A New Look at Stratospheric Sudden Warmings. Part II: Evaluation of Numerical Model Simulations. *Journal of Climate*, *20*(3), 470-488. Retrieved from https://doi.org/10.1175/JCLI3994.1 doi: 10.1175/JCLI3994.1

Cox, C. S., & Jacobs, D. C. (1989). Cartesian diver observations of double frequency pressure fluctuations in the upper levels of the ocean. *Geophys. Res. Lett.*, *16*(8), 807–810.

Daniels, F. B. (1952). Acoustical energy generated by the ocean waves. *The Journal of the Acoustical Society of America*, *24*(1), 83-83. doi: 10.1121/1.1906855

Daniels, F. B. (1953). The mechanism of generation of infrasound by the ocean waves. *The Journal of the Acoustical Society of America*, *25*(4), 796-796. doi: 10.1121/1.1907180

Daniels, F. B. (1962). Generation of infrasound by ocean waves. *The Journal of the Acoustical Society of America*, *34*(3), 352-353. doi: 10.1121/1.1928128

Davies, D., Kelly, E., & Filson, J. (1971). Vespa process for analysis of seismic signals. *Nature Physical Science*, *232*(27), 8–13.

de Groot-Hedlin, C. D., & Hedlin, M. A. (2014). Infrasound detection of the chelyabinsk meteor at the usarray. *Earth and Planetary Science Letters*, *402*, 337 - 345. (Special issue on USArray science) doi: https://doi.org/10.1016/j.epsl.2014.01.031

De Carlo, M., Ardhuin, F., & Le Pichon, A. (2020). Atmospheric infrasound generation by ocean waves in finite depth: unified theory and application to radiation patterns. *Geophysical Journal International*, *221*(1), 569-585. Retrieved from https://doi

`.org/10.1093/gji/ggaa015` doi: 10.1093/gji/ggaa015

De Carlo, M., Hupe, P., Le Pichon, A., Ceranna, L., & Ardhuin, F. (2021). Global microbarom patterns: A first confirmation of the theory for source and propagation. *Geophysical Research Letters*, *48*(3), e2020GL090163. Retrieved from `https://agupubs.onlinelibrary.wiley.com/doi/abs/10.1029/2020GL090163` (e2020GL090163 2020GL090163) doi: https://doi.org/10.1029/2020GL090163

den Ouden, O. F. C., Assink, J. D., Smets, P. S. M., Shani-Kadmiel, S., Averbuch, G., & Evers, L. G. (2020, 01). CLEAN beamforming for the enhanced detection of multiple infrasonic sources. *Geophysical Journal International*, *221*(1), 305-317. Retrieved from `https://doi.org/10.1093/gji/ggaa010` doi: 10.1093/gji/ggaa010

Dessa, J.-X., Virieux, J., & Lambotte, S. (2005). Infrasound modeling in a spherical heterogeneous atmosphere. *Geophysical Research Letters*, *32*(12). Retrieved from `https://agupubs.onlinelibrary.wiley.com/doi/abs/10.1029/2005GL022867` doi: 10.1029/2005GL022867

Donn, W. L., & Naini, B. (1973). Sea wave origin of microbaroms and microseisms. *Journal of Geophysical Research*, *78*(21), 4482–4488.

Donn, W. L., & Posmentier, E. S. (1967). Infrasonic waves from the marine storm of april 7, 1966. *Journal of Geophysical Research*, *72*(8), 2053–2061.

Donn, W. L., & Rind, D. (1971). Natural infrasound as an atmospheric probe. *Geophys. J. R. Astron. Soc.*, *26*(1), 111–133. doi: 10.1111/j.1365-246x.1971.tb03386.x

Donn, W. L., & Rind, D. (1972). Microbaroms and the temperature and wind of the upper atmosphere. *J. Atmos. Sci.*, *29*(1), 156–172. doi: 10.1175/1520-0469(1972)029<0156%3AMATTAW>2.0.CO%3B2

Drob, D. (2019). Meteorology, climatology, and upper atmospheric composition for infrasound propagation modeling. In A. Le Pichon, E. Blanc, & A. Hauchecorne (Eds.), *Infrasound monitoring for atmospheric studies: Challenges in middle atmosphere dynamics and societal benefits* (pp. 485–508). Cham: Springer International Publishing. Retrieved from `https://doi.org/10.1007/978-3-319-75140-5_14` doi: 10.1007/978-3-319-75140-5_14

Drob, D. P., Meier, R., Picone, J. M., & Garcés, M. M. (2010). Inversion of infrasound signals for passive atmospheric remote sensing. In *Infrasound monitoring for atmospheric studies* (pp. 701–731). Springer.

Evers, L. G., & Haak, H. W. (2010). The characteristics of infrasound, its propagation and some early history. In *Infrasound monitoring for atmospheric studies* (pp. 3–27). Springer.

Farrell, W. E., & Munk, W. (2008). What do deep sea pressure fluctuations tell about short surface waves? *Geophys. Res. Lett.*, *35*(7), L19605. doi: 10.1029/2008GL035008

Fyen, J., Roth, M., & W., L. P. (2014). IS37 infrasound station in Bardufoss, Norway. *NORSAR Scientific Report*(2-2013), 29–39.

Gagnaire-Renou, E., Benoit, M., & Forget, P. (2010). Ocean wave spectrum properties as derived from quasi-exact computations of nonlinear wave-wave interactions. *J. Geophys. Res.*, *115*, C12058. doi: 10.1029/2009JC005665

Garcés, M., Drob, D. P., & Picone, J. M. (2002). A theoretical study of the effect of geomagnetic fluctuations and solar tides on the propagation of infrasonic waves in the upperatmosphere. *Geophys. J. Int.*, *148*, 77–87. doi: 10.1046/j.0956-540x.2001.01563.x

Garcés, M. A., Hansen, R. A., & Lindquist, K. G. (1998, 10). Traveltimes for infrasonic waves propagating in a stratified atmosphere. *Geophysical Journal International*, *135*(1), 255-263. Retrieved from `https://doi.org/10.1046/j.1365-246X.1998.00618.x` doi: 10.1046/j.1365-246X.1998.00618.x

Gualtieri, L., Stutzmann, E., Farra, V., Capdeville, Y., Schimmel, M., Ardhuin, F., & Morelli, A. (2014). Modelling the ocean site effect on seismic noise body waves. *Geophys. J. Int.*, *193*, 1096–1106. doi: 10.1093/gji/ggu042

Gutenberg, B., & Benioff, H. (1941). Atmospheric-pressure waves near pasadena. *Eos, Transactions American Geophysical Union*, *22*(2), 424–426.

Hasselmann, K. (1962). On the non-linear energy transfer in a gravity wave spectrum, part 1: general theory. *J. Fluid Mech.*, *12*, 481–501.

Hasselmann, K. (1963). A statistical analysis of the generation of microseisms. *Rev. of Geophys.*, *1*(2), 177–210.

Hasselmann, K. (1966, February). Feynman diagrams and interaction rules of wave-wave scattering processes. *Rev. of Geophys.*, *4*(1), 1–32.

Hasselmann, K., Barnett, T. P., Bouws, E., Carlson, H., Cartwright, D. E., Enke, K., . . . Walden, H. (1973). Measurements of wind-wave growth and swell decay during the Joint North Sea Wave Project. *Deut. Hydrogr. Z.*, *8*(12), 1–95. (Suppl. A)

Hasselmann, S., & Hasselmann, K. (1985). Computation and parameterizations of the nonlinear energy transfer in a gravity-wave spectrum. part I: a new method for efficient computations of the exact nonlinear transfer. *J. Phys. Oceanogr.*, *15*, 1369–1377.

Hedin, A. E. (1987). Msis-86 thermospheric model. *Journal of Geophysical Research: Space Physics*, *92*(A5), 4649-4662. Retrieved from https://agupubs.onlinelibrary.wiley.com/doi/abs/10.1029/JA092iA05p04649 doi: 10.1029/JA092iA05p04649

Hedin, A. E. (1991). Extension of the msis thermosphere model into the middle and lower atmosphere. *Journal of Geophysical Research: Space Physics*, *96*(A2), 1159-1172. Retrieved from https://agupubs.onlinelibrary.wiley.com/doi/abs/10.1029/90JA02125 doi: 10.1029/90JA02125

Hedin, A. E., Biondi, M. A., Burnside, R. G., Hernandez, G., Johnson, R. M., Killeen, T. L., . . . Virdi, T. S. (1991). Revised global model of thermosphere winds using satellite and ground-based observations. *Journal of Geophysical Research: Space Physics*, *96*(A5), 7657-7688. Retrieved from https://agupubs.onlinelibrary.wiley.com/doi/abs/10.1029/91JA00251 doi: 10.1029/91JA00251

Hedin, A. E., Fleming, E. L., Manson, A. H., Schmidlin, F., Avery, S., Clark, R., . . . Vincent, R. (1996). Empirical wind model for the upper, middle and lower atmosphere. *Journal of Atmospheric and Terrestrial Physics*, *58*(13), 1421 - 1447. Retrieved from http://www.sciencedirect.com/science/article/pii/0021916995001220 doi: https://doi.org/10.1016/0021-9169(95)00122-0

Hedlin, M., Walker, K., Drob, D., & de Groot-Hedlin, C. (2012). Infrasound: Connecting the solid earth, oceans, and atmosphere. *Annual Review of Earth and Planetary Sciences*, *40*(1), 327-354. Retrieved from https://doi.org/10.1146/annurev-earth-042711-105508 doi: 10.1146/annurev-earth-042711-105508

Högbom, J. A. (1974). Aperture synthesis with a non-regular distribution of interferometer baselines. *Astronomy and Astrophysics Supplement Series*, *15*, 417.

Hupe, P., Ceranna, L., Pilger, C., de Carlo, M., Le Pichon, A., Kaifler, B., & Rapp, M. (2018, 12). Assessing middle atmosphere weather models using infrasound detections from microbaroms. *Geophysical Journal International*, *216*(3), 1761-1767. Retrieved from https://doi.org/10.1093/gji/ggy520 doi: 10.1093/gji/ggy520

Komen, G. J., Cavaleri, L., Donelan, M., Hasselmann, K., Hasselmann, S., & Janssen, P. A. E. M. (1994). *Dynamics and modelling of ocean waves.* Cambridge: Cambridge University Press.

Landès, M., Ceranna, L., Le Pichon, A., & Matoza, R. S. (2012). Localization of microbarom sources using the ims infrasound network. *Journal of Geophysical Research: Atmospheres*, *117*(D6).

Landès, M., Hubans, F., Shapiro, N. M., Paul, A., & Campillo, M. (2010). Origin of deep ocean microseisms by using teleseismic body waves. *J. Geophys. Res.*, *115*, B05302. doi: 10.1029/2009JB006918

Landès, M., Le Pichon, A., Shapiro, N. M., Hillers, G., & Campillo, M. (2014, 09). Explaining global patterns of microbarom observations with wave action models. *Geophysical Journal International*, *199*(3), 1328-1337. Retrieved from https://doi.org/10.1093/gji/ggu324 doi: 10.1093/gji/ggu324

Le Pichon, A., De Carlo, M., Fatout, R., Bowman, D., & Ardhuin, F. (2020, May). Evaluating microbarom source models using infrasound recorded on a stratospheric balloon. In *Egu general assembly conference abstracts* (p. 19317).

Leckler, F., Ardhuin, F., Peureux, C., Benetazzo, A., Bergamasco, F., & Dulov, V. (2015). Analysis and interpretation of frequency-wavenumber spectra of young wind waves. *J. Phys. Oceanogr.*, *45*, 2484–2496. doi: 10.1175/JPO-D-14-0237.1

Lee, C., Smets, P., Charlton-Perez, A., Evers, L., Harrison, G., & Marlton, G. (2019). The potential impact of upper stratospheric measurements on sub-seasonal forecasts

in the extra-tropics. In A. Le Pichon, E. Blanc, & A. Hauchecorne (Eds.), *Infrasound monitoring for atmospheric studies: Challenges in middle atmosphere dynamics and societal benefits* (pp. 889–907). Cham: Springer International Publishing. Retrieved from `https://doi.org/10.1007/978-3-319-75140-5_29` doi: 10.1007/978-3-319-75140-5_29

Le Pichon, A., Assink, J., Heinrich, P., Blanc, E., Charlton-Perez, A., Lee, C. F., ... others (2015). Comparison of co-located independent ground-based middle atmospheric wind and temperature measurements with numerical weather prediction models. *Journal of Geophysical Research: Atmospheres*, *120*(16), 8318–8331.

Le Pichon, A., Blanc, E., Drob, D., Lambotte, S., Dessa, J. X., Lardy, M., ... Vergniolle, S. (2005). Infrasound monitoring of volcanoes to probe high-altitude winds. *Journal of Geophysical Research: Atmospheres*, *110*(D13). Retrieved from `https://agupubs.onlinelibrary.wiley.com/doi/abs/10.1029/2004JD005587` doi: 10.1029/2004JD005587

Le Pichon, A., Ceranna, L., & Vergoz, J. (2012). Incorporating numerical modeling into estimates of the detection capability of the ims infrasound network. *Journal of Geophysical Research: Atmospheres*, *117*(D5). Retrieved from `https://agupubs.onlinelibrary.wiley.com/doi/abs/10.1029/2011JD016670` doi: 10.1029/2011JD016670

Longuet-Higgins, M. S. (1950). A theory of the origin of microseisms. *Phil. Trans. Roy. Soc. London A*, *243*, 1–35.

Longuet-Higgins, M. S. (1957b). The statistical analysis of a random, moving surface. *Proc. Roy. Soc. Lond. A*, *249*.

Marty, J. (2019). The ims infrasound network: Current status and technological developments. In A. Le Pichon, E. Blanc, & A. Hauchecorne (Eds.), *Infrasound monitoring for atmospheric studies: Challenges in middle atmosphere dynamics and societal benefits* (pp. 3–62). Cham: Springer International Publishing. Retrieved from `https://doi.org/10.1007/978-3-319-75140-5_1` doi: 10.1007/978-3-319-75140-5_1

Matoza, R., Fee, D., Green, D., & Mialle, P. (2019). Volcano infrasound and the international monitoring system. In A. Le Pichon, E. Blanc, & A. Hauchecorne (Eds.), *Infrasound monitoring for atmospheric studies: Challenges in middle atmosphere dynamics and societal benefits* (pp. 1023–1077). Cham: Springer International Publishing. Retrieved from `https://doi.org/10.1007/978-3-319-75140-5_33` doi: 10.1007/978-3-319-75140-5_33

Matoza, R. S., Landès, M., Le Pichon, A., Ceranna, L., & Brown, D. (2013). Coherent ambient infrasound recorded by the international monitoring system. *Geophysical Research Letters*, *40*(2), 429-433. Retrieved from `https://agupubs.onlinelibrary.wiley.com/doi/abs/10.1029/2012GL054329` doi: 10.1029/2012GL054329

McNamara, D. E., & Boaz, R. I. (2019). Visualization of the seismic ambient noise spectrum. *Seismic Ambient Noise*, 1–29.

Mei, C. C. (1989). *Applied dynamics of ocean surface waves* (second ed.). Singapore: World Scientific. (740 p.)

Meschede, M., Stutzmann, E., Farra, V., Schimmel, M., & Ardhuin, F. (2017). The effect of water-column resonance on the spectra of secondary microseism p-waves. *J. Geophys. Res.*, *122*, 8121–8142. doi: 10.1002/2017JB014014

Mialle, P., Brown, D., & Arora, N. (2019). Advances in operational processing at the international data centre. In A. Le Pichon, E. Blanc, & A. Hauchecorne (Eds.), *Infrasound monitoring for atmospheric studies: Challenges in middle atmosphere dynamics and societal benefits* (pp. 209–248). Cham: Springer International Publishing. Retrieved from `https://doi.org/10.1007/978-3-319-75140-5_6` doi: 10.1007/978-3-319-75140-5_6

Miche, A. (1944). Mouvements ondulatoires de la mer en profondeur croissante ou décroissante. Première partie. Mouvements ondulatoires périodiques et cylindriques en profondeur constante. *Annales des Ponts et Chaussées*, *Tome 114*, 42–78.

Munk, W. H., Miller, G. R., Snodgrass, F. E., & Barber, N. F. (1963). Directional recording of swell from distant storms. *Phil. Trans. Roy. Soc. London A*, *255*, 505–584.

Munk, W. H., & Traylor, M. A. (1947, January). Refraction of ocean waves: a process linking underwater topography to beach erosion. *Journal of Geology*, *LV*(1), 1–26.

Obrebski, M., Ardhuin, F., Stutzmann, E., & Schimmel, M. (2012). How moderate sea

states can generate loud seismic noise in the deep ocean. *Geophys. Res. Lett.*, *39*, L11601. doi: 10.1029/2012GL051896

Obrebski, M., Ardhuin, F., Stutzmann, E., & Schimmel, M. (2013). Detection of microseismic compressional (p) body waves aided by numerical modeling of oceanic noise sources. *J. Geophys. Res.*, *118*, 4312–4324. doi: 10.1002/jgrb.50233

Peureux, C., Benetazzo, A., & Ardhuin, F. (2018). Note on the directional properties of meter-scale gravity waves. *Ocean Science*, *14*(1), 41–52.

Pilger, C., Ceranna, L., Le Pichon, A., & Brown, P. (2019). Large meteoroids as global infrasound reference events. In A. Le Pichon, E. Blanc, & A. Hauchecorne (Eds.), *Infrasound monitoring for atmospheric studies: Challenges in middle atmosphere dynamics and societal benefits* (pp. 451–470). Cham: Springer International Publishing. Retrieved from https://doi.org/10.1007/978-3-319-75140-5_12 doi: 10.1007/978-3-319-75140-5__12

Pineau-Guillou, L., Ardhuin, F., Bouin, M.-N., Redelsperger, J.-L., Chapron, B., Bidlot, J., & Quilfen, Y. (2018). Strong winds in a coupled wave-atmosphere model during a north atlantic storm event: evaluation against observations. *Quart. Journ. Roy. Meteorol. Soc.*, *144*, 317–332. doi: 10.1002/qj.3205

Posmentier, E. (1967). A theory of microbaroms. *Geophys. J. R. Astron. Soc.*, *13*, 487–501.

Rascle, N., & Ardhuin, F. (2013). A global wave parameter database for geophysical applications. part 2: model validation with improved source term parameterization. *Ocean Modelling*, *70*, 174–188. doi: 10.1016/j.ocemod.2012.12.001

Raspet, R., Abbott, J.-P., Webster, J., Yu, J., Talmadge, C., Alberts II, K., ... Noble, J. (2019). New systems for wind noise reduction for infrasonic measurements. In A. Le Pichon, E. Blanc, & A. Hauchecorne (Eds.), *Infrasound monitoring for atmospheric studies: Challenges in middle atmosphere dynamics and societal benefits* (pp. 91–124). Cham: Springer International Publishing. Retrieved from https://doi.org/10.1007/978-3-319-75140-5_3 doi: 10.1007/978-3-319-75140-5__3

Shuleykin, V. V. (1935). The voice of the sea. *Dokl. Akad. Nauk SSSR*, *3*, 259–262.

Smets, P. S. M. (2018). *Infrasound and the dynamical stratosphere: a new application for operational weather and climate prediction* (PhD thesis). Delft University of Technology.

Smets, P. S. M., & Evers, L. G. (2014). The life cycle of a sudden stratospheric warming from infrasonic ambient noise observations. *J. Geophys. Res.*, *119*, 12,084–12,099. doi: 10.1002/2014JD021905

Stoneley, R. (1926). The effect of the ocean on Rayleigh waves. *Mon. Not. Roy. Astron. Soc.*, *Geophys. Suppl. 1*, 349–356.

Stutzmann, E., Ardhuin, F., Schimmel, M., Mangeney, A., & Patau, G. (2012, 11). Modelling long-term seismic noise in various environments. *Geophysical Journal International*, *191*(2), 707-722. doi: 10.1111/j.1365-246X.2012.05638.x

Sutherland, L. C., & Bass, H. E. (2004). Atmospheric absorption in the atmosphere up to 160 km. *The Journal of the Acoustical Society of America*, *115*(3), 1012-1032. Retrieved from https://doi.org/10.1121/1.1631937 doi: 10.1121/1.1631937

Szuberla, C. A. L., & Olson, J. V. (2004). Uncertainties associated with parameter estimation in atmospheric infrasound arrays. *The Journal of the Acoustical Society of America*, *115*(1), 253-258. doi: 10.1121/1.1635407

Tailpied, D. (2016). *Évaluation et optimisation de réseau infrason pour la surveillance volcanique* (PhD thesis). Institut de Physique du Globe de Paris.

Tavernier, P. (1996). L'adoption du traité d'interdiction complète des essais nucléaires. *Annuaire Français de Droit International*, *42*(1), 118–136.

The WAVEWATCH III ® Development Group. (2016). *User manual and system documentation of WAVEWATCH III ® version 5.16* (Tech. Note No. 329). College Park, MD, USA: NOAA/NWS/NCEP/MMAB. (326 pp. + Appendices)

Tolman, H. L. (1990). The influence of unsteady depths and currents of tides on wind-wave propagation in shelf seas. *J. Phys. Oceanogr.*, *20*, 1166–1174. Retrieved from http://ams.allenpress.com/archive/1520-0485/20/8/pdf/i1520-0485-20-8-1166.pdf

Tolman, H. L., Accensi, M., Alves, H., Ardhuin, F., Bidlot, J., Booij, N., ... Zieger, S. (2014). *User manual and system documentation of WAVEWATCH-III*[TM] *version 2020* (Tech. Rep. No. 316). NOAA/NWS/NCEP/MMAB.

Vanderbecken, P., Mahfouf, J.-F., & Millet, C. (2020). Bayesian selection of atmospheric profiles from an ensemble data assimilation system using infrasonic observations of may 2016 mount etna eruptions. *Journal of Geophysical Research: Atmospheres*, *125*(2), e2019JD031168.

Waxler, R., & Assink, J. (2019). Propagation modeling through realistic atmosphere and benchmarking. In A. Le Pichon, E. Blanc, & A. Hauchecorne (Eds.), *Infrasound monitoring for atmospheric studies: Challenges in middle atmosphere dynamics and societal benefits* (pp. 509–549). Cham: Springer International Publishing. Retrieved from https://doi.org/10.1007/978-3-319-75140-5_15   doi: 10.1007/978-3-319-75140-5_15

Waxler, R., Gilbert, K., Talmadge, C., & Hetzer, C. (2007). The effects of finite depth of the ocean on microbarom signals. In *8th International Conference on Theoretical and Computational Acoustics (ICTCA), Crete, Greece.*

Waxler, R., & Gilbert, K. E. (2006). The radiation of atmospheric microbaroms by ocean waves. *J. Acoust. Soc. Amer.*, *119*, 2651–2664.

Whitaker, R. W. (1995). Infrasonic monitoring. In *17th annual seismic research symposium on monitoring a comprehensive test ban treaty, scottsdale, az (us).*

Whitaker, R. W., Sondoval, T., & Mutschlecner, J. P. (2003). Recent infrasound analysis. In *Proceedings of the 25th seismic research review-nuclear explosion monitoring: Building the knowledge base* (pp. 646–654).

Supporting information for "Atmospheric infrasound radiation..." De Carlo et al. (2020)

Contents

This appendix presents all the details of derivations necessary to support the paper "Atmospheric infrasound radiation from ocean waves in finite depth: a unified generation theory and application to radiation patterns". It follow (Brekhovskikh et al., 1973, hereinafter BGKN73), as much as possible. Because we use the more common convention that the velocity vector is $\mathbf{v} = \nabla\phi$ this leads to changes in signs that are highlighted in red. A notable difference with (Waxler & Gilbert, 2006, hereinafter WG06) is the non-zero value of $\mathbf{k}\cdot\mathbf{k}' + kk'$ and similar terms. Some of these were obtained by WG06 using the divergence equation, but not all of them, which misses the azimuthal dependence of the solution.

For convenience we repeat in table 1 the list of notations from the paper, including a few more symbols that were not used in the paper.

A.1 Equations up to eq. (9) in BGKN73

We start with the **Euler equation** for a perfect fluid (no viscosity), we then use the compressible form of the Bernoulli Equation

$$\rho_l\left(\frac{\partial \mathbf{v}_l}{\partial t} + (\mathbf{v}_l \cdot \nabla)\mathbf{v}_l\right) = -\nabla p_l - g\rho_l\nabla z \tag{A.1.1}$$

Table A.1 – Notations used in different papers: LH50 stands for Longuet-Higgins (1950), BGKN73 stands for Brekhovskikh et al. (1973), WG06 stands for Waxler & Gilbert (2006) and AH13 stands for Ardhuin & Herbers (2013).

quantity	this paper	LH50	BGKN73	WG06	AH13
vertical coordinate	z	$-z$	z	z	z
angle relative to vertical	θ_a or θ_w	$-$	θ	$-$	$-$
surface elevation	ζ	ζ	ζ	ξ	ζ
azimuth of spectrum	φ	θ	φ	θ	θ
azimuth of acoustic signal	θ_2	$-$	φ_a	$-$	$-$
velocity potential	ϕ	$-\phi$	$-\varphi$	ϕ	ϕ
layer index	l	$-$	j	σ	$-$
sound speed	α_l	c	c_j	c_σ	α
density ratio	m	$-$	m	$-$	$-$
horizontal wavenumber	$\mathbf{K}$	$-$	$\mathbf{q}$	$-$	$\mathbf{K}$
radian frequency	Ω	$-$	Ω	$-$	$2\pi f_s$
horizontal wavenumbers	$\mathbf{k}, \mathbf{k}'$	$(-uk, -vk)$	$\varkappa, \varkappa_1$	$\mathbf{k}, \mathbf{q}$	$\mathbf{k}, \mathbf{k}'$
radian frequencies	$\sigma\sigma'$	σ	$\omega(\varkappa), \omega(\varkappa_1)$	$\omega(\mathbf{k}), \omega(\mathbf{q})$	$\sigma\sigma'$
pressure	p	p	$\rho\mathcal{P}$	p	p
vertical wavenumbers	$\nu_\pm, \mu_\pm$	$-, \alpha$	λ_1, λ_2	$-$	l_a, l
upward amplification	$g/2\alpha_l$	γ	$-$	$-$	$-$

where g is the acceleration of gravity, the subscript l represents the layer, $\mathbf{v}_l$, ρ_l and p_l are respectively the velocity, the density and the pressure of the considered layer. And the **mass conservation equation** gives.

$$\frac{\partial \rho_l}{\partial t} + \nabla(\rho_l \mathbf{v}_l) = 0 \tag{A.1.2}$$

Equations (2) to (6) in BGKN73 are respectively :

- the **Equation of state** in the linear approximation in the form :

$$p_l - p_{l0}(0) = \alpha_l^2 [\rho_l - \rho_{l0}(0)] \tag{A.1.3}$$

- the **boundary conditions equations** to be respected at the interface $z = \zeta(x, y, t)$, which are both the dynamic and kinematic boundary conditions:

$$p_w = p_a, \quad \mathbf{v}_l \nabla z = \partial \zeta / \partial t \quad \text{at} \quad z = \zeta(x, y, t) \tag{A.1.4}$$

- the **equilibrium density and pressure profiles** for ocean and atmosphere are obtained by putting $\mathbf{v}_l = 0$ and $\zeta = 0$:

$$\begin{aligned} \rho_{l0}(z) &= \rho_{l0}(0)\exp\left\{-gz/\alpha_l^2\right\}, \\ p_{l0}(z) &= p_{l0} + \left[\rho_{l0}(z) - \rho_{l0}(0)\right]\alpha_l^2 \\ p_{l0} &= p_{a0}(0) = p_{w0}(0) \end{aligned} \tag{A.1.5}$$

- the **expansion of all quantities in a certain small parameter** ϵ for $\mathbf{v}_l \neq 0$:

$$\begin{aligned} \rho_l &= \rho_{l0}(z) + \epsilon\rho_{l1} + \epsilon^2\rho_{l2} + ... \\ p_l &= p_{l0}(z) + \epsilon p_{l1} + \epsilon^2 p_{l2} + ... \\ \mathbf{v}_l &= \epsilon\mathbf{v}_{l1} + \epsilon^2\mathbf{v}_{l2} + ... \\ \zeta_l &= \epsilon\zeta_{l1} + \epsilon^2\zeta_{l2} + ... \end{aligned} \tag{A.1.6}$$

- the **relation between** p_{li} **and** ρ_{li}, obtained from the precedent equations and a series expansion in ζ and the definition of the quantity $\mathcal{P}_{li}$:

$$p_{li} = \alpha_l^2 \rho_{li} \tag{A.1.7}$$

$$\text{and} \quad p_{li} = \rho_{l0}(z)\mathcal{P}_{li} \tag{A.1.8}$$

where the subscript i is the order of expansion in ϵ

A.1.1   About Euler's equation in BGKN73

Using the expansion in order of the small parameter ϵ, eq. (A.1.1) can be rewritten as

$$
(\rho_0 \;+\; \epsilon \rho_1 + \epsilon^2 \rho_2) \left(\frac{\partial \left(\epsilon \mathbf{v}_1 + \epsilon^2 \mathbf{v}_2 \right)}{\partial t} + (\epsilon \mathbf{v}_1 + \epsilon^2 \mathbf{v}_2) \cdot \nabla (\epsilon \mathbf{v}_1 + \epsilon^2 \mathbf{v}_2) \right)
$$
$$
= \; -\nabla(p_0 + \epsilon p_1 + \epsilon^2 p_2) - g(\rho_0 + \epsilon \rho_1 + \epsilon^2 \rho_2)\nabla z. \tag{A.1.7}
$$

here the subscript layer l is not written to lighten the equations, because the calculation is the same for ocean and atmosphere. Its truncation at the different orders in wave slope ϵ gives,
• Order 0,
$$
-\nabla p_0 = g\rho_0 \nabla z \tag{A.1.8}
$$

• Order 1,
$$
\rho_0 \frac{\partial \mathbf{v}_1}{\partial t} + 0 = -\nabla p_1 - g\rho_1 \nabla z \tag{A.1.9}
$$

• Order 2:
$$
\rho_0 \frac{\partial \mathbf{v}_2}{\partial t} + \rho_1 \frac{\partial \mathbf{v}_1}{\partial t} + \rho_0 \mathbf{v}_1 \nabla \mathbf{v}_1 = -\nabla p_2 - g\rho_2 \nabla z \tag{A.1.10}
$$

Simplifications from relations between p and ρ

Then some simplifications arise from eq. (A.1.7) and eq. (A.1.8)
• Order 1:

$$
\nabla p_1 = \nabla(\rho_0 \mathcal{P}_1) = \mathcal{P}_1 \nabla(\rho_0) + \rho_0 \nabla(\mathcal{P}_1) = \mathcal{P}_1 \rho_0 \cdot \frac{-g}{\alpha^2} \nabla z + \rho_0 \nabla(\mathcal{P}_1)
$$

And then, remembering from eq. (A.1.7) and eq. (A.1.8) that $\mathcal{P}_i = \alpha^2 \rho_i / \rho_0$, it simplifies to:

$$
\mathcal{P}_1 \rho_0 \cdot \frac{-g}{\alpha^2} \nabla z + \rho_0 \nabla(\mathcal{P}_1) \;=\; \frac{\alpha^2 \rho_1}{\rho_0} \cdot \rho_0 \cdot \frac{-g}{\alpha^2} \nabla z + \rho_0 \nabla(\mathcal{P}_1)
$$
$$
= \; -g\rho_1 \nabla z + \rho_0 \nabla(P_1)
$$

Finally, Equation (A.1.7) for order 1 becomes

$$
\frac{\partial \mathbf{v}_1}{\partial t} + \nabla \mathcal{P}_1 = 0. \tag{A.1.11}
$$

• Order 2: We similarly obtain

$$
-\nabla p_2 - g\rho_2 \nabla z = -\nabla(\rho_0 \mathcal{P}_2) - g\rho_2 \nabla z = -\rho_0 \nabla(\mathcal{P}_2) - \alpha^2 \frac{\rho_2}{\rho_0} \nabla(\rho_0) - g\rho_2 \nabla z
$$
$$
= -\rho_0 \nabla(\mathcal{P}_2) - \alpha^2 \frac{\rho_2}{\rho_0} \cdot \frac{-g}{\alpha^2} \nabla z - g\rho_2 \nabla z = -\rho_0 \nabla(\mathcal{P}_2).
$$

Leading to,

$$
\frac{\partial \mathbf{v}_2}{\partial t} + \frac{\rho_1}{\rho_0} \frac{\partial \mathbf{v}_1}{\partial t} + \mathbf{v}_1 \nabla \mathbf{v}_1 = -\nabla \mathcal{P}_2.
$$

Remembering from order 1 that $\dfrac{\partial \mathbf{v}_1}{\partial t} = -\nabla \mathcal{P}_1$ (eq. A.1.11) , one obtains

$$
\frac{\partial \mathbf{v}_2}{\partial t} + \nabla \mathcal{P}_2 = -\frac{\rho_1}{\rho_0} \frac{\partial \mathbf{v}_1}{\partial t} - \mathbf{v}_1 \nabla \mathbf{v}_1 = \frac{\rho_1 \alpha^2}{\rho_0 \alpha^2} \nabla \mathcal{P}_1 - \mathbf{v}_1 \nabla \mathbf{v}_1
$$
$$
= \frac{1}{\alpha^2} \mathcal{P}_1 \nabla \mathcal{P}_1 - \mathbf{v}_1 \nabla \mathbf{v}_1 = \frac{1}{2} \nabla \left(\frac{\mathcal{P}_1^2}{\alpha^2} - \mathbf{v}_1^2 \right) + \mathbf{v}_1 \times \mathbf{rot v}_1
$$

Finally, Equation (A.1.7) for order 2 becomes

$$
\frac{\partial \mathbf{v}_2}{\partial t} + \nabla \mathcal{P}_2 = \frac{1}{2} \nabla \left(\frac{\mathcal{P}_1^2}{\alpha^2} - \mathbf{v}_1^2 \right) + \mathbf{v}_1 \times \mathbf{rot v}_1 \tag{A.1.12}
$$

Simplifications from existence of a velocity potential

From $\vec{\mathbf{rot}}(A.1.9)$, it follows that $\partial\vec{\mathbf{rot}}(\mathbf{v}_1)/\partial t = 0$. Then, $\vec{\mathbf{rot}}(\mathbf{v}_1)$ can be put to 0. Consequently, it follows from $\vec{\mathbf{rot}}(A.1.10)$ that $\vec{\mathbf{rot}}(\mathbf{v}_2)$ can be put to 0. Therefore, the velocity can be expressed as the gradient of a potential velocity ϕ,

$$\mathbf{v}_i = +\nabla\phi_i. \tag{A.1.13}$$

This gives,

$$\nabla\mathcal{P}_1 = -\frac{\partial\nabla\phi_1}{\partial t}$$

$$\nabla\mathcal{P}_2 = -\frac{\partial\nabla\phi_2}{\partial t} + \frac{1}{2}\nabla\left(\frac{\mathcal{P}_1^2}{\alpha^2} - (\nabla\phi_1)^2\right)$$

Which can also be written

$$\mathcal{P}_1 = -\frac{\partial\phi_1}{\partial t} \tag{A.1.14}$$

$$\mathcal{P}_2 = -\frac{\partial\phi_2}{\partial t} + \left(\frac{\mathcal{P}_1^2}{2\alpha^2} - \frac{(\nabla\phi_1)^2}{2}\right). \tag{A.1.15}$$

A.1.2 About mass conservation equation in BGKN73 and the acoustic wave equation

The same truncation by orders can be done for the mass conservation equation (A.1.2):
• Order 1:

$$\frac{\partial\rho_1}{\partial t} + \nabla(\rho_0\mathbf{v}_1) = 0$$

$$\Longleftrightarrow \quad \frac{\partial\rho_1}{\partial t} + \rho_0\nabla\mathbf{v}_1 + \mathbf{v}_1\nabla\rho_0 = 0$$

$$\Longleftrightarrow \quad \frac{\partial\rho_1}{\partial t} = -\rho_0\Delta\phi_1 - \nabla\phi_1\nabla\rho_0 \tag{A.1.16}$$

$\frac{\partial}{\partial t}\left(\rho_0 \cdot A.1.14\right) - \alpha^2 \cdot A.1.16$ leads to

$$\frac{\partial\rho_0\mathcal{P}_1}{\partial t} - \alpha^2\frac{\partial\rho_1}{\partial t} - \alpha^2\rho_0\Delta\phi_1 - \alpha^2\nabla\phi_1\nabla\rho_0 = -\frac{\partial^2\rho_0\phi_1}{\partial t^2}$$

$$\Longleftrightarrow \frac{\partial p_1}{\partial t} - \alpha^2\frac{\partial\alpha^{-2}p_1}{\partial t} - \alpha^2\rho_0\Delta\phi_1 + \alpha^2\nabla\phi_1\rho_0\frac{g}{\alpha^2}\nabla z = -\rho_0\frac{\partial^2\phi_1}{\partial t^2}$$

$$\Longleftrightarrow -\alpha^2\Delta\phi_1 + g\frac{\partial\phi_1}{\partial z} + \frac{\partial^2\phi_1}{\partial t^2} = 0$$

$$\Longleftrightarrow \Delta\phi_1 - \frac{g}{\alpha^2}\frac{\partial\phi_1}{\partial z} - \frac{1}{\alpha^2}\frac{\partial^2\phi_1}{\partial t^2} = 0 \tag{A.1.17}$$

• Order 2:

$$\frac{\partial\rho_2}{\partial t} + \nabla(\rho_0\mathbf{v}_2 + \rho_1\mathbf{v}_1) = 0$$

$$\Longleftrightarrow \quad \frac{\partial\rho_2}{\partial t} + \rho_0\nabla\mathbf{v}_2 + \mathbf{v}_2\nabla\rho_0 + \rho_1\nabla\mathbf{v}_1 + \mathbf{v}_1\nabla\rho_1 = 0$$

$$\Longleftrightarrow \quad \frac{\partial\rho_2}{\partial t} = -\rho_0\Delta\phi_2 - \nabla\phi_2\nabla\rho_0 - \rho_1\Delta\phi_1 - \nabla\phi_1\nabla\rho_1 \tag{A.1.18}$$

$\frac{\partial}{\partial t}\left(\rho_0 \cdot A.1.15\right) - \alpha^2 \cdot A.1.18$ leads to:

$$\frac{\partial\rho_0\mathcal{P}_2}{\partial t} - \alpha^2\frac{\partial\rho_2}{\partial t} - \alpha^2\rho_0\Delta\phi_2 - \alpha^2\nabla\phi_2\nabla\rho_0 - \alpha^2\rho_1\Delta\phi_1 - \alpha^2\nabla\phi_1\nabla\rho_1 = -\frac{\partial^2\rho_0\phi_2}{\partial t^2} + \rho_0\frac{\partial}{\partial t}\left(\frac{\mathcal{P}_1^2}{2\alpha^2} - \frac{(\nabla\phi_1)^2}{2}\right)$$

140

$$\Longleftrightarrow \frac{\partial p_2}{\partial t} - \alpha^2 \frac{\partial \alpha^{-2} p_2}{\partial t} - \alpha^2 \rho_0 \Delta \phi_2 + \alpha^2 \rho_0 \frac{g}{\alpha^2} \frac{\partial \phi_2}{\partial z} - p_1 \Delta \phi_1 - \nabla \phi_1 \nabla p_1 = -\rho_0 \frac{\partial^2 \phi_2}{\partial t^2} + \rho_0 \frac{\partial}{\partial t} \left(\frac{\mathcal{P}_1^2}{2\alpha^2} - \frac{(\nabla \phi_1)^2}{2} \right)$$

$$\Longleftrightarrow -\alpha^2 \rho_0 \Delta \phi_2 + \alpha^2 \rho_0 \frac{g}{\alpha^2} \frac{\partial \phi_2}{\partial z} - \rho_0 \mathcal{P}_1 \Delta \phi_1 - \mathcal{P}_1 \nabla \phi_1 \nabla \rho_0 - \rho_0 \nabla \phi_1 \nabla \mathcal{P}_1 = -\rho_0 \frac{\partial^2 \phi_2}{\partial t^2} + \rho_0 \frac{\partial}{\partial t} \left(\frac{\mathcal{P}_1^2}{2\alpha^2} - \frac{(\nabla \phi_1)^2}{2} \right)$$

$$\Longleftrightarrow -\alpha^2 \rho_0 \Delta \phi_2 + \rho_0 g \frac{\partial \phi_2}{\partial z} - \rho_0 \mathcal{P}_1 \Delta \phi_1 + \mathcal{P}_1 \rho_0 \frac{g}{\alpha^2} \frac{\partial \phi_1}{\partial z} - \rho_0 \nabla \phi_1 \nabla \mathcal{P}_1 = -\rho_0 \frac{\partial^2 \phi_2}{\partial t^2} + \rho_0 \frac{\partial}{\partial t} \left(\frac{\mathcal{P}_1^2}{2\alpha^2} - \frac{(\nabla \phi_1)^2}{2} \right)$$

$$\Longleftrightarrow -\alpha^2 \rho_0 \Delta \phi_2 + \rho_0 g \frac{\partial \phi_2}{\partial z} - \rho_0 \mathcal{P}_1 \left(\Delta \phi_1 - \frac{g}{\alpha^2} \frac{\partial \phi_1}{\partial z} \right) - \rho_0 \nabla \phi_1 \nabla \mathcal{P}_1 = -\rho_0 \frac{\partial^2 \phi_2}{\partial t^2} + \rho_0 \frac{\partial}{\partial t} \left(\frac{\mathcal{P}_1^2}{2\alpha^2} - \frac{(\nabla \phi_1)^2}{2} \right)$$

$$\Longleftrightarrow -\alpha^2 \rho_0 \Delta \phi_2 + \rho_0 g \frac{\partial \phi_2}{\partial z} - \rho_0 \mathcal{P}_1 \frac{1}{\alpha^2} \frac{\partial^2 \phi_1}{\partial t^2} - \rho_0 \nabla \phi_1 \nabla \mathcal{P}_1 = -\rho_0 \frac{\partial^2 \phi_2}{\partial t^2} + \rho_0 \frac{\partial}{\partial t} \left(\frac{\mathcal{P}_1^2}{2\alpha^2} - \frac{(\nabla \phi_1)^2}{2} \right)$$

$$\Longleftrightarrow -\alpha^2 \rho_0 \Delta \phi_2 + \rho_0 g \frac{\partial \phi_2}{\partial z} + \rho_0 \mathcal{P}_1 \frac{1}{\alpha^2} \frac{\partial \mathcal{P}_1}{\partial t} - \rho_0 \nabla \phi_1 \nabla \mathcal{P}_1 = -\rho_0 \frac{\partial^2 \phi_2}{\partial t^2} + \rho_0 \frac{\partial}{\partial t} \left(\frac{\mathcal{P}_1^2}{2\alpha^2} - \frac{(\nabla \phi_1)^2}{2} \right)$$

$$\Longleftrightarrow -\alpha^2 \rho_0 \Delta \phi_2 + \rho_0 g \frac{\partial \phi_2}{\partial z} + \rho_0 \nabla \phi_1 \nabla \frac{\partial \phi_1}{\partial t} = -\rho_0 \frac{\partial^2 \phi_2}{\partial t^2} - \rho_0 \frac{\partial}{\partial t} \frac{(\nabla \phi_1)^2}{2}$$

$$\Longleftrightarrow -\alpha^2 \rho_0 \Delta \phi_2 + \rho_0 g \frac{\partial \phi_2}{\partial z} + \rho_0 \frac{\partial}{\partial t} \frac{(\nabla \phi_1)^2}{2} = -\rho_0 \frac{\partial^2 \phi_2}{\partial t^2} - \rho_0 \frac{\partial}{\partial t} \frac{(\nabla \phi_1)^2}{2}$$

$$\Longleftrightarrow -\alpha^2 \rho_0 \Delta \phi_2 + \rho_0 g \frac{\partial \phi_2}{\partial z} + \rho_0 \frac{\partial^2 \phi_2}{\partial t^2} = -\rho_0 \frac{\partial}{\partial t} (\nabla \phi_1)^2$$

$$\Longleftrightarrow \Delta \phi_2 - \frac{g}{\alpha^2} \frac{\partial \phi_2}{\partial z} - \frac{1}{\alpha^2} \frac{\partial^2 \phi_2}{\partial t^2} = +\frac{1}{\alpha^2} \frac{\partial}{\partial t} (\nabla \phi_1)^2 \tag{A.1.19}$$

And we retrieve the acoustic wave equation for both first (A.1.17) and second (A.1.19) orders.

A.1.3 About Boundary conditions

We use the same boundary conditions as in BGKN73 for $z = 0$ for velocity,

$$- \frac{\partial \phi_1}{\partial z} \Big|_{z=0} + \frac{\partial \zeta_1}{\partial t} = 0 \tag{A.1.20}$$

$$- \frac{\partial \phi_2}{\partial z} \Big|_{z=0} + \frac{\partial \zeta_2}{\partial t} = - \left(- \frac{\partial^2 \phi_1}{\partial z^2} \Big|_{z=0} \zeta_1 + \nabla \phi_1 |_{z=0} \nabla \zeta_1 \right) \tag{A.1.21}$$

And for pressure,

$$(\mathcal{P}_{w,1} - m \mathcal{P}_{a,1})_{z=0} - g(1-m)\zeta_1 = 0 \tag{A.1.22}$$

$$(\mathcal{P}_{w,2} - m \mathcal{P}_{a,2})_{z=0} - g(1-m)\zeta_2 = - \left(\frac{\partial \mathcal{P}_{w,1}}{\partial z} - m \frac{\partial \mathcal{P}_{a,1}}{\partial z} \right)_0 \zeta_1 \tag{A.1.23}$$

$$+ \frac{g}{\alpha_a^2} (n^2 \mathcal{P}_{w,1} - m \mathcal{P}_{a,1})_0 \zeta_1 - \frac{g^2}{2\alpha_a^2}(n^2 - m^2)\zeta_1^2$$

Here is a summary of the system of equation that corresponds to eq. (9) in BGKN73

$$\Delta\phi_{l,i} - \frac{g}{\alpha_l^2}\frac{\partial\phi_{l,i}}{\partial z} - \frac{1}{\alpha_l^2}\frac{\partial^2\phi_{l,i}}{\partial t^2} = S_{l,i} \qquad\qquad \mathcal{P}_{l,i} = -\frac{\partial\phi_{l,i}}{\partial t} + F_{l,i}$$

$$-\left.\frac{\partial\phi_{l,i}}{\partial z}\right|_{z=0} + \frac{\partial\zeta_i}{\partial t} = Q_{l,i} \qquad\qquad (\mathcal{P}_{w,i} - m\mathcal{P}_{a,i})_{z=0} - g(1-m)\zeta_i = R_i$$

where,

$$F_{l,1} = S_{l,1} = Q_{l,1} = R_1 = 0$$

$$F_{l,2} = \frac{\mathcal{P}_{l,1}^2}{2\alpha_l^2} - \frac{(\nabla\phi_{l,1})^2}{2}, \qquad S_{l,2} = +\frac{1}{\alpha_l^2}\frac{\partial}{\partial t}(\nabla\phi_{l,1})^2$$

$$Q_{l,2} = -\nabla\phi_{l,1}|_0\nabla\zeta_1 + \left.\frac{\partial^2\phi_{l,1}}{\partial z^2}\right|_{z=0}\zeta_1$$

$$R_2 = -\left(\frac{\partial\mathcal{P}_{w,1}}{\partial z} - m\frac{\partial\mathcal{P}_{a,1}}{\partial z}\right)_0\zeta_1 + \frac{g}{\alpha_a^2}(n^2\mathcal{P}_{w,1} - m\mathcal{P}_{a,1})_0\zeta_1 - \frac{g^2}{2\alpha_a^2}(n^2 - m^2)\zeta_1^2$$

$$m = \rho_{a,0}/\rho_{w,0}, \qquad n = \alpha_a/\alpha_w, \qquad \delta_a = \left(\frac{g}{\alpha_a^2 k}\right)^{1/2} = \frac{\sigma}{\alpha_a k}, \qquad \delta_w = n\delta_a$$

A.2 Solving for first order and expressing the second order problem

A.2.1 First order

From the Fourier transform in horizontal space and time we can take

$$\phi_{l,1} = -\mathrm{i}s\sigma\sum\Phi_{l,1}(z)Z\mathrm{e}^{\mathrm{i}(\mathbf{k}\cdot\mathbf{x}-s\sigma t)} \tag{A.2.24}$$

The boundary condition in $z = 0$ leads to

$$\Phi_{l,1}(z = 0) = 1. \tag{A.2.25}$$

Assuming $\Phi_{l,1}(z) = f_l(z)\mathrm{e}^{\gamma_l z}$ with $\gamma_l = g/2\alpha_l^2$ one obtains,
• for the air

$$\phi_{a,1} = \sum\mathrm{i}\frac{s\sigma}{k_a}\mathrm{e}^{-k_a z}Z\mathrm{e}^{\mathrm{i}(\mathbf{k}\cdot\mathbf{x}-s\sigma t)} \tag{A.2.26}$$

with

$$k_a = -\gamma_a + k_{a0}$$

$$= -\frac{g}{2\alpha_a^2} + \sqrt{k^2 - \gamma_a^2 + \frac{g\gamma_a}{\alpha_a^2} - \frac{\sigma^2}{\alpha_a^2}}$$

$$= -\frac{g}{2\alpha_a^2} + k(1 - \frac{g^2}{4\alpha_a^4 k^2} + \frac{g^2}{2\alpha_a^4 k^2} - \frac{\sigma^2}{k^2\alpha_a^2}$$

$$= -k\frac{g}{2k\alpha_a^2} + k\left(1 - \frac{\delta_a^4}{4} + \frac{\delta_a^4}{2} - \delta_a^2\right)^{1/2}$$

$$= -k\frac{\delta_a^2}{2} + k\left(1 - \frac{\delta_a^2}{2}\right)$$

$$= k\left(1 - \delta_a^2\right)$$

• for the water :

$$\phi_{w,1} = \sum -\mathrm{i}s\sigma\frac{k_{w0}\cosh(k_{w0}(z+h)) - \gamma_w\sinh(k_{w0}(z+h))}{k_w^2\sinh(k_{w0}h)}\mathrm{e}^{\gamma_w z}Z\mathrm{e}^{\mathrm{i}(\mathbf{k}\cdot\mathbf{x}-s\sigma t)} \tag{A.2.27}$$

with $k_w^2 = k_{w0}^2 - \gamma_w^2 = k^2(1 - 2\delta_w^2)$

If we consider δ_w^2 to be negligible ($\delta_w = n^2\delta_a^2 \simeq 0.05\delta_a^2$) we obtain :

$$\phi_{w,1} = \sum -\mathrm{i}s\sigma \frac{\cosh(k_{w0}(z+h))}{k\sinh(k_{w0}h)} \mathrm{e}^{\gamma_w z} Z \mathrm{e}^{\mathrm{i}(\mathbf{k}\cdot\mathbf{x} - s\sigma t)} \tag{A.2.28}$$

For simplicity, from now on we will write that under the form:

$$\phi_{w,1} = \sum -\mathrm{i}s\sigma f_{w,k}(z) \mathrm{e}^{\gamma_w z} Z \mathrm{e}^{\mathrm{i}(\mathbf{k}\cdot\mathbf{x} - s\sigma t)} \tag{A.2.29}$$

A.2.2 Second order

At second order, the effects of waves comes into the pressure and velocity boundary conditions at the interfaces, but also as forcing terms on the right hand side of the wave equation. All these different terms take different forms, in particular for waves in intermediate or shallow water (Ardhuin & Herbers, 2013). In the limit of deep water waves, $kh \gg 1$, and neglecting δ_w^2 terms, all the wave forcing terms can be expressed as a function of $\hat{p}_{2,u}$, defined as

$$\hat{p}_{2,u}(x, y, z) = \rho_w |\nabla \phi_1|^2 = \frac{\rho_w g^2}{s\sigma s'\sigma'} \sum \left(\mathbf{k}\cdot\mathbf{k}' - kk'\right) ZZ' \mathrm{e}^{(k+k')z} \mathrm{e}^{\mathrm{i}\Theta} \tag{A.2.30}$$

with $\Theta = \mathbf{K}\cdot\mathbf{x} - \Omega t$, $\mathbf{K} = \mathbf{k} + \mathbf{k}'$, and $\Omega = s\sigma + s'\sigma'$. A the surface, $z = 0$, this equivalent pressure, correspond to the pressure that drives microseisms as given by (K. Hasselmann, 1963, eq. 2.12).

In the following, we will neglect all the short wavelength components that correspond to the middle line of eq. (2.13) of K. Hasselmann (1963), keeping only the large wavelengths that excite microbaroms, and for which $|\mathbf{k} + \mathbf{k}'| \ll |\mathbf{k}|$.

Given that acoustic waves in the atmosphere are much slower than those in water, we will retain δ_a^2 terms. As a result, following Brekhovskikh et al. (1973), we cannot use the approximation $\mathbf{k}\cdot\mathbf{k}' \simeq 0$, but instead, using $\mathbf{k}\cdot\mathbf{k}' < 0$ for those components that produce microseisms, we can use

$$\frac{K}{k} = \frac{K\alpha_a}{2\sigma} \frac{2\sigma}{k\alpha_a} = 2\sin\theta_a\delta_a \tag{A.2.31}$$

and the law of cosine in triangles,

$$2\mathbf{k}\cdot\mathbf{K} = k^2 + K^2 - k'^2 \tag{A.2.32}$$

this gives,

$$
\begin{aligned}
kk' + \mathbf{k}\cdot\mathbf{k}' &= kk'\left[1 - \left(\left(\frac{-\mathbf{k}\cdot\mathbf{k}'}{kk'}\right)^2\right)^{1/2}\right] = kk'\left[1 - \left(\left(\frac{\mathbf{K}\cdot\mathbf{k}' - \mathbf{k}'\cdot\mathbf{k}'}{kk'}\right)\left(\frac{\mathbf{k}\cdot\mathbf{K} - \mathbf{k}\cdot\mathbf{k}}{kk'}\right)\right)^{1/2}\right] \\
&= kk'\left[1 - \left(\left(\frac{-\mathbf{K}\cdot\mathbf{k} + K^2 - k'^2}{kk'}\right)\left(\frac{\mathbf{k}\cdot\mathbf{K} - k^2}{kk'}\right)\right)^{1/2}\right] \\
&= kk'\left[1 - \left(\frac{k^2 k'^2 - (\mathbf{K}\cdot\mathbf{k})^2 + \mathbf{K}\cdot\mathbf{k}\left(k^2 + K^2 - k'^2\right) - k^2 K^2}{k^2 k'^2}\right)^{1/2}\right] \\
&= kk'\left[1 - \left(1 + \frac{-(\mathbf{K}\cdot\mathbf{k})^2 + 2\mathbf{K}\cdot\mathbf{k}(\mathbf{K}\cdot\mathbf{k}) - k^2 K^2}{k^2 k'^2}\right)^{1/2}\right] \\
&= kk'\left[1 - \left(1 + \frac{(\mathbf{K}\cdot\mathbf{k})^2 - k^2 K^2}{k^2 k'^2}\right)^{1/2}\right] \\
&\simeq kk'\left[-\frac{1}{2}\left(\frac{(\mathbf{K}\cdot\mathbf{k})^2}{k^2 k'^2} - \frac{K^2}{k'^2}\right)\right] \simeq kk'\frac{1}{2}\frac{K^2}{k'^2}\left[1 - \left(\frac{(\mathbf{K}\cdot\mathbf{k})^2}{k^2 K^2}\right)\right] \\
&\simeq 2kk'\sin^2\theta_a\delta_a^2\left[1 - \left(\frac{(\mathbf{k}\cdot\mathbf{K})^2}{k^2 K^2}\right)\right] = 2kk'\sin^2\theta_a\delta_a^2\left[1 - \cos^2(\varphi_2 - \varphi)\right]
\end{aligned} \tag{A.2.33}
$$

which is a function of the azimuth φ_2 of the acoustic wave propagation, with $\cos(\varphi_2 - \varphi) = \mathbf{k}{\cdot}\mathbf{K}/(kK)$.

Then,

$$\mathbf{k}{\cdot}\mathbf{k}' - kk' \simeq -2kk' \left(1 - \sin^2\theta_a \delta_a^2 \left[1 - \cos^2(\varphi_2 - \varphi)\right]\right) \tag{A.2.34}$$

This gives,

$$\hat{p}_{2,u}(x,y,z) \simeq -2\rho_w \sigma\sigma' \sum \left(1 - \sin^2\theta_a \delta_a^2 \left[1 - \cos^2(\varphi_2 - \varphi)\right]\right) ZZ'\mathrm{e}^{(k+k')z}\mathrm{e}^{\mathrm{i}\Theta} \tag{A.2.35}$$

Other similar terms have more simple forms with no azimuthal dependency

$$\frac{1}{2}\left(k^2 + \mathbf{k}{\cdot}\mathbf{k}' + k'^2 + \mathbf{k}{\cdot}\mathbf{k}'\right) = \frac{1}{2}\left(\mathbf{k}{\cdot}\mathbf{K} + \mathbf{k}'{\cdot}\mathbf{K}\right) = \frac{1}{2}K^2 \simeq 2k^2\sin^2\theta_a\delta_a^2. \tag{A.2.36}$$

A.3   Second order solution

A.3.1   General form of the solution in the water layer

The homogeneous solution is obtained for $S_{w,2} = 0$,

$$\phi_{w,2,h}(x,y,z,t) = \sum \Phi_{w,2,h}\mathrm{e}^{\mathrm{i}\Theta}, \quad \text{with} \quad \Theta = \mathbf{K}{\cdot}\mathbf{x} - \Omega t, \quad \mathbf{K} = \mathbf{k} + \mathbf{k}', \quad \Omega = s\sigma + s'\sigma' \tag{A.3.37}$$

Assuming a $\mathrm{e}^{\mathrm{i}\mu z}$ variation over the vertical and replacing eq. (A.3.37) in the homogeneous equation (A.1.19) gives,

$$\mu^2 + \mathrm{i}\frac{g}{\alpha_w^2}\mu + (K^2 - \Omega^2/\alpha_w^2) = 0 \tag{A.3.38}$$

with solutions,

$$\mu_\pm = -\mathrm{i}\frac{g}{\alpha_w^2} \pm \sqrt{\frac{g^2}{2\alpha_w^4} + (\Omega^2/\alpha_w^2 - K^2)} \simeq \pm k_{w2,0}(1 + O(\delta_w^2)) \tag{A.3.39}$$

with the complex wavenumber $k_{w2,0} = \sqrt{\Omega^2/\alpha_w^2 - K^2}$ so that the homogeneous solution is

$$\Phi_{w,2,h} = W_+\mathrm{e}^{\mathrm{i}\mu_+ z} + W_-\mathrm{e}^{\mathrm{i}\mu_- z}. \tag{A.3.40}$$

We recall that the wave equation is forced by,

$$S_{w,2} = +\frac{1}{\alpha_w^2}\frac{\partial}{\partial t}\left(\nabla\phi_1\right)^2 = +\frac{1}{\rho_w\alpha^2}\frac{\partial\hat{p}_{2,u}}{\partial t} \tag{A.3.41}$$

This forcing adds a particular solution of order δ_w^2 that could be neglected here but we will only keep the lowest order term to be consistent with BGKN73. This is also discussed by Longuet-Higgins (1950) and Waxler & Gilbert (2006). We will only give its expression in the limit of deep water, i.e. $kh \gg 1$.

We recall the right hand side of eq. eq:Sw2,

$$S_{w,2}(x,z,t) \simeq +\frac{1}{\rho_w\alpha_w^2}\frac{\partial\hat{p}_{2,u}(x,y,z,t)}{\partial t} = -\frac{g^2}{\alpha_a^2}\sum\mathrm{i}\frac{s\sigma + s\sigma'}{s\sigma s\sigma'}\left(\mathbf{k}{\cdot}\mathbf{k}' - kk'\right)ZZ'\mathrm{e}^{(k_w + k_w')z}\mathrm{e}^{\mathrm{i}\Theta}. \tag{A.3.42}$$

Looking for a solution of the form

$$\phi_{w,2,p} = \sum \Phi_{w,2,p}\mathrm{e}^{\mathrm{i}\Theta} \tag{A.3.43}$$

We replace it in the wave equation (A.1.19) and find

$$\Phi_{w,2,p} \simeq -\mathrm{i}\frac{g^2}{u}\cdot\frac{s\sigma + s\sigma'}{s\sigma s\sigma'}\left(\mathbf{k}{\cdot}\mathbf{k}' - kk'\right)ZZ'\mathrm{e}^{(k_w + k_w')z}. \tag{A.3.44}$$

with the denominator defined by

$$u = \alpha_w^2\left[-K^2 + \frac{\Omega^2}{\alpha_w^2} + (k_w + k_w')^2\right] + g(k_w + k_w') \simeq \alpha_w^2(k_w + k_w')^2 \simeq 4\alpha_w^2 k^2. \tag{A.3.45}$$

Of particular interest is the long-wavelength part – with $s = s'$ – of the vertical derivative of $\phi_{w,2,p}$, given by,

$$
\begin{aligned}
\frac{\partial \phi_{w,2,p}}{\partial z} &\simeq \sum -\mathrm{i}s \frac{g^2}{4\alpha_w^2 k^2} \frac{2\sigma(k_w + k_w')}{\sigma\sigma'} \left(\mathbf{k}\cdot\mathbf{k}' - kk' \right) ZZ' \mathrm{e}^{(k_w + k_w')z} \mathrm{e}^{\mathrm{i}\Theta}, \\
&\simeq +\sum \mathrm{i}s\delta_w^2 \frac{g}{\sigma} 2k^2 ZZ' \mathrm{e}^{(k_w + k_w')z} \mathrm{e}^{\mathrm{i}\Theta}.
\end{aligned} \tag{A.3.46}
$$

A.3.2 General form of the solution in the air layer

For the air, we only consider acoustic waves radiating upward, giving the homogeneous solution,

$$
\phi_{a,2,h}(x,y,z,t) = \sum sA_+ ZZ' \mathrm{e}^{\nu_+ z} \mathrm{e}^{\mathrm{i}\Theta}, \tag{A.3.47}
$$

where

$$
\nu_+ = \frac{g}{\alpha_a^2} + \mathrm{i}\sqrt{\frac{g^2}{2\alpha^4} + (\Omega^2/\alpha_w^2 - K^2)}. \tag{A.3.48}
$$

For the particular solution, we recall the right hand side,

$$
S_{a,2}(x,z,t) \simeq +\frac{1}{\rho_w \alpha_a^2} \frac{\partial \hat{p}_{2,u}(x,y,-z,t)}{\partial t} = -\frac{g^2}{\alpha_a^2} \sum \mathrm{i} \frac{s\sigma + s\sigma'}{s\sigma s\sigma'} \left(\mathbf{k}\cdot\mathbf{k}' - k_a k_a' \right) ZZ' \mathrm{e}^{-(k_a + k_a')z} \mathrm{e}^{\mathrm{i}\Theta}. \tag{A.3.49}
$$

Looking for a solution of the form

$$
\phi_{a,2,p} = \sum \Phi_{a,2,p} \mathrm{e}^{\mathrm{i}\Theta} \tag{A.3.50}
$$

We replace it in the wave equation (A.1.19) and find

$$
\Phi_{a,2,p} \simeq -\mathrm{i} \frac{g^2}{u} \frac{s\sigma + s\sigma'}{s\sigma s\sigma'} \left(\mathbf{k}\cdot\mathbf{k}' - k_a k_a' \right) ZZ' \mathrm{e}^{-(k_a + k_a')z}. \tag{A.3.51}
$$

with the denominator defined by

$$
u = \alpha_a^2 \left[-K^2 + \frac{\Omega^2}{\alpha_a^2} + (k_a + k_a')^2 \right] + g(k_a + k_a') \simeq \alpha_a^2 (k_a + k_a')^2 \simeq 4\alpha_a^2 k^2. \tag{A.3.52}
$$

The derivation of eq. (A.3.52) is detailed below:

$$
\begin{aligned}
u &= \alpha_a^2 \left[-K^2 + \frac{\Omega^2}{\alpha_a^2} + (k_a + k_a')^2 \right] + g(k_a + k_a') \\
&\simeq \alpha_a^2 k^2 \left(4\delta_a^2 \cos^2\theta_a + \left(1 + \frac{k'}{k}\right)^2 (1 - 2\delta_a^2) + \frac{g}{\alpha_a^2 k^2}(k_a + k_a') \right) \\
&\simeq \alpha_a^2 k^2 (4\delta_a^2 \cos^2\theta_a + 4(1 - 2\delta_a^2) + 2\delta_a^2(1 - \delta_a^2)) \\
&\simeq 4\alpha_a^2 k^2 (1 - \delta_a^2(\sin^2\theta_a + \frac{1}{2})) \simeq 4\alpha_a^2 k^2 (1 + O(\delta_a^2))
\end{aligned} \tag{A.3.53}
$$

Of particular interest is the long-wavelength part – with $s = s'$ – of the vertical derivative of $\phi_{a,2,p}$, given by,

$$
\begin{aligned}
\frac{\partial \phi_{a,2,p}}{\partial z} &\simeq +\sum \mathrm{i}s \frac{g^2}{4\alpha_a^2 k^2} (1 - O(\delta_a^2)) \frac{2\sigma(k_a + k_a')}{\sigma\sigma'} \left(\mathbf{k}\cdot\mathbf{k}' - k_a k_a' \right) ZZ' \mathrm{e}^{-(k_a + k_a')z} \mathrm{e}^{\mathrm{i}\Theta}, \\
&\simeq +\sum \mathrm{i}s \frac{g^2}{4\alpha_a^2 k^2} (1 - O(\delta_a^2)) \frac{2\sigma(k + k')(1 - \delta_a^2)}{\sigma\sigma'} \left(\mathbf{k}\cdot\mathbf{k}' - kk' - 2kk'\delta_a^2 \right) ZZ' \mathrm{e}^{-(k_a + k_a')z} \mathrm{e}^{\mathrm{i}\Theta}, \\
&\simeq +\sum \mathrm{i}s\delta_a^2 \frac{g}{\sigma} \left(\mathbf{k}\cdot\mathbf{k}' - kk' \right) (1 + O(\delta_a^2)) ZZ' \mathrm{e}^{-(k_a + k_a')z} \mathrm{e}^{\mathrm{i}\Theta}, \\
&\simeq -\sum \mathrm{i}s\delta_a^2 2\sigma' k ZZ' \mathrm{e}^{-(k_a + k_a')z} \mathrm{e}^{\mathrm{i}\Theta}.
\end{aligned} \tag{A.3.54}
$$

A.3.3   The BGKN terms - $F_{l,2}$, $Q_{l,2}$, R_2

In the water layer

To simplify the calculation of these terms we use $kh \gg 1$ for waves in deep water, and $k_{w0} \simeq k$, we may also use eq. (A.2.33) and eq. (A.2.34). These simplifications lead to :

$$\phi_{w,1} = \sum -\mathrm{i}\frac{s\sigma}{k}\mathrm{e}^{k_{w0}z}\mathrm{e}^{\gamma_w z}Z\mathrm{e}^{\mathrm{i}(\mathbf{k}\cdot\mathbf{x}-s\sigma t)} \tag{A.3.55}$$

And then we obtain the second order terms :

$$
\begin{aligned}
F_{w,2}(z=0) &= \left.\frac{\mathcal{P}_{w,1}^2}{2\alpha_w^2}\right|_0 - \left.\frac{(\nabla\phi_{w,1})^2}{2}\right|_0 \\
&= \sum \frac{ss'\sigma\sigma'}{2kk'}\left[\left(\frac{s\sigma s'\sigma'}{\alpha_w^2} - \mathbf{k}\mathbf{k}' + kk'\right)\right]ZZ'\mathrm{e}^{\mathrm{i}\Theta} \\
&\simeq \sum \sigma^2\left[1 + \delta_a^2(\frac{n^2}{2} - \sin^2\theta_a\left[1 - \cos^2(\varphi_2-\varphi)\right])\right]ZZ'\mathrm{e}^{\mathrm{i}\Theta}.
\end{aligned}
\tag{A.3.56}
$$

Using the law of cosines in a triangle,

$$k'^2 = k^2 + K^2 - 2\mathbf{k}\cdot\mathbf{K} \tag{A.3.57}$$

so that

$$\sqrt{k'} = \sqrt{k}\left(1 + \frac{K^2 - 2\mathbf{k}\cdot\mathbf{K}}{k^2}\right)^{1/4} \simeq \sqrt{k}\left(1 + \frac{1}{4}\frac{K^2 - 2\mathbf{k}\cdot\mathbf{K}}{k^2}\right) \tag{A.3.58}$$

we get

$$
\begin{aligned}
Q_{w,2}|_{z=0} &= +\left.\frac{\partial^2\phi_{w,1}}{\partial z^2}\right|_0 \zeta_1 - \nabla\phi_{w,1}|_0\cdot\nabla\zeta_1 \\
&\simeq -\mathrm{i}\sum\left[\frac{s\sigma k + s'\sigma'k'}{2} + \frac{\mathbf{k}\cdot\mathbf{k}'}{2}\left(\frac{s\sigma}{k} + \frac{s'\sigma'}{k'}\right)\right]ZZ'\mathrm{e}^{\mathrm{i}\Theta} \\
&= -\mathrm{i}\sum\left[s\sigma\frac{1}{2k}\left(k^2 + \mathbf{k}\cdot\mathbf{k}'\right) + s'\frac{\sigma'}{2k'}\left(k'^2 + \mathbf{k}\cdot\mathbf{k}'\right)\right]ZZ'\mathrm{e}^{\mathrm{i}\Theta} \\
&\simeq -\mathrm{i}\sum\left[s\sigma\frac{\mathbf{k}\cdot(\mathbf{k}+\mathbf{k}')}{2k} + s'\sigma'\frac{\mathbf{k}'\cdot(\mathbf{k}'+\mathbf{k})}{2k'}\right]ZZ'\mathrm{e}^{\mathrm{i}\Theta} \\
&\simeq -\mathrm{i}\sum\left[s\sigma\frac{\mathbf{k}\cdot\mathbf{K}}{2k} + s'\sigma'\frac{\mathbf{k}'\cdot\mathbf{K}}{2k'}\right]ZZ'\mathrm{e}^{\mathrm{i}\Theta} \\
&\simeq -\mathrm{i}\sum s\left[\frac{\sigma}{2k}\left(\mathbf{k}\cdot\mathbf{K} + \mathbf{k}'\cdot\mathbf{K}\right) + \frac{\sigma'k - \sigma k'}{2k'k}\left(\mathbf{k}'\cdot\mathbf{K}\right)\right]ZZ'\mathrm{e}^{\mathrm{i}\Theta} \\
&\simeq -\mathrm{i}\sum s\sigma k\left[\frac{K^2}{2k^2} + \sqrt{g}\frac{\sqrt{k}-\sqrt{k'}}{2k\sigma\sqrt{kk'}}\left(-\mathbf{k}\cdot\mathbf{K} + K^2\right)\right]ZZ'\mathrm{e}^{\mathrm{i}\Theta} \\
&\simeq -\mathrm{i}\sum s\sigma k\left[2\delta_a^2\sin^2\theta_a + \frac{1}{4k^2}\left(2\mathbf{k}\cdot\mathbf{K} - K^2\right)\right)\frac{1}{2k^2}\left(-\mathbf{k}\cdot\mathbf{K} + K^2\right)\right]ZZ'\mathrm{e}^{\mathrm{i}\Theta} \\
&\simeq -\mathrm{i}\sum s\sigma k\left[2\delta_a^2\sin^2\theta_a - \frac{K^2}{4k^2}\left(\frac{\mathbf{k}\cdot\mathbf{K}}{kK}\right)^2\right]ZZ'\mathrm{e}^{\mathrm{i}\Theta} \\
&\simeq -\mathrm{i}\sum s\sigma k\left[2\delta_a^2\sin^2\theta_a\left(1 - \frac{1}{2}\cos^2(\varphi_2-\varphi)\right)\right]ZZ'\mathrm{e}^{\mathrm{i}\Theta}.
\end{aligned}
\tag{A.3.59}
$$

In the air

In a similar way we obtain :

$$F_{a,2}(z=0) = \left.\frac{\mathcal{P}_{w,1}^2}{2\alpha_w^2}\right|_0 - \left.\frac{(\nabla\phi_{w,1})^2}{2}\right|_0$$

$$= \sum \frac{ss'\sigma\sigma'}{2k_a k'_a} \left[\frac{s\sigma s'\sigma'}{\alpha_a^2} - \mathbf{k}\mathbf{k}' + k_a k'_a \right] ZZ' \mathrm{e}^{\mathrm{i}\Theta}$$

$$= \sum ss'\sigma\sigma' (1 + 2\delta_a^2) \left[\frac{s\sigma s'\sigma'}{2kk'\alpha_a^2} - \frac{\mathbf{k}\mathbf{k}' - kk' + 2\delta_a^2 kk'}{2kk'} \right] ZZ' \mathrm{e}^{\mathrm{i}\Theta}$$

$$\simeq \sum \sigma^2 \left[1 + \delta_a^2 \left(\frac{3}{2} - \sin^2\theta_a \left[1 - \cos^2(\varphi_2 - \varphi) \right] \right) \right] ZZ' \mathrm{e}^{\mathrm{i}\Theta} \qquad (A.3.60)$$

And using :

$$\frac{s\sigma k + s'\sigma' k'}{2} - \frac{\mathbf{k}\cdot\mathbf{k}'}{2} \left(\frac{s\sigma}{k} + \frac{s'\sigma'}{k'} \right) = \quad s\sigma \frac{1}{2k} \left(k^2 - \mathbf{k}\cdot\mathbf{k}' \right) + s' \frac{\sigma'}{2k'} \left(k'^2 - \mathbf{k}\cdot\mathbf{k}' \right)$$

$$= \quad s\sigma \frac{1}{2k} \left(2k^2 - \mathbf{k}\cdot\mathbf{K} \right) + s' \frac{\sigma'}{2k'} \left(2k'^2 - \mathbf{k}'\cdot\mathbf{K} \right)$$

$$= \quad s\sigma k + s'\sigma' k' - \left[s\sigma \frac{\mathbf{k}\cdot\mathbf{K}}{2k} + s'\sigma' \frac{\mathbf{k}'\cdot\mathbf{K}}{2k'} \right]$$

$$\simeq \quad s\sigma k \left[2 - 2\delta_a^2 \sin^2\theta_a \left(1 - \frac{1}{2}\cos^2(\varphi_2 - \varphi) \right) \right]$$

$$(A.3.61)$$

one gets :

$$Q_{a,2}\big|_{z=0} = + \left. \frac{\partial^2 \phi_{a,1}}{\partial z^2} \right|_0 \zeta_1 - \nabla\phi_{a,1}\big|_0 \cdot \nabla\zeta_1$$

$$= +\mathrm{i} \sum \left[\frac{s\sigma k_a + s'\sigma' k'_a}{2} + \frac{\mathbf{k}\cdot\mathbf{k}'}{2} \left(\frac{s\sigma}{k_a} + \frac{s'\sigma'}{k'_a} \right) \right] ZZ' \mathrm{e}^{\mathrm{i}\Theta}$$

$$= +\mathrm{i} \sum \left[\frac{s\sigma k + s'\sigma' k'}{2} (1 - \delta_a^2) + \frac{\mathbf{k}\cdot\mathbf{k}'}{2} \left(\frac{s\sigma}{k} + \frac{s'\sigma'}{k'} \right) (1 + \delta_a^2) \right] ZZ' \mathrm{e}^{\mathrm{i}\Theta}$$

$$= +\mathrm{i} \sum \left[\frac{s\sigma k + s'\sigma' k'}{2} + \frac{\mathbf{k}\cdot\mathbf{k}'}{2} \left(\frac{s\sigma}{k} + \frac{s'\sigma'}{k'} \right) - \delta_a^2 \cdot \left(\frac{s\sigma k + s'\sigma' k'}{2} - \frac{\mathbf{k}\cdot\mathbf{k}'}{2} \left(\frac{s\sigma}{k} + \frac{s'\sigma'}{k'} \right) \right) \right] ZZ' \mathrm{e}^{\mathrm{i}\Theta}$$

$$\simeq +\mathrm{i} \sum s\sigma k 2\delta_a^2 \left[\sin^2\theta_a \left(1 - \frac{1}{2}\cos^2(\varphi_2 - \varphi) \right) - \left[1 - \delta_a^2 \sin^2\theta_a \left(1 - \frac{1}{2}\cos^2(\varphi_2 - \varphi) \right) \right] \right] ZZ' \mathrm{e}^{\mathrm{i}\Theta}$$

$$\simeq -\mathrm{i} \sum s\sigma k 2\delta_a^2 \left[1 - \sin^2\theta_a \left(1 - \frac{1}{2}\cos^2(\varphi_2 - \varphi) \right) (1 + \delta_a^2) \right] ZZ' \mathrm{e}^{\mathrm{i}\Theta} \qquad (A.3.62)$$

R_2 coefficient

$$R_2 = \quad -\left(\frac{\partial \mathcal{P}_{w,1}}{\partial z} - m \frac{\partial \mathcal{P}_{a,1}}{\partial z} \right)_0 \zeta_1 + \frac{g}{\alpha_a^2} (n^2 \mathcal{P}_{w,1} - m\mathcal{P}_{a,1})_0 \zeta_1 - \frac{g^2}{2\alpha_a^2} (n^2 - m^2)\zeta_1^2$$

$$= \quad \sum \left[\frac{\sigma^2 + \sigma'^2}{2} \cdot (1 - m) - \delta_a^2 \frac{\sigma^2 + \sigma'^2}{2} (n^2 + m(1 + \delta_a^2)) - \frac{\delta_a^2}{2} \frac{\sigma^2 + \sigma'^2}{2} (n^2 - m^2) \right] ZZ' \mathrm{e}^{\mathrm{i}\Theta}$$

$$\simeq \quad \sum \left[\sigma^2 \cdot \left(1 - m - \delta_a^2 \left(\frac{3n^2}{2} + m \left(1 - \frac{m}{2} + \delta_a^2 \right) \right) \right) \right] ZZ' \mathrm{e}^{\mathrm{i}\Theta} \qquad (A.3.63)$$

A.4   Matrix problem for the second order amplitudes

- Velocity continuity at $z = 0$

$$\left.\frac{\partial \phi_{a,2}}{\partial z}\right|_0 + Q_{a,2} = \left.\frac{\partial \phi_{w,2}}{\partial z}\right|_0 + Q_{w,2} \tag{A.4.64}$$

$$\Longleftrightarrow \nu_+ A_+ - \mu_- W_- - \mu_+ W_+ = \left.\frac{\partial \Phi_{w,2,p}}{\partial z}\right|_0 - \left.\frac{\partial \Phi_{a,2,p}}{\partial z}\right|_0 - Q_{a,2} + Q_{w,2} \tag{A.4.65}$$

- Pressure continuity at $z = 0$

$$\left(\frac{\partial \mathcal{P}_{w,2}}{\partial t} - m\frac{\partial \mathcal{P}_{a,2}}{\partial t}\right)_0 - g(1-m)\frac{\partial \zeta_2}{\partial t} = \frac{\partial R_2}{\partial t}$$

$$\Longleftrightarrow \left(\frac{\partial \mathcal{P}_{w,2}}{\partial t} - m\frac{\partial \mathcal{P}_{a,2}}{\partial t}\right)_0 - g(1-m)\left.\frac{\partial \phi_{a,2}}{\partial z}\right|_0 - g(1-m)Q_{a,2} = \frac{\partial R_2}{\partial t}$$

$$\Longleftrightarrow -\left.\frac{\partial^2 \phi_{w,2}}{\partial t^2}\right|_0 + \left.\frac{\partial F_{w,2}}{\partial t}\right|_0 + m\left.\frac{\partial^2 \phi_{a,2}}{\partial t^2}\right|_0 - m\left.\frac{\partial F_{a,2}}{\partial t}\right|_0 - g(1-m)\left.\frac{\partial \phi_{a,2}}{\partial z}\right|_0 - g(1-m)Q_{a,2} = \frac{\partial R_2}{\partial t}$$

$$\Longleftrightarrow -\Omega^2\left(-\phi_{w,2,p}(0) - W_+ - W_- + m\phi_{a,2,p}(0) + mA_+\right) + \mathrm{i}\Omega(mF_{a,2}(0) - F_{w,2}(0))$$

$$-g(1-m)(\phi'_{a,2,p}(0) + \nu A_+ + Q_{a,2}) = \frac{\partial R_2}{\partial t} \tag{A.4.66}$$

- Boundary condition at $z = -h$

This boundary condition is given as an example below. A more realistic boundary condition will be developed further:

$$\frac{\partial \Phi_{w,2,p}}{\partial z}(-h) + \mu_- W_- \mathrm{e}^{-\mu_- h} + \mu_+ W_2 \mathrm{e}^{-\mu_+ h} = 0 \tag{A.4.67}$$

Then we can write the boundary conditions system as a matrix problem,

$$\begin{pmatrix} \nu & -\mu_- & -\mu_+ \\ -m\Omega^2 - g(1-m)\nu & \Omega^2 & \Omega^2 \\ 0 & \mu_- \mathrm{e}^{-\mu_- h} & \mu_+ \mathrm{e}^{-\mu_+ h} \end{pmatrix} \cdot \begin{pmatrix} A_+ \\ W_- \\ W_+ \end{pmatrix} = \begin{pmatrix} \Lambda_1 \\ \Lambda_2 \\ \Lambda_3 \end{pmatrix} \tag{A.4.68}$$

Because we have assumed $kh \gg 1$ we can neglect the p_{bot} term of Ardhuin & Herbers (2013) in Λ_3, and the Λ forcing terms are,

$$\Lambda_1 = \left.\frac{\partial \phi_{w,2,p}}{\partial z}\right|_0 - \left.\frac{\partial \phi_{a,2,p}}{\partial z}\right|_0 - Q_{a,2} + Q_{w,2} \tag{A.4.69}$$

$$\Lambda_2 = -\Omega^2\left(\phi_{w,2,p}(0) - m\phi_{a,2,p}(0)\right) - \mathrm{i}\Omega\left(mF_{a,2}(0) - F_{w,2}(0)\right) + g(1-m)(\phi'_{a,2,p}(0) + Q_{a,2}) + \frac{\partial R_2}{\partial t}$$

$$\Lambda_3 = -\left.\frac{\partial \phi_{w,2,p}}{\partial z}\right|_{-h} \tag{A.4.70}$$

SIMPLIFIED FORMS USED:

$$F_{w,2}(z=0) \simeq \sum \sigma^2[1-\sin^2\theta_a\delta_a^2(1-\cos^2(\varphi_2-\varphi))+\frac{\delta_a^2 n^2}{2}]ZZ'e^{i\Theta} \qquad \mathbf{O(\sigma^2)+O(\sigma^2\delta_a^2\sin^2\theta_a)}$$

$$Q_{w,2}(z=0) \simeq -i\sum s\sigma k2\sin^2\theta_a\delta_a^2(1-\frac{1}{2}\cos^2(\varphi_2-\varphi))ZZ'e^{i\Theta} \qquad \mathbf{O(\sigma\delta_a^2\sin^2\theta_a)}$$

$$F_{a,2}(z=0) \simeq \sum \sigma^2[1-\sin^2\theta_a\delta_a^2(1-\cos^2(\varphi_2-\varphi))+\frac{3}{2}\delta_a^2]ZZ'e^{i\Theta} \qquad \mathbf{O(\sigma^2)+O(\sigma^2\delta_a^2\sin^2\theta_a)}$$

$$Q_{a,2}(z=0) \simeq -i\sum s\sigma k2\delta_a^2[1-\sin^2\theta_a(1-\frac{1}{2}\cos^2(\varphi_2-\varphi))]ZZ'e^{i\Theta} \qquad \mathbf{O(\sigma\delta_a^2)+O(\sigma\delta_a^2\sin^2\theta_a)}$$

$$\phi_{w,2,p}(z=0) \simeq i\sum s\sigma\delta_a^2 n^2 ZZ'e^{i\Theta} \qquad \mathbf{O(\sigma\delta_a^2 n^2)}$$

$$\left.\frac{\partial\phi_{w,2,p}}{\partial z}\right|_{z=0} \simeq i\sum s\sigma 2k\delta_a^2 n^2 ZZ'e^{i\Theta} \qquad \mathbf{O(\sigma\delta_a^2 n^2)}$$

$$\phi_{a,2,p}(z=0) \simeq i\sum s\sigma\delta_a^2 ZZ'e^{i\Theta} \qquad \mathbf{O(\sigma\delta_a^2)+O(\sigma\delta_a^2\sin^2\theta_a)}$$

$$\left.\frac{\partial\phi_{a,2,p}}{\partial z}\right|_{z=0} \simeq -i\sum s\sigma 2k\delta_a^2 ZZ'e^{i\Theta} \qquad \mathbf{O(\sigma\delta_a^2)}$$

$$R_2 \simeq \sum -\sigma^2(1-m-\delta_a^2(3n^2/2+m))ZZ'e^{i\Theta} \qquad \mathbf{O(\sigma^2)}$$

$$\frac{\partial R_2}{\partial t} \simeq is\sum 2\sigma^3(1-m-\delta_a^2(3n^2/2+m))ZZ'e^{i\Theta} \qquad \mathbf{O(\sigma^3)}$$

$$\nu_{\pm} = 2i\delta_a k\left(\pm\cos\theta_a - i\frac{\delta_a}{4}\right)$$

$$\mu_{\pm} = 2i\delta_a k\left(\mp il - i\frac{\delta_a}{4}n^2\right)$$

$$\sin\theta_a = \frac{K\alpha_a}{\Omega},$$

$$\Omega \simeq 2\sigma, \qquad n = \frac{\alpha_a}{\alpha_w}, \qquad l = (\sin^2\theta_a - n^2)^{1/2},$$

$$\delta_w = \left(\frac{g}{k\alpha_a^2}\right)^{1/2}\frac{\alpha_a}{\alpha_w} = \delta_a n$$

A.4.1 Matrix 2x2 : BGKN73

When the ocean is assumed to have an infinite depth, we consider the atmosphere and ocean to be half spaces, with the continuity of velocity and pressure at $z = 0$ giving a 2 by 2 matrix,

$$M = \begin{pmatrix} \nu & -\mu_- \\ -m\Omega^2 - g(1-m)\nu & \Omega^2 \end{pmatrix} \tag{A.4.71}$$

The solution is given by Cramer's method

$$A_+ = \frac{\det \mathbf{M}_1}{\det \mathbf{M}} \tag{A.4.72}$$

with

$$\det \mathbf{M}_1 = \begin{vmatrix} \Lambda_1 & -\mu_- \\ \Lambda_2 & \Omega^2 \end{vmatrix} \tag{A.4.73}$$

$$\det \mathbf{M} = \begin{vmatrix} \nu & -\mu_- \\ -m\Omega^2 - g(1-m)\nu & \Omega^2 \end{vmatrix} = \nu\Omega^2 - m\mu_-\Omega^2 - g(1-m)\nu\mu_- \tag{A.4.74}$$

Here are the different pieces of $\det \mathbf{M}$,

- $\nu\Omega^2$:

$$\nu\Omega^2 = 4\sigma^2 \left(\frac{g}{2\alpha_a^2} + i\frac{\Omega}{\alpha_a}\cos\theta_a \right)$$

$$= i8\sigma^2 k \left(-i\frac{g}{4k\alpha^2} + \frac{\sigma}{k\alpha_a}\cos\theta_a \right)$$

$$= {\color{magenta}8i\sigma^2 k\delta_a} \left(\cos\theta_a - i\frac{\delta_a}{4} \right)$$

- $-m\mu_-\Omega^2$:

$$-m\mu_-\Omega^2 \simeq -m4\sigma^2 \cdot 2i\delta_a k \left[il - i\frac{\delta_a}{2}n^2 \right]$$

$$\simeq -8i\sigma^2 k\delta_a m\,[il]$$

- $-g(1-m)\nu\mu_-$:

$$-g(1-m)\nu\mu_- \simeq -g(1-m)2i\delta_a k \left(\cos\theta_a - i\frac{\delta_a}{4} \right) 2i\delta_a k \left(il + i\frac{\delta_a}{4}n^2 \right)$$

$$\simeq 4\sigma^2 \delta_a k\delta_a (il\cos\theta_a + O(\delta_a))$$

$$\simeq 8i\sigma^2 k\delta_a \left[\frac{1}{2}\delta_a l\cos\theta_a \right]$$

This gives $\det \mathbf{M}$, keeping only the second order in δ_a (the δ_a that is a factor should be remove alongside with all the factors in ${\color{magenta}\text{magenta}}$ when doing the ratio giving us a first order in δ_a).

$$\det \mathbf{M} = i8\sigma^2 \delta_a k \left[-i\frac{\delta_a}{4} + \cos\theta_a - iml + \frac{\delta_a}{2}\cos\theta_a l \right]$$

$$\det \mathbf{M} \simeq {\color{magenta}8i\sigma^2 k\delta_a} \left[\cos\theta_a \left(1 + {\color{green}\frac{\delta_a}{2}}l \right) - i\left(\frac{\delta_a}{4} + ml \right) \right] \tag{A.4.75}$$

The term in ${\color{green}\textit{green}}$ is different from BGKN73 denominator. The difference is coming from the $\partial\zeta_2/\partial t$ term in the Bernoulli equation for the pressure at $z = 0$.
Now the numerator is,

$$\det \mathbf{M}_1 = \Lambda_1\Omega^2 + \mu_-\Lambda_2$$

$$= \Omega^2 \left(\left.\frac{\partial\phi_{w,2,p}}{\partial z}\right|_0 - \left.\frac{\partial\phi_{a,2,p}}{\partial z}\right|_0 - Q_{a,2} + Q_{w,2} \right) + \mu_- \left(-\Omega^2 \big(\Phi_{w,2,p}(0) \right.$$

$$-m\Phi_{a,2,p}(0)) - \mathrm{is}\Omega\big(mF_{a,2}(0) - F_{w,2}(0)\big) + g(1-m)(\Phi'_{a,2,p}(0) + Q_{a,2}) + \frac{\partial R_2}{\partial t}\bigg)$$

$$\simeq \quad \Omega^2\left(\left.\frac{\partial\phi_{w,2,p}}{\partial z}\right|_0 - \left.\frac{\partial\phi_{a,2,p}}{\partial z}\right|_0 - Q_{a,2} + Q_{w,2}\right)$$

$$+\mu_-\left(\mathrm{is}\Omega F_{w,2}(0) + \frac{\partial R_2}{\partial t}\right) \tag{A.4.76}$$

where eqs. (A.3.46), (A.3.54) , (A.3.62), (A.3.56) give

$$\Omega^2\left.\frac{\partial\phi_{w,2,p}}{\partial z}\right|_0 \quad = \quad 4\sigma^2\cdot\mathrm{is}\delta_a^2 n^2\sigma 2k$$

$$\simeq \quad 8\mathrm{i}\sigma^2 k\delta_a s\sigma\delta_a n^2 \tag{A.4.77}$$

$$-\Omega^2\left.\frac{\partial\phi_{a,2,p}}{\partial z}\right|_0 \quad = \quad -4\sigma^2\cdot(-\mathrm{i})s2\sigma k\delta_a^2$$

$$\simeq \quad 8\mathrm{i}\sigma^2 k\delta_a s\sigma\delta_a \tag{A.4.78}$$

$$-\Omega^2 Q_{a,2} \quad \simeq \quad -4\sigma^2\cdot(-\mathrm{i})s2\sigma k\delta_a^2\left(1-\sin^2\theta_a\left(1-\frac{1}{2}\cos^2(\varphi_2-\varphi)\right)\right)$$

$$\simeq \quad 8\mathrm{i}\sigma^2 k\delta_a\sigma s\delta_a\left(1-\sin^2\theta_a\left(1-\frac{1}{2}\cos^2(\varphi_2-\varphi)\right)\right) \tag{A.4.79}$$

$$+\Omega^2 Q_{w,2} \quad \simeq \quad 4\sigma^2\cdot\mathrm{i}2\sigma sk\delta_a^2\left(-\sin^2\theta_a\left(1-\frac{1}{2}\cos^2(\varphi_2-\varphi)\right)\right)$$

$$\simeq \quad 8\mathrm{i}\sigma^2 k\delta_a\sigma s\delta_a\left(-\sin^2\theta_a\left(1-\frac{1}{2}\cos^2(\varphi_2-\varphi)\right)\right) \tag{A.4.80}$$

$$+\mathrm{is}\Omega\mu_- F_{w,2}(0) \quad \simeq \quad \mathrm{i}2s\sigma\cdot 2\delta_a k(\frac{\delta_a}{4}n^2 - l)\cdot\sigma^2[1-\sin^2\theta_a\delta_a^2(1-\cos^2(\varphi_2-\varphi)) + \delta_a^2 n^2/2]$$

$$\simeq \quad -8\mathrm{i}\sigma^2 k\delta_a\sigma s\left[\frac{l}{2} - \frac{\delta_a}{8}n^2 - \frac{l}{2}\sin^2\theta_a\delta_a^2\left[1-\cos^2(\varphi_2-\varphi)\right]\right] \tag{A.4.81}$$

$$\mu_-\frac{\partial R_2}{\partial t} \quad = \quad 2\delta_a k\left(\frac{\delta_a}{4}n^2 - l\right)\mathrm{is}2\sigma^3(1-m)$$

$$\simeq \quad -8\mathrm{i}\delta_a k\sigma^2\sigma s\left[\frac{l}{2} - \frac{\delta_a}{8}n^2\right]$$

Collecting all the terms we find,

$$\det\mathbf{M}_1 \simeq -8\mathrm{i}\sigma^2 k\delta_a\sigma s\left[l - \frac{\delta_a}{4}n^2 - \delta_a + 2\delta_a\sin^2\theta_a(1-\frac{1}{2}\cos^2\varphi_2) - \delta_a\left(n^2+1\right)\right]$$

$$\simeq -8\mathrm{i}\sigma^2 k\delta_a\sigma s\left[l - \delta_a\left[2 - 2\sin^2\theta_a(1-\frac{1}{2}\cos^2\varphi_2) + \frac{5}{4}n^2\right]\right]$$

$$\simeq -8\mathrm{i}\sigma^2 k\delta_a\sigma s\left[l - 2\delta_a\left[1 - \sin^2\theta_a(1-\frac{1}{2}\cos^2\varphi_2) + \frac{5}{8}n^2\right]\right] \tag{A.4.82}$$

Then, we find the same expression as in BGKN73 numerator and the δ_a term is larger than the one in WG06, with 2 instead of $3/2$.

The main term arises from the pressure boundary condition and from the difference between the pressure and the temporal derivative of the potential velocity.

We recall that the homogeneous atmospheric potential that radiates from the surface is given by eq. (A.3.47),

$$\phi_{a,h,2}(z) = \sum sA_+ ZZ'\mathrm{e}^{\nu+z}\mathrm{e}^{\mathrm{i}\Theta}, \tag{A.4.83}$$

with

$$\nu \simeq \frac{g}{2\alpha_a^2} + \mathrm{i}\frac{\Omega}{\alpha_a}\cos\theta_a \tag{A.4.84}$$

and

$$A_+ \simeq -\sigma\frac{l - 2\delta_a\left[1 - \sin^2\theta_a\left(1-\frac{1}{2}\cos^2(\varphi_2-\varphi)\right) + \frac{5}{8}n^2\right]}{\cos\theta_a\left(1+\frac{\delta_a}{2}l\right) - \mathrm{i}\left(\frac{\delta_a}{4}+ml\right)}. \tag{A.4.85}$$

A.5 Adding the solid Earth

The solid Earth is characterised by density ρ_s, compression velocity α_s and shear velocity β.

Then the velocity potentials write as,

$$\phi_{w,2} = \sum \left[\left(W_- e^{\mu_- z} + W_+ e^{\mu_+ z} \right) ZZ' + \Phi_{w,2,p} \right] e^{i\Theta}, \qquad \text{for} \ -h < z < \zeta$$

$$\phi_{a,2} = \sum \left[sA_+ e^{\nu_+ z} ZZ' + \Phi_{w,2,p} \right] e^{i\Theta}, \qquad \text{for} \ \zeta < z$$

All the potentials share the same phase, $\Theta = \mathbf{K}\cdot\mathbf{x} - \Omega t$, $\Omega = s(\sigma + \sigma')$, but they differ by their vertical structures and amplitudes.

The boundary conditions for ocean/atmosphere interfaces remain the same. For the ocean bottom, the motion in the crust is given by velocity potentials for compression and shear waves in the solid Earth, we follow here the treatment in Ardhuin & Herbers (2013). Neglecting the effect of gravity, crustal motions can be separated into an irrotational part with a velocity potential ϕ_c and a rotational part with a stream function ψ, both solutions to Laplace's equation.

$$\phi_c = C_p e^{\chi_p(z+h)} e^{i\Theta}, \tag{A.5.86}$$

$$\psi = C_s e^{\chi_s(z+h)} e^{i\Theta}, \tag{A.5.87}$$

with

$$\chi_p = \sqrt{K^2 - \frac{\Omega^2}{\alpha_s^2}}, \quad \text{and} \quad \chi_s = \sqrt{K^2 - \frac{\Omega^2}{\beta^2}}. \tag{A.5.88}$$

where α_s and β are respectively the compression and the shear wave speed in the crust. Typically β ranges from 2800 to 3200 m s^{-1}; $\alpha_s = \sqrt{3}\beta$. And $\rho_s \simeq 2500$ kg m^{-3}. The constants C_p and C_s have dimensions of m^2/s and are determined by the boundary conditions at the ocean bottom.

With λ_e and μ_e the Lame elasticity parameters of the crust, Hooke's law of elasticity gives

$$\tau_{zz} = \lambda_e \left(\frac{\partial \xi_x}{\partial x} + \frac{\partial \xi_z}{\partial z} \right) + 2\mu_e \frac{\partial \xi_z}{\partial z}, \tag{A.5.89}$$

$$\tau_{xz} = \mu_e \left(\frac{\partial \xi_x}{\partial z} + \frac{\partial \xi_z}{\partial x} \right). \tag{A.5.90}$$

We recall that the compression and shear velocity are related to the Lame parameters,

$$\alpha_c^2 = \frac{\lambda_e + 2\mu_e}{\rho_s}, \tag{A.5.91}$$

$$\beta^2 = \frac{\mu_e}{\rho_s}. \tag{A.5.92}$$

The zero tangential stress on the ocean bottom $\tau_{xz}(z = -h) = 0$ yields the following relationship between C_p and C_s, which is typical of seismic Rayleigh waves (Stoneley, 1926),

$$C_s = \frac{2iK\chi_p}{\chi_s^2 + K^2} C_p = \frac{2i\beta^2 K\chi_p}{2\beta^2 K^2 - \Omega^2} C_p. \tag{A.5.93}$$

We can now eliminate C_p, using the continuity of the vertical velocity at the bottom,

$$\frac{\partial \phi_2}{\partial z} = \frac{\partial \phi_c}{\partial z} + \frac{\partial \psi}{\partial x} \quad \text{at} \quad z = -h \tag{A.5.94}$$

$$W_+\mu_+ e^{-\mu_+ h} + W_-\mu_- e^{-\mu_- h} = \chi_p C_p + iKC_s \tag{A.5.95}$$

$$= \chi_p C_p + iK \frac{2i\beta^2 K\chi_p}{2\beta^2 K^2 - \Omega^2} C_p \tag{A.5.96}$$

$$= \frac{\chi_p \Omega^2}{\Omega^2 - 2K^2\beta^2} C_p \tag{A.5.97}$$

and the continuity of normal stresses, using the result from Ardhuin et al. (2013) :

$$-\rho_w \frac{\partial \phi_2}{\partial t} = \tau_{zz} \quad z = -h \tag{A.5.98}$$

$$\rho_w \Omega \mathrm{i} s e^{-\mu_+ h} W_+ + \rho_w \Omega \mathrm{i} s W_- e^{-\mu_- h} = r_{AH} C_p \tag{A.5.99}$$

$$\tag{A.5.100}$$

where

$$r_{AH} = \frac{\mathrm{i}s}{\Omega}\rho_s \left[-\frac{4\beta^4 K^2 \chi_p \chi_s}{\Omega^2 - 2K^2\beta^2} + \left(\Omega^2 - 2K^2\beta^2\right) \right]. \tag{A.5.101}$$

Defining

$$r_{\pm} = \frac{\mathrm{i}s\rho_w\Omega \dfrac{\chi_p \Omega^2}{\Omega^2 - 2K^2\beta^2}}{\mu_{\pm} r_{AH}} \tag{A.5.102}$$

$$= \frac{\mathrm{i}s\rho_w\Omega \dfrac{\chi_p \Omega^2}{\Omega^2 - 2K^2}}{\dfrac{\mathrm{i}}{\Omega}\mu_{\pm}\rho_s \left[-\dfrac{4\beta^4 K^2 \chi_p \chi_s}{\Omega^2 - 2K^2\beta^2} + \left(\Omega^2 - 2K^2\beta^2\right) \right]}, \tag{A.5.103}$$

$$= \frac{\rho_w \chi_p \Omega^4}{\mu_{\pm}\rho_s \left[\left(\Omega^2 - 2K^2\beta^2\right)^2 - 4\beta^4 K^2 \chi_p \chi_s \right]} \tag{A.5.104}$$

we combine these two boundary conditions by subtracting r times the second equation to find a condition for the bottom velocities on the water side,

$$\mu^+(1 - r_+)e^{-\mu_+ h}W_+ + \mu^-(1 - r_-)\mu_- e^{-\mu_- h}W_- = 0. \tag{A.5.105}$$

We thus have the matrix equation

$$\mathbf{M}(A_+, \, W_-, \, W_+)^T = (\Lambda_1, \, \Lambda_2, \, 0)^T \tag{A.5.106}$$

with

$$\mathbf{M} = \begin{pmatrix} \nu_+ & -\mu_- & -\mu_+ \\ -m\Omega^2 - g(1-m)\nu_+ & \Omega^2 & \Omega^2 \\ 0 & (1 - r_-)\,\mu_- e^{-\mu_- h} & (1 - r_+)\,\mu_+ e^{-\mu_+ h} \end{pmatrix} \tag{A.5.107}$$

and we use the following simplification,

$$\Lambda_1 = \left.\frac{\partial \Phi_{w,2,p}}{\partial z}\right|_0 - \left.\frac{\partial \Phi_{a,2,p}}{\partial z}\right|_0 - Q_{a,2} + Q_{w,2} \tag{A.5.108}$$

$$\Lambda_2 = \mathrm{i}\Omega F_{w,2}(0) + \frac{\partial R_2}{\partial t} \tag{A.5.109}$$

Assuming $\mu_+ \simeq -\mu_- \simeq \mu$ the matrix equation simplifies as:

$$\mathbf{M} = \begin{pmatrix} \nu_+ & \mu & -\mu \\ -m\Omega^2 - g(1-m)\nu_+ & \Omega^2 & \Omega^2 \\ 0 & -(1 + r)\,\mu e^{\mu h} & (1 - r)\,\mu e^{-\mu h} \end{pmatrix} \tag{A.5.110}$$

A.6   From amplitude to power

A.6.1   Particular case of a pair of wave trains

Here we first consider the pressure amplitude and variance in the water layer, which has been well studied and measured (Cox & Jacobs, 1989; Ardhuin et al., 2013).

In the case of only two wave trains of opposing direction with wave numbers k_1 and $k_2 \simeq -k_1$ with surface elevation

$$\zeta = a_1 \cos(k_1 x - \sigma_1 t) + a_2 \cos(k_2 x - \sigma_2 t) \tag{A.6.111}$$

and velocity field

$$w(z = 0) = a_1 \sigma_1 \sin(k_1 x - \sigma_1 t) + a_2 \sigma_2 \sin(k_2 x - \sigma_2 t) \tag{A.6.112}$$

$$u(z = 0) = a_1 \sigma_1 \cos(k_1 x - \sigma_1 t) - a_2 \sigma_2 \cos(k_2 x - \sigma_2 t) \tag{A.6.113}$$

the second order pressure is, keeping only the small wavenumber components,

$$p_2 = \rho_w(u^2 + w^2) = -2\rho \sigma_1 \sigma_2 a_1 a_2 \cos\left[Kx + \Omega t\right] \tag{A.6.114}$$

Now we consider the variance of the pressure,

$$
\begin{aligned}
< p_2^2 > & = 4\rho_w^2 \sigma_1^2 \sigma_2^2 a_1^2 a_2^2 / 2 & \text{(A.6.115)} \\
& = 2\rho_w^2 \sum_{k+k'=K} \sigma^2 \sigma'^2 a^2 a'^2 / 2 & \text{(A.6.116)} \\
& = 8\rho_w^2 \sigma_1^2 \sigma_2^2 \frac{a_1^2}{2} \frac{a_2^2}{2} & \text{(A.6.117)} \\
& \simeq \frac{1}{2}\rho_w^2 \Omega^4 E_1 E_2 & \text{(A.6.118)} \\
& = \frac{1}{4}\rho_w^2 \Omega^4 \sum_{k+k'=K} EE'. & \text{(A.6.119)}
\end{aligned}
$$

A.6.2   Case of random waves

$$F_{p,2h}(\mathbf{K}, f_s) = 2 \lim_{|d\mathbf{K}|\to 0, df_s \to 0} \frac{\left\langle |P_{2h}^+|^2 \right\rangle}{dK_x dK_y df_s} \tag{A.6.120}$$

with

$$
\begin{aligned}
P_{2h}^s & = \rho_a \mathcal{P}_{a,2,h} = -\rho_a \frac{\partial \phi_{a,2,h}}{\partial t} \\
& = -\rho_a \frac{\partial}{\partial t}\left(\frac{R_a(\mathbf{K})}{\rho_w 2\sigma'} p_{\text{surf}}^{s,s'}(\mathbf{K}, \Omega)\right)
\end{aligned}
$$

remembering

$$p_{\text{surf}}^{s,s'}(\mathbf{K}, \Omega) = \rho_w \sum_{\mathbf{k},s,\mathbf{k}',s'} D_z(\mathbf{k}, s, \mathbf{k}', s') ZZ' e^{i\Theta} \tag{A.6.121}$$

one gets :

$$
\begin{aligned}
P_{2h}^s & = \rho_a \sum_{\mathbf{k},s,\mathbf{k}',s'} i R_a(\mathbf{K}) \frac{(s\sigma + s'\sigma')}{2\sigma'} D_z(\mathbf{k}, s, \mathbf{k}', s') ZZ' e^{i\Theta} \\
& = \rho_a \sum_{\mathbf{k},s,\mathbf{k}'} i s R_a(\mathbf{K}) \frac{(\sigma + \sigma')}{2\sigma'} D_z(\mathbf{k}, s, \mathbf{k}', s) ZZ' e^{i\Theta} & \text{(A.6.122)}
\end{aligned}
$$

Then,

$$2|P_{2h}^+|^2 = 2\rho_a^2 \left| \sum_{\mathbf{k}+\mathbf{k}'=\mathbf{K}, \sigma+\sigma'=\Omega} R_a(\mathbf{K}) \frac{(\sigma + \sigma')}{2\sigma'} D_z(\mathbf{k}, +, \mathbf{k}', +) ZZ' e^{i\Theta} \right|^2$$

$$= 2\rho_a^2 \cdot 2 \sum_{\mathbf{k}+\mathbf{k}'=\mathbf{K},\sigma+\sigma'=\Omega} |R_a(\mathbf{K})|^2 \frac{(\sigma+\sigma')^2}{4\sigma'^2} |D_z(\mathbf{k},+,\mathbf{k}',+)|^2 |Z|^2 |Z'|^2 \quad \text{(A.6.123)}$$

And the spectrum density of the source writes :

$$F_{p,2h}(\mathbf{K},f_s) = \lim_{|d\mathbf{K}|\to0,df_s\to0} \frac{1}{K_x dK_y df_s} \sum_{\mathbf{k}+\mathbf{k}'=\mathbf{K},\sigma+\sigma'=\Omega} \frac{(\sigma+\sigma')^2}{\sigma'^2} R_a(\mathbf{K})^2 \rho_a^2 |D_z(\mathbf{k},+,\mathbf{k}',+)|^2 |Z|^2 |Z'|^2$$

(A.6.124)

using the definition :

$$E(k_x,k_y) = 2 \lim_{dk_x,dk_y\to0} \frac{|Z|^2}{dk_x dk_y} \quad \text{(A.6.125)}$$

$$F_{p,2h}(\mathbf{K},f_s) = \lim_{|d\mathbf{K}|\to0,df_s\to0} \frac{dk_x dk_x dk_x' dk_y'}{4dK_x dK_y df_s} \sum_{\mathbf{k},s,\mathbf{k}'} \frac{(\sigma+\sigma')^2}{\sigma'^2} R_a(\mathbf{K})^2 \rho_a^2 |D_z(\mathbf{k},+,\mathbf{k}',+)|^2 E(k_x,k_y) E(k_x',k_y')$$

(A.6.126)

Taking the limit to continuous sums and using a change of variable from (k_x,k_y,k_x',k_y') to (f_s,φ,K_x,K_y), with $K_x = k_x + k_x'$, $K_y = k_y + k_y'$ and $f_s = (\sqrt{gk} + \sqrt{gk'})/(2\pi)$ the Jacobian of the coordinate transform is

$$\det\left(\frac{\partial f_s \partial\varphi \partial K_x \partial K_y}{\partial k_x \partial k_y \partial k_x' \partial k_y'}\right) = \begin{vmatrix} g\cos\varphi/(4\pi\sigma) & -\sin\varphi/k & 1 & 0 \\ g\sin\varphi/(4\pi\sigma) & \cos\varphi/k & 0 & 1 \\ g\cos\varphi'/(4\pi\sigma') & 0 & 1 & 0 \\ g\sin\varphi'/(4\pi\sigma') & 0 & 0 & 1 \end{vmatrix} = \frac{g^2}{4\pi\sigma^3\sigma'}\left[\sigma' - \sigma\cos(\varphi-\varphi')\right],$$

(A.6.127)

$$\int F_{p,2h}(\mathbf{K},f_s) dK_x dK_y df_s = \rho_a^2 \int \frac{(\sigma+\sigma')^2}{4\sigma'^2} |R_a|^2 |D_z|^2 E(k_x,k_y) E(k_x,k_y) dk_x dk_y dk_x' dk_y'$$

$$= \rho_a^2 \int \frac{(\sigma+\sigma')^2}{4\sigma'^2} |R_a|^2 |D_z|^2 \frac{E(k_x,k_y) E(k_x',k_y') 4\pi\sigma^3\sigma'}{g^2 \left[\sigma' - \sigma\cos(\varphi-\varphi')\right]} df_s d\varphi dK_x dK_y.$$

To transform the spectra to frequency-direction spectra we use the Jacobian :

$$E(f,\varphi) = \frac{4\pi\sigma^3}{g^2} E(k_x,k_y) \quad \text{(A.6.128)}$$

And then obtain :

$$\int F_{p,2h}(\mathbf{K},f_s) dK_x dK_y df_s = \frac{1}{2} g^2 \rho_a^2 \int f_s \frac{(\sigma+\sigma')}{4\sigma'^4} |R_a|^2 |D_z|^2 \frac{E(f,\varphi) E(f',\varphi')}{\left[\sigma' - \sigma\cos(\varphi-\varphi')\right]} df_s d\varphi dK_x dK_y.$$

Now we use the unicity of the Fourier transform to identify the spectral density in the left and right hand sides and considering $|D_z(\mathbf{k},+,\mathbf{k}',+)| \simeq 2\sigma\sigma'$:

$$F_{p,2h}(\mathbf{K},f_s) = \frac{1}{2} g^2 \rho_a^2 f_s \int_0^{2\pi} \frac{\sigma^2(\sigma+\sigma')}{\sigma'^2} |R_a|^2 \frac{E(f,\varphi) E(f',\varphi')}{\sigma' - \sigma\cos(\varphi-\varphi')} d\varphi. \quad \text{(A.6.129)}$$

A.6.3 Acoustic energy in the water column

We take the acoustic energy per unit of horizontal surface to be twice the kinetic energy. Considering only $K < \Omega/\alpha_w$, we have

$$E_w = \rho_w \int_{-h}^0 \left(u^2 + w^2\right) dz \quad \text{(A.6.130)}$$

Now using eq. (45)

$$E_w = \rho_w \int_{-h}^0 \sum \left(K^2 + \mu^2\right) W_-^2 \left(\frac{1+r}{1-r}\right)^2 \cos^2(|\mu|z) dz \quad \text{(A.6.131)}$$

155

$$= \rho_w \int_{\theta_{a,1}}^{\theta_{a,2}} \left(K^2 + |\mu|^2\right) F_{p,2h}(\theta_a, \varphi_2, f_s) \left| \frac{A}{P_{2,h}^+} \frac{W_-}{A} \frac{1+r}{1-r} \right|^2 \left(\frac{h}{2} + \frac{\sin 2|\mu|h}{4|\mu|} \right) \mathrm{d}\theta_a \mathrm{d}\varphi_2$$

$$(A.6.132)$$

with

$$\left| \frac{W_-}{A} \frac{1+r}{1-r} \right| = \left| \frac{2\nu(1+r)}{\mu \left[\mathrm{i} \sin(|\mu|h) + r \cos(|\mu|h) \right]} \right| \qquad (A.6.133)$$

and

$$\left| \frac{A}{P_{2,h}^+} \right| = \frac{1}{(\sigma + \sigma')\rho_a}. \qquad (A.6.134)$$

Now, looking at the ratio of the acoustic energy and radiated power for any θ_a and φ_2 we have,

$$Q_{max} = \frac{\Omega E_w}{F_{p,2h}(\theta_a, \varphi_2, f_s)/(\rho_a \alpha_a)} \qquad (A.6.135)$$

$$= \Omega \rho_w \rho_a \alpha_a \left(K^2 + |\mu|^2\right) \left| \frac{A}{P_{2,h}^+} \frac{W_-}{A} \frac{1+r}{1-r} \right|^2 \left(\frac{h}{2} + \frac{\sin 2|\mu|h}{4|\mu|} \right) \qquad (A.6.136)$$

$$= \frac{\rho_w \alpha_a}{\rho_a \Omega} \left(K^2 + |\mu|^2\right) \left| \frac{W_-}{A} \frac{1+r}{1-r} \right|^2 \left(\frac{h}{2} + \frac{\sin 2|\mu|h}{4|\mu|} \right) \qquad (A.6.137)$$

Microbarom radiation and propagation model assessment using infrasound recordings: a vespagram-based approach[1]

Ekaterina Vorobeva[1,2] (ekaterina.vorobeva@ntnu.no), Marine De Carlo[3,4], Sven Peter Näsholm[2,5], Alexis Le Pichon[3], Fabrice Ardhuin[4]

[1] Department of Physics, Norwegian University of Science and Technology, Trondheim, Norway

[2] NORSAR, Kjeller, Norway

[3] CEA, DAM, DIF, F-91297, Arpajon, France

[4] Univ. Brest, CNRS, IRD, Ifremer, Laboratoire d'Océanographie Physique et Spatiale (LOPS), IUEM, Brest, France

[5] Department of Informatics, University of Oslo, Oslo, Norway

Contents

Keypoints:

- Vespa array signal processing as a tool to compare infrasound recordings to modelled microbarom soundscapes in all directions simultaneously.

- Model resolution is harmonized by smoothing with a kernel corresponding to the frequency-dependent array resolution.

- Vespagrams can capture (sub)-seasonal variations of microbarom's parameters, in particular, during sudden stratospheric warming events.

Abstract

This study investigates the use of a vespagram-based approach as a tool for multi-directional comparison between simulated microbarom soundscapes and infrasound data recorded at ground-based array stations. Data recorded at the IS37 station in northern Norway during $2014 - 2019$ have been processed to generate vespagrams (velocity spectral analysis) for five frequency bands between 0.1 and 0.6 Hz. The back-azimuth resolution between

---

vespagrams and microbarom model is harmonized by smoothing the modelled soundscapes along the back-azimuth axis with a kernel corresponding to the frequency-dependent array resolution. An estimate of similarity between the output of a microbarom radiation and propagation model and infrasound observations is then generated based on the image processing approach of mean-square difference. The analysis revealed that vespagrams can monitor (sub)-seasonal variations in microbarom azimuth distribution, amplitude, and frequency, as well as changes during sudden stratospheric warming. Vespagram-based approach is computationally inexpensive, can uncover microbarom source variability and has potential for near-real-time stratospheric diagnostics and atmospheric model assessment.

Key words: infrasound, vespa, microbaroms, array signal processing, stratosphere, atmospheric models

B.1 Introduction

Microbaroms are infrasound waves with frequencies typically between 0.1 and 0.6 Hz generated by non-linear interaction between counter-propagating ocean waves. Because of the low frequencies, microbaroms can penetrate the middle atmosphere and return back to ground at long ranges. Hence there is potential to exploit this source to probe the dynamics of this altitude range, where the representation of the atmospheric dynamics in model products is often poorly constrained (Polavarapu et al., 2005; Rienecker et al., 2011; Smith, 2012; Amezcua et al., 2020).

The term "microbarom" was established by Benioff & Gutenberg (1939) who described quasi-continuous pressure fluctuations with periods of $0.5 - 5$ s recorded by two electromagnetic barographs installed by the Seismological Laboratory, California Institute of Technology, Pasadena, USA. Following Benioff & Gutenberg (1939), several microbarom studies were performed by scientists around the globe. Joint observation of microbaroms and microseisms (quasi-continuous fluctuations of ground displacement generated by the ocean waves) in California, USA (Gutenberg & Benioff, 1941), Christchurch, New Zealand (Baird & Banwell, 1940), Fribourg, Switzerland (Saxer, 1945, 1954; Dessauer et al., 1951) and New York, USA (Donn & Posmentier, 1967) demonstrated that the microbarom signals originate from the ocean.

Thereafter, efforts were made to develop theories to explain the physical mechanisms of microbarom generation (Brekhovskikh et al., 1973; Waxler et al., 2007). A recent model proposed by De Carlo et al. (2020) unifies aforementioned theories of microbarom generation, taking into consideration both finite ocean-depth and the source radiation dependence on elevation and azimuth angles. This model allows for prediction of location and intensity of the source when coupled with an ocean wave spectrum model. However, for comparison with infrasonic observations at distant ground-based stations, it is necessary to consider the influence of the atmospheric structure on the microbarom propagation and ducting. This can, for example, be estimated using a semi-empirical range-dependent attenuation model in a horizontally homogeneous atmosphere (Le Pichon et al., 2012), or wave propagation simulation using 3-D ray tracing (Smets & Evers, 2014). Details on our suggested vespagram-based comparison approach to microbaroms modeled by a state-of-the-art microbarom radiation theory (De Carlo et al., 2020) are presented in Section B.2.2.

In array signal processing, velocity spectral analysis (vespa) is an approach which analyzes recorded signals in terms of signal power as a function of time (Davies et al., 1971). The power is evaluated either at a fixed slowness, i.e. a constant apparent velocity with varying back-azimuth — corresponding to a circle in the slowness space — or at a fixed back-azimuth with varying apparent velocity — corresponding to a line in slowness space. The vespa power estimate can therefore be visualized as an image, called vespagram, with time on one axis and either back-azimuth (for a fixed apparent velocity) or apparent velocity (for a fixed back-azimuth) as the other axis.

In this study, vespagrams estimated from infrasound array data for a fixed apparent velocity of 350 m/s corresponding to the stratospheric arrival regime are exploited. For a given frequency band, such vespagrams can straightforwardly be compared to microbarom soundscapes modeled for a station location after applying a smoothing kernel which harmonizes the resolution given by the array response function main lobe with the resolution of the microbarom model output. Both the vespagram and the microbarom model provide power

estimates as function of time and back-azimuth which can be displayed as an image, and we suggest image comparison approach based on mean-square difference for benchmarking. The study considers 6 consecutive years of infrasound observations between 2014 and 2019 at a ground-based infrasound array located at Bardufoss, Norway (69.07 N, 18.61 E), denoted IS37 or I37NO (Fyen et al., 2014). See Section B.2.1 for details on the station configuration, data, and the processing applied in this study.

The proposed vespagram-based approach is computationally low-cost and can monitor microbarom source variability over a year (Section B.3.1) as well as detect changes during extreme atmospheric events such as sudden stratospheric warmings (Section B.3.2). It might be further refined for applications such as near-real time diagnostics of ocean wave and atmospheric models, as well as for long-term assessment of model product uncertainties — in particular when applied to data from a global network of infrasound stations. A key aspect of this approach is that benchmarking between model and infrasound vespagrams considers all back-azimuth directions rather than just the direction of the dominant microbarom source, as done in several previous studies (Garcés et al., 2004; Hupe et al., 2019; De Carlo et al., 2019; Smirnov et al., 2020; De Carlo et al., 2020). The microbarom soundscape at a station is typically a sum of components stemming from a wide spatial distribution of ocean regions, and recently den Ouden et al. (2020) demonstrated that an iterative decomposition of the array spatial covariance matrix using the CLEAN algorithm (Högbom, 1974) can be exploited to resolve the back-azimuth and trace velocity of the most coherent wave front arrivals.

A long-term ambition is to exploit microbarom infrasound datasets to enhance the representation of stratospheric dynamics in atmospheric model products and hence increase the accuracy of both medium-range weather forecasting and sub-seasonal climate modeling (Büeler et al., 2020; Dorrington et al., 2020; Domeisen, Butler, Charlton-Perez, Ayarzagüena, et al., 2020; Domeisen, Butler, Charlton-Perez, Ayarzagüena, et al., 2020). In addition to prospective numerical weather prediction improvements, the suggested vespagram-based approach may be applied in multi-technology studies of atmospheric dynamics, for example initiatives building on the Atmospheric dynamics Research InfraStructure in Europe (ARISE) projects (Blanc et al., 2018, 2019). These aim at harvesting from synergies between ground-based infrasound observations, radar and lidar systems, as well as airglow and satellite observations to monitoring the middle atmosphere (Chunchuzov et al., 2015; Le Pichon et al., 2015; Blanc et al., 2018; Hupe et al., 2019; Smets et al., 2019; Hibbins et al., 2019; Assink et al., 2019; Le Pichon et al., 2019).

The study is organized as follows. The data and method are described in Section 2; the main results are presented in Section 3 followed by discussion in Section 4.

B.2   Materials and Methods

B.2.1   Infrasound dataset and signal processing

The infrasound array denoted IS37 or I37NO was initially planned to be co-located with the ARCES seismic array in Karasjok, Norway, (69.5 N, 25.5 E) as part of the International Monitoring System (IMS) which verifies compliance with the Comprehensive Nuclear Test-Ban Treaty (CTBT) (Dahlman et al., 2009; Marty, 2019). Instead, the station was installed at a favorable location in Bardufoss, Norway (69.1 N, 18.6 E), and equipped with ten MB3 type (MB2005 prior to 2016) microbarometers over an aperture of 2 km (Figure B.1a) (Fyen et al., 2014). The station was certified by the CTBTO on 19 December 2013 and is operated by NORSAR institute, Kjeller, Norway. Besides being a part of IMS, IS37 is also part of a regional network of European infrasound stations (Gibbons et al., 2007, 2015, 2019) that resolves significantly smaller events than the global IMS network (Le Pichon et al., 2008). In the framework of the regional network, data from IS37 has been used for multi-station studies characterizing European infrasound sources (e.g., Pilger et al., 2018).

The IS37 station routinely detects microbaroms within $0.1 - 0.6$ Hz originating from the North Atlantic, the Barents Sea, and beyond. An analytical expression for a plane-wave front incident on the IS37 array was used to characterize the array's integrated, frequency-dependent response in 0.1 Hz wide frequency bands from 0.1 to 0.6 Hz. The wave front was representative of a microbarom signal from the Atlantic Ocean, with a back-azimuth of $225°$
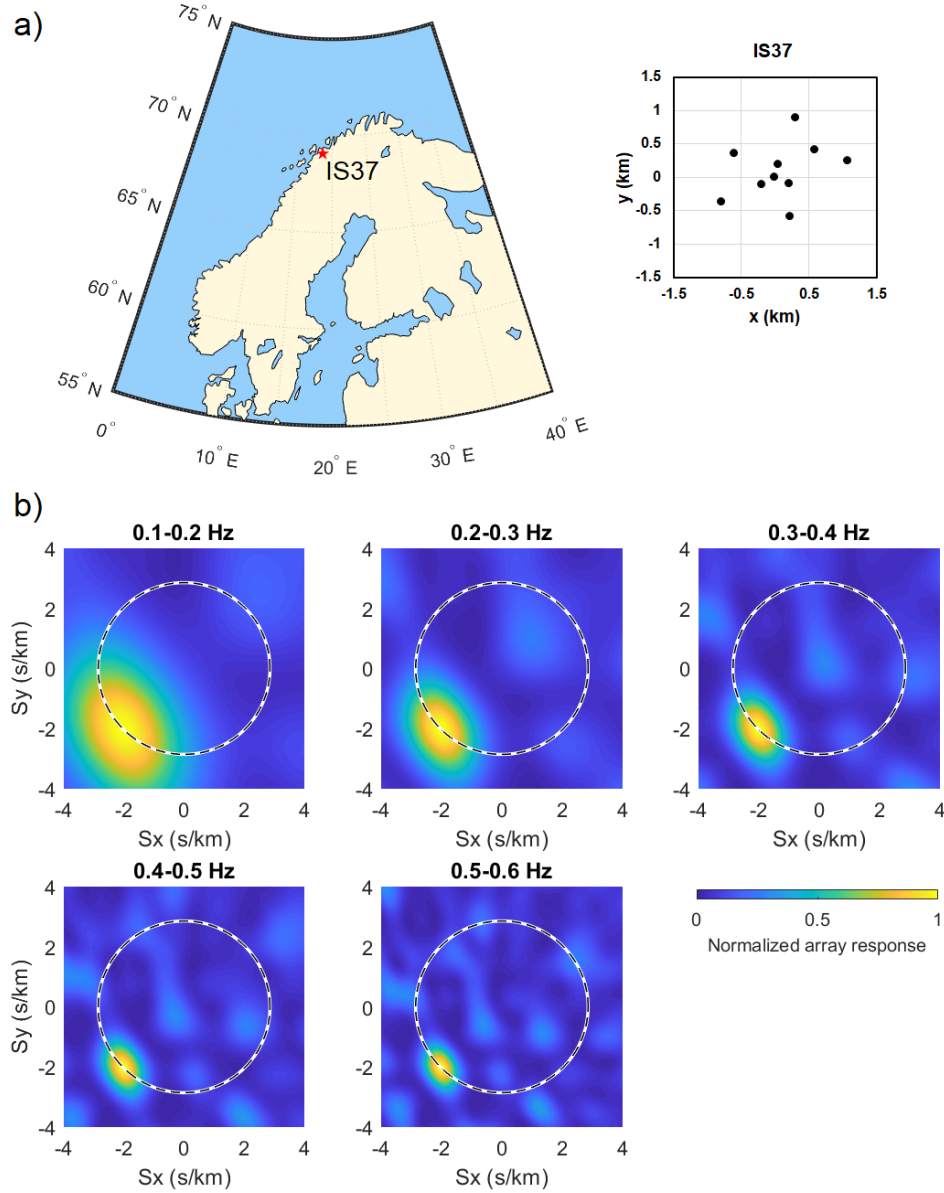
Figure B.1 – a) The IS37 infrasound array location and geometry. b) Integrated steered array response for 0.1 Hz wide frequency bands assuming a plane wave impinging at $225°$ backazimuth and 350 m/s apparent velocity (indicated with a dashed circle).

and a 350 m/s apparent velocity typical of the stratospheric regime (Garcés et al., 1998; Whitaker & Mutschlecner, 2008; Nippress et al., 2014; Lonzaga, 2015). The base resolution of the array was taken to be the 1-sigma beam width of the Gaussian fitted to the array response at a constant velocity of 350 m/s (dashed line in Figure B.1b) for each frequency band. The resulting resolution was found to be: $35°$, $23°$, $16°$, $13°$ and $10°$ for $0.1 - 0.2$ Hz, $0.2 - 0.3$ Hz, $0.3 - 0.4$ Hz, $0.4 - 0.5$ Hz and $0.5 - 0.6$ Hz band, respectively. It should be noted that this analysis only examines the time delays between the array elements and does not take into account meteorological conditions at the station, noise, or other coherence loss mechanisms that may result in a wider beam width.

An important part of array signal processing is the separation of coherent and incoherent parts of the recorded signal. When all components of the slowness vector (apparent velocity and back-azimuth) are known, delay-and-sum beamforming (Ingate et al., 1985) is usually used. This method focuses on signal coming with a specific velocity and from a specific direction amplifying phases with the appropriate slowness and suppressing others. However, slowness vector components are not always accurately known (Gibbons et al., 2020). In

particular, the actual direction of the wave front arrival may differ from theoretical estimates due to meteorological conditions at the station. In this case, the use of the beamforming may lead to an incorrect result, expressed in lower signal amplitude and signal distortion (Rost & Thomas, 2002). To determine an unknown slowness vector component, one can use the vespa (velocity spectral analysis) processing. This not only enhances the signal as the beamforming does, but also allows one to determine either the direction or apparent velocity of incoming signal. The vespa method evaluate power of the signal either at a fixed apparent velocity with varying back-azimuth or at a fixed back-azimuth with varying apparent velocity. The result of the vespa processing is usually presented as an image displaying the power of incoming signal as a function of time and back-azimuth (or apparent velocity) called vespagram. Despite that vespa is a widely applied in seismological array data studies (e.g., Davies et al., 1971; Kanasewich et al., 1973; Muirhead & Datt, 1976; McFadden et al., 1986), it has not been exploited in peer-reviewed microbarom infrasound studies.

The vespa processing procedure described below is applied to each analyzed time window and frequency band:

1) For each sensor n of an array, we extract signal recording $x_n(t)$ that corresponds to the time window of interest. The analysis here is done for an 1h moving time window, evaluated every 30 min. In general, the time series recorded at sensor n at the location $\mathbf{r}_n$ can be written as

$$x_n(t) = y(t - \mathbf{r}_n \cdot \mathbf{s}_{\text{hor}}), \qquad (\text{B.2.1})$$

where $y(t)$ represents a plane wave front signal, and $\mathbf{s}_{\text{hor}}$ is the horizontal component of the slowness vector.

2) Remove the mean.

3) Apply a Butterworth bandpass filter to recordings. Calculations are performed for five equally spaced frequency bands that cover microbaroms frequency range (see Figure B.1b).

4) Beam traces or delay-and-sum traces of an array with N sensors are computed as

$$b(t) = \frac{1}{N} \sum_{n=1}^{N} x_n(t + \mathbf{r}_n \cdot \mathbf{s}_{\text{hor}}). \qquad (\text{B.2.2})$$

In this study, classical linear vespa processing (Davies et al., 1971) is applied where the noise suppression is proportional to square root of N (Rost & Thomas, 2002). A beam is generated at each 1° in back-azimuth, for the fixed apparent velocity of 350 m/s, which is within stratospheric arrival regime (Garcés et al., 1998; Whitaker & Mutschlecner, 2008; Nippress et al., 2014; Lonzaga, 2015). That allows to estimate signals coming from all directions but from approximately the same height corresponding to stratospheric altitudes.

5) Calculate mean squared pressure (power) of each beam to get an estimate of incoming signal strength as a function of back-azimuth and time.

Steps (1) – (5) are applied to all analyzed years of data.

B.2.2 Microbarom source and propagation modeling

In this section we summarize the approach applied to get directional spectrum of microbarom soundscape as a function of time. The procedure is as follows.

1. *Ocean wave model:* The WAVEWATCH III ® (The WW3 Development Group, 2016) code gives an estimate of the generation and variation of the wave spectrum based on surface winds. The interaction of counter propagating waves is calculated from these wave spectra as described in (Ardhuin et al., 2011). Studies on microseisms (Landès et al., 2014; Hillers et al., 2012) have demonstrated the limitations of a model that does not account for coastal reflection. Therefore in this study, the parametrization used to run the WW3 model accounts for fixed reflection coefficients of 10% for the continents, 20% for the islands and 40% for ice sheets (Ardhuin et al., 2011) and

provides the spectral density of equivalent surface pressure forcing microbaroms on a global scale with $0.5°$ latitudinal - longitudinal resolution and a 3-hours time-step (corresponding to the variable 'p2l' available at `ftp://ftp.ifremer.fr/ifremer/ww3/HINDCAST/SISMO/`).

2. *Microbarom source model:* A microbarom source model is basically a model transforming ocean wave model output into acoustic radiation spectrum in the atmosphere. Here, calculations are based on the model of De Carlo et al. (2020), taking into consideration both finite ocean-depth and a source radiation depending on elevation and azimuth angles. This microbarom model allows prediction of the location and intensity of the microbarom sources when applied to the Hasselmann integral. The Hasselmann integral is derived from the output of the wave model and establishes a relationship between the source spectrum and the spectral densities of counter propagating waves for a given frequency (Hasselmann, 1963). The output of this step is an acoustic spectrum for each cell of the wave model.

3. *Microbarom propagation in the atmosphere:* A semi-empirical attenuation law (Le Pichon et al., 2012) is applied to the microbarom spectra obtained through the previous step. This law accounts for the distance between the source and the station as well as for frequency but assumes horizontally homogeneous atmosphere. The atmospheric conditions are considered as the $V_{\text{eff-ratio}}$, the ratio of effective sound speed in the propagation direction between the stratosphere at 50 km and ground. Atmospheric wind and temperature needed to assess $V_{\text{eff-ratio}}$ are derived from the European Center for Medium range Weather Forecasting (ECMWF) models (http://www.ecmwf.int). $V_{\text{eff-ratio}}$ is calculated from the atmospheric profile at the station in order to assess the possibility of wave front arrival from different directions.

4. *Sources summation:* At this step, for each cell of the wave model, an acoustic spectrum is generated and attenuated to reflect what would be seen by the station. To obtain the directional spectrum at the station, all attenuated spectra from model cells within a $1°$ azimuth band and less than 5000 km away from the station are summed. The distance limitation comes from the attenuation law definition. Although this attenuation law is widely used for propagation over very long distances (Smirnov et al., 2020; Pilger et al., 2019; Hupe et al., 2019; De Carlo et al., 2019, 2020), it was defined for distances up to 3000 km only. For IS37, as the main sources are quite close to the station, expanding this attenuation law all around a great circle can lead to misrepresentation of remote sources. Thus, all sources that are more than 5000 km away from the station are excluded from the study.

After applying these steps, and integrating over the frequency bands, we get an estimate of microbarom amplitude as function of time and back-azimuth, just as vespagrams. However, vespagrams cannot be directly compared to the modelled microbarom soundscapes since the latter do not take into account the frequency-dependent resolution of array. Therefore, we smooth the modelled microbarom soundscapes by convolving with a Gaussian kernel at each time step taking into account cyclical nature of back-azimuth when smoothing near $360°/0°$. Kernels are normalized to have sum of 1 and standard deviations (width) decrease with frequency (see Section 2.1).

B.3 Results

B.3.1 Comparison for full seasons

Figures B.3 and B.4 present benchmarking microbarom model and vespa processing images (vespagrams) for two frequency bands, namely $0.1 - 0.2$ Hz and $0.5 - 0.6$, for 2016. Panel 1 from the top shows the seasonal behavior of the dominant signal amplitude over a year. Enhanced ocean source activity during winter is accompanied with eastward stratospheric wind favorable for ducting infrasound over long distances (Le Pichon et al., 2006). This results in a peak of microbarom pressure amplitude both in model and vespagrams regardless of frequency band. As seen from panels $2 - 4$, the microbarom radiation model by De Carlo et al. (2020) accompanied with semi-empirical wave attenuation law accurately reproduces
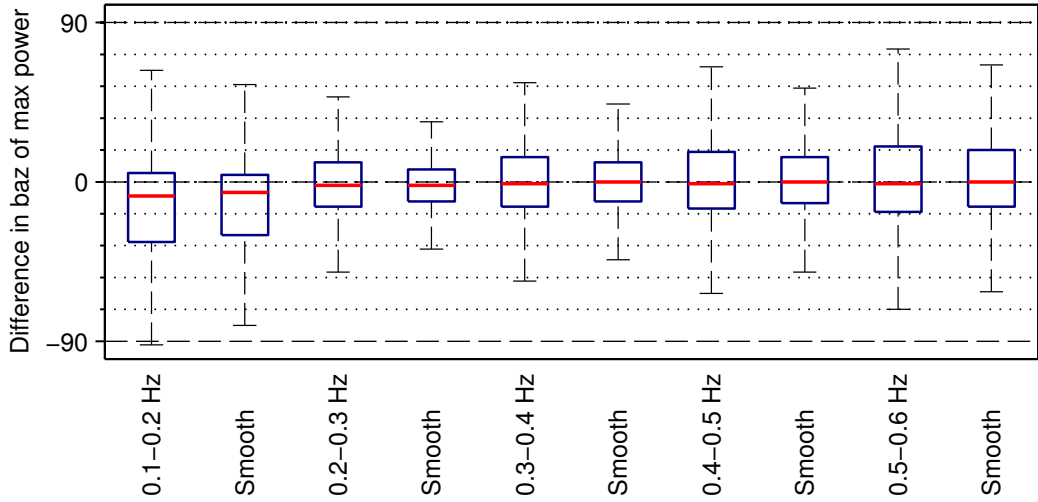
Figure B.2 – A difference in direction of maximum power between i) model and vespagram (indicated with a frequency band name in x-axis) and ii) smoothed model and vespagram (indicated as "smooth" in x-axis) over 6 years of data. Red lines present median, blue boxes indicate a range between 25 and 75 percentiles, whiskers correspond to $\pm 3\sigma$.

infrasound detections. This is especially true after applying smoothing, which results in better agreement between direction of the dominant signal in model and vespagrams (Figure B.2).

Due to the strong seasonal variability of microbarom amplitude it is difficult to compare the direction of winter to summer detections on an absolute amplitude scale. Thus, we normalize panels $2-4$ at each time step (panels $5-7$ right) and estimate directional distribution of dominant signal in $10°$ bins (panels $5-7$ left). For a frequency band of $0.1-0.2$ Hz the North Atlantic is the dominant source direction throughout the year. (Figure B.3). Going to higher frequencies, there is a pronounced change in the dominant direction of the source from the Atlantic in winter to the Barents Sea in summer (Figure B.4). This is associated with the change of wind direction in the stratosphere from eastward to westward. Analysis of 6 years dataset in terms of the dominant source direction indicates three prevailing microbarom source regions associated with the North Atlantic, the Greenland Sea, and the Barents Sea. These appear at the vespagram (model) back-azimuths of -94 ± 14 (-95 ± 16), -21 ± 14 (-15 ± 8) and 26 ± 6 (34 ± 7).

A similarity index (SI), taken from an imaging processing approach, is introduced as

$$\mathrm{SI}(t) = 1 - \mathrm{MSE}(t) = \frac{1}{N_\theta} \sum_\theta \left[\bar{P}_{\mathrm{model}}(t,\theta) - \bar{P}_{\mathrm{vespa}}(t,\theta) \right]^2 \qquad (\mathrm{B.3.3})$$

where MSE is a mean squared error between normalized smoothed model output, $\bar{P}_{\mathrm{model}}(t,\theta)$, and normalized vespagram, $\bar{P}_{\mathrm{vespa}}(t,\theta)$, calculated at each time step, θ is back-azimuth, t is time. The use of normalized data is justified by the influence of the smoothing procedure on the magnitude of the model data. MSE provides information on how accurate the model reproduces the directional pressure spectrum (zero indicates full match between model and infrasound vespagram). Panel 7 in Figures B.3 and B.4 presents obtained values of SI over a year.

In winter, SI for lower frequencies is stable and has values ~ 1, with exceptions corresponding to increased noise level in vespagrams or to SSW events (see next subsection). Relatively low SI for high frequencies can be explained either by spurious apparent sources corresponding to array response function side-lobes (Figure B.1b) or by presence of sources in the vespagram that are missed or not-well reproduced in the model because of a 5000 km distance limit (see Section B.2.2). In summer, SI values are quite variable and unstable but never fall below 0.5. Such behavior is typical regardless of year and frequency band (Figure B.5). One possible explanation is the changing weather conditions present at the station throughout the year. For example, Orsolini & Sorteberg (2009) have shown an enhance-
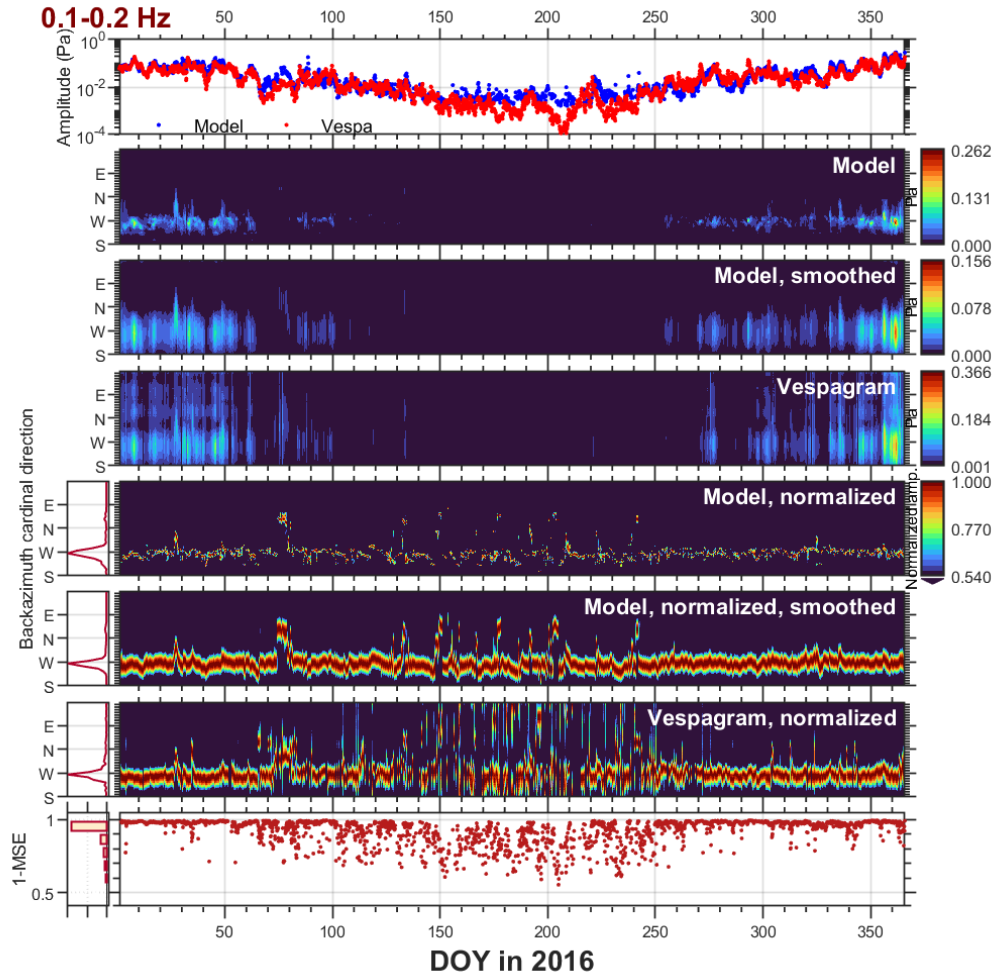
Figure B.3 – Benchmarking microbarom model and infrasound vespagram for $0.1 - 0.2$ Hz in 2016. Panels: 1 - amplitude of dominant signal (blue - vespa processing, red - model); 2 - microbarom model output; 3 - model output after smoothing (Section B.2.2); 4 - infrasound vespagram (Section B.2.1); 5 - 7 (right) same as panels 2 - 4 but after normalization at each time step; 5 - 7 (left) normalized directional distribution of dominant signal ($10°$ bins); 8 - similarity score between panels 6 and 7 (right) and its normalized distribution (left).

ment in the number and intensity of summer cyclones the Arctic and Northern Eurasia. This would result in additional wind and rain noise in the infrasound recordings that would especially be enhanced at the lower frequencies. Another possible contribution would be the poor resolution of the array at low frequencies that can mix stratospheric signals with those from higher altitudes which sometimes dominate at IS37 in summer (Näsholm et al., 2020) but are not included in the model. The relative stability of the model's results in Figure B.4 relative to the vespagram would indicate that there are additional sources of variability, either atmospheric, source region, or propagation path, that are not well characterized in the model.

To summarize, vespagram-based approach revealed a good agreement in modelled microbarom soundscapes and vespagrams in both time (seasonal variations) and space (directional distribution). The similarity estimation proposed allows detection of inconsistencies between the microbarom model and the vespa processing which might be used for identifying biases in atmospheric models. This is especially promisingly for low frequencies where side-lobes of array response do not appreciably affect analysis.
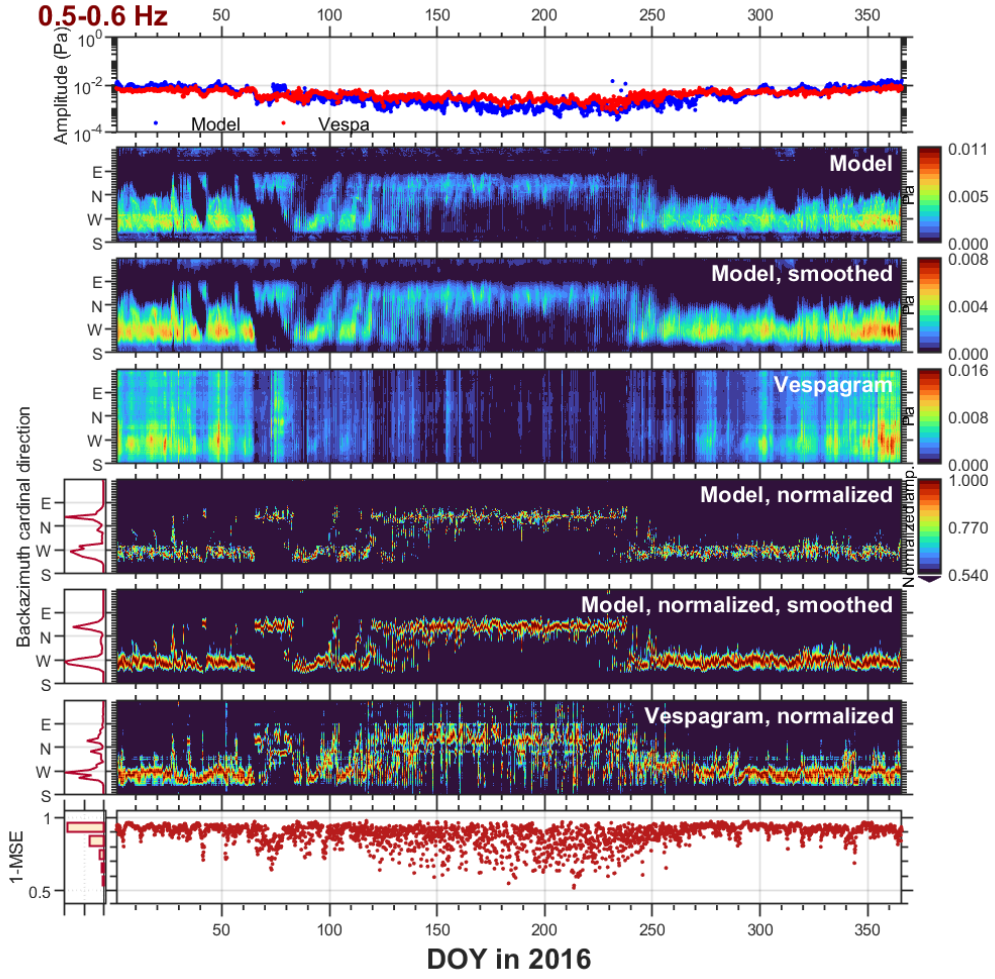
Figure B.4 – Same as Figure B.3 but for 0.5 - 0.6 Hz.

B.3.2 Examination of major sudden stratospheric warmings

Although this is not a main objective of the current study, in this section we inspect the ability of the vespagrams to detect extreme atmospheric events, such as sudden stratospheric warmings (SSWs).

SSWs usually occur in wintertime and are, in general, associated with a sudden and short increase in stratospheric temperature and mesospheric cooling at high / middle latitudes (Shepherd et al., 2014; Butler et al., 2015; Limpasuvan et al., 2016; Zülicke et al., 2018). SSWs are often classified into minor and major warmings, depending on whether there was a weakening or reversal of the zonal wind (Butler et al., 2015). During the period of our consideration, three major and three minor SSWs occured with onsets on 5-6 March 2016 (Manney & Lawrence, 2016), 11 February 2018 (Rao et al., 2018; Lü et al., 2020) and 1 January 2019 (Rao et al., 2019, 2020) for major, and 4 January 2015 (Manney et al., 2015; Mitnik et al., 2018), 1 and 26 February 2017 (Eswaraiah et al., 2020) for minor. Note that error in determining SSW onset day can reach up to several days since there is no single way to define this phenomena and different authors use different definitions. A prime example is the first SSW in 2017. According to the definition of the World Meteorological Organization, this event is classified as minor, but in several studies it is referred to as major (Xiong et al., 2018; Conte et al., 2019). Vertical dashed lines in Figures B.5 – B.6 correspond to days when SSW criteria were met (onsets of the warmings).

The infrasound signature reported by Donn & Rind (1971) and Evers & Siegmund (2009), which showed a significant change in direction of the infrasound arrival due to change in favorable stratospheric waveguide, can be seen in Figure B.6 for all SSWs under consideration
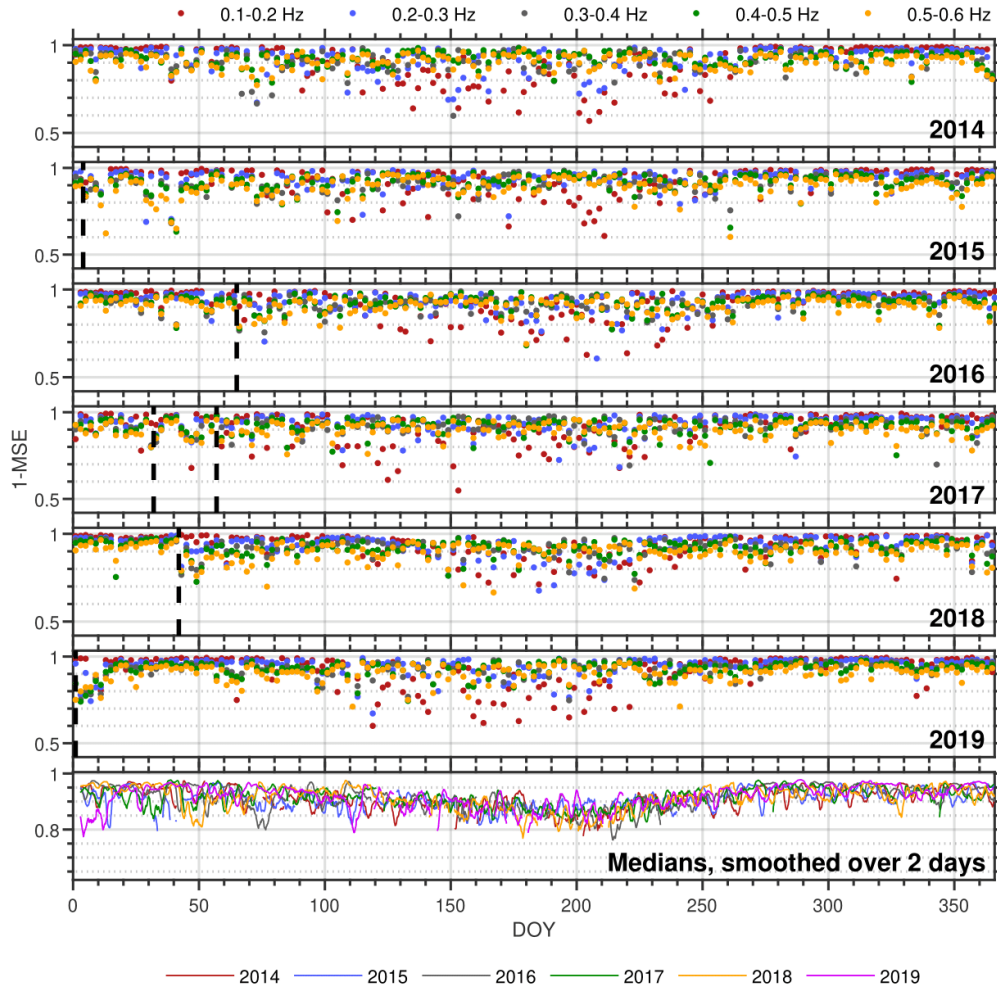
Figure B.5 – Multi-year comparison between modelled microbarom soundscapes and vespagrams. The similarity index is color-coded depending on frequency band: $0.1 - 0.2$ Hz - red, $0.2 - 0.3$ Hz - blue, $0.3 - 0.4$ Hz - grey, $0.4 - 0.5$ Hz - green, $0.5 - 0.6$ Hz - orange. Data are presented with 3 days interval. Black dashed lines present SSWs onsets. Medians over frequency bands in the last panel are color-coded depending on year: 2014 - red, 2015 - blue, 2016 - grey, 2017 - green, 2018 - yellow, 2019 - magenta.

and in Figures B.3 and B.4 (panels $5, 6, 7$) for SSW 2016. The change in direction from the North Atlantic to the Barents Sea is clearly pronounced in both model and vespagrams around SSWs onset days. Figure B.3 (panels 6 - 7) demonstrates that the signature appears late in the model data and its duration is much shorter than in vespagram, analogous to study by Smets et al. (2016). For higher frequencies (Figure B.4) the duration of a change from eastward to westward pattern is longer and continues until late March - early April that corresponds to reanalysis data (Manney & Lawrence, 2016).

Another feature revealed is a significant decrease in similarity index between model and vespa processing during SSWs (Figure B.5) which is characteristic for all events under consideration. The smallest discrepancies in the direction of the dominant wave front between the model and infrasound data during SSWs reach about $5° - 7°$, but the largest reach as much as $90° - 100°$ (Figure B.6). This may be caused by the following factors. The back-azimuth change during SSW usually appears earlier in the vespagrams than in the model with the difference of 3 to 24 hours. Similar results were previously obtained by Smets & Evers (2014) and can be explained by the presence of an error in determining SSW onset day from reanalysis data because of a scarcity of observations at stratospheric altitudes (Charlton-Perez et al., 2013) or by inadequate stratospheric analysis and forecast during SSW as addressed by
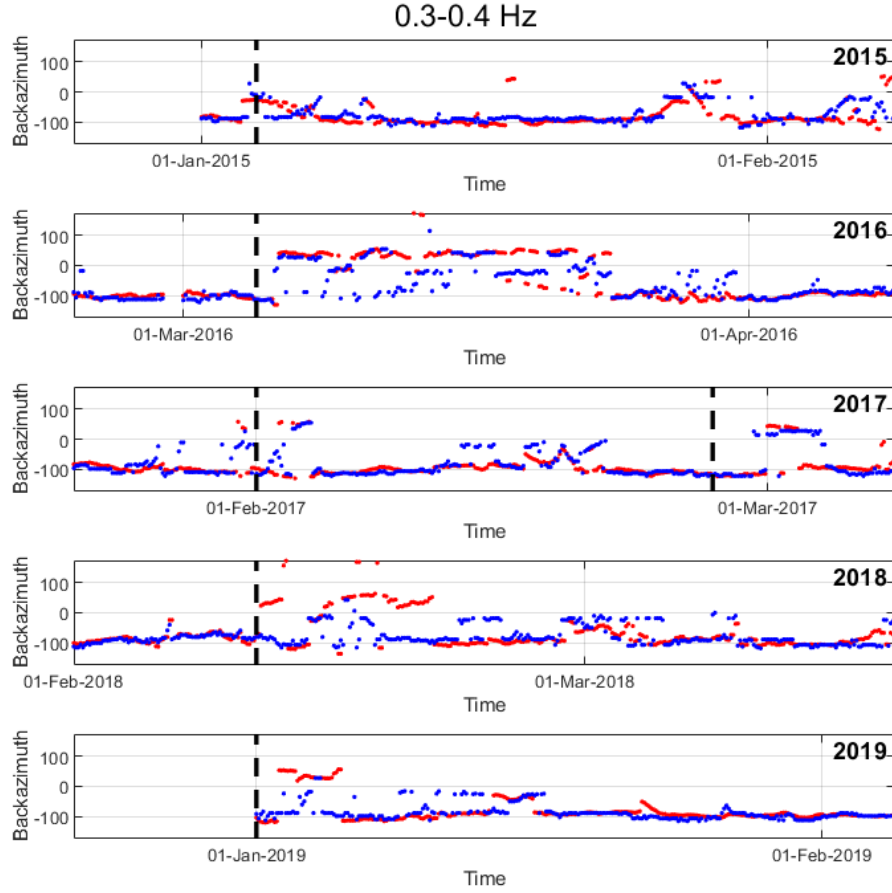
Figure B.6 – Changes in the dominant direction of the wave front (blue - vespa, red - model) around SSWs 2015 - 2019 for $0.3 - 0.4$ Hz band. Black dashed lines indicate days when SSWs (minor or major) criteria were met.

(Diamantakis, 2014; Smets et al., 2016). Sometimes the SSW signature does not appear in the vespagrams while appearing in the model (see Figure B.6 around SSW 2018 onset day for example). This can arise when employing horizontally homogeneous atmosphere and overly constraining the model with the ECMWF wind and temperature at 50 km altitude. Such approach does not allow a full, altitude dependent description of infrasonic waves in the atmosphere (considering long propagation path for microbaroms, net wind effect along the propagation path can be equal to zero) and causes discrepancies between model and vespa processing. It has been demonstrated by (Evers & Siegmund, 2009; Smets & Evers, 2014) that ECMWF wind direction not always characterize the actual infrasound path, resulting is model-vespagram discrepancies.

Despite slight difference in the dominant direction of wave front arrival during SSW, both model and vespagrams reproduce changes in infrasound pattern correctly in time. Moreover, since vespagrams can detect changes in stratospheric dynamics during extreme events, there is a potential in using it in near-real-time stratospheric diagnostics.

B.4   Discussion and Conclusions

In this study, we compare observed and predicted microbaroms soundscapes using a vespagram-based approach. Analysis is performed based on calculation of microbaroms power as a function of time and back-azimuth with a constant apparent velocity of 350 m/s. Note, however, that the vespagram-family of time-dependent microbarom data visualizations can

be constructed also using other array processing techniques that estimate power as function of the slowness of the wave front, e.g., using robust estimators as explored by Bishop et al. (2020), or adaptive high-resolution approaches like Capon's method (Capon, 1969). An advantage of the vespagram-approach is that microbarom radiation and propagation models can be benchmarked against recorded infrasound data for all directions simultaneously, as opposed to methods where only the back-azimuth direction of maximum power is considered (e.g., Hupe et al., 2019; Smirnov et al., 2020). In addition to being computationally low-cost, vespa processing can track changes in microbarom parameters over a year as well as changes in infrasound signatures during extreme atmospheric events and paves the way for near-real time assessment of atmospheric model data sets and stratospheric diagnostics.

Limitations in this study are predominantly related to microbarom propagation modelling. In addition to the scarcity of observations at the stratospheric altitudes (Charlton-Perez et al., 2013) that affect the accuracy of directional distribution of predicted microbarom soundscapes, the horizontally homogeneous atmospheric approximation used in the study creates significant limitations. These are especially pronounced for long-distance propagation when infrasound waves pass through several atmospheric regions which disturb the wind on smaller scales, such as tidal phases or SSW events. Moreover, the modelling would benefit from applying a full-waveform simulation code for the propagation of the radiated microbaroms to the station (e.g., Assink, Pichon, et al., 2014; Kim & Rodgers, 2017; Brissaud et al., 2017; Petersson & Sjögreen, 2018). This would provide more refined modelling of the atmospheric ducting compared to the semi-empirical transition loss approach (Le Pichon et al., 2012) applied in the current study. As an alternative to the computational costs associated with this method, a 3-D ray-tracing code can be used to account for both range-dependent atmospheric models and cross-wind effect (e.g., Smets & Evers, 2014; Smets et al., 2016). However, the inherent high-frequency approximation of the ray-theory can limit the modelling of diffraction and scattering effects (Chunchuzov et al., 2015) that can be important for the low-frequency microbaroms.

A more elaborate microbarom propagation model could also allow for an estimate of the full microbarom wavefield impinging an infrasound station, hence providing an estimate of its power within the full horizontal slowness space of plane wave front directions (or a selected relevant region). This way, we could benchmark the modelled and recorded microbarom field at an infrasound array for each sliding time window without restricting the analysis to the region around a fixed apparent velocity as carried out in the current study. Notably, such "f-k plots" of modelled and recorded microbaroms are also (time-varying) images which can be assessed and compared using the versatile image processing and comparison algorithms.

Future developments can include compilation of long-term time-dependent statistics of similarity between model and infrasound recordings for multiple stations on global and regional scales, in order to define anomaly flag criteria which indicate that there is unexpected inconsistency between model and observations due to, for example, biases in atmospheric model products. Moreover, we suggest applying the presented approach in global assessment and comparisons of ocean wave-action model products, as well as in validation and further refinement of microbarom radiation estimation algorithms.

Acknowledgements

References

Amezcua, J., Näsholm, S. P., Blixt, E. M., & Charlton-Perez, A. J. (2020). Assimilation of atmospheric infrasound data to constrain tropospheric and stratospheric winds. *Quarterly Journal of the Royal Meteorological Society*.

Ardhuin, F., Stutzmann, E., Schimmel, M., & Mangeney, A. (2011). Ocean wave sources of seismic noise. *Journal of Geophysical Research: Oceans*, *116*(C9).

Assink, J., Pichon, A. L., Blanc, E., Kallel, M., & Khemiri, L. (2014). Evaluation of wind and temperature profiles from ECMWF analysis on two hemispheres using volcanic infrasound. *Journal of Geophysical Research: Atmospheres*, *119*(14), 8659–8683.

Assink, J., Smets, P., Marcillo, O., Weemstra, C., Lalande, J.-M., Waxler, R., & Evers, L. (2019). Advances in infrasonic remote sensing methods. In *Infrasound monitoring for atmospheric studies* (pp. 605–632). Springer.

Baird, H., & Banwell, C. (1940). Recording of air-pressure oscillations associated with microseisms at christchurch. *NZJ Sci. Technol., Sect. B*, *21*, 314–329.

Benioff, H., & Gutenberg, B. (1939). Waves and currents recorded by electromagnetic barographs. *Bulletin of the American Meteorological Society*, *20*(10), 421–428.

Bishop, J. W., Fee, D., & Szuberla, C. A. L. (2020). Improved infrasound array processing with robust estimators. *Geophysical Journal International*, *221*(3), 2058–2074. doi: 10.1093/gji/ggaa110

Blanc, E., Ceranna, L., Hauchecorne, A., Charlton-Perez, A., Marchetti, E., Evers, L., ... Chum, J. (2018). Toward an improved representation of middle atmospheric dynamics thanks to the ARISE project. *Surveys in Geophysics*, *39*(2), 171–225. doi: 10.1007/s10712-017-9444-0

Blanc, E., Pol, K., Le Pichon, A., Hauchecorne, A., Keckhut, P., Baumgarten, G., ... Smets, P. (2019). Middle atmosphere variability and model uncertainties as investigated in the framework of the ARISE project. In *Infrasound monitoring for atmospheric studies* (pp. 845–887). Springer.

Brekhovskikh, L. M., Goncharov, V. V., Kurtepov, V. M., & Naugolnykh, K. A. (1973). Radiation of infrasound into atmosphere by surface-waves in ocean. *Izvestiya Akademii Nauk SSSR Fizika Atmosfery i Okeana*, *9*(9), 899–907.

Brissaud, Q., Martin, R., Garcia, R. F., & Komatitsch, D. (2017). Hybrid Galerkin numerical modelling of elastodynamics and compressible Navier–Stokes couplings: applications to seismo-gravito acoustic waves. *Geophysical Journal International*, *210*(2), 1047–1069.

Büeler, D., Beerli, R., Wernli, H., & Grams, C. M. (2020). Stratospheric influence on ECMWF sub-seasonal forecast skill for energy-industry-relevant surface weather in european countries. *Quarterly Journal of the Royal Meteorological Society*.

Butler, A. H., Seidel, D. J., Hardiman, S. C., Butchart, N., Birner, T., & Match, A. (2015). Defining sudden stratospheric warmings. *Bulletin of the American Meteorological Society*, *96*(11), 1913–1928.

Capon, J. (1969). High-resolution frequency-wavenumber spectrum analysis. *Proceedings of the IEEE*, *57*(8), 1408–1418.

Charlton-Perez, A. J., Baldwin, M. P., Birner, T., Black, R. X., Butler, A. H., Calvo, N., ... Watanabe, S. (2013). On the lack of stratospheric dynamical variability in low-top versions of the CMIP5 models. *Journal of Geophysical Research: Atmospheres*, *118*(6), 2494–2505.

Chunchuzov, I., Kulichkov, S., Perepelkin, V., Popov, O., Firstov, P., Assink, J., & Marchetti, E. (2015). Study of the wind velocity-layered structure in the stratosphere, mesosphere, and lower thermosphere by using infrasound probing of the atmosphere. *Journal of Geophysical Research: Atmospheres*, *120*(17), 8828–8840.

Conte, J. F., Chau, J. L., & Peters, D. H. (2019). Middle-and high-latitude mesosphere and lower thermosphere mean winds and tides in response to strong polar-night jet oscillations. *Journal of Geophysical Research: Atmospheres*, *124*(16), 9262–9276.

Dahlman, O., Mykkeltveit, S., & Haak, H. (2009). *Nuclear test ban: converting political visions to reality*. Springer Science & Business Media.

Davies, D., Kelly, E., & Filson, J. (1971). Vespa process for analysis of seismic signals. *Nature Physical Science*, *232*(27), 8–13.

De Carlo, M., Ardhuin, F., Ceranna, L., Hupe, P., Le Pichon, A., & Vergoz, J. (2020). Global comparison between ocean ambient noise modelling and infrasound network observations. In *EGU general assembly conference abstracts* (p. 17475). doi: 10.5194/egusphere-egu2020-17475

De Carlo, M., Ardhuin, F., & Le Pichon, A. (2020, January). Atmospheric infrasound generation by ocean waves in finite depth: unified theory and application to radiation patterns. *Geophysical Journal International*, *221*(1), 569–585. doi: 10.1093/gji/ggaa015

De Carlo, M., Le Pichon, A., Vergoz, J., Ardhuin, F., Näsholm, S., Ceranna, L., . . . Pilger, C. (2019). Characterizing ocean ambient noise in the North Atlantics and the barents sea regions [Conference material]. doi: 10.1002/2015JD024401

den Ouden, O. F. C., Assink, J. D., Smets, P. S. M., Shani-Kadmiel, S., Averbuch, G., & Evers, L. G. (2020). CLEAN beamforming for the enhanced detection of multiple infrasonic sources. *Geophysical Journal International*, *221*(1), 305–317.

Dessauer, F., Graffunder, W., & Schaffhauser, J. (1951). Über atmosphärische pulsationen. *Archiv für Meteorologie, Geophysik und Bioklimatologie, Serie A*, *3*(5), 453–463.

Diamantakis, M. (2014). Improving ECMWF forecasts of sudden stratospheric warmings. *ECMWF Newsletter*, *141*, 30–36.

Domeisen, D. I. V., Butler, A. H., Charlton-Perez, A. J., Ayarzagüena, B., Baldwin, M. P., Dunn-Sigouin, E., . . . Taguchi, M. (2020). The role of the stratosphere in subseasonal to seasonal prediction: 1. predictability of the stratosphere. *Journal of Geophysical Research: Atmospheres*, *125*(2), e2019JD030920.

Domeisen, D. I. V., Butler, A. H., Charlton-Perez, A. J., Ayarzagüena, B., Baldwin, M. P., Dunn-Sigouin, E., . . . Taguchi, M. (2020). The role of the stratosphere in subseasonal to seasonal prediction: 2. predictability arising from stratosphere-troposphere coupling. *Journal of Geophysical Research: Atmospheres*, *125*(2), e2019JD030923.

Donn, W. L., & Posmentier, E. S. (1967). Infrasonic waves from the marine storm of April 7, 1966. *Journal of Geophysical Research*, *72*(8), 2053–2061.

Donn, W. L., & Rind, D. (1971). Natural infrasound as an atmospheric probe. *Geophysical Journal International*, *26*(1-4), 111–133.

Dorrington, J., Finney, I., Palmer, T., & Weisheimer, A. (2020). Beyond skill scores: exploring sub-seasonal forecast value through a case study of french month-ahead energy prediction. *Quarterly Journal of the Royal Meteorological Society*.

Eswaraiah, S., Kumar, K. N., Kim, Y. H., Chalapathi, G. V., Lee, W., Jiang, G., . . . others (2020). Low-latitude mesospheric signatures observed during the 2017 sudden stratospheric warming using the fuke meteor radar and era-5. *Journal of Atmospheric and Solar-Terrestrial Physics*, 105352.

Evers, L., & Siegmund, P. (2009). Infrasonic signature of the 2009 major sudden stratospheric warming. *Geophysical Research Letters*, *36*(23).

Fyen, J., Roth, M., & W., L. P. (2014). IS37 infrasound station in Bardufoss, Norway. *NORSAR Scientific Report*(2-2013), 29–39.

Garcés, M., Hansen, R. A., & Lindquist, K. G. (1998). Traveltimes for infrasonic waves propagating in a stratified atmosphere. *Geophysical journal international*, *135*(1), 255–263.

Garcés, M., Willis, M., Hetzer, C., Le Pichon, A., & Drob, D. (2004). On using ocean swells for continuous infrasonic measurements of winds and temperature in the lower, middle, and upper atmosphere. *Geophysical research letters*, *31*(19).

Gibbons, S., Asming, V., Eliasson, L., Fedorov, A., Fyen, J., Kero, J., . . . Vinogradov, Y. (2015). The European Arctic: A Laboratory for Seismoacoustic Studies. *Seismological Research Letters*, *86*(3), 917–928. doi: 10.1785/0220140230

Gibbons, S., Kværna, T., & Näsholm, S. (2019). Characterization of the infrasonic wavefield from repeating seismo-acoustic events. In *Infrasound monitoring for atmospheric studies* (pp. 387–407). Springer.

Gibbons, S., Ringdal, F., & Kværna, T. (2007). Joint seismic-infrasonic processing of recordings from a repeating source of atmospheric explosions. *The Journal of the Acoustical Society of America*, *122*(5), EL158–EL164.

Gibbons, S. J., Kværna, T., Tiira, T., & Kozlovskaya, E. (2020, 07). A Benchmark Case Study for Seismic Event Relative Location. *Geophysical Journal International*. doi: 10.1093/gji/ggaa362

Gutenberg, B., & Benioff, H. (1941). Atmospheric-pressure waves near Pasadena. *Eos, Transactions American Geophysical Union*, *22*(2), 424–426.

Hasselmann, K. (1963). A statistical analysis of the generation of microseisms. *Reviews of Geophysics*, *1*(2), 177–210.

Hibbins, R., Espy, P., & de Wit, R. (2019). Gravity-wave detection in the mesosphere using airglow spectrometers and meteor radars. In *Infrasound monitoring for atmospheric studies* (pp. 649–668). Springer.

Hillers, G., Graham, N., Campillo, M., Kedar, S., Landès, M., & Shapiro, N. (2012). Global oceanic microseism sources as seen by seismic arrays and predicted by wave action models. *Geochemistry, Geophysics, Geosystems*, *13*(1).

Högbom, J. A. (1974). Aperture synthesis with a non-regular distribution of interferometer baselines. *Astronomy and Astrophysics Supplement Series*, *15*, 417.

Hupe, P., Ceranna, L., Pilger, C., De Carlo, M., Le Pichon, A., Kaifler, B., & Rapp, M. (2019). Assessing middle atmosphere weather models using infrasound detections from microbaroms. *Geophysical Journal International*, *216*(3), 1761–1767.

Ingate, S., Husebye, E., & Christoffersson, A. (1985). Regional arrays and optimum data processing schemes. *Bulletin of the Seismological Society of America*, *75*(4), 1155–1177.

Kanasewich, E., Hemmings, C., & Alpaslan, T. (1973). Nth-root stack nonlinear multichannel filter. *Geophysics*, *38*(2), 327–338.

Kim, K., & Rodgers, A. (2017). Influence of low-altitude meteorological conditions on local infrasound propagation investigated by 3-D full-waveform modeling. *Geophysical Journal International*, *210*(2), 1252–1263.

Landès, M., Le Pichon, A., Shapiro, N. M., Hillers, G., & Campillo, M. (2014). Explaining global patterns of microbarom observations with wave action models. *Geophysical Journal International*, *199*(3), 1328–1337.

Le Pichon, A., Assink, J. D., Heinrich, P., Blanc, E., Charlton-Perez, A., Lee, C. F., . . . Claud, C. (2015). Comparison of co-located independent ground-based middle atmospheric wind and temperature measurements with numerical weather prediction models. *Journal of Geophysical Research: Atmospheres*, *120*(16), 8318–8331.

Le Pichon, A., Ceranna, L., Garcés, M., Drob, D., & Millet, C. (2006). On using infrasound from interacting ocean swells for global continuous measurements of winds and temperature in the stratosphere. *Journal of Geophysical Research: Atmospheres*, *111*(D11).

Le Pichon, A., Ceranna, L., & Vergoz, J. (2012). Incorporating numerical modeling into estimates of the detection capability of the IMS infrasound network. *Journal of Geophysical Research: Atmospheres*, *117*(D5), 1–12. Retrieved from https://agupubs.onlinelibrary.wiley.com/doi/abs/10.1029/2011JD016670 doi: 10.1029/2011JD016670

Le Pichon, A., Ceranna, L., Vergoz, J., & Tailpied, D. (2019). Modeling the detection capability of the global IMS infrasound network. In *Infrasound monitoring for atmospheric studies* (pp. 593–604). Springer.

Le Pichon, A., Vergoz, J., Herry, P., & Ceranna, L. (2008). Analyzing the detection capability of infrasound arrays in Central Europe. *Journal of Geophysical Research: Atmospheres*, *113*(D12).

Limpasuvan, V., Orsolini, Y. J., Chandran, A., Garcia, R. R., & Smith, A. K. (2016). On the composite response of the MLT to major sudden stratospheric warming events with elevated stratopause. *Journal of Geophysical Research: Atmospheres*, *121*(9), 4518-4537. doi: 10.1002/2015JD024401

Lonzaga, J. B. (2015). A theoretical relation between the celerity and trace velocity of infrasonic phases. *The Journal of the Acoustical Society of America*, *138*(3), EL242–EL247.

Lü, Z., Li, F., Orsolini, Y. J., Gao, Y., & He, S. (2020). Understanding of european cold extremes, sudden stratospheric warming, and siberian snow accumulation in the winter of 2017/18. *Journal of Climate*, *33*(2), 527–545.

Manney, G. L., & Lawrence, Z. D. (2016). The major stratospheric final warming in 2016: Dispersal of vortex air and termination of arctic chemical ozone loss. *Atmospheric Chemistry & Physics*, *16*(23).

Manney, G. L., Lawrence, Z. D., Santee, M. L., Read, W. G., Livesey, N. J., Lambert, A., . . . Schwartz, M. J. (2015). A minor sudden stratospheric warming with a major impact: Transport and polar processing in the 2014/2015 arctic winter. *Geophysical Research Letters*, *42*(18), 7808–7816.

Marty, J. (2019). The IMS infrasound network: current status and technological developments. In *Infrasound monitoring for atmospheric studies* (pp. 3–62). Springer.

McFadden, P., Drummond, B., & Kravis, S. (1986). The N th-root stack: Theory, applications, and examples. *Geophysics*, *51*(10), 1879–1892.

Mikhailov, A. (2019, August 20). *Turbo, an improved rainbow colormap for visualization.* Retrieved from https://ai.googleblog.com/2019/08/turbo-improved-rainbow-colormap-for.html (Accessed: 25 July 2020)

Mitnik, L. M., Kuleshov, V., Pichugin, M. K., & Mitnik, M. L. (2018). Sudden stratospheric warming in 2015–2016: Study with satellite passive microwave data and era5 reanalysis. In *Igarss 2018-2018 ieee international geoscience and remote sensing symposium* (pp. 5556–5559).

Muirhead, K., & Datt, R. (1976). The N-th root process applied to seismic array data. *Geophysical Journal International*, *47*(1), 197–210.

Näsholm, S. P., Vorobeva, E., Le Pichon, A., Orsolini, Y. J., Turquet, A. L., Hibbins, R. E., . . . Rodriguez, I. V. (2020). Semidiurnal tidal signatures in microbarom infrasound array measurements. In *Egu general assembly conference abstracts* (p. 19035).

Nippress, A., Green, D. N., Marcillo, O. E., & Arrowsmith, S. J. (2014). Generating regional infrasound celerity-range models using ground-truth information and the implications for event location. *Geophysical Journal International*, *197*(2), 1154–1165.

Orsolini, Y. J., & Sorteberg, A. (2009). Projected changes in eurasian and arctic summer cyclones under global warming in the Bergen climate model. *Atmospheric and Oceanic Science Letters*, *2*(1), 62–67.

Petersson, N. A., & Sjögreen, B. (2018). High order accurate finite difference modeling of seismo-acoustic wave propagation in a moving atmosphere and a heterogeneous earth model coupled across a realistic topography. *Journal of Scientific Computing*, *74*(1), 290–323.

Pilger, C., Ceranna, L., Ross, J. O., Vergoz, J., Le Pichon, A., Brachet, N., . . . Mialle, P. (2018). The European Infrasound Bulletin. *Pure and Applied Geophysics*, *175*(10), 3619–3638.

Pilger, C., Gaebler, P., Ceranna, L., Le Pichon, A., Vergoz, J., Perttu, A., . . . Taisne, B. (2019). Infrasound and seismoacoustic signatures of the 28 september 2018 Sulawesi super-shear earthquake. *Natural Hazards and Earth System Sciences*, *19*(12), 2811–2825. Retrieved from https://nhess.copernicus.org/articles/19/2811/2019/ doi: 10.5194/nhess-19-2811-2019

Polavarapu, S., Shepherd, T., Rochon, Y., & Ren, S. (2005). Some challenges of middle atmosphere data assimilation. *Quarterly Journal of the Royal Meteorological Society: A journal of the atmospheric sciences, applied meteorology and physical oceanography*, *131*(613), 3513–3527.

Rao, J., Garfinkel, C. I., Chen, H., & White, I. P. (2019). The 2019 New Year stratospheric sudden warming and its real-time predictions in multiple S2S models. *Journal of Geophysical Research: Atmospheres*, *124*(21), 11155–11174.

Rao, J., Garfinkel, C. I., & White, I. P. (2020). Predicting the downward and surface influence of the February 2018 and january 2019 sudden stratospheric warming events in subseasonal to seasonal (S2S) models. *Journal of Geophysical Research: Atmospheres*, *125*(2), e2019JD031919.

Rao, J., Ren, R., Chen, H., Yu, Y., & Zhou, Y. (2018). The stratospheric sudden warming event in February 2018 and its prediction by a climate system model. *Journal of Geophysical Research: Atmospheres*, *123*(23), 13–332.

Rienecker, M. M., Suarez, M. J., Gelaro, R., Todling, R., Bacmeister, J., Liu, E., . . . Woollen, J. (2011). MERRA: NASA's modern-era retrospective analysis for research and applications. *Journal of climate*, *24*(14), 3624–3648.

Rost, S., & Thomas, C. (2002). Array seismology: Methods and applications. *Reviews of geophysics*, *40*(3), 2–1.

Saxer, L. (1945). Elektrische messung kleiner atmospharischer druckschwankungen. *HELVETICA PHYSICA ACTA*, *18*(7), 527–550.

Saxer, L. (1954). Über entstehung und ausbreitung quasiperiodischer luftdruckschwankungen. *Archiv für Meteorologie, Geophysik und Bioklimatologie, Serie A*, *6*(3-4), 451–463.

Shepherd, M., Beagley, S., & Fomichev, V. (2014). Stratospheric warming influence on the mesosphere/lower thermosphere as seen by the extended CMAM. In *Annales geophysicae* (Vol. 32, p. 589).

Smets, P., Assink, J., & Evers, L. (2019). The study of sudden stratospheric warmings using infrasound. In *Infrasound monitoring for atmospheric studies* (pp. 723–755). Springer.

Smets, P., Assink, J., Le Pichon, A., & Evers, L. (2016). ECMWF SSW forecast evaluation using infrasound. *Journal of Geophysical Research: Atmospheres*, *121*(9), 4637–4650.

Smets, P., & Evers, L. (2014). The life cycle of a sudden stratospheric warming from infrasonic ambient noise observations. *Journal of Geophysical Research: Atmospheres*, *119*(21), 12–084.

Smirnov, A., De Carlo, M., Le Pichon, A., Shapiro, N. M., & Kulichkov, S. (2020). Characterizing the global ocean ambient noise as recorded by the dense seismo-acoustic Kazakh network. *Solid Earth Discussions*, *2020*, 1–25. doi: 10.5194/se-2020-8

Smith, A. K. (2012). Global dynamics of the MLT. *Surveys in Geophysics*, *33*(6), 1177–1230.

Waxler, R., Gilbert, K., Talmadge, C., & Hetzer, C. (2007). The effects of the finite depth of the ocean on microbarom signals. In *8th International Conference on Theoretical and Computational Acoustics (ICTCA), Crete, Greece.*

Whitaker, R. W., & Mutschlecner, J. P. (2008). A comparison of infrasound signals refracted from stratospheric and thermospheric altitudes. *Journal of Geophysical Research: Atmospheres*, *113*(D8).

Xiong, J., Wan, W., Ding, F., Liu, L., Hu, L., & Yan, C. (2018). Two day wave traveling westward with wave number 1 during the sudden stratospheric warming in january 2017. *Journal of Geophysical Research: Space Physics*, *123*(4), 3005–3013.

Zülicke, C., Becker, E., Matthias, V., Peters, D. H., Schmidt, H., Liu, H.-L., ... Mitchell, D. M. (2018). Coupling of stratospheric warmings with mesospheric coolings in observations and simulations. *Journal of Climate*, *31*(3), 1107–1133.

Résumé : Des signaux infrasons sont enregistrés en continu par les stations du Système de Surveillance International (SSI). Entre 0.1 et 0.6 Hz, des signaux cohérents d'origine océanique, appelés microbaroms, dominent ces enregistrements. L'objectif de cette thèse est de caractériser ces sources de bruit cohérent pour aider à l'analyse des signaux d'intérêt dans le cadre du Traité d'Interdiction Complète des Essais nucléaires. Basés sur les interactions non linéaires de vagues, les modèles de sources existants considèrent soit un océan de profondeur infinie et un rayonnement dépendant de l'angle d'élévation, soit un rayonnement monopolaire impliquant un effet important de la bathymétrie. Ces modèles sont étendus pour combiner les effets de bathymétrie et de directivité de la source. Le nouveau modèle de source prédit un impact négligeable de la bathymétrie sur les ondes acoustiques rasantes qui représentent l'essentiel de l'énergie acoustique enregistrée. Un modèle global est implémenté en intégrant un terme d'interaction de vagues, un modèle de source et des effets d'atténuation atmosphérique. Une validation quantitative est réalisée en comparant les spectres directionnels modélisés avec l'ensemble des observations du réseau du SSI sur une période de sept ans. Cette thèse montre que le nouveau modèle de source est plus performant que les précédents et que l'intégration de réflexion à la côte dans le modèle de vagues et de l'atténuation atmosphérique dépendante du vent améliorent les prédictions. Au-delà des aspects de surveillance opérationnelle, ce travail ouvre des perspectives pour caractériser en continu, et à l'échelle globale, les effets de propagation dans la moyenne atmosphère.

Abstract: Infrasound signals are continuously detected by the International Monitoring System (IMS) network. Between 0.1 and 0.6 Hz, coherent signals originating from the ocean, known as microbaroms, dominate the recorded signals. This thesis aims at better characterizing these sources of coherent noise for discrimination purpose in the framework of the Comprehensive nuclear Test Ban Treaty. Different theoretical microbarom models had been previously developed based on second-order non-linear interactions of ocean waves. While early theories considered an infinite ocean depth and a source radiation depending on the acoustic wave elevation angle, other works have found a significant effect of the water depth by considering a monopolar radiation. This thesis extends these models by combining the effects of both finite depth and source directivity. The new source model predicts that the water depth has a negligible effect for the near-horizontally propagating acoustic waves that dominate the recorded microbarom signals. A global model of microbaroms arrivals at ground stations is set up including ocean wave models, source models and atmospheric attenuation effects. A quantitative validation is performed by comparing modelling results with microbaroms detected by the IMS infrasound network over seven years. This thesis demonstrates that the new source model performs better than previous ones, and that the predictions are further enhanced by using wind-dependent attenuation and an ocean wave model including coastal reflection. Beyond operational monitoring objectives, this work offers new perspectives to globally and continuously characterize infrasound propagation effect in the middle atmosphere.